POLITECNICO
MILANO 1863

School of Civil, Environmental and Land Management Engineering
Master of Science in Civil Engineering

A 2D INVERSION PROCEDURE OF ACCELERATIONS TO DEVELOP A DYNAMIC LOAD SPECTRUM FOR UNDERGROUND TRAINS IN THE CITY OF MILAN

MSc THESIS BY:
Werner Andrés ARIZMENDI CASTRO
Matr. n. 214450

ADVISOR:
Prof. Luca MARTINELLI

CO-ADVISOR:
Eng. Valerio MAUGERI

ACADEMIC YEAR 2024-25

Abstract

Complaints related to ground-borne vibrations have been reported along Lines M1 and M2 of the Milan metro system. While previous studies have focused on a typical section of Line M1 near Corso Buenos Aires, no specific investigations have been conducted on other sections of the M1 or M2 lines, despite similar vibration concerns. Moreover, no academic work has applied the inversion procedure to estimate the dynamic load spectrum for Milan's underground network. This study addresses that gap by applying an inversion procedure to in-situ acceleration measurements collected at seven tunnel sections across Lines M1 and M2. A two-dimensional (2D) finite element model is used to compute the load–acceleration transfer functions required for the inversion, due to its computational efficiency and suitability for parametric analysis. The resulting dynamic load spectra are then compared across sections and validated against the UNI 11389 standard. Frequency-domain analysis of the measured responses revealed recurring spectral features. A consistent peak around 60 Hz appeared in nearly all sections, independent of track type, which is associated with the resonance of the unsprung mass in the wheel–track system. A secondary peak near 100 Hz was observed mainly in ballasted track sections, suggesting a resonance effect linked to the ballast layer. The study also examined the influence of tunnel geometry, depth, and elastomeric pad stiffness normalization. Circular tunnel sections, typically shallower and with ballastless track types, showed slightly higher response magnitudes in the 20–140 Hz range compared to deeper, box-shaped sections. While most of the dynamic load spectra showed a similar order of magnitude to the UNI 11389 standard, none of the analysed spectral trends matched the standard's curve. This discrepancy is attributed to the fact that the standard was developed under experimental conditions different from those in this study. This work suggests that the proposed 2D inversion procedure of accelerations provides valuable insights into the dynamic behaviour of tunnel sections and enables efficient parametric comparisons.

Acknowledgements

Three years ago, I made the decision to radically change my life. I left my job, my home, my family, and my country to explore new places and experiences. My main motivation was to deepen my understanding of structural engineering and to develop my skills in an international environment with diverse perspectives. It had also been a dream of mine to live in Europe, and particularly in Italy. The path was not easy, I must admit. In the beginning, adapting was very difficult: learning to live alone, facing the language barrier, experiencing culture shock, and feeling like I was missing out on the moments happening back home without me. However, looking back, I can confidently say that I don't regret the path I chose. Academically, I've learned to understand the logical foundations behind structural engineering and to think like an engineer in every new project I face. Personally, I've gained a great deal of self-confidence and met wonderful people and friends I know will last a lifetime. I've come to see that even though we come from different places, deep down we are all very similar. We miss our families, we enjoy time with our friends, and we all dream of a better future.

If there's someone I must thank above all for this great opportunity, and for all the good things in my life, it's my parents: Guadalupe and Andrés. They have been my support through every fall, helping me get back on my feet. Through their example and their words, they've taught me the value of hard work and the importance of maintaining a positive attitude, even when facing apparently unbeatable challenges. From school to university, from work to now my master's degree, they have never left me alone. They are my greatest support in life. I also want to thank my sister, Angela, with whom I grew up until I decided to move to Italy. Her words of encouragement and willingness to help, even from afar, have meant a lot to me. These three are the people I love most in the world.

I must also thank my uncles, aunts, and my grandmother. Their words of support and advice have been invaluable over these three years. Of course, I am also grateful for my friends, both those in Peru and the ones I've met here. With the latter, I've shared unforgettable moments: from helping each other prepare for exams to simply being there when spirits were low. With them, I've felt like I had a second home.

A special mention goes to my advisor, Valerio Maugeri, who has supported me throughout the nine months of this thesis, always providing the necessary guidance and being available to answer my questions with thoughtful and accurate feedback. His support has been essential for the completion of this work. I also thank Professor Luca Martinelli for the opportunity to work on this thesis topic and for the resources provided throughout the project. Finally, I want to thank the Politecnico di Milano for giving me the opportunity to grow and develop both professionally and personally.

Content

List of Figures

List of Tables

Chapter 1
Introduction

The constant population growth, together with the industrialization of society, has led to the most densely populated cities in human history. This has prompted many urban areas to invest in more efficient transportation systems. Among the most effective, underground railways offer a promising solution, as they help alleviate traffic congestion, reduce noise and air pollution, and serve densely built-up areas [1].

The most common type of these systems is the underground tunnel railway, also known as metro or subway lines, which have seen rapid expansion in recent years [2]. This is true for the city of Milan, which inaugurated its first metro line, Line 1 (M1), in 1964. It initially featured 21 stations along 11.8 km, running from Lotto station in the west to Sesto Marelli in the northeast, passing through the city centre at Duomo station. This line has undergone several extensions, with the latest completed in 2005. Milan's second metro line, M2, was opened in 1969, connecting the eastern part of the city (Caiazzo station) to Cascina Gobba, and was later extended to the southwest with work finished in 2005. The system is now composed of five lines: M1, M2, M3, M4, and M5 [3].

Despite their many advantages, underground railways pose some important challenges, particularly related to ground-borne vibrations. As trains travel through tunnels, vibrations are generated that can be felt not only within the train but also at the surface and in nearby buildings. These vibrations may cause discomfort to residents or even malfunctions in sensitive equipment near the tunnels [4]. A thorough understanding of ground-borne vibrations is therefore essential—not only for environmental noise control but also to ensure the long-term serviceability of tunnel structures subjected to repeated train traffic loading [5].

In Milan, complaints related to ground-borne vibrations have been increasing, particularly near metro lines M1 and M2. The platform *Missione Rumore* has collected reports between January 2021 and June 2024 [6] as illustrated in **Figure 1.1**. Most alerts are located along the older M1 (red) and M2 (green) lines. This trend underscores the need to understand the causes of vibration increases and to assess the effectiveness of mitigation strategies [7].

To simulate and analyse ground vibrations caused by underground trains, several predictive models have been proposed in the literature. Analytical and semi-analytical models were among the first used to describe the dynamic interaction between trains, tunnels, and surrounding soil. While these methods are computationally efficient and useful for conceptual or parametric studies, they are typically based on idealized assumptions, which limits their applicability to specific geometries, soil conditions, or loading frequencies. The Finite Element Method (FEM), on the other hand, is a powerful numerical technique that can model complex geometries, layered soils, and nonlinear material behaviour. FEM is widely used for site-specific, detailed analyses of tunnel–track–soil interaction.

In the context of Milan's metro system, 2D plane strain FEM models have been used in parametric studies to examine the influence of the water table level, partial saturation, and tunnel geometry on

vibration levels [8][9]. Although 3D FEM models offer greater accuracy, they are often computationally expensive, leading researchers to adopt 2D approaches [10]. A recent report used in-situ acceleration measurements, provided by *Metropolitana Milanese SpA*, to estimate the dynamic load spectrum by inverting the measured data through a transfer function derived from a 2D FEM model [11]. The resulting dynamic spectrum was then compared to the one prescribed in the UNI-11389 standard [12].

However, these studies focused only on a typical M1 section near Corso Buenos Aires. No specific studies have been conducted on other sections of the M1 or on sections of the M2 line, where vibration complaints have also been reported. Additionally, no academic studies have applied the inversion procedure to estimate the dynamic load spectrum for the city of Milan. In [11], it is noted that while the measured dynamic spectrum resembles the standard, discrepancies exist. These may be originated from differences in test conditions or from the limitations of 2D models in capturing fully 3D dynamic behaviour. Expanding this methodology to other tunnel sections could help clarify these discrepancies.

This research aims to investigate the key factors influencing ground-borne vibrations by applying the inversion procedure to estimate dynamic load spectra using in-situ acceleration measurements and 2D FEM models for seven different sections of Milan's metro lines M1 and M2. Specifically, the study addresses the following questions: How does the acceleration response spectrum vary across different sections based on geometry and measurement conditions? Can the observed behaviour of the acceleration spectrum be explained using existing literature? To what extent an elastic 2D plane strain FEM model accurately represents the transfer function, despite its limitations compared to 3D models? Are the dynamic load spectra obtained through the inversion procedure consistent with the UNI-11389 standard and prior studies?

This study contributes to the understanding of ground-borne vibrations by analysing the accelerometric response of various metro sections, helping to identify patterns based on local characteristics. It highlights the effectiveness and limitations of 2D FEM in modelling underground vibrations and provides validation for the inversion method to estimate dynamic spectra. The findings offer valuable insights for refining current standard load spectra, with implications for both academic research and engineering practice.

Despite its aims, the study has limitations. The results may not be directly generalizable to other metro lines without considering local conditions such as soil properties and water table levels. The models assume linear elastic behaviour, longitudinal invariance, and constant geometry and stratigraphy along the tunnel axis. Furthermore, the models do not account for full 3D dynamic effects.

The structure of this thesis is organized as follows: Chapter 1 introduces the research context, defines the problem, and outlines the research aims, significance, limitations, and questions to be addressed. Chapter 2 presents a comprehensive literature review, beginning with an analysis of the main sources of vibrations in underground railways, followed by a review of elastic wave theory, signal processing techniques, modelling strategies, including analytical, numerical, and hybrid approaches, and the theoretical basis of the inversion procedure used to estimate dynamic load spectra. Chapter 3 describes the complete methodology applied in this research, including the geometric and mechanical characterization of the investigated tunnel sections, an overview of the train characteristics, details of the acceleration measurements and signal processing, the development of the 2D finite element models used to calculate transfer functions, and the final inversion procedure to obtain the dynamic load spectrum. Chapter 4 presents and interprets the results, with particular focus on comparisons with the dynamic load spectrum prescribed in the UNI-11389 standard and on

the identification and interpretation of dominant frequency components. Chapter 5 summarizes the main conclusions of the research, and, finally, Chapter 6 contains the complete bibliography of the references used throughout the study.

Figure 1.1 *Milano metro network together with reported alters in "Missione Rumore" platform from [6]*

Chapter 2
Literature review

2.1 Sources of vibration

When dealing with railway-induced vibrations, several factors such as motion induced by quasi-static loads, dynamic interaction between the vehicle, track, and soil, and mechanical degradations or defects can significantly influence and amplify vibration levels. This subchapter discusses the main sources of such vibrations.

2.1.1 Motion induced by the quasi-static loads

One fundamental source of vibration is the motion induced by quasi-static loads. These loads originate from the weight of the train and its components. Although the forces are static in nature, their movement along the track introduces time dependency into the system's response. The resulting vibrations are inherently three-dimensional, as the disturbances propagate not only transversally but also longitudinally along the train's direction of travel [9].

When train speeds approach the critical velocity of the track–soil system, these effects become particularly significant. When a simple dynamic track model is done by considering a Euler Bernoulli beam on elastic foundation, the critical speed can be determined as [13]

$$v_{cr}^2 = \frac{2}{m}\sqrt{kEI} \tag{2.1}$$

Where, m is the rail mass per length, k the track stiffness and EI the bending stiffness.

Studies have been carried out considering more complex coupled models to investigate the influence of the train quasi-static load speed on the vibration response.

For instance, in [14] a numerical model is used to predict railway-induced vibrations by evaluating both quasi-static and dynamic excitations, the latter caused by random track unevenness. The study shows that while quasi-static loads dominate the track response, free-field vibrations are mainly driven by dynamic effects. The model, validated with field data from the Brussels–Köln high-speed line, predicts vibration levels within 5 dB accuracy. The authors conclude that the quasi-static track response increases moderately with the train speed.

Similarly, Zhou et al [4] propose an efficient method to predict vibrations induced by underground trains in a saturated poroelastic half-space, considering both soil saturation and free surface effects. The study combines an analytical train–track–tunnel model with a 2.5D boundary integral formulation using Green's functions. Results show that when train speed is below the Rayleigh wave velocity, tunnel deformation is quasi-static and uniform, except near the train ends. The study highlights that vibration amplitudes rise sharply as train speed approaches the Rayleigh wave velocity.

From the presented studies can be concluded that, for low-speed trains, the quasi-static effect is often negligible, as train velocity typically remains below the critical wave velocity. However, when speeds approach this threshold, substantial vibrations may arise [13].

2.1.2 Dynamic interaction between the vehicle, track and tunnel-soil system

The second major source of vibration is the dynamic interaction between the vehicle, track, and tunnel–soil system. This coupled interaction is particularly significant at frequencies ranging from 0 to 250 Hz [15] . It involves complex dynamic behaviours among the various subsystems: first, within the train itself (i.e., the car body, bogies, and wheelsets), and second, within the track system (i.e., rail pads, sleepers, and ballast or slab). This system is investigated in [13] and illustrated in **Figure 2.1**.

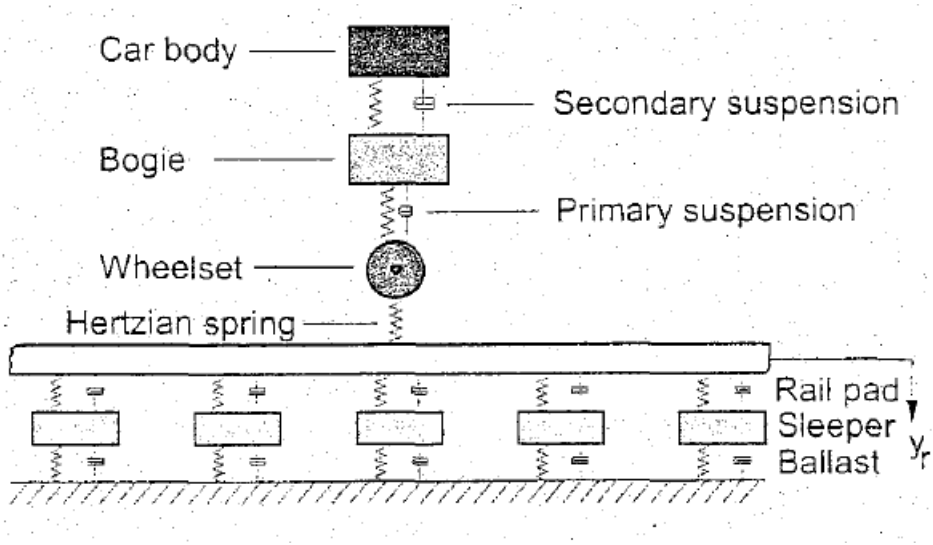

Figure 2.1 *Dynamic model of vehicle-track interaction from [13]*

In [13], the different excitation mechanisms in vehicle–track interactions are explained for ground-level trains. While this study does not consider tunnel–soil interaction, it provides valuable insights into the dynamics of vehicle–track systems. **Figure 2.2** shows how different components of the system respond to different excitation wavelengths. The natural frequency of bogies is around 20–25 Hz, whereas the sprung mass has a lower natural frequency, between 0.7 and 5 Hz, and primarily influences the ballast and subgrade.

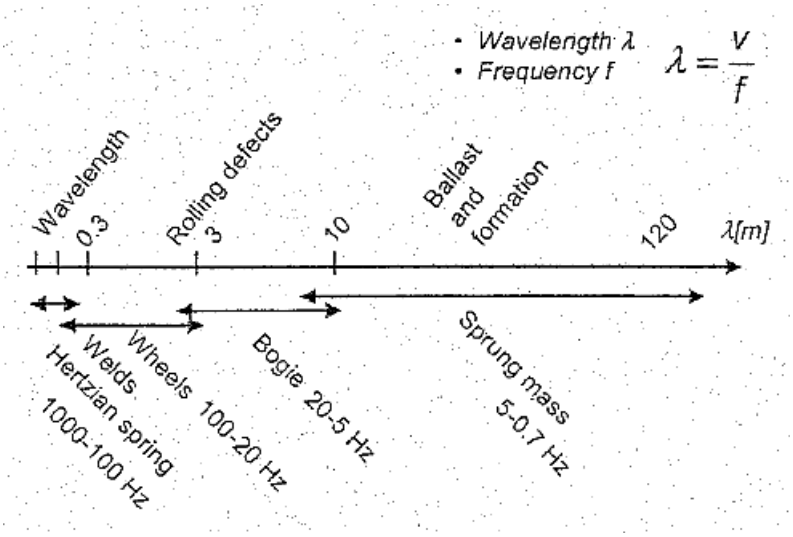

Figure 2.2 *Track excitation in relation to frequency from [13]*

A more recent study on ground-level trains [16] reviews and synthesizes over 230 technical papers related to railway vibration. The authors identify numerous dynamic excitation mechanisms contributing to vibration, as illustrated in **Figure 2.3**. It can be seen that the excitations associated with the locomotive are found at low frequencies and the excitations associated with the wheel, rail and track are found at higher frequencies. These higher frequencies often manifest themselves in the form of air-borne noise, while the lower frequencies generate ground vibration. Bands have been drawn to illustrate a variety of frequency ranges relevant for perception, in accordance with BS ISO 14837. The authors noted that train–track resonant conditions can develop where the natural track frequencies are excited and that these effects and their interaction with the underlying soil are still not fully understood and are currently the focus of much research.

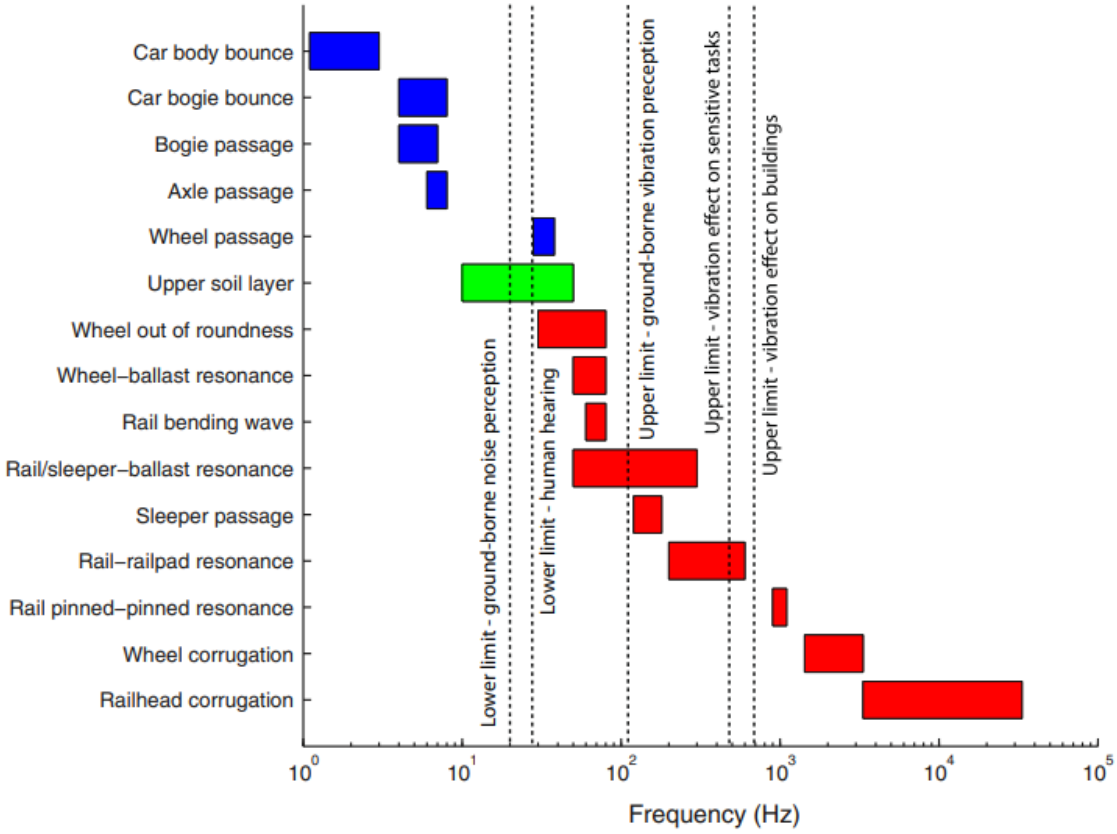

Figure 2.3 *Typical frequency ranges of excitation from [16]*

In the case of underground trains, it is essential to account for the influence of the tunnel–soil system. This coupling introduces modal excitations not present in ground-level configurations. Moreover, ballastless track systems, such as direct fixation and floating slab types, are common in underground railways and must be considered.

In Zhou et al [4] , a train–track–tunnel model is used to study the influence of various parameters, including the effect of floating slab tracks. The study finds that increasing soil permeability reduces vibration amplitudes, and although floating slabs can help isolate vibrations, they may, under certain conditions, amplify transmission instead of attenuating it.

Similarly, Xu et al [17] developed a mixed 2D–3D finite element model to simulate the dynamic interaction between the train, ballastless track, tunnel, and soil. This study compared direct fixation and floating slab systems by incorporating train motion, suspension stiffness, and track irregularities.

It was observed that short-wavelength irregularities significantly affect vibrations in direct fixation tracks due to high-frequency responses, while medium-wavelength irregularities dominate in floating slab systems due to their resonance at lower frequencies. The authors emphasize the importance of accurately characterizing track irregularities: for direct fixation tracks, wheel and rail smoothness is critical, whereas for floating slabs, foundation settlement must be controlled.

Furthermore, in [18] a combination of field measurements and numerical simulations was used to analyse the dynamic response of the track–tunnel–soil system. The study found that dominant vibration frequencies varied among components: the rail showed peaks between 25–400 Hz and 1000–1500 Hz; the track bed had dominant frequencies below 400 Hz; the soil layers below 200 Hz; and the ground surface below 100 Hz. High-frequency vibrations (>500 Hz) attenuated rapidly through the ground. Additionally, a transverse amplification of acceleration was observed at specific distances from the tunnel's upper and lower haunches, and the zone significantly affected by train-induced vibrations in soft soils extended approximately 30 meters from the tunnel.

2.1.3 Mechanical degradation and defects

Mechanical degradation and structural defects in the track or vehicle components can significantly influence the dynamic loads transmitted during train passage. Elements such as fatigue cracks in the rails, damaged or "walking" sleepers, and deterioration in carriage components (e.g., worn wheel bearings or broken gears) can greatly amplify vibration levels [15].

As illustrated in **Figure 2.2**, short-wavelength irregularities, on the order of centimetres, are predominantly caused by rail corrugation, wheel defects, and welding imperfections. These defects excite high-frequency vibrations, sometimes reaching up to 2000 Hz, where the Hertzian contact spring[1] between the wheel and rail must be taken into account due to its nonlinear behaviour. Additionally, rail rolling defects often have wavelengths around 3 meters, contributing to medium-frequency excitation [13].

Several types of track irregularities and mechanical issues contribute to vibration generation. Wheel defects such as wheel-flats, often caused by locked brakes, and out-of-roundness, resulting from manufacturing imperfections or fatigue, can generate high-frequency impacts [16]. Rail surface corrugation, with wavelengths typically ranging from 30 to 100 mm, leads to periodic excitation of the wheel–rail system. In addition, poor welds or joints may result in short-wavelength irregularities (approximately 200 mm), which commonly excite the resonance of the unsprung wagon masses [15]. Medium-wavelength irregularities, ranging from 300 to 1500 mm, are often associated with variations in the stiffness of the rail support, a factor that critically affects the vibration response. If the support stiffness is too low, the ballast and subgrade may undergo excessive strain, potentially causing settlement and long-wavelength irregularities. Conversely, if the support is too stiff, local stress concentrations can lead to short-wavelength corrugation, further amplifying vibration levels [16].

[1] A Hertzian spring is a nonlinear spring that follows Hertzian contact theory. This theory considers a stiffness relationship different from that of a Hookean spring, accounting for the dynamic interaction between the elastic deformation of the steel in the wheel and the rail.

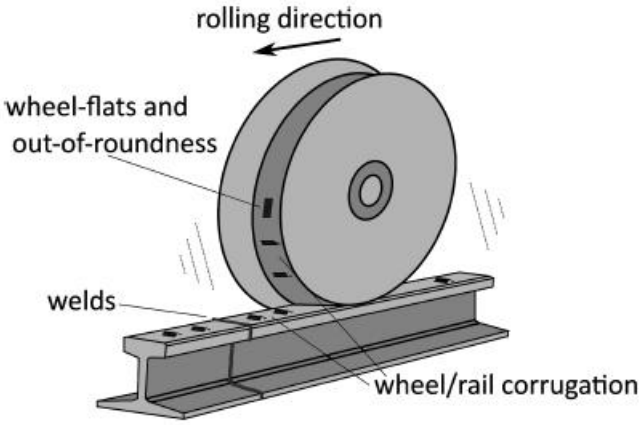

Figure 2.4 *Typical imperfections of the wheel and the rail from [9]*

2.2 Elastic wave theory

The presence of an underground train passage creates a disturbance in the surrounding medium. When a disturbance is generated in an elastic medium, energy is transmitted outward from the origin as a wave that travels without any mass transportation. The characteristics of wave propagation depend on the type of deformation that particles experience, as well as the properties of the medium.

In a three-dimensional unbounded elastic medium, two types of waves can be identified: P-waves, characterized by compressional deformation of particles, which generates motion in the direction of propagation but not in the other two directions; and S-waves, characterized by particle distortion with no volume change **Figure 2.5** . For this reason, S-waves are also known as shear waves, generating motion only in the two directions perpendicular to the direction of propagation, hence they are also called transverse waves. The names P-wave and S-wave are associated with their velocities. P-waves, also known as primary waves, have a higher propagation velocity than S-waves, also called secondary waves, as they arrive second.

For the case of train metro tunnels which are relatively close to the surface, the unbounded infinite domain encounters a discontinuity at the surface. Then, the general solution of the body waves is restricted by a boundary condition at the free surface. This generates two other types of waves whose energy focuses near the surface and decreases exponentially with depth. These are known as Rayleigh and Love waves **Figure 2.5**. Regarding the case of plane waves, assuming the wave propagation is on the x direction and coordinate system as in **Figure 2.8**, the former are characterized for an in-plane particle motion of a retrograde ellipse in the $z - x$ plane, while the latter exhibit an out-of-plane motion in the y direction.

In this subchapter, the derivation of the governing equations for the general case of body waves in a three-dimensional elastic unbounded medium, P waves and S waves, will be detailed following as a reference [19]. From these, the case of surface waves in an elastic half-space domain will be derived, for the interest of this work, only the case of Rayleigh waves in a plane surface will be depicted. These expressions will serve as the fundamental mathematical background for the subsequent linear elastic numerical analysis conducted to estimate wave-induced vibrations.

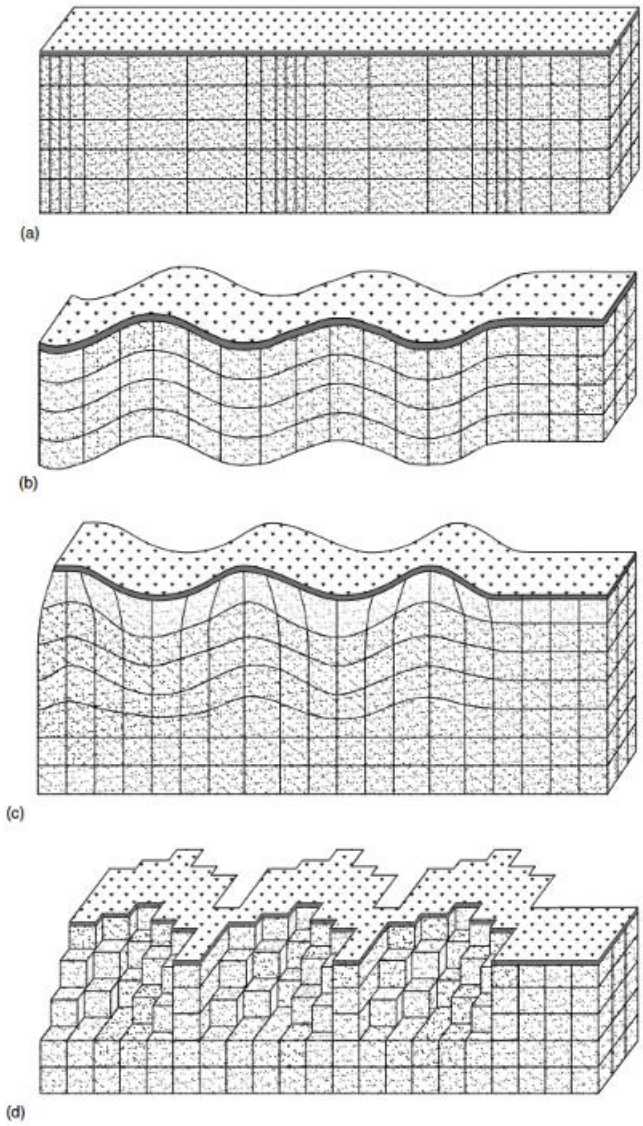

Figure 2.5 *Motion generated by P waves (a), S waves (b), Rayleigh waves (c) and Love waves (d) from [19]*

2.2.1 Body waves in elastic 3D medium

2.2.1.1 Linear elastic problem

The linear elastic problem is set by defining equilibrium, kinematic compatibility, constitutive laws, and boundary conditions for an infinitesimal element. To begin, let's consider an infinitesimal element of dimensions dx, dy and dz where stress components are applied on each face according to the cartesian system. This is also known as the Cauchy stress tensor and defines the complete state of stresses of this element. Its graphical representation together with the stress convention adopted is shown in Figure 2.6.

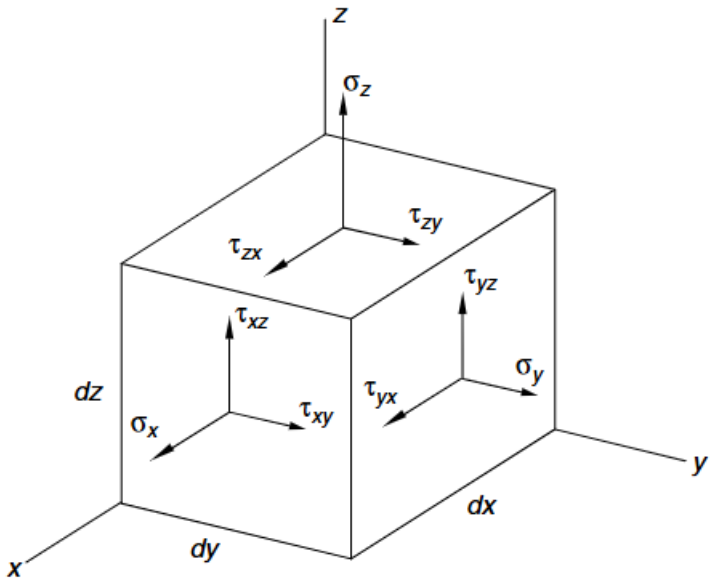

Figure 2.6 *Stress convention for the Cauchy stress tensor from [19]*

For this stress convention σ_x, σ_y , σ_z represent the three normal stress components and τ_{xy}, τ_{xz}, τ_{yz}, τ_{yx}, τ_{zx}, τ_{zy} the six shear stress components. By applying the rotational equilibrium, it can be easily derived that

$$\tau_{xy} = \tau_{yx} \qquad \tau_{xz} = \tau_{zx} \qquad \tau_{yz} = \tau_{zy} \tag{2.2}$$

Hence, the number of independent components can be reduced to six to define the state of stresses in the element.

The equilibrium equations can be derived by considering a disturbance of the infinitesimal element as in **Figure 2.7**.

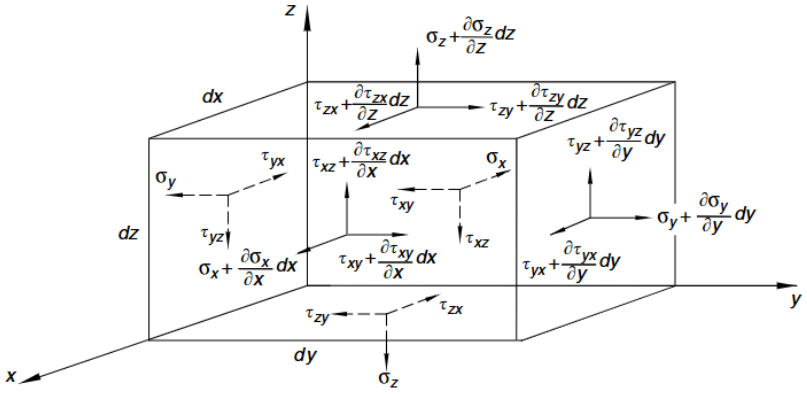

Figure 2.7 *Free body diagram of three-dimensional differential element from [19]*

By applying Newton's law for each of the Cartesian directions, where u, v, w represent the three displacement components in the x, y, z directions respectively and ρ is the material density, the resulting equilibrium equations are the following.

$$\frac{\partial \sigma_x}{\partial x} + \frac{\partial \tau_{yx}}{\partial y} + \frac{\partial \tau_{zx}}{\partial z} = \rho \frac{\partial^2 u}{\partial t^2} \tag{2.3}$$

$$\frac{\partial \sigma_y}{\partial y} + \frac{\partial \tau_{xy}}{\partial x} + \frac{\partial \tau_{zy}}{\partial z} = \rho \frac{\partial^2 v}{\partial t^2} \tag{2.4}$$

$$\frac{\partial \sigma_z}{\partial z} + \frac{\partial \tau_{xz}}{\partial x} + \frac{\partial \tau_{yz}}{\partial y} = \rho \frac{\partial^2 w}{\partial t^2} \tag{2.5}$$

The second set of equations to solve the problem are the kinematic compatibility ones. These describes the continuity within an element and can be determined by six independent strain components: the normal strains ε_x, ε_y, ε_z and the shear strains and γ_{xy}, γ_{yz}, γ_{zx}. These strain components are related to the corresponding displacements as follows:

$$\varepsilon_x = \frac{\partial u}{\partial x} \qquad \varepsilon_y = \frac{\partial v}{\partial y} \qquad \varepsilon_z = \frac{\partial w}{\partial z} \tag{2.6}$$

$$\gamma_{xy} = \frac{\partial v}{\partial x} + \frac{\partial u}{\partial y} \qquad \gamma_{yz} = \frac{\partial w}{\partial y} + \frac{\partial v}{\partial z} \qquad \gamma_{zx} = \frac{\partial u}{\partial z} + \frac{\partial w}{\partial x} \tag{2.7}$$

In the same way, the three displacement components relate with the rigid body rotations about each axis can be written as:

$$\bar{\omega}_x = \frac{1}{2}\left(\frac{\partial w}{\partial y} - \frac{\partial v}{\partial z}\right) \qquad \bar{\omega}_y = \frac{1}{2}\left(\frac{\partial u}{\partial z} - \frac{\partial w}{\partial x}\right) \qquad \bar{\omega}_z = \frac{1}{2}\left(\frac{\partial v}{\partial x} - \frac{\partial u}{\partial y}\right) \tag{2.8}$$

The third set are the constitutive laws, these relate the stresses and strains by means of the generalized Hooke's law for an elastic, homogeneous and isotropic material. The normal strains and stresses are related by the following expressions.

$$\varepsilon_x = \frac{1}{E}[\sigma_x - \nu(\sigma_y + \sigma_z)] \qquad \varepsilon_y = \frac{1}{E}[\sigma_y - \nu(\sigma_x + \sigma_z)] \qquad \varepsilon_z = \frac{1}{E}[\sigma_z - \nu(\sigma_x + \sigma_y)] \tag{2.9}$$

Where E and ν are the Young and Poisson modulus respectively. The shear strains and stresses are related with the following expressions

$$\gamma_{xy} = \frac{\tau_{xy}}{G} \qquad \gamma_{yz} = \frac{\tau_{yz}}{G} \qquad \gamma_{zx} = \frac{\tau_{zx}}{G} \tag{2.10}$$

Where G is the shear modulus. Equations (2.9) can be rearranged to obtain the stresses in terms of strains as in equations (2.11).

$$\sigma_x = \lambda\bar{\varepsilon} + 2G\varepsilon_x \qquad \sigma_y = \lambda\bar{\varepsilon} + 2G\varepsilon_y \qquad \sigma_z = \lambda\bar{\varepsilon} + 2G\varepsilon_z \tag{2.11}$$

$$\lambda = \frac{\nu E}{(1+\nu)(1-2\nu)} \tag{2.12}$$

$$G = \frac{E}{2(1+\nu)} \tag{2.13}$$

$$\bar{\varepsilon} = \varepsilon_x + \varepsilon_y + \varepsilon_z \tag{2.14}$$

Where the terms (2.12) and (2.13) are known as the Lame's constants and $\bar{\varepsilon}$, under the assumption of small strains and displacements, represents the volumetric strain i.e. the ratio of the volume variation due to the applied stresses with respect to the original volume.

2.2.1.2 Governing equations

Once the general linear elastic problem is set, it is possible to determine the equations of motion for the differential three-dimensional element in an unbounded medium. To this end, is convenient to express the equilibrium equations in terms of displacements and strains. By replacing equations (2.2),(2.10) and (2.11) in (2.3) the following expression can be obtained.

$$\frac{\partial(\lambda\bar{\varepsilon} + 2G\varepsilon_x)}{\partial x} + \frac{\partial G\gamma_{xy}}{\partial y} + \frac{\partial G\gamma_{zx}}{\partial z} = \rho\frac{\partial^2 u}{\partial t^2} \tag{2.15}$$

By replacing (2.6) and (2.7) the expression (2.15) can be expressed as

$$\lambda\frac{\partial\bar{\varepsilon}}{\partial x} + G\left(\frac{\partial^2 u}{\partial x^2} + \frac{\partial^2 v}{\partial x\partial y} + \frac{\partial^2 w}{\partial x\partial z}\right) + G(\frac{\partial^2 u}{\partial x^2} + \frac{\partial^2 u}{\partial y^2} + \frac{\partial^2 u}{\partial z^2}) = \rho\frac{\partial^2 u}{\partial t^2} \tag{2.16}$$

The expression (2.16) can be rearranged in terms of $\bar{\varepsilon}$ and by used of the Laplacian operator in compact form as

$$(\lambda + G)\frac{\partial\bar{\varepsilon}}{\partial x} + G\nabla^2 u = \rho\frac{\partial^2 u}{\partial t^2} \tag{2.17}$$

In the same way, equations (2.4) and (2.5) can written as

$$(\lambda + G)\frac{\partial\bar{\varepsilon}}{\partial y} + G\nabla^2 v = \rho\frac{\partial^2 v}{\partial t^2} \tag{2.18}$$

$$(\lambda + G)\frac{\partial\bar{\varepsilon}}{\partial z} + G\nabla^2 w = \rho\frac{\partial^2 w}{\partial t^2} \tag{2.19}$$

Starting from these general equations of motion, boundary conditions can be applied to obtain the particular solutions associated with each type of wave. The derivations for each case are explained in the following subchapter.

2.2.1.3 P waves

From the general equations of motion derived before, some particular solutions can be obtained by imposing chosen boundary conditions. In particular, the rigid body rotations can be restricted in all directions by making expressions (2.8) equal to zero.

$$\bar{\omega}_x = \bar{\omega}_y = \bar{\omega}_z = 0 \tag{2.20}$$

For simplicity in the mathematical manipulation, is convenient to define the displacement components in terms of a potential function φ

$$u = \frac{\partial \varphi}{\partial x} \qquad v = \frac{\partial \varphi}{\partial y} \qquad w = \frac{\partial \varphi}{\partial z} \tag{2.21}$$

Given that in such a case we have for rotation in x

$$\bar{\omega}_x = \frac{1}{2}\left(\frac{\partial w}{\partial y} - \frac{\partial v}{\partial z}\right) = \frac{1}{2}\left(\frac{\partial^2 \varphi}{\partial y \partial z} - \frac{\partial^2 \varphi}{\partial y \partial z}\right) = 0 \tag{2.22}$$

And similarly, for $\bar{\omega}_y$ and $\bar{\omega}_z$. By replacing (2.21) in (2.14) it results in

$$\bar{\varepsilon} = \frac{\partial^2 \varphi}{\partial x^2} + \frac{\partial^2 \varphi}{\partial y^2} + \frac{\partial^2 \varphi}{\partial z^2} = \nabla^2 \varphi \tag{2.23}$$

While applying the first derivatives with respect to x, y and z the following expression can be derived.

$$\frac{\partial \bar{\varepsilon}}{\partial x} = \frac{\partial^2 (\partial \varphi / \partial x)}{\partial x^2} + \frac{\partial^2 (\partial \varphi / \partial x)}{\partial y^2} + \frac{\partial^2 (\partial \varphi / \partial x)}{\partial z^2} = \nabla^2 u \tag{2.24}$$

$$\frac{\partial \bar{\varepsilon}}{\partial y} = \frac{\partial^2 (\partial \varphi / \partial y)}{\partial x^2} + \frac{\partial^2 (\partial \varphi / \partial y)}{\partial y^2} + \frac{\partial^2 (\partial \varphi / \partial y)}{\partial z^2} = \nabla^2 v \tag{2.25}$$

$$\frac{\partial \bar{\varepsilon}}{\partial z} = \frac{\partial^2 (\partial \varphi / \partial z)}{\partial x^2} + \frac{\partial^2 (\partial \varphi / \partial z)}{\partial y^2} + \frac{\partial^2 (\partial \varphi / \partial z)}{\partial z^2} = \nabla^2 w \tag{2.26}$$

Then, by replacing (2.24), (2.25) and (2.26) in (2.17), (2.18) and (2.19) respectively the following relations can be obtain

$$\frac{\partial^2 u}{\partial t^2} = v_p^2 \nabla^2 u \tag{2.27}$$

$$\frac{\partial^2 v}{\partial t^2} = v_p^2 \nabla^2 v \tag{2.28}$$

$$\frac{\partial^2 w}{\partial t^2} = v_p^2 \nabla^2 w \tag{2.29}$$

Where v_p is constant defined as

$$v_p = \sqrt{\frac{\lambda + 2G}{\rho}} \tag{2.30}$$

By replacing the expressions (2.12) and (2.13) in (2.30) the constant v_p can be written as

$$v_p = \sqrt{\frac{E(1-\nu)}{\rho(1+\nu)(1-2\nu)}} \tag{2.31}$$

For a better interpretation of the equations is convenient to transform them into spherical coordinates by means of the following expression.

$$r^2 = x^2 + y^2 + z^2 \tag{2.32}$$

After some mathematical manipulations explained in detail in [19] the expressions (2.27) through (2.29) can be expressed as

$$\frac{\partial^2(ru)}{\partial t^2} = v_p^2 \frac{\partial^2(ru)}{\partial r^2} \tag{2.33}$$

$$\frac{\partial^2(rv)}{\partial t^2} = v_p^2 \frac{\partial^2(rv)}{\partial r^2} \tag{2.34}$$

$$\frac{\partial^2(rw)}{\partial t^2} = v_p^2 \frac{\partial^2(rw)}{\partial r^2} \tag{2.35}$$

These differential equations have a solution of the form.

$$ru = F_{pu}(r - v_p t) + G_{pu}(r + v_p t) \tag{2.36}$$

$$rv = F_{pv}(r - v_p t) + G_{pv}(r + v_p t) \tag{2.37}$$

$$rw = F_{pw}(r - v_p t) + G_{pw}(r + v_p t) \tag{2.38}$$

Where F_{pu}, F_{pv}, F_{pw} and G_{pu}, G_{pv}, G_{pw} are arbitrary functions of $r - v_p t$ and $r + v_p t$ respectively, which depend on the initial conditions of the problem. Finally, the displacement in each of the Cartesian directions from the aforementioned equations can written as:

$$u = \frac{1}{r}(F_{pu}(r - v_p t) + G_{pu}(r + v_p t)) \tag{2.39}$$

$$v = \frac{1}{r}(F_{pv}(r - v_p t) + G_{pv}(r + v_p t)) \tag{2.40}$$

$$w = \frac{1}{r}(F_{pw}(r - v_p t) + G_{pw}(r + v_p t)) \tag{2.41}$$

The equations from (2.39) to (2.41) indicate that an initial disturbance in an unbounded elastic medium propagates in all directions with a waveform velocity equal to v_p. Furthermore, these displacements decay proportionally with the radial distance r from the origin. From (2.31), it can be seen that this propagation velocity depends on the modulus of elasticity, Poisson's ratio, and the material density. Moreover, these equations are valid under the assumption that rigid body rotations are zero while the volumetric strain is non-zero. This indicates that particle motion results from volumetric expansions and contractions, with no rotational movement (**Figure 2.5**). This type of wave, which induces particle motion in the direction of propagation and not in the two perpendicular directions, is known as a primary wave or P wave.

2.2.1.4 S waves

Considering the condition where the volumetric strain is equal to zero $\bar{\varepsilon} = 0$, a second particular solution can be obtained by applying this condition to equations (2.17) to (2.19). After some mathematical manipulations, the following expressions are derived.

$$\frac{\partial^2 u}{\partial t^2} = v_s^2 \nabla^2 u \tag{2.42}$$

$$\frac{\partial^2 v}{\partial t^2} = v_s^2 \nabla^2 v \tag{2.43}$$

$$\frac{\partial^2 w}{\partial t^2} = v_s^2 \nabla^2 w \tag{2.44}$$

Where v_s is a constant define as

$$v_s = \sqrt{\frac{G}{\rho}} \tag{2.45}$$

By replacing the expression (2.13) in (2.45) the constant v_s can be written as

$$v_s = \sqrt{\frac{E}{2\rho(1+\nu)}} \tag{2.46}$$

Similarly, is convenient to express equations from (2.42) to (2.44) in spherical coordinates by means of the expression (2.32). The resultant expressions are the following.

$$\frac{\partial^2 (ru)}{\partial t^2} = v_s^2 \frac{\partial^2 (ru)}{\partial r^2} \tag{2.47}$$

$$\frac{\partial^2 (rv)}{\partial t^2} = v_s^2 \frac{\partial^2 (rv)}{\partial r^2} \tag{2.48}$$

$$\frac{\partial^2 (rw)}{\partial t^2} = v_s^2 \frac{\partial^2 (rw)}{\partial r^2} \tag{2.49}$$

Where the solutions to these classical wave differential equations corresponds to the following expressions.

$$u = \frac{1}{r}(F_{su}(r - v_s t) + G_{su}(r + v_s t)) \tag{2.50}$$

$$v = \frac{1}{r}(F_{sv}(r - v_s t) + G_{sv}(r + v_s t)) \tag{2.51}$$

$$w = \frac{1}{r}(F_{sw}(r - v_s t) + G_{sw}(r + v_s t)) \tag{2.52}$$

Where F_{su}, F_{sv}, F_{sw} and G_{pu}, G_{pv}, G_{pw} are arbitrary functions of $r - v_s t$ and $r + v_s t$ respectively, which depend on the initial conditions of the problem.

Expressions from (2.50) to (2.52) reveal the presence of another type of wave distinct from P waves. This type of wave also decreases proportionally with the distance r but travels at a velocity equal to the constant v_s. From expression (2.45) , it can be observed that this velocity depends on the shear modulus G and the density of the material. Given that, for this kind of wave, the assumption

is that the volumetric strain is zero while the rotations are non-zero, it can be inferred that the particle motion is due to distortions with no volumetric changes. Moreover, this indicates that the particle motion occurs only in the two directions perpendicular to the propagation direction (**Figure 2.5**).

The relation between the velocities of these two types of waves can be obtained by dividing (2.31) by (2.44) as follows.

$$\frac{v_p}{v_s} = \sqrt{\frac{2(1-\nu)}{1-2\nu}} \tag{2.53}$$

It can be observed that for any admissible value of ν the expression (2.53) is always greater than one. For that reason, since this type of wave always arrives after the P waves, it is known as the secondary wave or simply the S wave.

For convenience, the S waves are often decomposed in their two perpendicular components and for the case of plane waves, the component contained in the horizontal plane is known as SH, while the one contained in the vertical plane is known as SV.

It is worth mentioning that both solutions derived above satisfy the general differential equations of motion for a three-dimensional element in an elastic unbounded medium. Hence, according to the theory of differential equations, the general solution is a linear combination of both. However, due to the difference in wave propagation velocities, they tend to separate as they travel away from the initial disturbance. For this reason, they are typically analysed separately in practical cases.

2.2.2 Surface waves in elastic half-space

Until this moment, wave motion has been considered in an unbounded three-dimensional space. However, in the context of ground-borne vibrations caused by underground trains, tunnels are usually located relatively close to the surface. In this sense, a more accurate representation for studying wave behaviour involves considering a semi-infinite medium. The presence of a surface imposes a boundary condition that generates another type of wave, known as surface waves. In the present study, a two-dimensional analysis in a semi-infinite space will be performed. Consequently, the expressions governing surface waves will be derived specifically for the case of plane waves.

2.2.2.1 Governing equations for plane waves

Let's consider a semi-infinite elastic domain and that the displacement components u and w do not vary along the y direction. In this sense, the value of the displacement component v is equal to zero. Moreover, let's assume the motion propagates positively in the x direction, causing the particle motion to occur in the x-z as in Figure 2.8.

In order to decoupled equations of motion (2.17) and (2.19) it is convenient to express the displacement components in terms of potential functions Φ and Ψ.

$$u = \frac{\partial \Phi}{\partial x} + \frac{\partial \Psi}{\partial z} \tag{2.54}$$

$$w = \frac{\partial \Phi}{\partial z} - \frac{\partial \Psi}{\partial x} \tag{2.55}$$

By doing so, the volumetric strain can be expressed as:

$$\bar{\varepsilon} = \frac{\partial u}{\partial x} + \frac{\partial w}{\partial z} = \frac{\partial}{\partial x}\left(\frac{\partial \Phi}{\partial x} + \frac{\partial \Psi}{\partial z}\right) + \frac{\partial}{\partial z}\left(\frac{\partial \Phi}{\partial z} - \frac{\partial \Psi}{\partial x}\right) = \frac{\partial^2 \Phi}{\partial x^2} + \frac{\partial^2 \Phi}{\partial z^2} = \nabla^2 \Phi \tag{2.56}$$

By replacing (2.54) and (2.55) in (2.17) and (2.19) and after some mathematical manipulations the following equations can be derived

$$\frac{\partial^2 \Phi}{\partial t^2} = v_p^2 \left(\frac{\partial^2 \Phi}{\partial x^2} + \frac{\partial^2 \Phi}{\partial z^2}\right) \tag{2.57}$$

$$\frac{\partial^2 \Psi}{\partial t^2} = v_s^2 \left(\frac{\partial^2 \Psi}{\partial x^2} + \frac{\partial^2 \Psi}{\partial z^2}\right) \tag{2.58}$$

Where v_p and v_s are defined as (2.30) and (2.45) respectively. Now the equations of motion are decoupled in terms of the potential functions Φ and Ψ reduced for the plane x-z wave case.

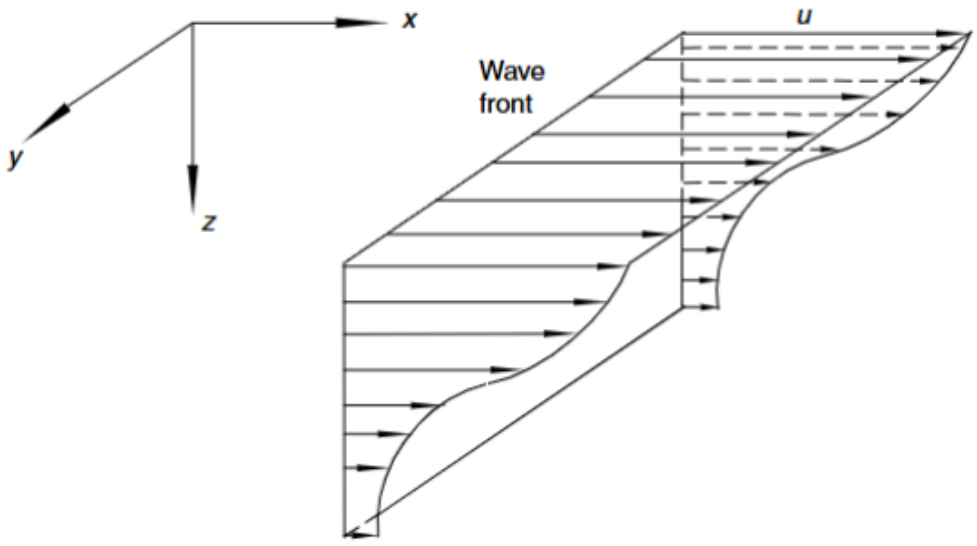

Figure 2.8 *Front of plane wave propagation from [19]*

2.2.2.2 Rayleigh waves

The solution that complies with the decoupled equations (2.56) and (2.57) may be expressed as an infinite sum of sins and cosines in the compact Eulerian form as:

$$\Phi = F(z)e^{i(kx-\omega t)} \tag{2.59}$$

$$\Psi = G(z)e^{i(kx-\omega t)} \tag{2.60}$$

Where $F(z)$ and $G(z)$ are functions that indicates the variation of the wave's amplitude by depth, e is the Euler's number, i is the imaginary unit, and k, ω and λ are the wave number, circular

frequency and wavelength respectively. Then by replacing (2.59) and (2.60) into (2.57) and (2.58) the following expressions can be obtained.

$$F''(z) - q^2 F(z) = 0 \tag{2.61}$$

$$G''(z) - s^2 G(z) = 0 \tag{2.62}$$

Where q^2 and s^2 are equal to

$$q^2 = k^2 - \frac{\omega^2}{v_p^2} \tag{2.63}$$

$$s^2 = k^2 - \frac{\omega^2}{v_s^2} \tag{2.64}$$

Then by recalling the definition of wave number

$$k = \frac{\omega}{v_R} \tag{2.65}$$

Where v_R is the velocity of Rayleigh of investigation. By means of (2.65) the expressions (2.63) and (2.64) can be written as follows

$$q^2 = \frac{\omega^2}{v_R^2}(1 - \alpha^2 V^2) \tag{2.66}$$

$$s^2 = \frac{\omega^2}{v_R^2}(1 - V^2) \tag{2.67}$$

Where α^2 and V are defined as

$$\alpha^2 = \frac{v_s^2}{v_p^2} = \frac{G}{\lambda + 2G} = \frac{1 - 2\nu}{2(1 - \nu)} \tag{2.68}$$

$$V = \frac{v_R}{v_s} \tag{2.69}$$

The solution for the expressions (2.61) and (2.62) are the ones of the typical second order ordinary differential equation of the form

$$F(z) = A_1 e^{-qz} + A_2 e^{qz} \tag{2.70}$$

$$G(z) = B_1 e^{-qz} + B_2 e^{qz} \tag{2.71}$$

Where A_1, A_2, B_1 and B_2 are general constants. Since the functions $F(z)$ and $G(z)$ cannot grow to infinity, as that would imply that displacement components u and w also grow up to infinity with depth, and given that, as derived in Section 2.2.1, they should decrease inversely proportional with depth, the constants A_2 and B_2 must be equal to zero. Then the equations (2.70) and (2.71) can be written as

$$F(z) = A_1 e^{-qz} \tag{2.72}$$

$$G(z) = B_1 e^{-qz} \tag{2.73}$$

Then the potential functions can be written as

$$\Phi = A_1 e^{-qz} e^{i(kx-\omega t)} \tag{2.74}$$

$$\Psi = B_1 e^{-sz} e^{i(kx-\omega t)} \tag{2.75}$$

Due to the presence of a free surface in the bounded medium, certain boundary conditions must be satisfied. In the case of plane waves, the normal and shear stresses on this surface must be equal to zero. According to expressions (2.10) and (2.11) these boundary conditions are as follows.

$$\sigma_z = |\lambda\bar{\varepsilon} + 2G\varepsilon_z|_{z=0} = \left|\lambda\left(\frac{\partial u}{\partial x} + \frac{\partial w}{\partial z}\right) + 2G\frac{\partial w}{\partial z}\right|_{z=0} = 0 \tag{2.76}$$

$$\tau_{zx} = |G\gamma_{zx}|_{z=0} = \left|G\left(\frac{\partial u}{\partial x} + \frac{\partial w}{\partial z}\right)\right|_{z=0} = 0 \tag{2.77}$$

By replacing (2.54) and (2.55) yields to

$$\left|\lambda\frac{\partial^2\Phi}{\partial x^2} + (\lambda + 2G)\frac{\partial^2\Phi}{\partial z^2} - 2G\frac{\partial^2\Psi}{\partial x\partial z}\right|_{z=0} = 0 \tag{2.78}$$

$$\left|2\frac{\partial^2\Phi}{\partial x\partial z} + \frac{\partial^2\Psi}{\partial z^2} - \frac{\partial^2\Psi}{\partial x^2}\right|_{z=0} = 0 \tag{2.79}$$

Then, by substitution of expressions (2.72) and (2.73) and z equal to zero the following two equations are obtained.

$$A_1[(\lambda + 2G)q^2 - \lambda k^2] - 2iB_1 Gks = 0 \tag{2.80}$$

$$2iA_1 kq + B_1(s^2 + k^2) = 0 \tag{2.81}$$

These expressions can be written as

$$\frac{A_1}{B_1} = \frac{2iGks}{(\lambda + 2G)q^2 - \lambda k^2} \tag{2.82}$$

$$\frac{A_1}{B_1} = -\frac{s^2 + k^2}{2ikq} \tag{2.83}$$

From which equating the right sides of the above equations

$$4Gk^2 sq = (s^2 + k^2)[(\lambda + 2G)q^2 - \lambda k^2] \tag{2.84}$$

By substituting expressions (2.66) to (2.69) it can be obtained

$$V^6 - 8V^4 - (16\alpha^2 - 24)V^2 - 16(1 - \alpha^2) = 0 \tag{2.85}$$

The expression (2.85) is a cubic equation in V^2. The solutions of this equation depend only on α which in turn depends exclusively on the Poisson's ratio ν. It can be observed that, for any admissible value of ν, the ratio $V = v_R/v_S$ is lower than one. This indicates that the velocity of Rayleigh waves is lower than that of S waves.

By means of equations for the potential functions (2.74) and (2.75) the displacement components can be written as

$$u = -(ikA_1 e^{-qz} + B_1 s e^{-sz}) e^{i(kx-\omega t)} \tag{2.86}$$

$$w = -(A_1 e^{-qz} - iB_1 k e^{-sz}) e^{i(kx-\omega t)} \tag{2.87}$$

By substituting (2.83) in the above expressions

$$u = A_1 ki(-e^{-qz} + \frac{2qs}{s^2+k^2} e^{-sz}) e^{i(kx-\omega t)} \tag{2.88}$$

$$w = A_1 q(-e^{-qz} + \frac{2k^2}{s^2+k^2} e^{-sz}) e^{i(kx-\omega t)} \tag{2.89}$$

By making use of the Euler's formula and taking only the real part, we obtain

$$u = A_1 k[e^{-qz} - 2qs(s^2+k^2)^{-1} e^{-sz}]\sin(kx-\omega t) \tag{2.90}$$

$$w = A_1 q[-e^{-qz} + 2k^2(s^2+k^2)^{-1} e^{-sz}]\cos(kx-\omega t) \tag{2.91}$$

Where A_1 is a constant that depends on the initial conditions.

Is worth noting that the displacement components depend on depth z, wave velocities v_p, v_s and v_R, as well as the wave number k, which is itself a function of the wavelength λ. Moreover, the presence of decaying exponential terms makes it evident that both u and w decrease with depth, meaning that significant displacements occur only near to the free surface. This justifies referring them as surface waves. Furthermore, equations (2.90) and (2.91) describe the shape of an ellipse whose major axis is parallel to the z-axis. Both the particle motion and its decay with depth are illustrated in **Figure 2.9**.

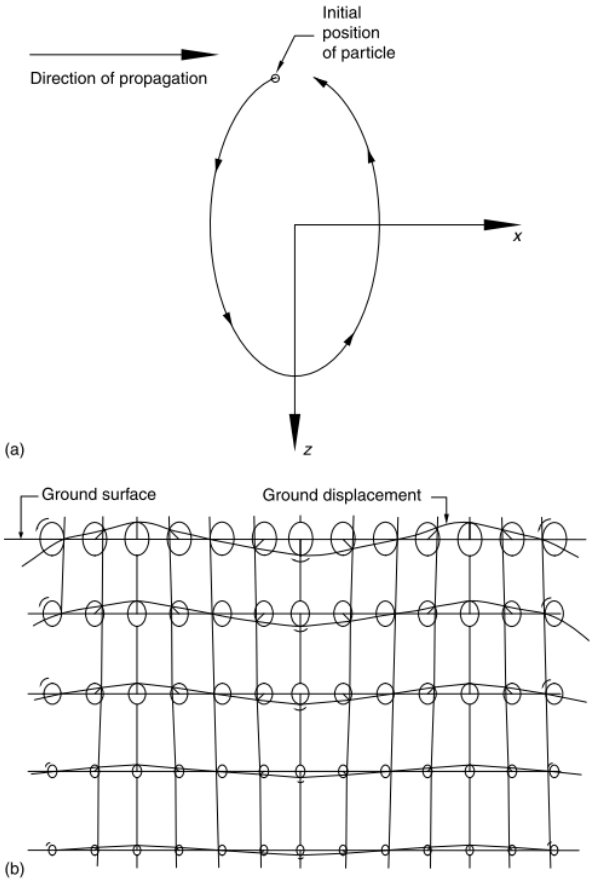

Figure 2.9 *Particle motion caused by Rayleigh waves (a); motion of subsurface segment due to Rayleigh waves (b) from [19]*

2.2.3 Reflection and refraction of body waves

2.2.3.1 Soil layering

It has been seen that the velocity of wave propagation depends on the material properties of the medium. Consequently, when a wave crosses from one material to another, a change in velocity is expected.

Soil, as a medium, cannot be considered homogenous. In fact, its composition, structure and properties result from its geological history. Factors such as weathering, transportation and depositional processes can significantly alter the state of homogeneity of any soil deposit [20]. In this context, the continuum soil is ideally discretized into layers based on characteristics such as particle size, shape, grain size distribution, and plasticity. These soil layers create discontinuities that affect wave propagation as waves travel from one medium to another e.g. the influence of soil layering by depth on the wave propagation response is discussed in [21].

Additionally, the presence of the water table, which tends to vary seasonally, introduces another discontinuity. Saturated soils exhibit different material behaviour compared to unsaturated or dry soils, further influencing wave propagation due to the refracted wave interference with surface waves [22].

A change in wave velocity leads to a corresponding change in the state of stresses and displacements before and after the discontinuity, as these directly depend on wave velocity, as shown in (2.39) and (2.50). This imbalance in forces and displacements across the interface is compensated by the formation of additional waves, i.e. refracted and reflected waves. In the case of a three-dimensional incident wave, a single P or S wave may generate two refracted and reflected waves: one as a P wave and the other as an S wave [19].

2.2.3.2 Relation among incident, refracted and reflected waves

The relationship between incident, reflected, and refracted waves follows Snell's law. This law states that the ratio of the sine of the wave's angle of inclination to its propagation velocity remains constant, regardless of the medium it travels through. Snell's law is derived from ray theory and is based on Fermat's principle of least time, which states that a disturbance propagates between two points along the path that minimizes travel time.

Considering for instance two media, the first characterized by a P wave velocity v_{p1}, S wave velocity v_{s1} and density ρ_1; and the second by a P wave velocity v_{p2}, S wave velocity v_{s2} and density ρ_2. As previously mentioned, boundary conditions must be satisfied at the interface between these two media. As shown in **Figure 2.10**, incident P, SH and SV waves generate refracted and reflected waves.

It is worth mentioning that after crossing the discontinuity, the generated waves are a combination of P and SV waves. In contrast, for an incident SH wave, which does not induce motion perpendicular to the plane of the interface, only refracted and reflected SH waves are required to maintain continuity at the interface.

By applying the Snell's law, the propagation directions for an incident P wave are defined by (see **Figure 2.10**a).

$$\alpha_2 = \alpha_1 \tag{2.92}$$

$$\frac{\sin(\beta_2)}{v_{s1}} = \frac{\sin(\alpha_3)}{v_{p2}} = \frac{\sin(\beta_3)}{v_{s2}} = \frac{\sin(\alpha_1)}{v_{p1}} \tag{2.93}$$

For an incident SV wave, the directions are defined as follows (see **Figure 2.10**b).

$$\beta_2 = \beta_1 \tag{2.94}$$

$$\frac{\sin(\alpha_2)}{v_{p1}} = \frac{\sin(\beta_3)}{v_{s2}} = \frac{\sin(\alpha_3)}{v_{p2}} = \frac{\sin(\beta_1)}{v_{s1}} \tag{2.95}$$

Finally, for an incident SH wave, the directions are defined as follows (see **Figure 2.10**c).

$$\beta_2 = \beta_1 \tag{2.96}$$

$$\frac{\sin(\beta_3)}{v_{s2}} = \frac{\sin(\beta_1)}{v_{s1}} \tag{2.97}$$

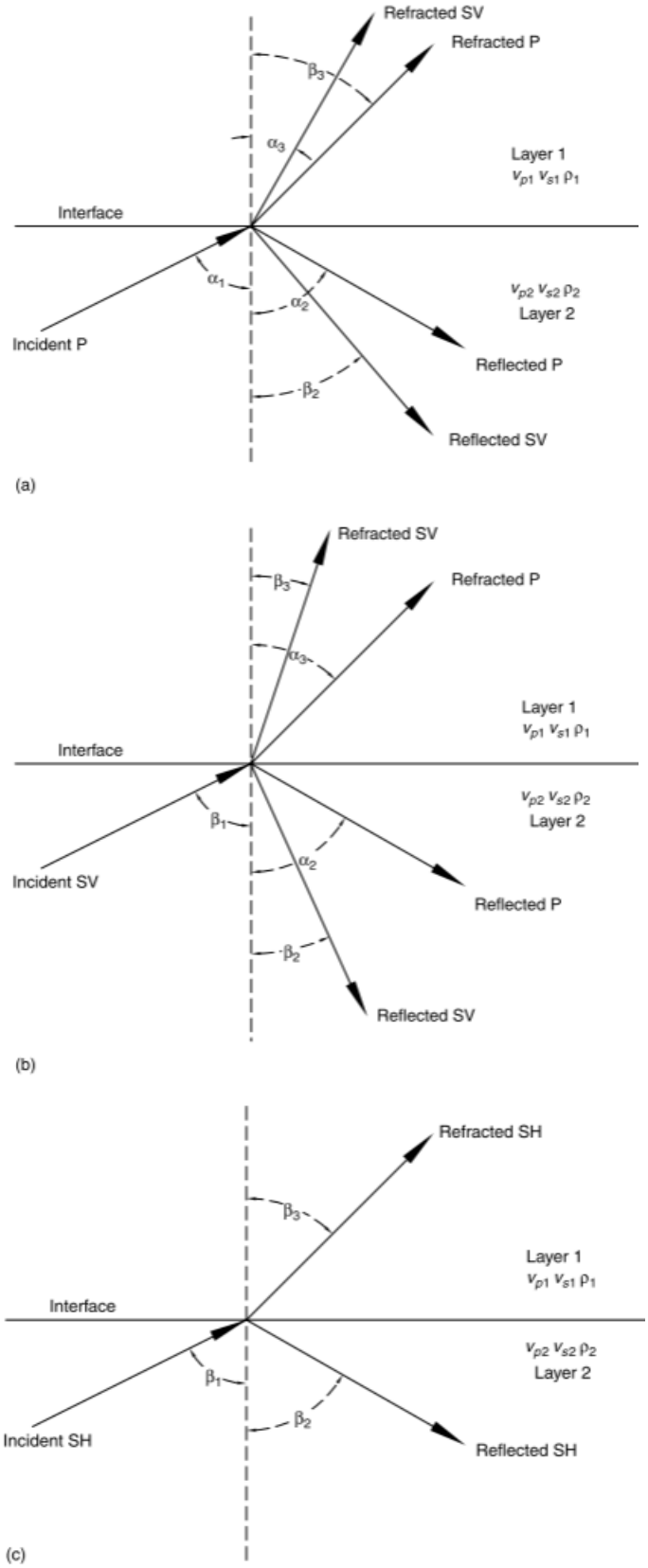

Figure 2.10 *Refracted and reflected waves generated by incident (a)P wave, (b) SV wave, and (c) SH wave from [19]*

2.3 Signal processing

2.3.1 Fourier transform

The collected data of the signal was done in the time domain, however when dealing with wave propagation, obtaining relevant information about the frequencies that compose the signal is not a straightforward procedure in this domain. The Fourier transform method is an algorithm that allows to convert the signal from the time domain to the frequency domain. By doing so, it is possible determine which frequencies are more excited and its corresponding amplitudes.

The expression of the direct Fourier transform in a continuous domain is the following:

$$X(f) = \int_{-\infty}^{+\infty} x(t) e^{-i2\pi f t}\, dt \tag{2.98}$$

Where $x(t)$ is the continuous time function, t is the time, f is the frequency, e is the Euler's number, i is the imaginary unit and $X(f)$ and is the continuous Fourier transform in the frequency domain.

This mathematical tool basically decomposes the function in a sum of sinusoidal components, each with a correspondent frequency, magnitude and phase. This transformation is achieved by multiplying the time-domain function by a complex exponential (which consists of sine and cosine terms) at each frequency and then integrating over time. The resulting values indicate how much of that particular frequency is present in the original function. This process provides both the real and imaginary components, from which the amplitude and phase information can be calculated in the frequency domain as in expressions (2.99) and (2.100) respectively.

$$|X(f)| = \sqrt{\left(Re\big(X(f)\big)\right)^2 + \left(Im\big(X(f)\big)\right)^2} \tag{2.99}$$

$$\varphi(f) = \frac{Im\big(X(f)\big)}{Re\big(X(f)\big)} \tag{2.100}$$

In practical applications, signals are sampled at a specific rate, meaning they are represented as discrete values rather than a continuous function. Consequently, the Fourier Transform must be applied in the discrete domain using the Discrete Fourier Transform (DFT). This algorithm computes the frequency components of a signal sampled at equal time intervals, providing a discrete representation of its spectral content. The mathematical expression for a signal with N samples is given by:

$$X(k) = \sum_{n=0}^{N-1} x_n e^{-\frac{i2\pi k n}{N}} \tag{2.101}$$

Where x_n is the discrete variable in the time domain, k is the discrete frequency variable and $X(k)$ and is the discrete Fourier transform in the frequency domain.

Some key properties of the DFT can be highlighted for the purpose of this work. The lowest nonzero frequency that can be obtained from a discrete, finite-length recording corresponds to a wavelength equal to the total duration of the signal. Additionally, a higher sampling rate allows for

the measurement of higher maximum frequencies, while a longer signal duration improves the frequency resolution.

Although the DFT is a powerful tool for computing the Fourier transform for any equally spaced discrete signal, it becomes computationally expensive when dealing with large amount of data. The Fast Fourier transform (FFT) take advantage of duplicate operations in the DFT and reduced the number of calculations from N^2 to $Nlog_2N$, making the process significantly more efficient.

In the present work, the FFT algorithm implemented in MATLAB will be used to convert recorded train passage accelerations signals from the time-domain to the frequency domain.

2.3.2 Sampling problem and the aliasing effect

Whenever a continuous signal is recorded, it must be sampled at a certain rate. This means the signal is converted from the analog (continuous) domain to the digital (discrete) domain. The choice of sampling rate is of pivotal importance. As explained in Chapter 2 of [23], sampling theory plays a crucial role in determining the accuracy and feasibility of any digital signal processing scheme. In the case of periodic sampling, the primary concern is how fast a given continuous signal must be sampled in order to preserve its information content.

Consider, for example, the case of discretely sampling a sine wave, as shown in **Figure 2.11** (a). It can be observed that with the chosen sampling rate; the captured sine wave appears to have a frequency that does not correspond to the original (grey curve). In fact, using only these sampled points, multiple sine waves of different frequencies could fit through the same data points, leading to ambiguity. This effect, when the true behaviour of a continuous signal cannot be captured accurately by a limited number of samples, is known as aliasing.

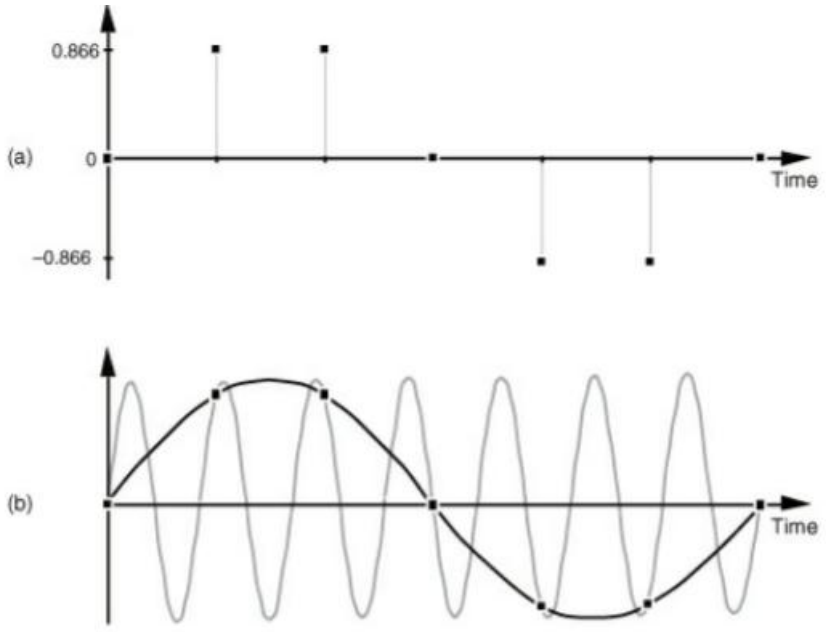

Figure 2.11 *Frequency ambiguity: (a) discrete-time sequence of values, (b) two different sinewaves that pass through the points of the discrete sequence from [23]*

To further illustrate the concept, consider a continuous low-pass signal that is band-limited to a maximum frequency B meaning the spectral amplitude is zero outside the range of $-B$ to $+B$. The continuous spectrum of such a signal is shown in **Figure 2.12** (a). When this signal is sampled, its

frequency spectrum is replicated periodically at intervals of the sampling frequency f_s as shown in **Figure 2.12** (b). If the sampling rate satisfies $f_s > 2B$, the replicated spectra do not overlap, and the original content is preserved in the discrete domain. This condition is known as the Nyquist criterion.

However, if $f_s < 2B$, as shown in, **Figure 2.12** (c), the replicated spectra overlap, and aliasing occurs. In this case, high-frequency components are "folded" into lower frequencies, distorting the reconstructed signal. Once aliasing has occurred, it becomes impossible to distinguish between original and aliased components based solely on the sampled data.

To avoid aliasing in practice, analog low-pass filters, known as anti-aliasing filters, are used before analog-to-digital conversion. These filters attenuate frequencies above the Nyquist frequency $f_s/2$ ensuring that only the desired baseband signal is preserved during sampling.

In the present study, the signal recordings were already provided in the discrete domain at a rate of $f_s = 4800\ Hz$. For the purposes of the inversion procedure, these must be resampled at a lower rate, targeting a maximum frequency of interest of $400\ Hz$. This process is known as Sample rate conversion and will be explain in the next subchapter. In this context, an appropriate low pass filtering step was required prior to resampling, in order to discard higher frequencies and to prevent aliasing effects.

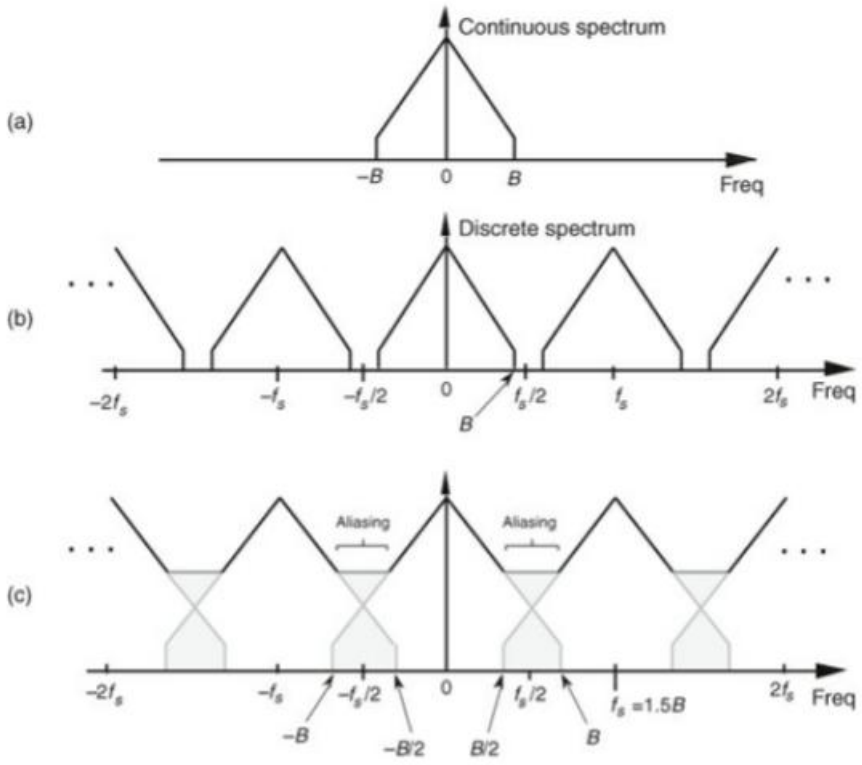

Figure 2.12 *Spectral replications: (a) original continuous lowpass signal spectrum, (b) spectral replications of the sampled lowpass signal for $f_s/2 > B$, (c) frequency overlap and aliasing when $f_s/2 < B$ from [23]*

2.3.3 Decimation

As previously mentioned, the recorded acceleration signals were initially sampled at a rate of $f_s = 4800\ Hz$. For the inversion procedure, these signals had to be resampled at a lower rate of $f_s = 400\ Hz$. To prevent aliasing, it is essential to remove frequency components above $400\ Hz$ using a

low-pass filter. This combined process of low-pass filtering followed by resampling (or downsampling) is referred to as decimation.

As explained in Chapter 10 of [23], decimation is the two-step process of lowpass filtering followed by an operation known as downsampling. In this process, is possible to downsample a sequence of sampled signal values by a factor of M in a way that this is reduced in size by retaining every M^{th} sample and discarding the others. If the original sampling rate is $f_{s,old}$, the sampled rate of the downsampled sequence can be defined by the expression (2.102).

$$f_{s,new} = \frac{f_{s,old}}{M} \tag{2.102}$$

For instance, given a continuous sinewave $x(t)$ that has been sampled to produce the $x_{old}(t)$ sequence shown in **Figure 2.13** (a). To downsample $x_{old}(t)$ by a factor of $M = 3$, we consider the first term and then select a sample every 3 terms. This can be mathematically described as in equation (2.103) and illustrated in **Figure 2.13**.

$$x_{new}(m) = x_{old}(Mm) \tag{2.103}$$

Is worth noting that in the equation (2.103) the index variable m is used to point out that the time period between the $x_{new}(m)$ samples is different from the time period between the $x_{old}(n)$ samples.

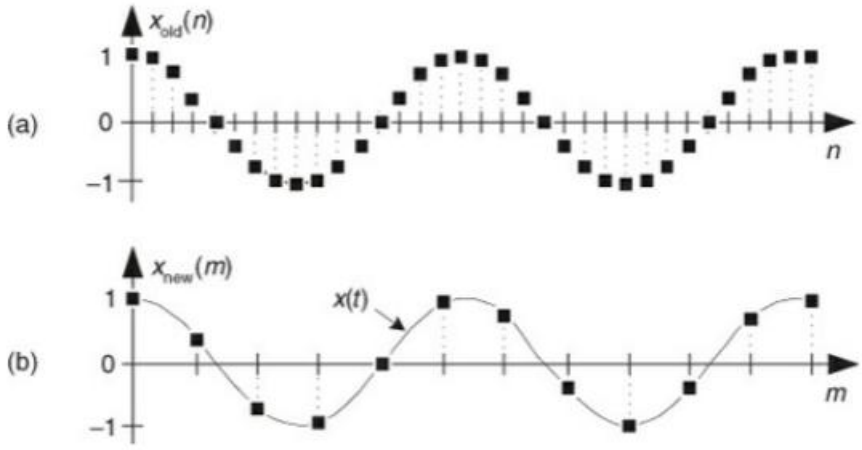

Figure 2.13 *Sample rate conversion: (a) original sequence, (b) downsampled by M = 3 sequence, from [23]*

The spectral implications of downsampling are what we should expect in **Figure 2.14**, where the spectrum of an original band-limited sampled $x_{old}(n)$ signal is indicated by the solid lines, and the spectral replications are indicated by the dashed lines. With $x_{new}(m) = x_{old}(3n)$, $x_{new}(m)$'s spectrum $X_{new}(f)$, as shown in **Figure 2.14** (b).

Important features are illustrated in **Figure 2.14**. First, $X_{new}(f)$ could have been obtained directly by sampling the original continuous $x(t)$ signal at a rate of $f_{s,new}$, as opposed to downsampling $x_{old}(n)$ by a factor of three. Second, there is a limit to the amount of downsampling that can be performed relative to the bandwidth B of the original signal. Hence, the Nyquist criterion, $f_{s,new} > 2B$, must be ensured to prevent overlapped spectral replications (aliasing errors) after downsampling.

If a decimation application requires $f_{s,new}$ to be less than $2B$, then $x_{old}(n)$ must be lowpass filtered before the downsampling process is performed as shown in **Figure 2.14** (c) . If the original signal has a bandwidth B, and we are interested in retaining only the band B', the signal spectrum above B' must be lowpass filtered, with full attenuation in the stopband beginning at f_{stop}, before

the downsample-by-M process is performed. In **Figure 2.14** (d) shows this in more detail where the frequency response of the lowpass filter, the bold lines, must attenuate the signal spectral components whose frequencies are greater than B'. It can be noticed that the lowpass filter's f_{stop} frequency can be as high as $f_{stop} = f_{s,new} - B'$ and no spectral aliasing will occur in the B' band of interest.

Finally, two important properties of downsampling can be identified. First, downsampling is not a time-invariant operation. This implies that a temporal shift in the input signal does not consistently translate to a corresponding temporal shift in the resulting downsampled output. Consequently, when downsampling is integrated with other signal processing steps, the order in which these operations are performed becomes significant and cannot be arbitrarily interchanged without potentially altering the final outcome.

Second, downsampling exhibits distinct effects on the signal's amplitude in different domains. In the time domain, the overall signal amplitude, such as the peak-to-peak value, remains unchanged by the downsampling process. However, in the frequency domain, the operation induces a reduction in the signal's magnitude. Specifically, when a signal is downsampled by a factor of M, its frequency spectrum experiences a magnitude scaling by a factor of $1/M$. This inverse relationship arises from the fundamental connection between the number of time-domain samples and the resulting magnitudes observed in the Discrete Fourier Transform (DFT).

In this study, the decimation factor is $M = 12$, derived from equation (2.102) using $f_{s,old} = 4800\ Hz$ and $f_{s,new} = 400\ Hz$. A low-pass filter was therefore applied before downsampling. The design and characteristics of this filter are described in the following section.

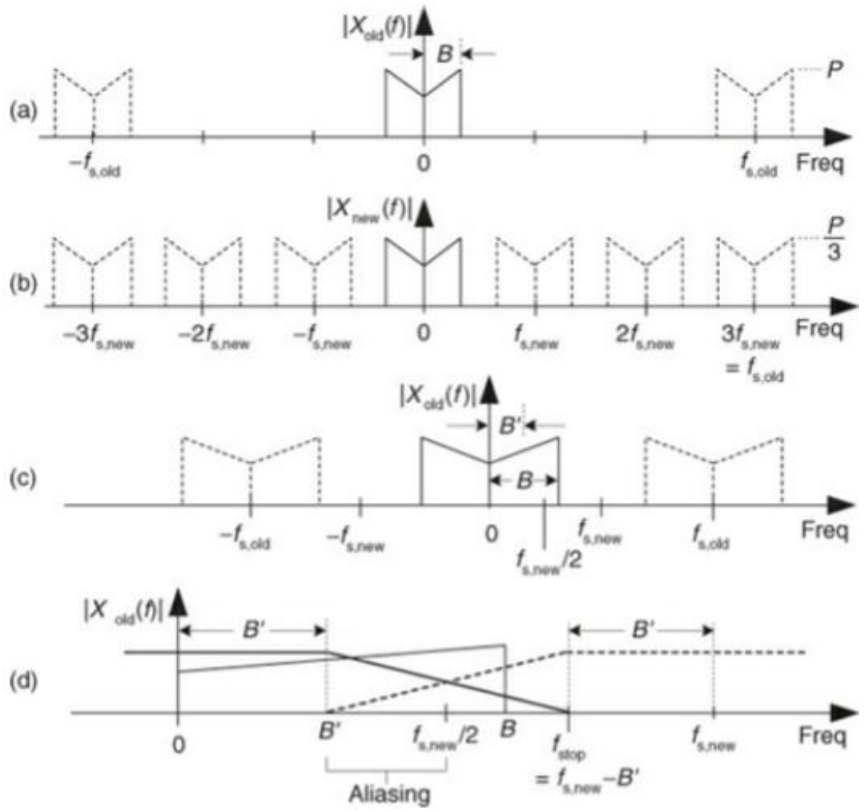

Figure 2.14 *Decimation by a factor of three: (a) spectrum of original $x_{old}(n)$ signal, (b) spectrum after downsampling by three, (c) bandwidth B' is to be retained, (d) lowpass filter's frequency response relative to bandwidth B', from [23]*

2.3.4 Filtering

2.3.4.1 Filtering implementation

As explained previously, to perform the decimation process and avoid aliasing after downsampling a lowpass filter is required. Filters are a particularly important class of linear time-invariant (LTI) systems that for this context a frequency-selective is one that passes certain frequency components while attenuating others. Filter design involves three main stages: (1) defining the desired specifications, (2) approximating these specifications using a realizable discrete-time system, and (3) implementing the system physically or computationally [24]. This section focuses on the first two stages, which are relevant to this study; implementation details typically depend on the specific hardware or software platform.

Since digital filtering is performed computationally, it is common to refer to these as discrete-time or digital filters. When filtering discrete-time signals derived from continuous analog signals (as shown in **Figure 2.15**), specifications for both the discrete-time filter and the effective continuous-time behaviour are typically given in the frequency domain.

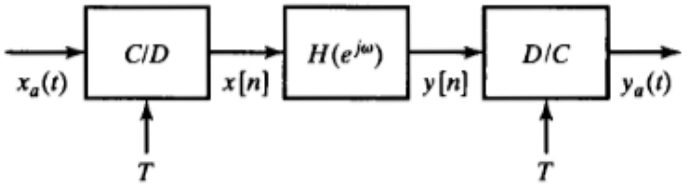

Figure 2.15 *Basic system for discrete-time filtering of continuous-time signals from [24]*

In a typical configuration, as in **Figure 2.15**, a continuous signal $x_a(t)$ is sampled with period T ,passing from the continuous to the discrete domain (C/D), yielding the discrete signal $x[n]$. After filtering, the output is $y[n]$, If the input is band-limited and the sampling rate satisfies the Nyquist criterion, i.e. the sampling frequency is high enough to avoid aliasing , the system behaves like an effective continuous-time LTI system with frequency as in equation (2.104).

$$H_{eff}(i\Omega) = \begin{cases} H(e^{i\Omega T}) & , |\Omega| < \pi/T \\ 0 & , |\Omega| > \pi/T \end{cases} \tag{2.104}$$

Where Ω is the frequency in radians for the continuous system, T is the sampled period, e is the Euler's number and i is the imaginary unit[2].

In such cases, it is straightforward to convert from specifications on the effective continuous-time filter to specifications on the discrete-time filter through the relation $\omega = \Omega T$. That is, $H\left(e^{i\omega}\right)$ is specified over one period by the equation (2.105).

$$H(e^{i\omega}) = H_{eff}(i\frac{\omega}{T}) \quad , |\omega| < \pi \tag{2.105}$$

[2] In the referenced textbook *Discrete-Time Signal Processing* by Oppenheim et al. [24], the imaginary unit is denoted by j. In this thesis, the symbol i has been adopted to represent the imaginary unit for consistency. However, in figures reproduced from the textbook, j refers to the same imaginary number and is equivalent to i as used in this work.

For the case of a lowpass filter, practical designs include tolerances in order to effectively implement the system as described in **Figure 2.15**. As an example, these limits from $(1+\delta_1)$ to $(1-\delta_1)$ for the passband and from 0 to δ_2 in the stopband are illustrated in **Figure 2.16**.

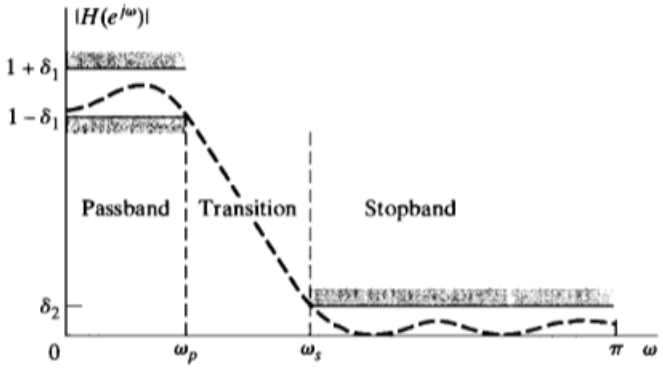

Figure 2.16 *Specifications for effective frequency filtering for the discrete-time system in the case of a lowpass filter from [24]*

2.3.4.2 Butterworth lowpass filter

As mentioned previously, many of the continuous-time filters used in practice are specified by tolerances in the passband and stopband regions with no constrains other than those imposed implicitly by stability and causality requirements. Several types of analog low-pass filters are commonly used, including Butterworth, Chebyshev, and Elliptic filters. In this study, a Butterworth filter is adopted due to its smooth, monotonic frequency response and maximally flat magnitude in the passband. Similar filtering has been used in the literature when selecting low frequencies of interest of the transfer function (Chapter 6 of [13]). In the following lines, the characteristics of this type of filter will be explained following the Appendix B of [7].

The squared magnitude response of an N-th order continuous-time Butterworth low-pass filter is given by the expression (2.106).

$$|H_c(i\Omega)|^2 = \frac{1}{1+\left(\frac{i\Omega}{i\Omega_c}\right)^{2N}} \tag{2.106}$$

This function is plotted in **Figure 2.17** , and its behaviour for increasing filter order N is shown in **Figure 2.18**. As N increases, the transition from passband to stopband becomes sharper, but the magnitude at the cutoff frequency Ω_C remains $1/\sqrt{2}$, or half power.

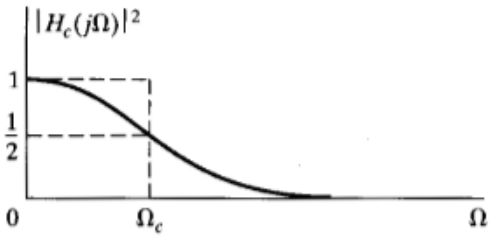

Figure 2.17 *Magnitude-squared function for continuous-time Butterworth filter from [24]*

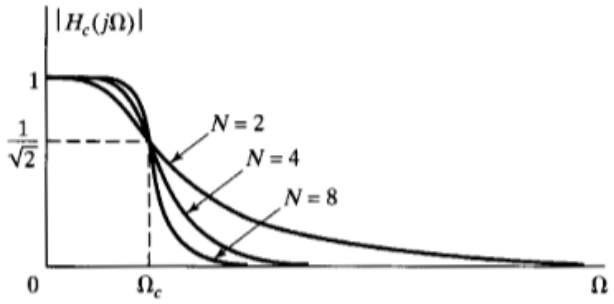

Figure 2.18 *Dependence of Butterworth magnitude characteristics on the order N from [24]*

From the magnitude-squared function in equation (2.106) we observe by substituting $i\Omega = s$ that $H(s)\,H(-s)$ must be of the form

$$H_c(s)H_c(-s) = \frac{1}{1 + (s/i\Omega_c)^{2N}} \tag{2.107}$$

The roots of the denominator polynomial (the poles of the magnitude-squared function) are therefore located at values of s satisfying.

$$1 + \left(\frac{s}{i\Omega_c}\right)^{2N} = 0 \tag{2.108}$$

Hence

$$s_k = (-1)^{\frac{1}{2N}}(i\Omega_c) = \Omega_c e^{(i\pi/2N)(2k+N-1)}, \quad k = 0,1,\ldots,2N-1 \tag{2.109}$$

Thus, there are $2N$ poles equally spaced in angle on a circle of radius Ω_c in the s-plane. The poles are symmetrically located with respect to the imaginary axis. A pole never falls on the imaginary axis, and one occurs on the real axis for N odd, but not for N even. The angular spacing between the poles on the circle is π/N radians. For example, for $N = 3$, the poles are spaced by $\pi/3$ radians, or 60 degrees, as indicated in **Figure 2.19**. To determine the system function of the analog filter to associate with the Butterworth magnitude-squared function, we must perform the factorization $H(s)H(-s)$. The poles of the magnitude-squared function always occur in pairs, i.e., if there is a pole at $s = s_k$, then a pole also occurs at $s = -s_k$. Consequently, to construct $H_c(s)$ from the magnitude squared function, we would choose one pole from each such pair. To obtain a stable and causal filter, we should choose the poles on the left-half-plane part of the s-plane.

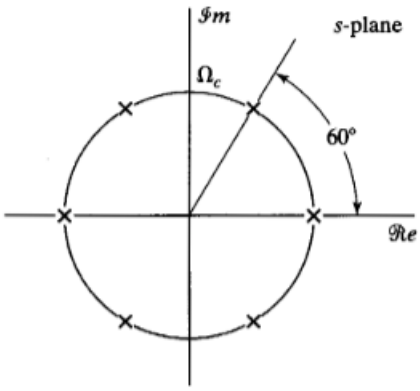

Figure 2.19 *S-plane locations for a third-order Butterworth filter from [24]*

2.3.4.3 Bilinear transformation

When designing a discrete-time filter by transforming a prototype continuous-time filter, the specifications of the continuous-time filter are derived from those of the desired discrete-time filter. These transformations are typically designed to preserve the key characteristics of the continuous-time frequency response in the resulting discrete-time filter.

The technique discussed in this subsection avoids the problem of aliasing by using the bilinear transformation, an algebraic transformation between the variables s and z that maps the entire $j\Omega$-axis in the s-plane to one revolution of the unit circle in the z-plane. Since $-\infty < \Omega < \infty$ maps onto $-\pi \leq \omega \leq \pi$, the transformation between the continuous-time and discrete-time frequency variables is inherently nonlinear. Consequently, the application of the bilinear transformation is best suited for scenarios where this resulting distortion, or warping, of the frequency axis is acceptable.

With $H_c(s)$ denoting the continuous-time system function and $H(z)$ the discretetime system function, the bilinear transformation corresponds to replacing s by

$$s = \frac{2}{T_d}\left(\frac{1 - z^{-1}}{1 + z^{-1}}\right) \tag{2.110}$$

That is

$$H(z) = H_c\left[\frac{2}{T_d}\left(\frac{1 - z^{-1}}{1 + z^{-1}}\right)\right] \tag{2.111}$$

As in impulse invariance, a "sampling" parameter T_d is included in the definition of the bilinear transformation. Following the derivations explained in Chapter 7 of [24] the following expression can be derived.

$$\Omega = \frac{2}{T_d}\tan\left(\frac{\omega}{2}\right) \tag{2.112}$$

Or

$$\omega = 2\arctan\left(\Omega\frac{T_d}{2}\right) \tag{2.113}$$

These mappings of the s-plane to the z-plane and the corresponding frequency axis transformations are visually summarized in **Figure 2.20** and **Figure 2.21** respectively. While the bilinear transformation effectively prevents aliasing it introduces a nonlinear compression of the frequency axis, as depicted in **Figure 2.21**. This frequency warping means that the technique is most effective when such compression is either tolerable or can be compensated for. This is often the case for filters designed to approximate ideal piecewise-constant magnitude-response characteristics. This is illustrated in **Figure 2.22**, where it can be observed how a continuous-time frequency response and tolerance scheme maps to a corresponding discrete-time frequency response and tolerance scheme through the frequency warping of equations (2.112) and (2.113). If the critical frequencies (such as the passband and stopband edge frequencies) of the continuous-time filter are prewarped according to equation (2.112) then, when the continuous-time filter is transformed to the discrete-time filter using equation (2.111), the discrete-time filter will meet the desired specifications.

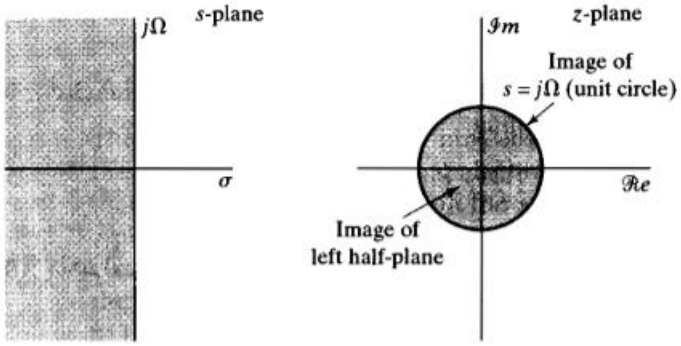

Figure 2.20 *Mapping of the s-plane onto the z-plane using the bilinear transformation from [24]*

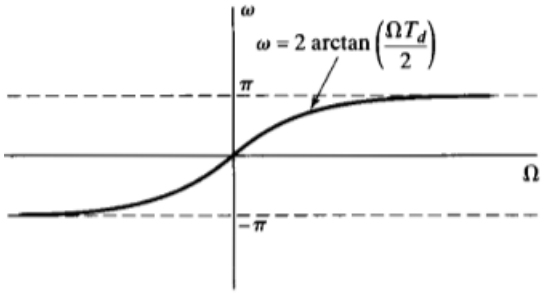

Figure 2.21 *Mapping of the continuous-time frequency axis onto the discrete-time frequency axis by bilinear transformation from [24]*

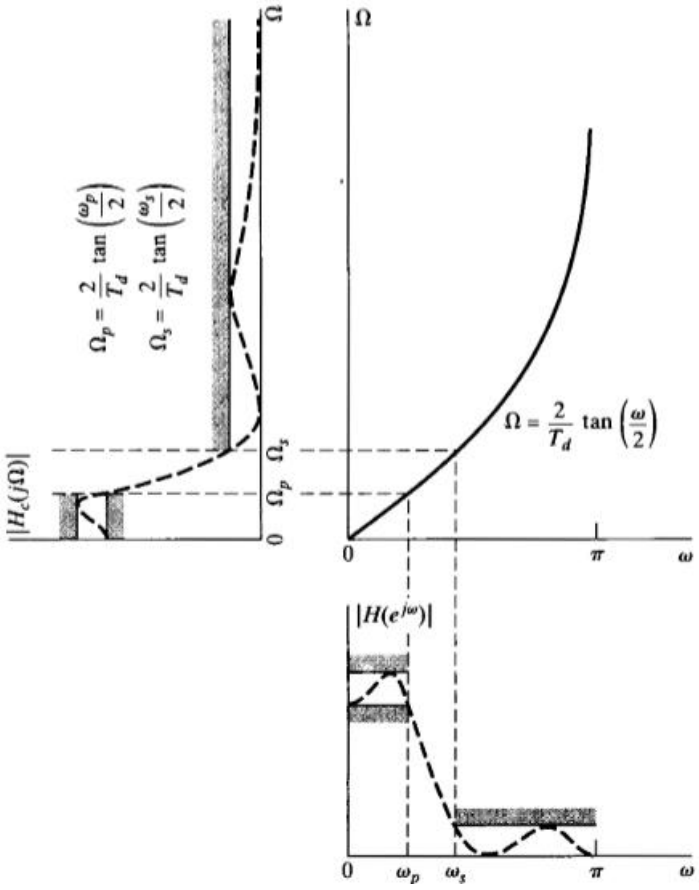

Figure 2.22 *Frequency warping inherent in the bilinear transformation of a continuous lowpass filter into a discrete time lowpass filter from [24]*

2.4 Modelling strategies

Several modelling approaches exist for simulating ground-borne vibrations induced by underground trains. Based on the comprehensive reviews presented in [25] and [9] the main strategies adopted in the literature are summarised in the present subchapter. Additionally, this subchapter provides the reasons behind the selection of a 2D plane strain finite element model for the present study.

2.4.1 Analytical and semi-analytical methods

Analytical and semi-analytical methods are widely adopted in the literature to model the dynamic interaction between underground trains, tunnels, and surrounding soil. These approaches offer efficient, low-computational-cost solutions, particularly useful for parametric studies and conceptual understanding. However, they are often constrained by idealized assumptions, limiting their applicability to specific geometries, soil conditions, or loading frequencies.

One of the simplest analytical strategies is to model the tunnel as an infinitely long Euler-Bernoulli beam embedded in a 2D viscoelastic soil. For instance,[26] theoretically examines the vibration of a 2D elastic layer's surface caused by a point load moving along an embedded Euler-Bernoulli beam. The study considers a layer with small viscosity, fixed at its base, and investigates surface vibrations under constant, harmonically varying, and stationary random loads. Displacement vectors and amplitude spectra are analysed for deterministic loads, while the variance of vibration is studied for random loads. Similarly, [27] analyses surface vibrations induced by a harmonically varying point load moving along an infinitely long Euler-Bernoulli beam embedded in a 2D viscoelastic layer resting on a half-space. This work derives analytical closed-form integral solutions for displacement amplitudes and spectra, examining the influence of layer damping and load speed, and employs a wavelet-based approximation method for calculating surface displacements. Both studies model the beam using Euler-Bernoulli theory and the surrounding medium with elastodynamic equations, providing insights into the surface vibrations generated by moving loads on embedded beam-like structures.

Although these methods are effective in capturing low-frequency excitations, they are unable to account for the cross-sectional tunnel behaviour or the complex wave propagation that occurs at higher frequencies [28].

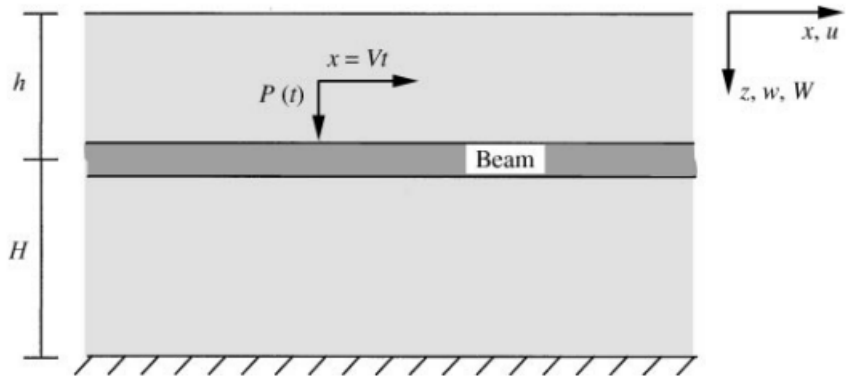

Figure 2.23 *Two-dimensional EB beam model considered in [26]*

A more advanced and widely used semi-analytical approach is the Pipe-in-Pipe (PiP) model, in which the tunnel is idealized as an infinitely long cylindrical thin shell embedded in an elastic or poroelastic full-space.

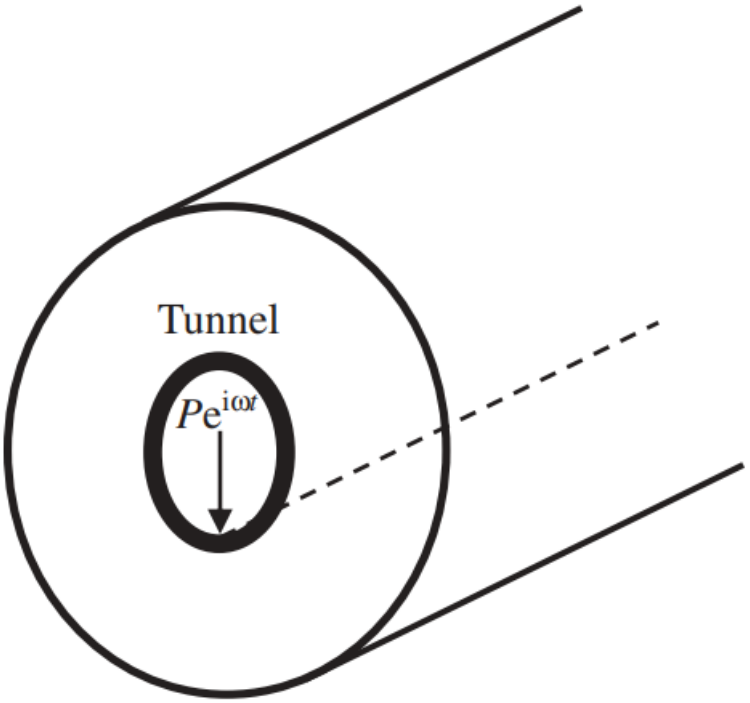

Figure 2.24 *PiP model from [25]*

This method is particularly suitable for deep circular tunnels, where free-surface effects are negligible and cylindrical symmetry can be assumed. In studies such as the one proposed by Forrest and Hunter [29], a frequency-domain analytical model is developed for a cylindrical tunnel in an elastic full-space. The model uses Fourier decomposition in the circumferential direction and wavenumber transformation along the tunnel axis. It is indicated that this method is especially well-suited for evaluating the dynamic response to axle loads and the influence of different track configurations on ground vibrations in the 20–100 Hz range. The model has been extended to include features such as floating slab tracks. [30] and multi-layered soil conditions [31].

Other studies, such as [32], combine the PiP model with a coupled periodic FEM–BEM formulation to conduct parametric analyses, identifying key tunnel and soil parameters that affect ground vibration. Furthermore, in [4], the PiP approach is extended to a poroelastic half-space, accounting for both saturated soil behavior and free-surface effects using a 2.5D boundary integral approach. The model couples a train–track–tunnel system and evaluates vibration transmission through saturated porous media.

While powerful for analytical insight and preliminary studies, these methods generally do not account for wave reflections at the free surface or non-cylindrical geometries and are thus less suited for detailed site-specific modelling. In such cases, numerical methods like Finite Element or Boundary Element methods offer a more versatile, though computationally intensive, alternative.

2.4.2 Finite elements

The Finite Element Method (FEM) is a powerful numerical tool widely employed in the modelling of underground train-induced vibrations due to its ability to accommodate complex geometries, layered soil conditions, and nonlinear material behaviour. Unlike analytical and semi-analytical approaches, FEM allows greater flexibility in representing the tunnel–soil–track system, making it suitable for detailed, site-specific analyses.

2.4.2.1 2D Plane strain FEM approaches

In studies like Balendra and Chua [33] [34], employed 2D plane strain models to study subway–soil–building interaction under different track systems (direct fixation and floating slab), showing that floating slabs can act as effective vibration isolators at high frequencies. The agreement between simulation and field data validated the reliability of this simplified approach.

Furthermore, studies using this modelling approach were carried out in Milano metro line. In Rigoni [8], a 2D FE plain strain model was developed to investigate the impact of the water table depth on the dynamic response of a subway tunnel-soil system (specifically Milan's M1 line). The study focused on boundary conditions, saturated soil modelling, and soil damping calibration using experimental data, using a load spectrum, applied in the frequency domain, to represent the train passage. It was concluded that 2D FEM can effectively be used to analyse the effects of environmental factors like the water table on train-induced vibrations in the soil.

Similarly, Pontani [9], conducted the analysis in the time domain, directly imposing a load history with a spectrum compatible with the axle load spectrum defined by UNI standards. The soil modelling, using the 2D FEM approach, realistically represents in-situ conditions in Milan, relying on data from geophysical surveys and exploring the effects of partial soil saturation.

While 2D models provide significant computational savings and are effective for parametric studies, they inherently neglect wave propagation along the train's longitudinal direction. This limitation often leads to overestimation of vibration levels and reduced accuracy in simulating dynamic effects.

2.4.2.2 3D FEM approaches

To overcome these limitations, full 3D models have been developed. Zhou et al. [35] proposed a train–track–tunnel–soil coupled model using cylindrical elements for both tunnel and soil, accounting for nonlinearities and allowing time-domain simulations. This model was validated against PiP, VICT software, and field data, demonstrating its accuracy in predicting the complex dynamic responses of metro systems.

Perotti et al. [36] addresses the need for an efficient method to detail train-track interaction and soil-transmitted vibrations without excessive computational cost. They propose a numerical procedure based on a substructuring approach, dividing the system into the train, the rail, and the "ground" (sleepers, ballast, subgrade, and actual ground). The procedure involves several steps: first, 3D FEM of the sleeper-ballast-subgrade system is developed to obtain frequency response functions at rail-sleeper interfaces. Second, a time-domain integration of the train's motion on a simplified track model (with spring-dampers for the subgrade) is carried out to compute moving loads, allowing for non-linear wheel-rail interaction. Third, frequency-domain analysis of the track (modeled with FE), loaded by the train forces and supported by sleepers is implemented, to determine track dynamics. Finally, the propagation of vibrations through the soil to receiver points is evaluated. This

approach leverages the advantages of frequency domain analysis for moving loads and allows for the inclusion of frequency-dependent material properties.

An extension of the three-step method proposed by Perotti et al. to underground trains is proposed in [10] , which also compares 2D and 3D FEM for analysing underground train vibrations via the Frequency Transfer Function. It found that 3D models are more accurate in capturing the three-dimensionality but are much more computationally expensive than 2D models, which are better suited for preliminary studies due to their lower cost. However, 2D FEM neglects wave propagation along the train's movement, crucial for accurate ground vibration simulation, while 3D FEM offers a more realistic representation but demands significantly more computational resources.

2.4.2.3 Mixed 2D and 3D FEM approaches

To address the high computational cost of full 3D FEM, several authors have proposed mixed strategies. Gardien and Stuit [37] used a three-step modular model consisting of a 3D static tunnel-soil model, a dynamic Timoshenko beam track model, and a 2D/3D propagation model. The overall response was constructed using impulse response convolution and superposition.

Xu et al.[17] developed a mixed 2D/3D model to simulate the dynamic interaction in underground railways with ballastless tracks, considering moving trains and track irregularities. They investigated the impact of different wavelength irregularities on environmental vibration for direct fixation and floating slab tracks, finding that irregularities significantly affect vibration, with short wavelengths being more impactful for direct fixation and less so for floating slab tracks. The proposed mixed model reduced problem size and allowed efficient computation.

Expanding on this in [38] it is developed and verified 2D and 3D models for environmental vibrations from underground railways with direct fixation and floating slab tracks. Comparing ground surface responses, it was found that 2D models were significantly faster (1/600th the computational time of 3D) and could provide quick results using equivalent forces. However, they concluded that 3D models offer greater accuracy and are necessary for absolute prediction and complex problems.

2.4.2.4 Remarks on the election of the 2D FEM model

While 2D FEM is computationally efficient and effective for parametric studies, it cannot capture longitudinal wave propagation or moving loads, often leading to overestimated vibration levels. This limitation has driven the development of full 3D models, which, though more accurate, are computationally demanding.

The literature highlights a trade-off between the computational cost and the accuracy of numerical models. While 3D models [37] [17] offer a more realistic representation of the problem, capturing the three-dimensional wave propagation and the longitudinal effects of the moving train, they required a significantly higher computational burden, as noted by [10][38].

On the other hand, 2D plane strain models provide a computationally efficient alternative, suitable for preliminary studies and parametric analyses. These models can effectively capture the cross-sectional behaviour of the tunnel-soil system and the resulting ground vibrations in the vertical plane perpendicular to the tunnel axis. Studies such as Balendra and Chua [33][34] , as well as the investigations on the Milan M1 line [9][19], demonstrate the capability of 2D FEM to provide reasonably accurate predictions of ground-borne vibrations and to analyse the influence of factors such as track support systems, water table levels , and partially saturated soil conditions.

Although 2D models neglect the wave propagation in the train's travel direction, which can be important for a complete understanding of the vibration field, for certain analyses, they are particularly valuable for analyses focusing on the tunnel's immediate vicinity and cross-sectional response. Their lower computational demand makes them especially advantageous for broad parametric investigations or when computational resources are limited.

Therefore, considering that in this study the train-induced acceleration responses are provided, a 2D plane strain FEM is deemed an appropriate choice. This approach enables a detailed investigation of tunnel–soil interaction in the transverse plane and allows for efficient parametric analysis, providing valuable insights into ground vibration levels while remaining computationally manageable.

2.4.3 Boundary elements

The Boundary Element Method (BEM) offers an efficient alternative to full-domain numerical schemes such as the Finite Element Method (FEM), particularly in problems involving unbounded domains like soil media. By requiring discretization only along boundaries, BEM significantly reduces the size of system matrices and computational effort. This efficiency is especially evident when frequency-domain Green's functions for homogeneous full-space media are available, allowing for accurate representation of radiation damping effects.

When using BEM in soil modelling, each layer and its upper and lower interfaces (the ground surface being the top interface of the first layer) require the application of boundary elements. Since these interfaces are theoretically infinite, they must be truncated for numerical implementation, resulting in the introduction of "edge" boundary elements. A 2D soil layer with two boundaries, each discretized with two such edge elements, is illustrated in **Figure 2.25**.

However, BEM has limitations in handling thin structural components (e.g., tunnel linings) and becomes impractical in the presence of material inhomogeneities or non-linearities, due to the need for closed-form Green's functions and the inability to apply the superposition principle [39]. In such cases, hybrid FE–BE models are often preferred. These combine the flexibility of FEM, suited for representing complex geometries and material interfaces, with the boundary efficiency of BEM. Notable applications include studies by Andersen and Jones [40] , who modelled underground tunnels using FEM for tunnel structures and BEM for surrounding soils.

Advanced strategies have also been developed to reduce the dimensionality of 3D problems while preserving their essential dynamics. Periodic and invariant structures, typical of railway tunnels, can be exploited via Floquet theory or Fourier transforms. In particular, 2.5D approaches enable full 3D responses to be computed from a 2D spatial discretization by assuming longitudinal invariance [41].

These modelling strategies provide a powerful compromise between accuracy and computational feasibility, particularly when full 3D modelling is impractical. Nonetheless, they require careful mathematical formulation and are best suited for systems with structural regularity and linear material behaviour.

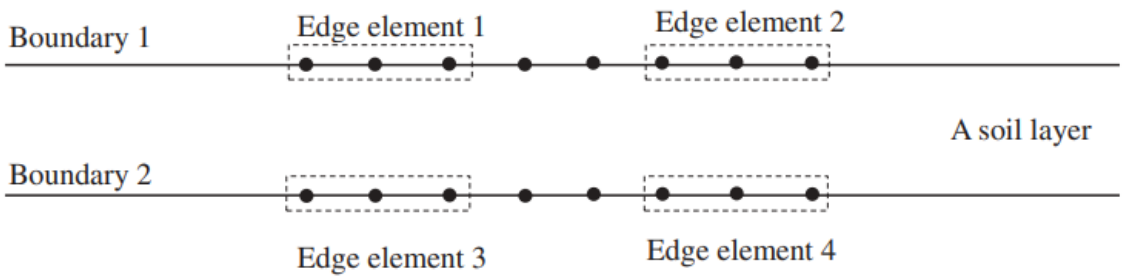

Figure 2.25 *A 2D soil layer with two boundaries each having two edge elements from [25]*

2.4.4 Spectral elements

Spectral Element Methods (SEM) have emerged as a promising alternative to traditional finite element or finite difference approaches for modelling ground vibrations induced by underground trains, particularly in cases involving lateral soil heterogeneity. In a study conducted at the Ledsgaard test site in Sweden [42], SEM was applied to simulate the ground vibrations generated by a passenger train. The train–track interaction was simplified by decoupling the train from the track and applying a series of equivalent static forces. The track–embankment system was modelled analytically as a beam on an elastic foundation.

A key advantage of SEM lies in its ability to resolve wave propagation phenomena using significantly fewer grid points compared to classical discretization methods, thereby reducing computational cost while allowing accurate modelling. The study showed that while conventional time-domain methods typically suffer from stability constraints that limit usable frequencies to around 2–3 Hz (especially in 3D) SEM allowed simulations up to 10 Hz with manageable computational time.

Although frequency-domain methods such as the thin-layer method [43] remain more efficient for horizontally layered media, SEM offers distinct advantages for complex site conditions with strong lateral variations, such as tunnels or vibration mitigation systems (e.g., trenches or pile barriers). The method's flexibility in handling 2D and 3D configurations makes it particularly well-suited for realistic and site-specific modelling of train-induced ground vibrations in heterogeneous environments.

2.5 The inversion procedure

2.5.1 Transfer function

When dealing with coupled damped systems subjected to a dynamic force, directly solving the equations of motion can be complex unless a transformation method is used. In this context, transformations such as the Fourier transform, explained in Subchapter 2.3.1 are useful tools to convert the governing vibration equations from the time domain to the frequency domain.

However, the Fourier transform is strictly defined only for continuous functions with domains extending from minus to plus infinity. While the use of rectangular window functions is a common workaround, alternative transformations offer more practical advantages. One such tool is the Laplace transform, which generalizes the Fourier transform and can be interpreted as the Fourier transform of a one-sided, exponentially weighted version of the original time-domain function. This method is widely used in vibration analysis and provides the basis for defining the transfer function, which generalizes the concept of a frequency response function.

The derivation of the transfer function, as presented in [44] , begins with the equation of motion for a damped single degree of freedom (SDOF).

$$m\ddot{x}(t) + c\dot{x}(t) + kx(t) = F(t) \tag{2.114}$$

The (one-sided) Laplace transformation of a time dependent function $x(t)$, denoted as $X(s) = \mathcal{L}x(t)$ is defined by the integral

$$X(s) = \mathcal{L}x(t) = \int_0^\infty e^{-st}x(t)\,dt \tag{2.115}$$

Where s is a general complex quantity referred to as a subsidiary variable of the form $s = a + i\omega$ where a is constant and ω is the circular frequency. The function e^{-st} is known as the kernel of the transformation and ensures the convergence of the integral. Since t is the variable of integration, the result is a function of s, which reflects frequency-dependent behaviour.

In order to solve equation (2.114) by the Laplace transform method, it is necessary to evaluate the transforms of the derivatives dx/dt and d^2x/dt^2. By means of integrating by parts leads to:

$$\mathcal{L}\frac{dx(t)}{dt} = \int_0^\infty e^{-st}\frac{dx(t)}{dt}dt = e^{-st}x(t)\Big|_0^\infty + s\int_0^\infty e^{-st}x(t)\,dt = sX(s) - x(0) \tag{2.116}$$

Where $x(0)$ is the value of the function $x(t)$ at $t = 0$. Physically, it represents the initial displacement of the mass m. Similarly, it is not difficult to show that

$$\begin{aligned}\mathcal{L}\frac{d^2x(t)}{dt^2} &= \int_0^\infty e^{-st}\frac{d^2x(t)}{dt^2}dt = e^{-st}\frac{dx(t)}{dt}\Big|_0^\infty + s\int_0^\infty e^{-st}\frac{dx(t)}{dt}dt \\ &= -\dot{x}(0) + s\mathcal{L}\frac{dx(t)}{dt} = s^2X(s) - sx(0) - \dot{x}(0)\end{aligned} \tag{2.117}$$

Where $\dot{x}(0)$ is initial velocity of m. The Laplace transformation of the excitation function $F(t)$ is simply

$$F(s) = \mathcal{L}F(t) = \int_0^\infty e^{-st}F(t)\,dt \tag{2.118}$$

By transforming both sides of equation (2.114) and rearranging it yields to

$$(ms^2 + cs + k)X(s) = F(s) + m\dot{x}(0) + (ms + c)x(0) \tag{2.119}$$

If we assume zero initial conditions $x(0) = \dot{x}(0) = 0$, which corresponds to neglecting the homogeneous solution, the ratio of the transformed excitation to the transformed response can be written in the form of

$$Z(s) = \frac{F(s)}{X(s)} = ms^2 + cs + k \tag{2.120}$$

Where $Z(s)$ is known as the *generalized impedance* of the system. More commonly, we consider the inverse ratio, defining the *Transfer function* $G(s)$ as the ratio of the system's response to the excitation in the Laplace domain. In the case of second-order systems as described in equation (2.114) the Transfer function has the form of:

$$G(s) = \frac{X(s)}{F(s)} = \frac{1}{ms^2 + cs + k} \tag{2.121}$$

The equation (2.121), can be rewrite as

$$X(s) = G(s)F(s) \tag{2.122}$$

Since $s = a + i2\pi f$ is a complex variable that depends on frequency, this expression directly relates the excitation and response in the frequency domain. While the theoretical derivation of the transfer function is presented in the Laplace domain for generality, the practical implementation of the inversion procedure is based on the one-sided Fourier transform, as it directly addresses the steady-state frequency-domain characteristics relevant to the recorded accelerometric data.

Chapter 3
Inversion procedure of accelerations

3.1 Introduction

In this chapter, the methodology for the inversion procedure used to estimate the dynamic load of an underground train in Milan's M1 and M2 metro lines will be explained. This technique provides insights into the interaction between the train, tunnel infrastructure, and surrounding soil and is based on a steady-state dynamic analysis in the frequency domain and is based on a previous study carried out in a gallery located in the Corso Buenos Aires zone of the M1 of the Milano metro [11]. The procedure involves measuring the frequency response from a set of recorded accelerations time histories. Subsequently, a detailed two-dimensional numerical model is used to estimate the transfer function. From these results, the load acting at the wheel-rail contact is determined for seven different metro sections.

The method can be lined up in the following steps.

1. Recording of accelerations

The process begins by measuring vertical accelerations on the inner face of the tunnel wall. These measurements are taken at regular time intervals to capture a representative period of rail track activity and to prevent aliasing during signal sampling.

2. Tunnel's Frequency Response to the train passage

After the acceleration time histories are acquired, they are transformed from the time domain into the frequency domain using the Fourier transform. Since the transfer function analysis focuses on a specific frequency range, proper signal processing is essential at this stage. This includes selecting a suitable sampling rate, defining the desired frequency resolution, and applying anti-aliasing filters to ensure the accuracy of the inversion procedure. Once transformed, the accelerations are represented as functions of frequency, enabling their comparison with the transfer function, which is likewise calculated in the frequency domain. After evaluating the tunnel's frequency response to trains passing at different times, the average magnitude of all spectra is used as a representative measure of the tunnel's dynamic behaviour. In this study, the average one-sided Fourier spectrum of the tunnel wall accelerations is referred to as $R(f)$, where f represents the frequency in Hertz.

3. Load-Acceleration Transfer Function

The frequency response function is defined in the frequency domain and allows the computation of a system's response under a dynamic load input. In the present study, this function is referred to as the load–acceleration transfer function, or simply transfer function, and is denoted as $H(f)$. It describes the relationship between the dynamic load applied at the wheel–rail interface and the resulting vertical acceleration measured on the tunnel wall. Mathematically, $H(f)$ is computed as the ratio between the tunnel's frequency response $R(f)$ and the dynamic load spectrum per axle $Q_d(f)$ according to equation (2.122). In this inversion procedure, the transfer function is numerically determined by means of applying a unit harmonic load in a two-dimensional Finite Element model.

4. Dynamic Load Spectrum per axle

Once the transfer function $H\ (f)$ and the frequency response $R(f)$ are available, the module of the dynamic load spectrum per axle is computed as the ratio of their modules, according to the following expression.

$$Q_d(f) = \frac{|R(f)|}{|H(f)|} \tag{3.1}$$

Finally, the results obtained through this procedure will be compared with those derived from alternative methods and with national standards available in the literature. Each of the aforementioned steps will be explained in detail in the following subchapters.

3.2 Tunnel's section geometry and properties

The sections of this study belong to the metro line network of the city of Milan. As previously mentioned, increasingly reports of noise and uncomfortable vibrations were reported by the citizens in the areas nearby the metro tunnels. Hence, strategically selected based on the areas where discomfort was reported, as well as the availability of access and geometric data, seven sections were chosen along the M1 and M2 metro lines. The locations of these selected sections are illustrated in **Figure 3.1**.

Figure 3.1 *Map of the analysed sections in Milan's metro network: M1 line (red), M2 line (green)*

The geometry was provided by *Metropolitana Milanese (MM)* through the original design drawings of the project. These drawings, hand-drafted in the 1960s, were later converted into CAD sections while preserving their original scale and accurately reflecting the tunnel conditions observed on site. All dimensions are expressed in meters. In cases where multiple sections were available, a representative one was selected for modelling.

The accelerometer height was considered to be 2 meters above the rail level, as indicated by MM. Section 2 (b-M2-Gallerie-Loreto-Piola) was modelled by merging two identical adjacent tunnels, based on in situ observations. Sections 4 and 5 (d-M1-Gallerie-Sesto Marelli–Villa SG and e-M1-Gallerie-Villa SG–Precotto) were assumed to be equivalent to Section 7 (h-M1-Gallerie-Wagner–De Angeli), as indicated by MM.

Both the ground level and rail level were included based on the information in the drawings. It can be noted that all sections are relatively shallow: for Sections 1 and 2, the tunnel depth does not exceed 12 meters, while for Sections 3 to 7, the depth is under 16 meters.

Lastly, where transversal beams, oriented orthogonally to the tunnel's axis, were present, their geometry was homogenized along the length of the slab. This adjustment is necessary because the transfer function is computed using a 2D plane strain model, while in reality these beams intersect the tunnel cross-section every 3.2 meters. Therefore, a homogenization approach is required to capture the representative stiffness of the actual 3D configuration within the simplified 2D domain.

Two limiting cases could be considered: one that considers only the slab thickness, resulting in a stiffness lower than reality, and another that assumes a fully rigid transverse beam, leading to a stiffer-than-real section. In practice, the actual stiffness lies somewhere between these two extremes. To better approximate this intermediate behaviour, homogenization provides a practical and reasonable solution.

The effect of transverse beams on vertical acceleration has been studied in the literature, particularly for 2D plane strain linear models of box-shaped tunnel sections similar to those analysed here on Milan's M1 metro line. In [9] and [8] , comparisons between tunnel roof configurations, with and without stiffening, showed that adding transverse stiffeners slightly increases the vertical acceleration in the ceiling slab and in the soil immediately above it. These studies suggest that increased slab thickness mainly influences the vertical acceleration along the roof and adjacent soil, but not significantly at lower elevations of the tunnel.

Specifically, [9] notes that a stiffer roof results in a box-like vibration mode, where the tunnel vibrates more uniformly with both lateral walls. However, this effect is more relevant to horizontal accelerations, and no specific conclusions were drawn about the point of interest in this study, located 2 meters above the rail level on the inner tunnel wall.

Similarly, [11] compared two cases, a 0.2 m thick roof slab versus a rigid beam of 0.5 m width and 1.0 m height and found no significant difference in the vertical component of the transfer function (i.e., acceleration response under unitary harmonic load) at a measurement point located 1.5 m above rail level.

In conclusion, homogenizing the transverse beams into an equivalent slab thickness is a valid and practical approach, especially since the focus of this study is on vertical acceleration at a fixed point on the inner tunnel wall. While this homogenization may influence local effects at the slab level or in the overlying soil, its impact at the measurement point of interest is expected to be minimal.

This homogenization approach was applied to sections 3 through 7, all of which feature box-shaped tunnel geometries. Taking section 3 as an example, the original tunnel section and the transverse beams to be homogenized are shown in **Figure 3.2** .

The beam dimensions are defined as height $H = 1.8\,m$ and width $B = 0.5\,m$, the spacing between the beams $S = 3.2\,m$, the height of the existing slab as $h_b = 0.3\,m$ and the height of the homogenized slab layer $h_e = 0.28\,m$. The height h_e is determined with expression

$$h_e = \frac{H * B}{S} \tag{3.2}$$

Thus, the total slab height of the modified section becomes $h_{tot} = h_b + h_e = 0.58\,m$. The modified section is shown in **Figure 3.3**.

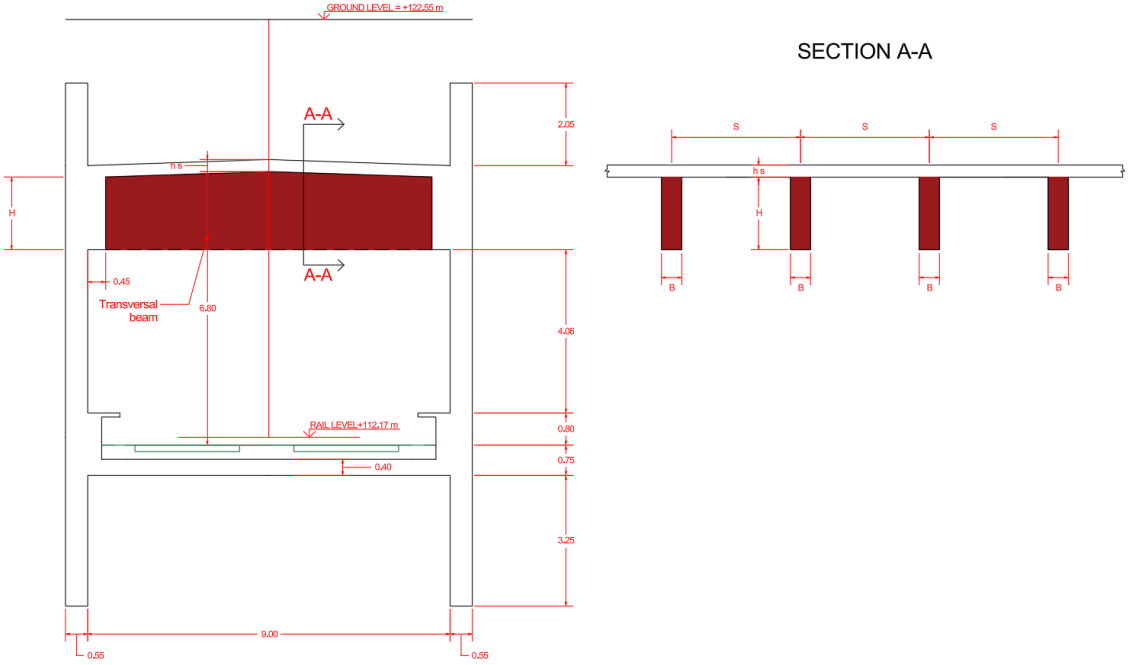

Figure 3.2 *Original section: Transversal beams to be homogenized in red*

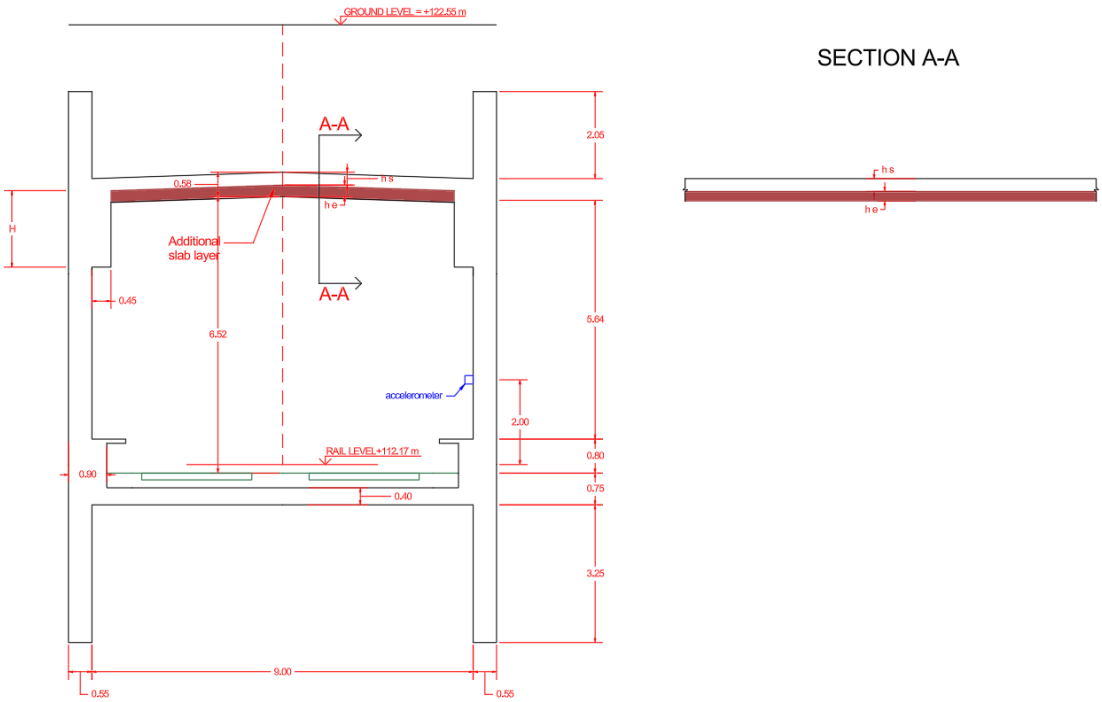

Figure 3.3 *Modified section: Homogenized slab layer in red*

3.2.1 Section 1

This section is located along the track between Moscova and Garibaldi stations of the M2 metro line. It consists of two independent hollow tunnels, each dedicated to a train traveling in opposite directions. According to MM, this section does not include ballast or wooden sleepers; instead, the rails are directly fixed to the concrete slab using a steel plate and an elastomeric pad **Figure 3.6**.

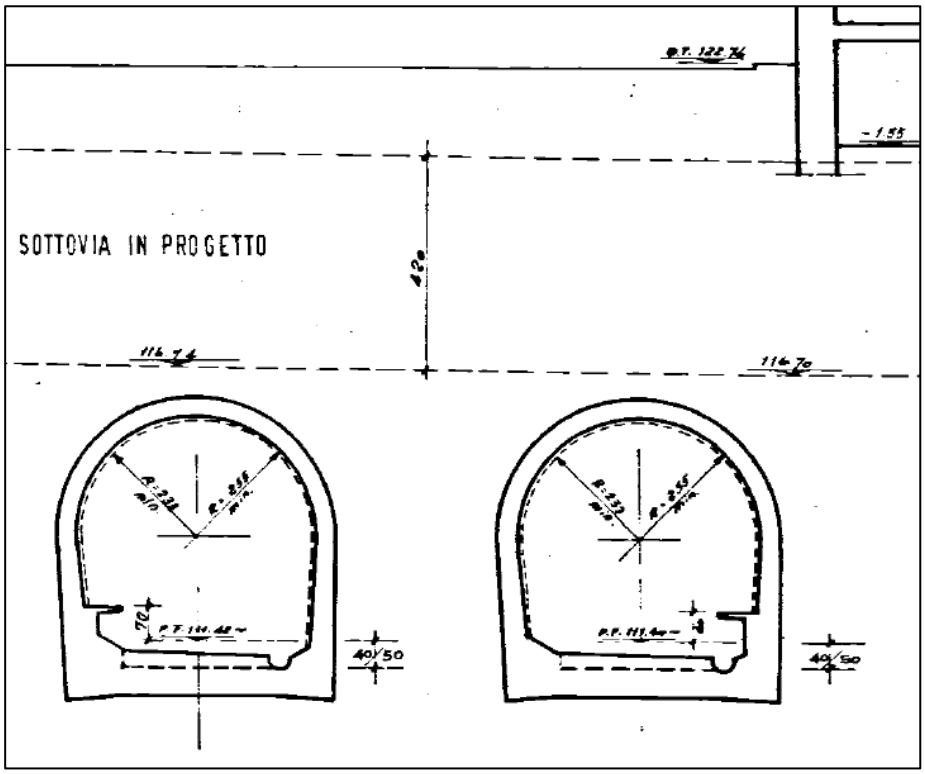

Figure 3.4 *Original drawing provided by MM for the section 1*

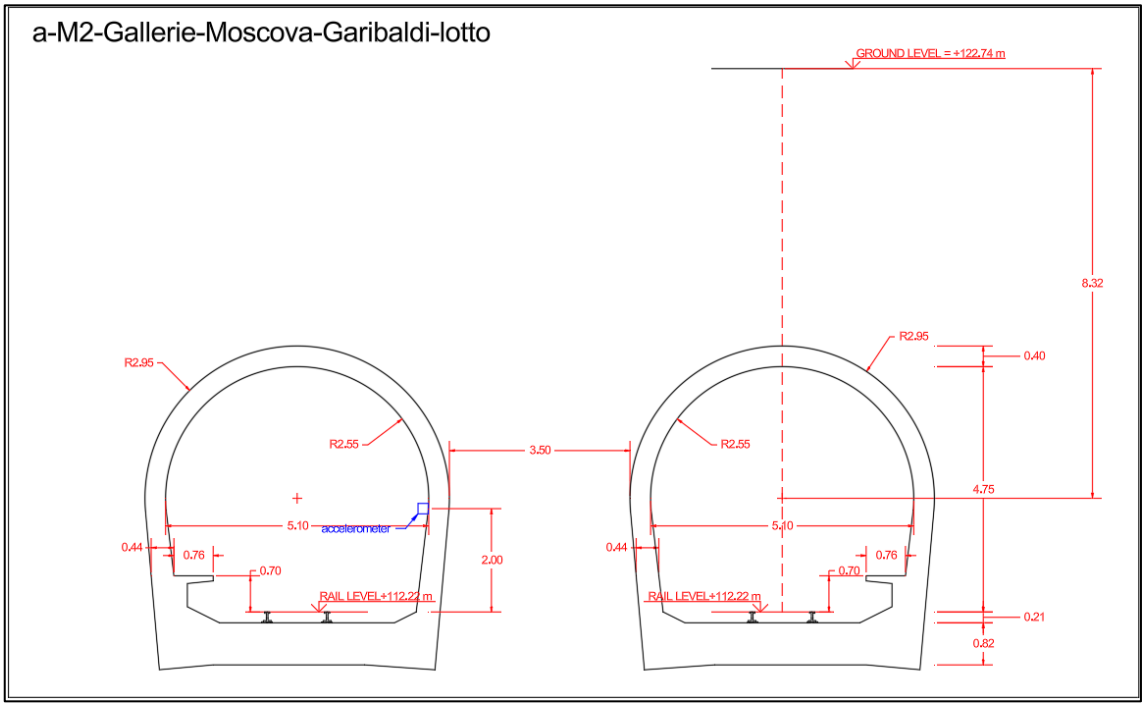

Figure 3.5 *Geometry of tunnel section 1 in meters*

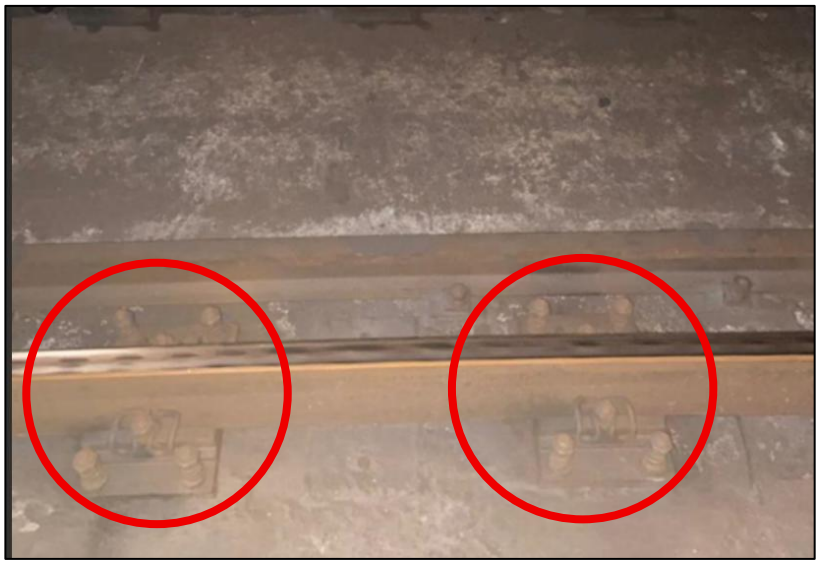

Figure 3.6 *Picture of the rail track connection support*

3.2.2 Section 2

This section corresponds to the track between Loreto and Piola stations on the M2 metro line. As mentioned before, it was indicated that the two tunnels merged along the section where the investigation was carried out, sharing a common wall, as shown in **Figure 3.8**. Additionally, the track support system is the same as in Section 1 (**Figure 3.6**), consisting of steel plates and elastomeric pads, with no presence of ballast or sleepers.

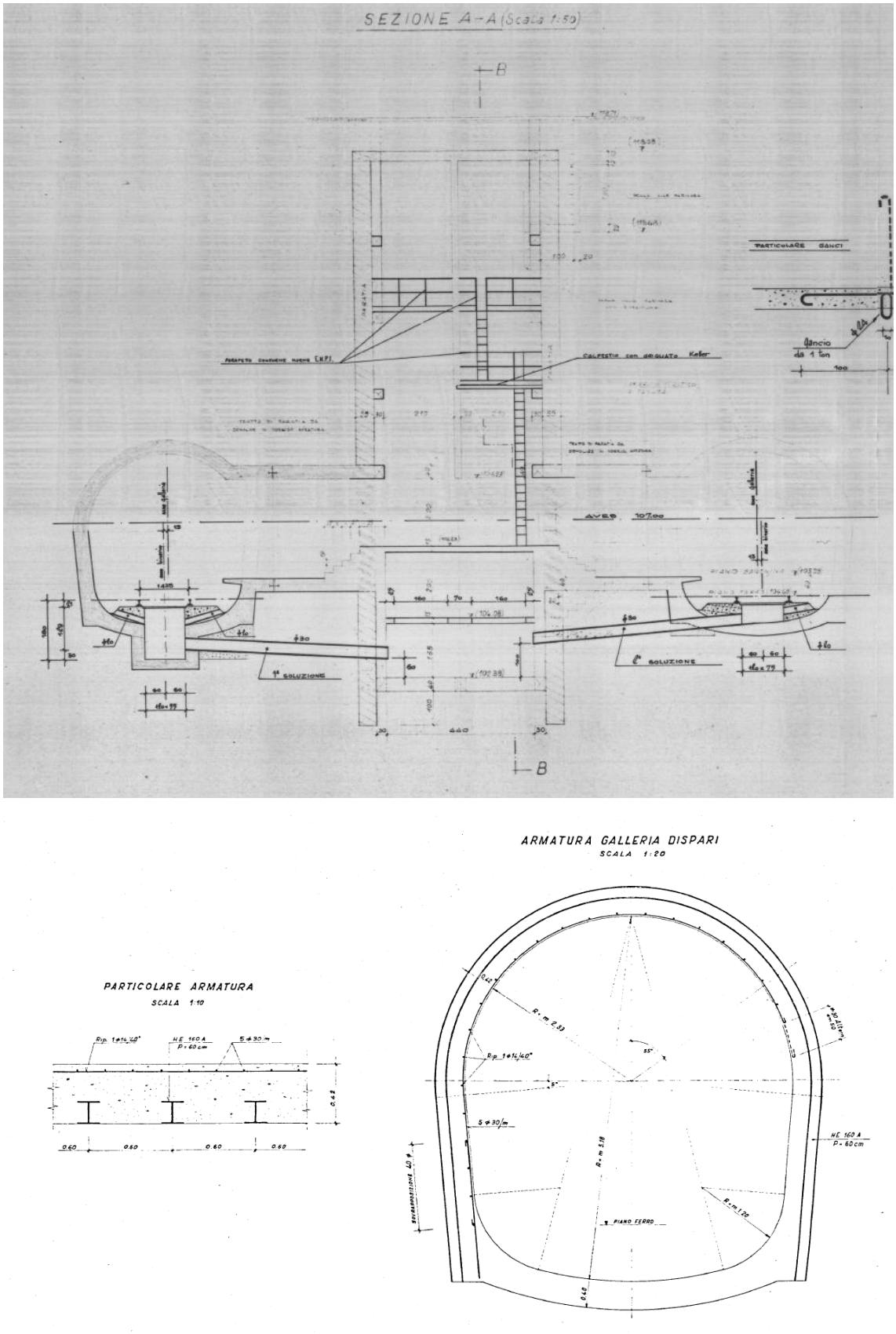

Figure 3.7 *Original drawing provided by MM for the section 2*

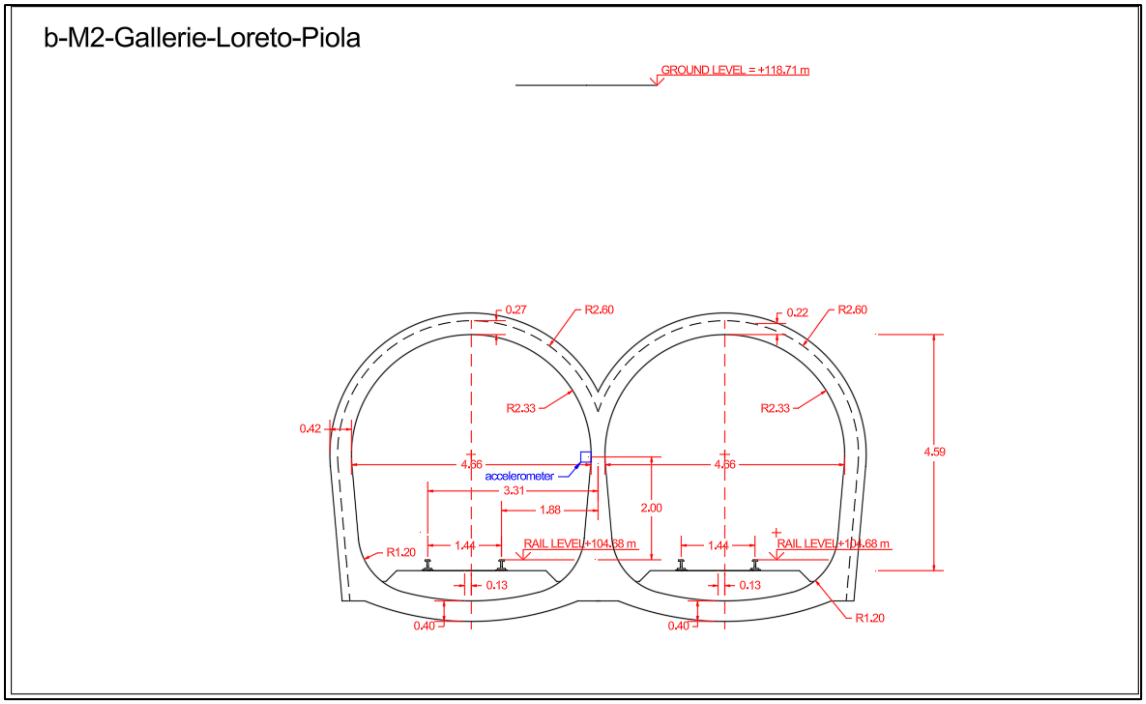

Figure 3.8 *Geometry of tunnel section 2 in meters*

3.2.3 Section 3

This section is located along the track between Udine and Cimiano stations on the M2 metro line. Unlike sections 1 and 2, it features a box-shaped tunnel characteristic of the "cut and cover" construction method. In this case, the ballast is absent, and the track consists of a reinforced concrete slab system with wooden sleepers embedded directly into it (see **Figure 3.11**). Additionally, the two rail tracks are not separated by a dividing wall; instead, they run side by side, as shown in the **Figure 3.10**.

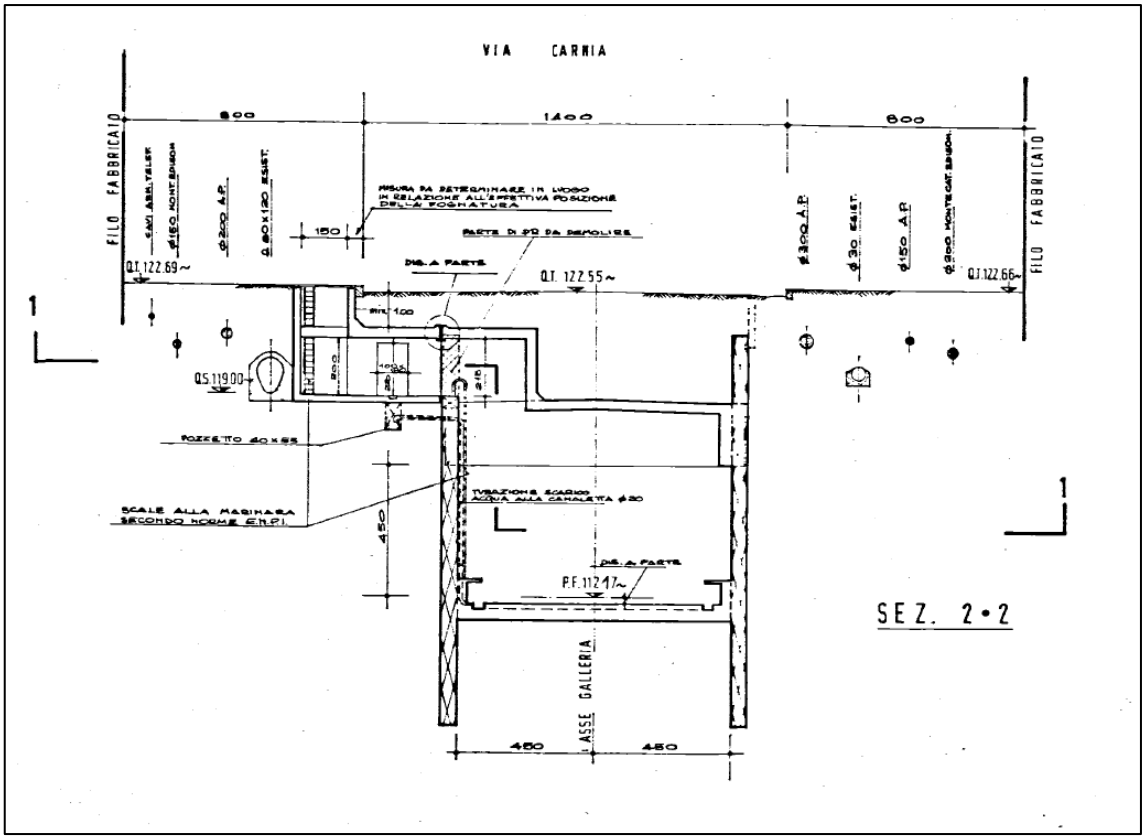

Figure 3.9 *Original drawing provided by MM for the section 3*

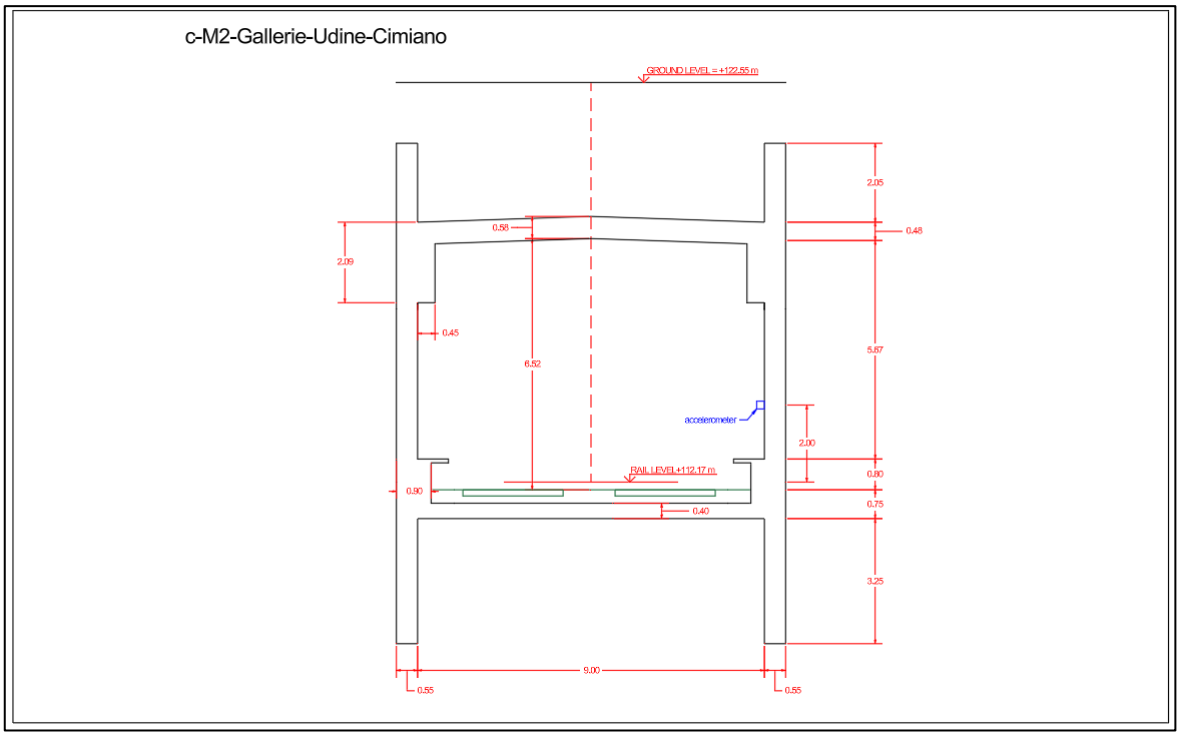

Figure 3.10 *Geometry of tunnel section 3 in meters*

Figure 3.11 *Picture of the wooden sleepers embedded in the reinforced concrete slab track for section 3*

3.2.4 Section 4

This section corresponds to the track between Sesto Marelli and Villa San Giovanni stations on the M1 metro line. These stations are located on the outskirts of Milan, with Sesto Marelli being one of the terminal stations of the line. Since direct design drawings for this section were not available, and as indicated in the introductory paragraph, it was assumed to be equivalent to Section 7 (corresponding to the track between Wagner and De Angeli stations on the M1 line). The tunnel has a box-shaped cross-section, with both tracks running side by side. In this case, ballast and wooden sleepers are present, with the latter spaced approximately 0.60 meters apart [45].

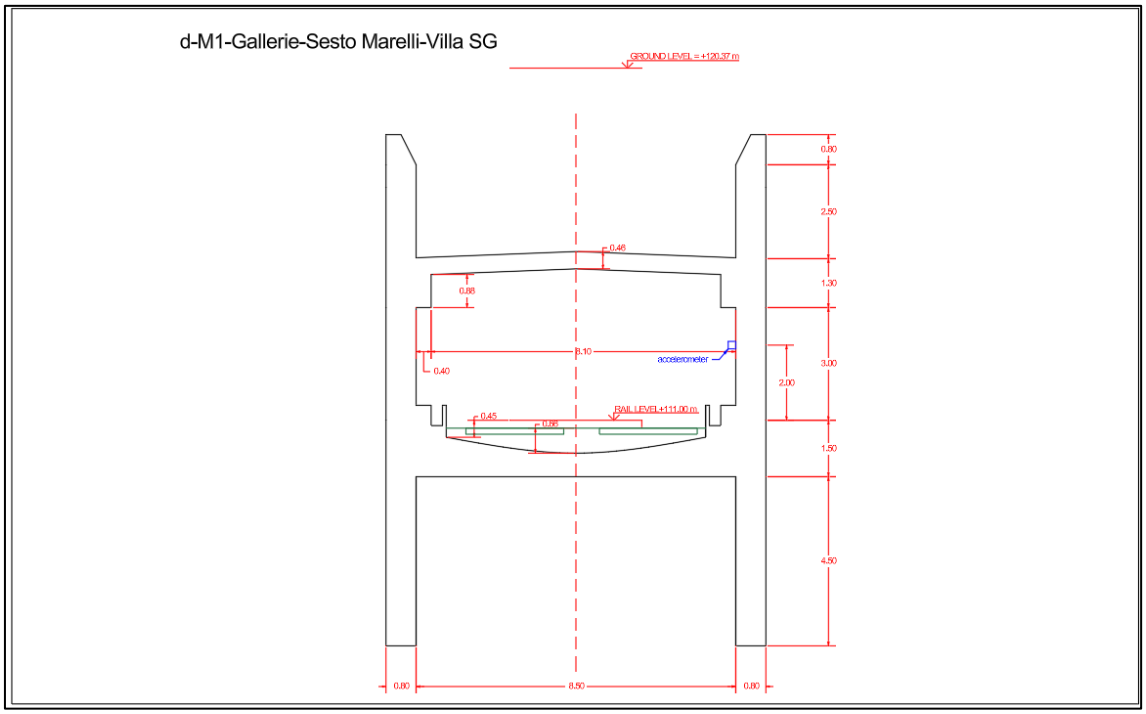

Figure 3.12 *Geometry of tunnel section 4 in meters*

3.2.5 Section 5

This section covers the track between Villa San Giovanni and Precotto stations on the M1 metro line, continuing from the track described in Section 4. As previously mentioned, this section was assumed to be equivalent to Section 7 as no original drawings were available. It features a box-shaped tunnel cross-section with both opposing tracks positioned side by side. Additionally, the track structure includes ballast and wooden sleepers for rail support.

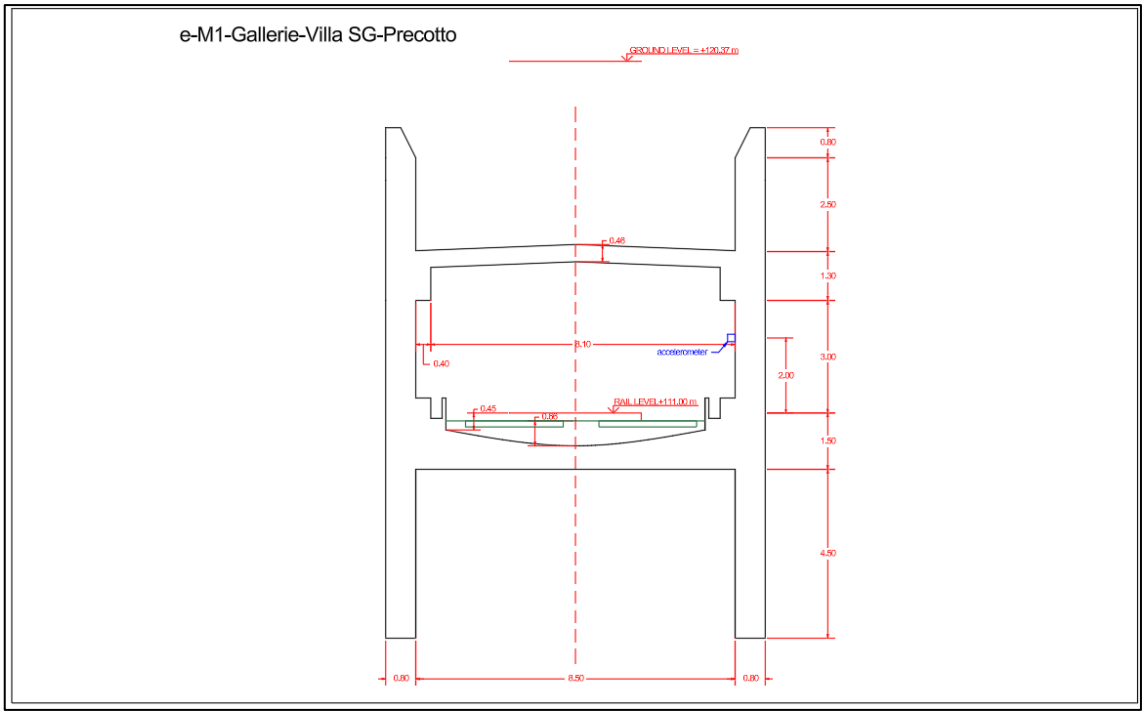

Figure 3.13 *Geometry of tunnel section 5 in meters*

3.2.6 Section 6

This section covers the track between Duomo and Cordusio stations on the M1 metro line, located in the central area of Milan. As shown in **Figure 3.15**, the tunnel has a double box-shaped cross-section and includes an additional central slab intended for pedestrian use. The tracks for opposing directions run side by side, and the rail support system consists of ballast and wooden sleepers, spaced approximately 0.60 meters apart.

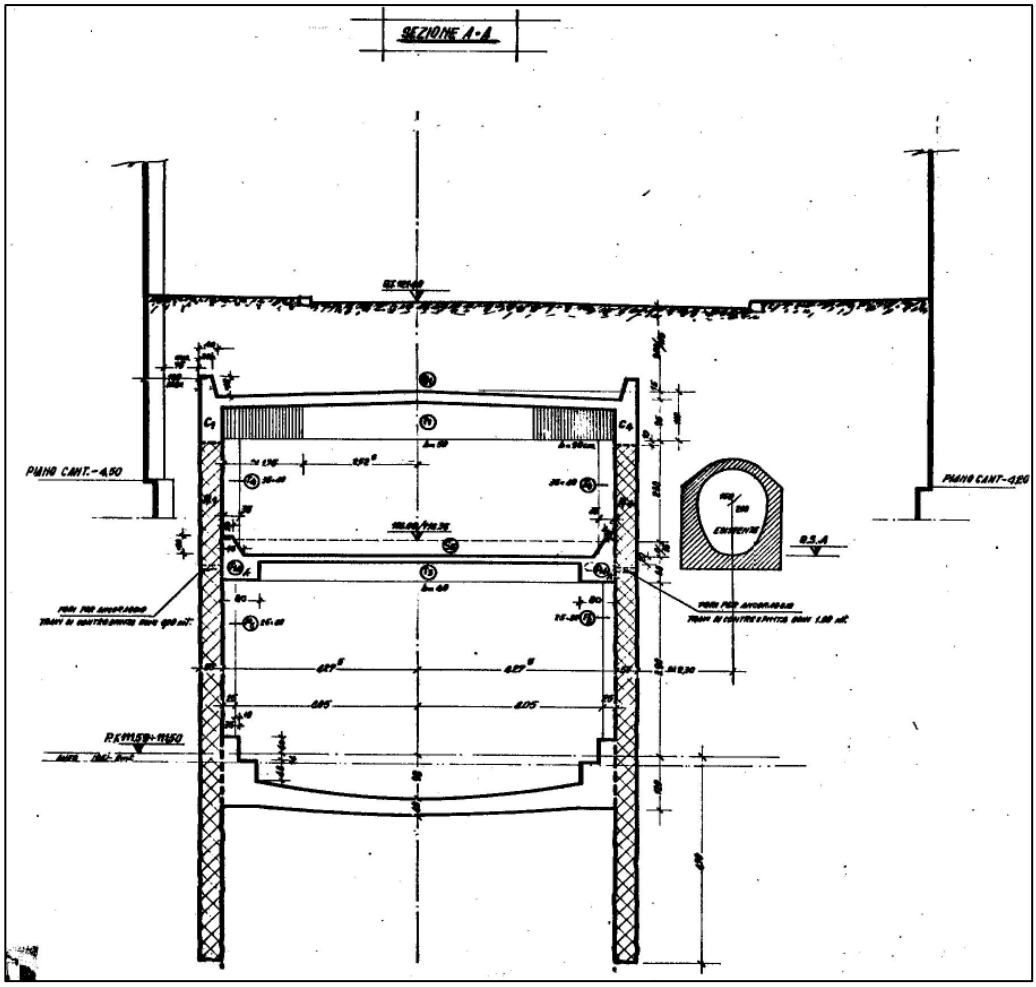

Figure 3.14 *Original drawing provided by MM for the section 6*

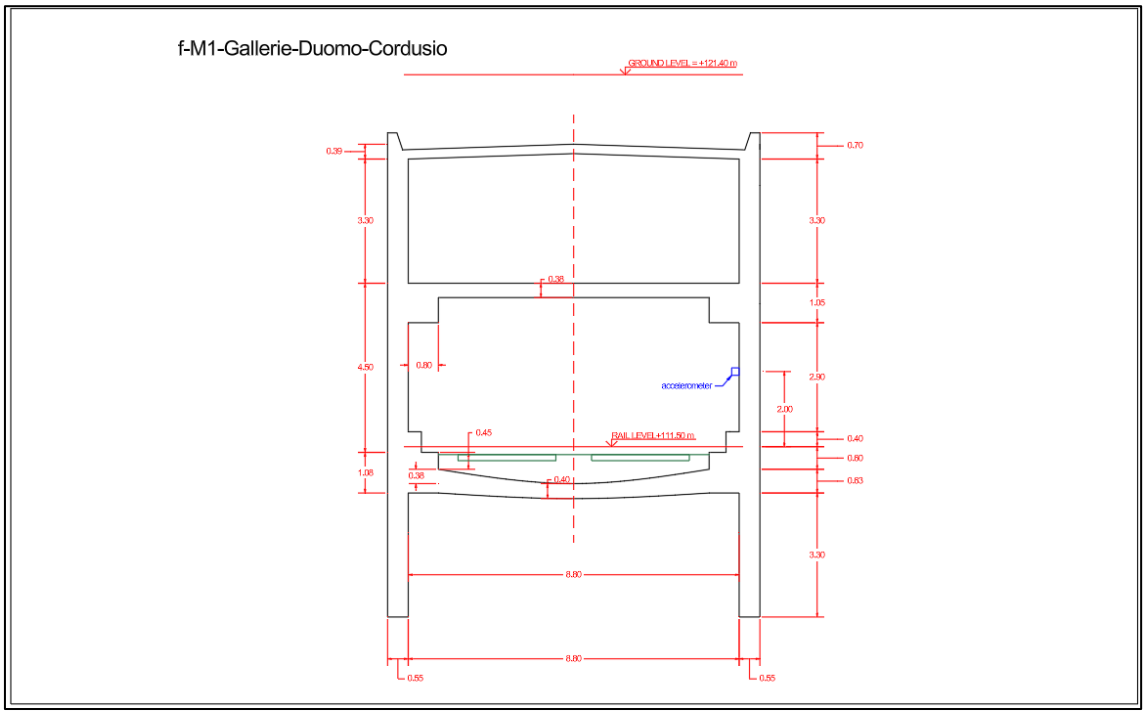

Figure 3.15 *Geometry of tunnel section 6 in meters*

3.2.7 Section 7

This section covers the track between Wagner and De Angeli stations on the M1 metro line. It features a box-shaped cross-section, with rails supported by ballast and wooden sleepers spaced at 0.60 meters. As previously mentioned, this section was used as a reference for sections 4 and 5, since original design drawings were available only for this configuration.

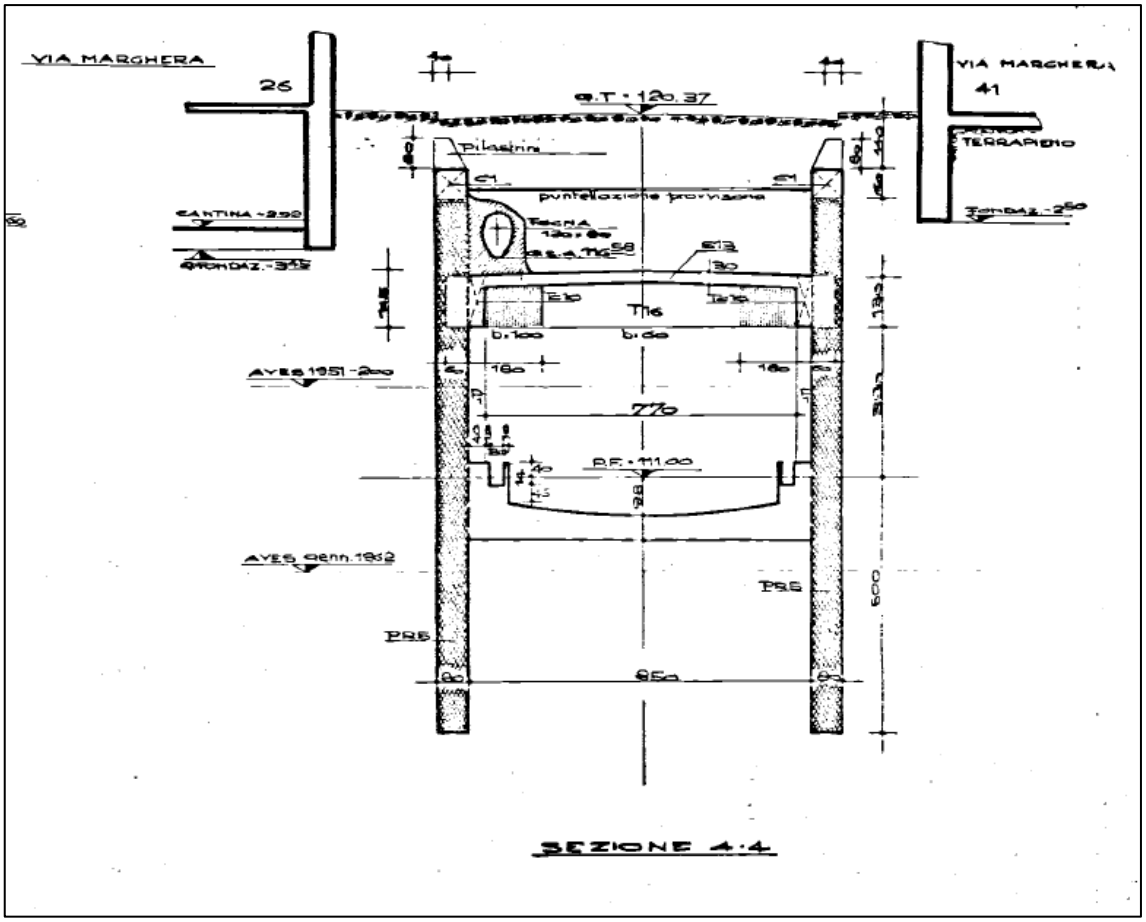

Figure 3.16 *Original drawing provided by MM for the section 7*

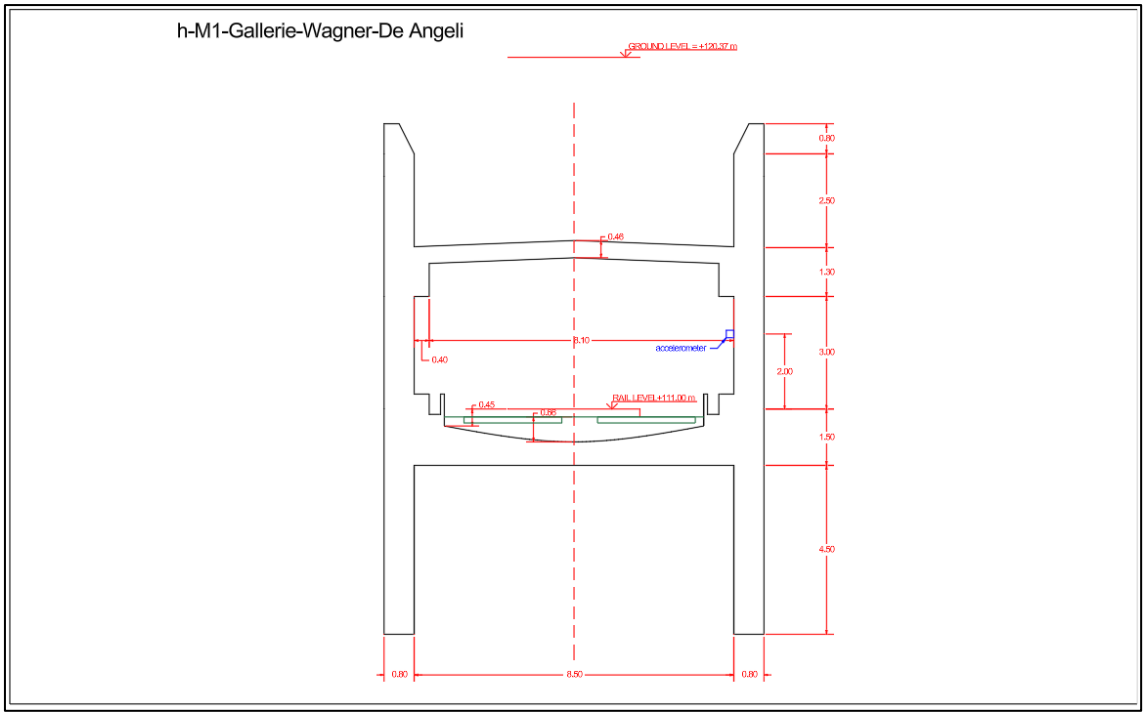

Figure 3.17 *Geometry of tunnel section 7 in meters*

The names, locations, section type, track type and inauguration date of the sections [3] are summarized in the following table.

Table 3.1 Metro Line Sections and Corresponding Locations

Section	Metro line	Location	Section type	Track type	Date
1	M2	Moscova – Garibaldi	Circular separated	RC slab + Elastomeric pads	1978
2	M2	Loreto – Piola	Circular merged	RC slab + Elastomeric pads	1969
3	M2	Udine – Cimiano	Box-shaped	RC slab + wooden sleepers	1969
4	M1	Sesto Marelli – Villa San Giovani	Box-shaped	Ballasted + wooden sleepers	1964
5	M1	Villa San Giovani – Precotto	Box-shaped	Ballasted + wooden sleepers	1964
6	M1	Duomo – Cordusio	Double box-shaped	Ballasted + wooden sleepers	1964
7	M1	Wagner – De Angeli	Box-shaped	Ballasted + wooden sleepers	1966

3.2.8 Train type description

The general characteristics of a typical "Leonardo" train, classified as a HRV (Heavy Rail Vehicle), correspond to an urban metro design intended for passenger transportation operating on both the M1 and M2 lines. Traction is provided by 16 asynchronous three-phase motors, two per trolley, mounted on eight of the twelve motorized trolleys, while the remaining four are trailer (non-motorized) trolleys [45]. The train type configuration is shown in **Figure 3.18** provided by Environmental Product Declaration published by Hitachi Rail Italy. Additionally, the Metro line features are summarised in Table 3.2 based on indications provided by MM and previous studies [9][11][45].

Figure 3.18 *Lateral and top view of "Leonardo" train from [45]*

Table 3.2 General features of Milan's M1 and M2 Metro Line adapted from [9][11]

Train length	m	106.94
Train width	m	2.85
Car length	m	17.6
Bogie spacing	m	11.1
Wheel spacing	m	2.15
Axles per bogie	-	2
Bogies per car	-	6
Number of cars	-	6
Track gauge	m	1.435
Sleeper dimensions	m	2.6 x 0.16 x 0.24
Sleeper spacing	m	0.6
Elastomeric pad spacing	m	0.75

3.3 Frequency response of the tunnel to train passage

3.3.1 Accelerometric measurements

The first step in determining the tunnel's frequency response, denoted as $R(f)$, involves recording vertical accelerations on the tunnel wall during train passages. For this purpose, accelerometers were installed on the inner side wall of each tunnel section, positioned at a height of 2.00 meters above the rail track level. The sensor placements for Sections 1 through 7 are illustrated in Subchapter 3.2.

The sensors were installed to ensure that the measurements accurately captured the dynamic forces generated by passing trains. The sampling frequency is 4800 Hz, corresponding to a sampling period of $2.0833\ x\ 10^{-4}$ seconds. The accelerometric data analysed correspond to recordings taken between 7:00 and 8:00 in the morning. The specific dates on which the measurements were recorded are summarized in Table 3.3.

Table 3.3 Dates of acceleration measurements by section

Section	Metro line	Date
1	M2	20/12/2021
2	M2	21/12/2021
3	M2	22/12/2021
4	M1	23/12/2021
5	M1	11/01/2022
6	M1	12/01/2022
7	M1	14/01/2022

In addition to acceleration measurements, displacements were also recorded using extensometers. This data will be used to estimate the train's velocity and to validate the data obtained from the accelerometers.

3.3.2 Disregarded recordings and pre-signal processing

In some instances, the recorded signals were affected by disturbances, most likely due to the simultaneous passage of two trains traveling in opposite directions. These disturbances were identified by inspecting the amplitude distribution in the time domain, where valid signals typically show a gradual increase and decrease in amplitude, while disturbed ones often exhibit sudden jumps. As a result, these affected recordings were excluded from the final analysis to preserve the reliability of the results. For example, in Section 2, 14 out of 32 total recordings were disregarded due to signs of disturbance or incompleteness, a plot of these disturbed signals is shown in **Figure 3.19**.

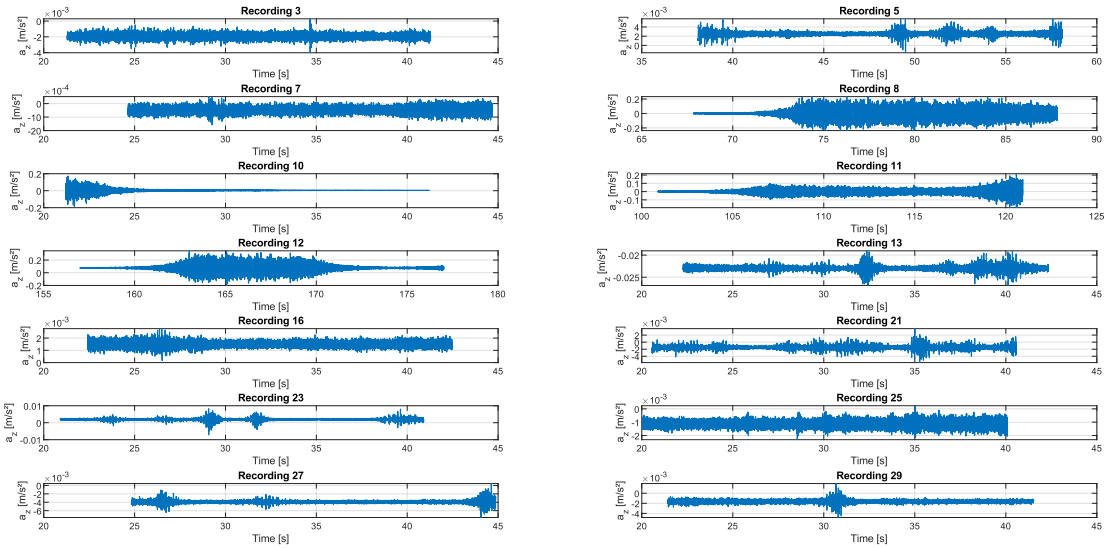

Figure 3.19 *Disturbed signals for section 2*

Following the same criteria for the rest of the sections, the number of total, disturbed and considered recordings is summarized in Table 3.4.

Table 3.4 Number of total, disturbed and remaining signals considered in the analysis

Section	Number of total recordings	Number of disturbed recordings	Number of considered recordings
1	25	0	25
2	32	14	18
3	23	8	15
4	21	4	17
5	22	1	21
6	23	7	16
7	12	0	12
Total	158	34	124

Additionally, some recordings, although not affected by disturbances, exhibited a shift from the zero-mean level. To ensure consistency in the analysis, these signals were adjusted by removing their mean values, resulting in zero-mean amplitudes.

Furthermore, all recordings needed to have the same time duration and be aligned to a common frequency step to enable a meaningful computation of the average magnitude spectrum. To achieve this, a normalization procedure was applied. Although the intended duration of each recording was approximately 20 seconds, slight variations occurred due to the nature of the recording process. To address this, signals longer than 20 seconds were truncated, while those shorter than 20 seconds were zero-padded to reach the exact target duration.

After applying these preprocessing steps in the time domain, **Figure 3.20** illustrates the comparison between the original and the zero-mean signal for a representative case recorded for Section 2.

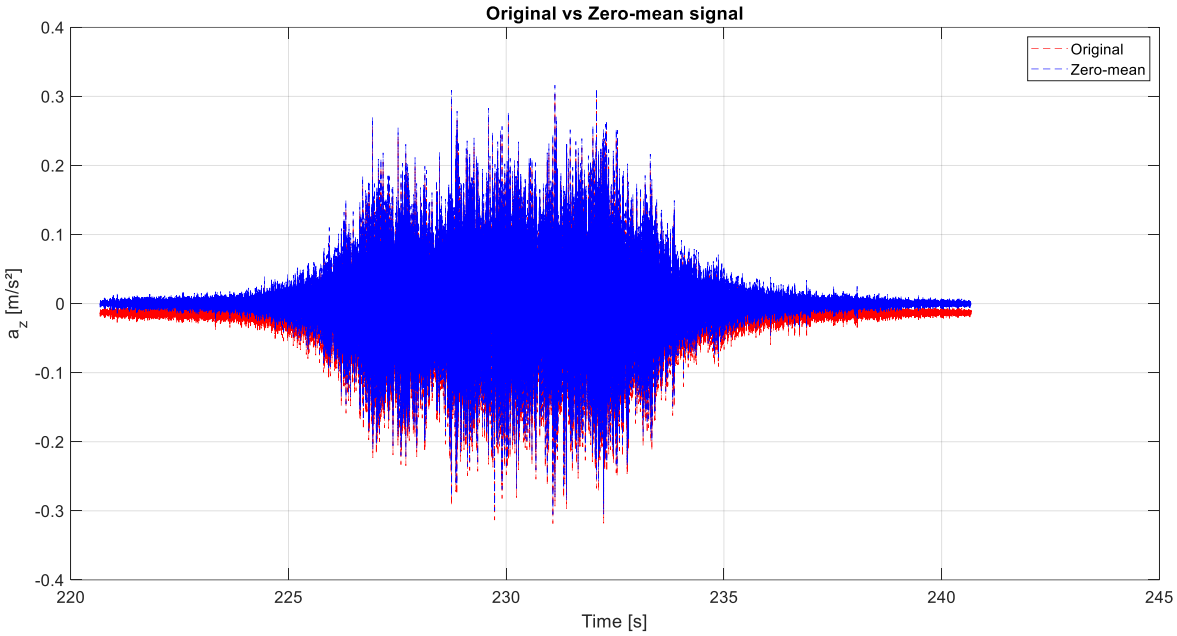

Figure 3.20 *Original vs Zero-mean signal for a representative case in Section 2*

3.3.3 Signal processing

The signals recorded in the time domain were converted to the frequency domain using the Fourier transform. However, since the original sampling frequency is Fs=4800 Hz and the transfer function is defined up to 200 Hz, the signal must be decimated so that the inversion procedure can be applied effectively.

To ensure the desired frequency range in the one-sided spectrum (up to the Nyquist frequency of 200 Hz), the time-domain signal is downsampled to 400 Hz. This corresponds to selecting one sample every 12 samples (4800Hz/400Hz) from the original signal.

However, downsampling a signal can introduce aliasing, where high-frequency components are incorrectly mapped to lower frequencies. To avoid this, the original signal must be filtered to remove all frequency content above 200 Hz before downsampling. The signal processing procedure followed the steps described below.

Filtering

First, the signal was low pass filtered to remove frequency components above 200 Hz. This was accomplished using an 8th-order Butterworth filter with zero-phase shift. Butterworth filters are known for their maximally flat magnitude response in the passband and their monotonic behaviour overall. This smoothness comes at the cost of a less steep roll-off as explained in Subchapter 2.3.4.2.

However, when designing a discrete-time filter from a continuous one, such as the Butterworth filter, a transformation is required in order to prevent for aliasing when passing from the continuous to the discrete domain. In this case, a bilinear transformation method is chosen as the resulting distortion, or warping, of the frequency axis of this method is considered acceptable as explained in Subchapter 2.3.4.3.

In MATLAB, the Butterworth filter is designed using the *butter* function, which internally applies the *buttap* function to compute poles and then uses the *bilinear* function for the continuous-to-discrete transformation [46]. The function returns the numerator and denominator coefficients of the digital filter.

To eliminate phase distortion, zero-phase filtering is performed using the MATLAB's *filtfilt* function. This function applies the filter in both the forward and backward directions, effectively doubling the filter order while eliminating phase shift. The result is a filtered signal with the same magnitude response as the original filter but with zero phase distortion.

This procedure takes advantage of the time-reversal property of the Discrete Fourier Transform (DFT), which states that for a discrete signal $x[n]$ with DFT $X[k]$, the DFT of its time-reversed version $x[-n]$ is the complex conjugate $X^*[k]$. Where n is the discrete time and k is the discrete frequency. To illustrate the procedure, let's consider the case of a continuous-time signal $x(t)$ with Fourier Transform $X(f)$.

First a forward filtering is applied by multiplying the filter's frequency response $H(f)$ with $X(f)$:

$$Z(f) = H(f)X(f) \tag{3.3}$$

Where $Z(f)$ is the Fourier transform of the forward-filtered signal $z(t)$.

Then, the backward filtering is performed by filtering the time reversed signal $z(-t)$ whose Fourier Transform id $Z^*(f)$. Applying the filter again yields:

$$V(f) = H(f)Z^*(f) = H(f)H^*(f)X^*(f) = |H(f)|^2X^*(f) \tag{3.4}$$

Finally, the final output $y(t)$ is obtained by time-reversing $v(t)$, which corresponds in the frequency domain to taking the complex conjugate of $V(f)$:

$$Y(f) = V^*(f) = |H(f)|^2X(f) \tag{3.5}$$

Therefore, the overall frequency response of the zero-phase filtered signal is $|H(f)|^2$, a real and positive function. Since the phase is zero across all frequencies, the output signal $y(t)$ is aligned in phase with the original input $x(t)$, ensuring zero-phase distortion. Although the above explanation is based on the continuous domain for clarity, this procedure is implemented in the discrete domain in MATLAB.

Decimation

Once the signal is filtered, it is safe to perform decimation without aliasing. The sampling interval is increased to $\frac{1}{400\ Hz} = 2.5 * 10^{-3}s$, compared to the original $\frac{1}{4800\ Hz} = 2.083 * 10^{-4}s$. This choice aligns with the fact that the transfer function is defined up to 200 Hz. As the Discrete Fourier Transform (DFT) reveals frequencies only up to half the sampling rate (the Nyquist frequency), resampling at 400 Hz ensures consistency. In MATLAB, one sample is selected for every 12 original samples.

One-sided Discrete Fourier Transformation

After filtering and decimation, the one-sided DFT is computed. First, the MATLAB *fft* function is used to compute the two-sided DFT P_2 of the signal with L time points. Then, the magnitude spectrum is computed by taking the absolute values of P_2 and the positive-frequency half is extracted to form the one-sided spectrum P_1 with $\frac{L}{2} + 1$ values. To conserve energy from the full spectrum, all

P_1 values, except for the first and Nyquist components, are multiplied by 2. Finally, the spectrum is normalized by the length L.

Figures in this study show a clear contrast between three cases:

- Original signal sampled at 4800Hz.
- Signal decimated to 400Hz, without applying the low-pass filter at 200Hz to the original signal.
- Signal decimated to 400Hz, with the application of the low-pass filter at 200Hz to the original signal.

Aliasing is evident in the unfiltered decimated signal. In contrast, the filtered and decimated signal shows a spectrum consistent with the original.

Average frequency response spectrum for the recordings

To obtain a representative frequency spectrum for each section, an average of the response spectra is computed. However, the frequency step of the averaged spectrum must match that of the transfer functions (1 Hz). The spectrum from a 20-second recording has a frequency step of $\frac{1}{20\ s} = 0.05\ Hz$. Therefore, resampling in the frequency domain is necessary: one value is selected every 20 bands to achieve a 1 Hz step. The average spectrum $|R(f)|$ is then computed as:

$$|R(f)| = \sum_{i=1}^{N_{sig}} \frac{|a_{z,i}(f)|}{N_{sig}} \tag{3.6}$$

Where $|a_{z,i}(f)|$ is the Fourier spectrum magnitude values corresponding to every recording i and N_{sig} is the total number of recordings.

The results for each section are shown in the figures below.

3.3.3.1 Section 1

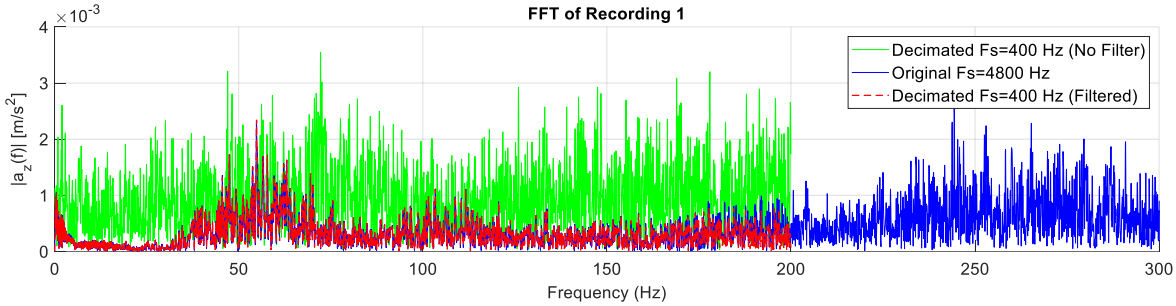

Figure 3.21 *Comparison among the original, decimated and decimated with filter signals for the first recording in the frequency domain for section 1*

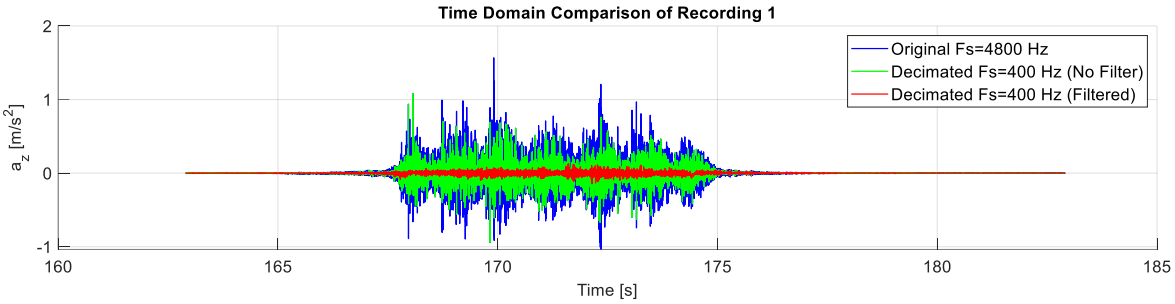

Figure 3.22 *Comparison among the original, decimated and decimated with filter signals for the first recording in the time domain for section 1*

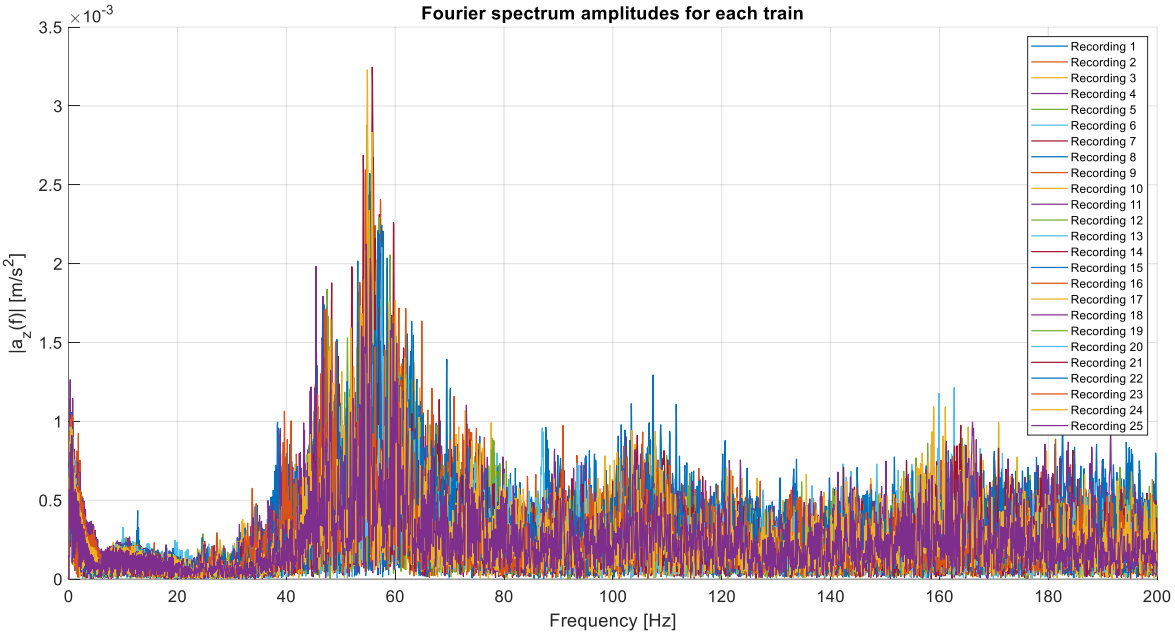

Figure 3.23 *Fourier transform of decimated and filtered signals for all the recordings in section 1*

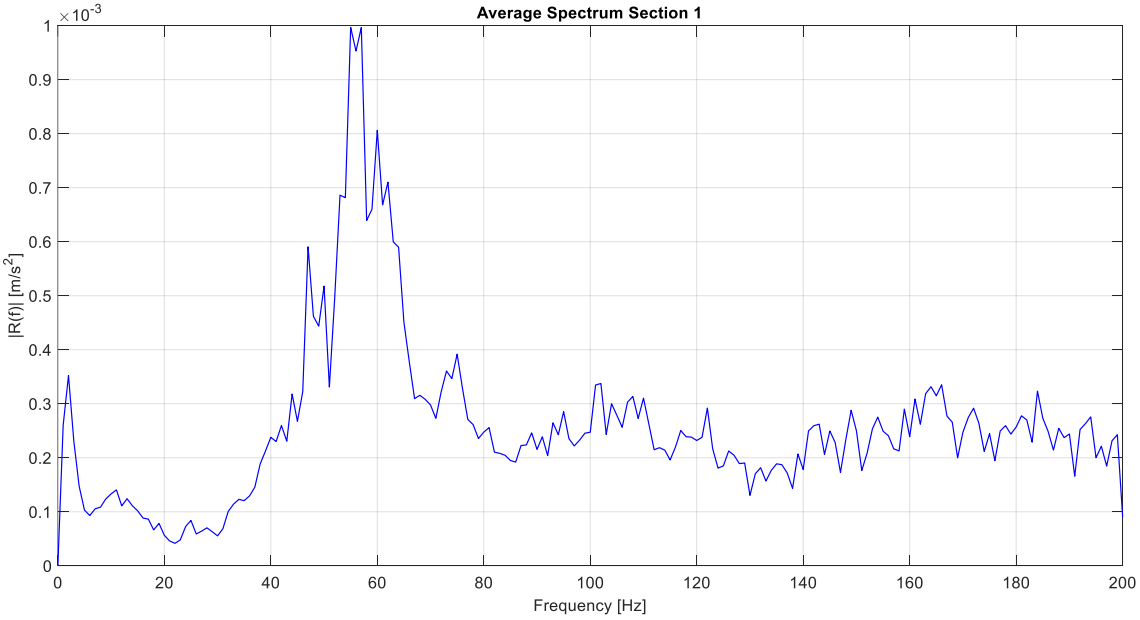

Figure 3.24 *Average spectrum R(f) of all recordings for section 1*

3.3.3.2 Section 2

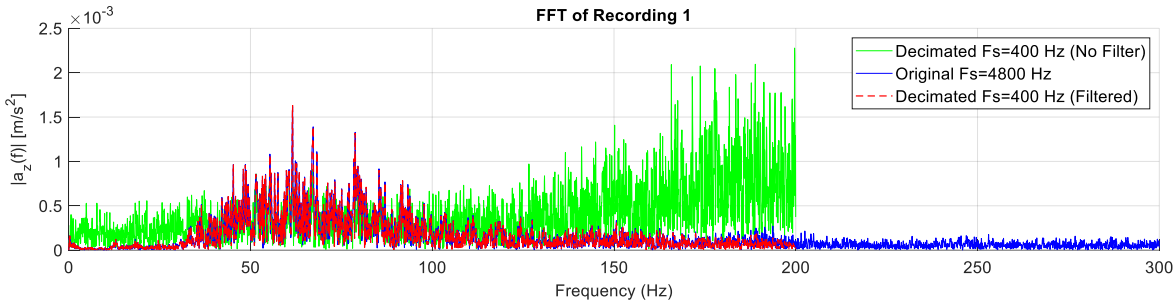

Figure 3.25 *Comparison among the original, decimated and decimated with filter signals for the first recording in the frequency domain for section 2*

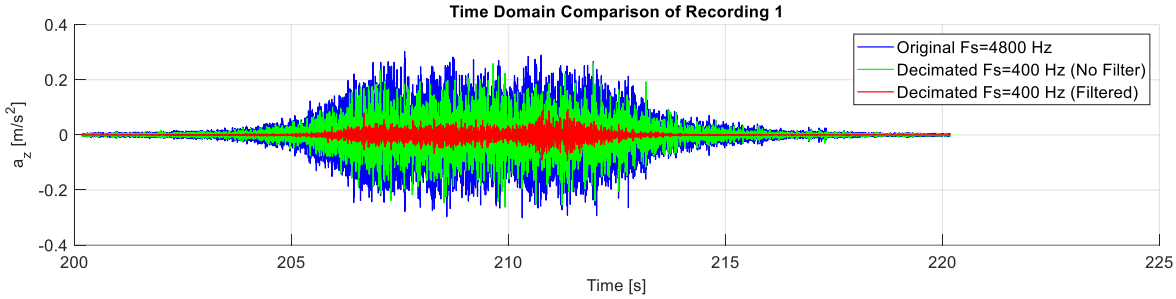

Figure 3.26 *Comparison among the original, decimated and decimated with filter signals for the first recording in the time domain for section 2*

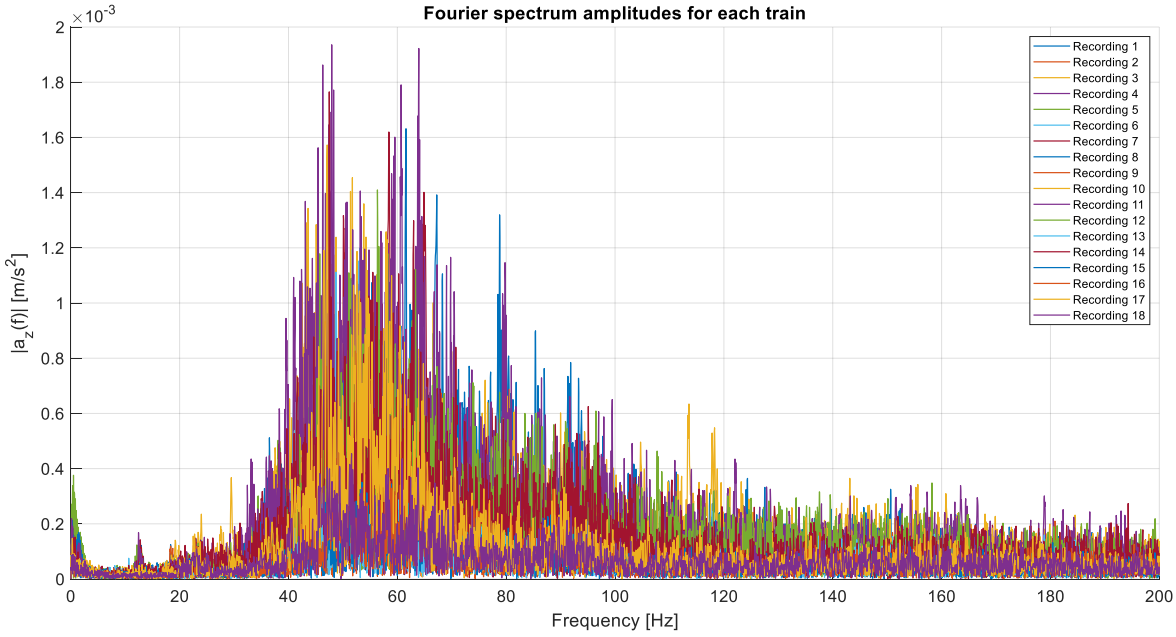

Figure 3.27 *Fourier transform of decimated and filtered signals for all the recordings in section 2*

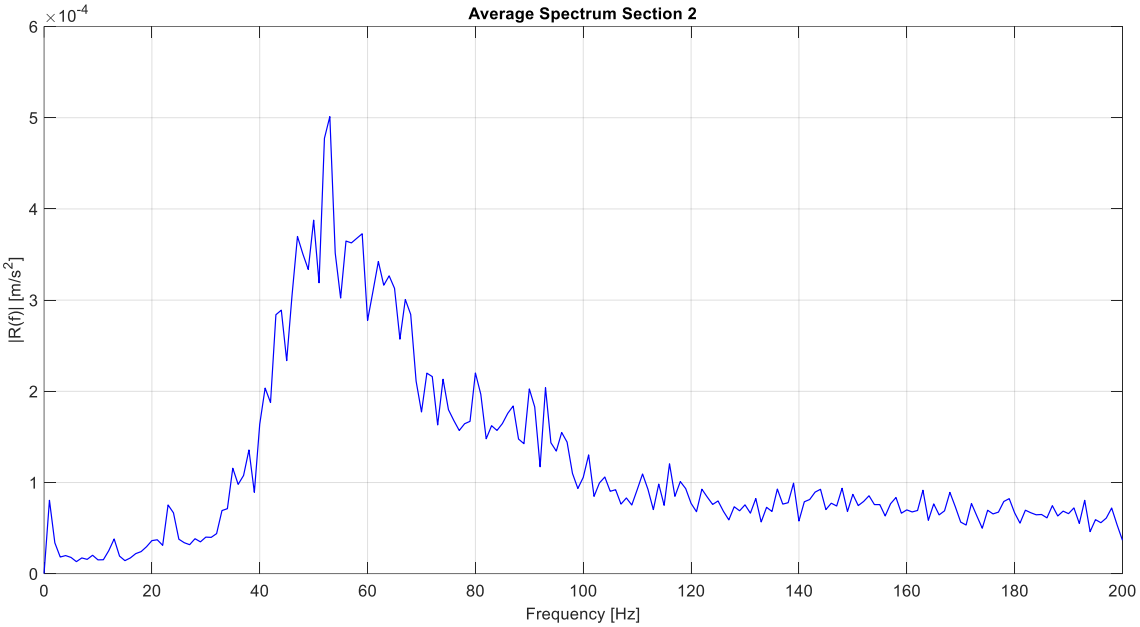

Figure 3.28 *Average spectrum R(f) of all recordings for section 2*

3.3.3.3 Section 3

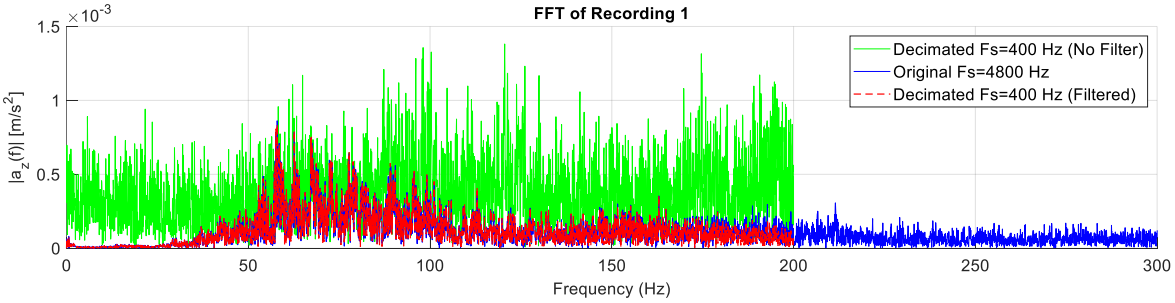

Figure 3.29 *Comparison among the original, decimated and decimated with filter signals for the first recording in the frequency domain for section 3*

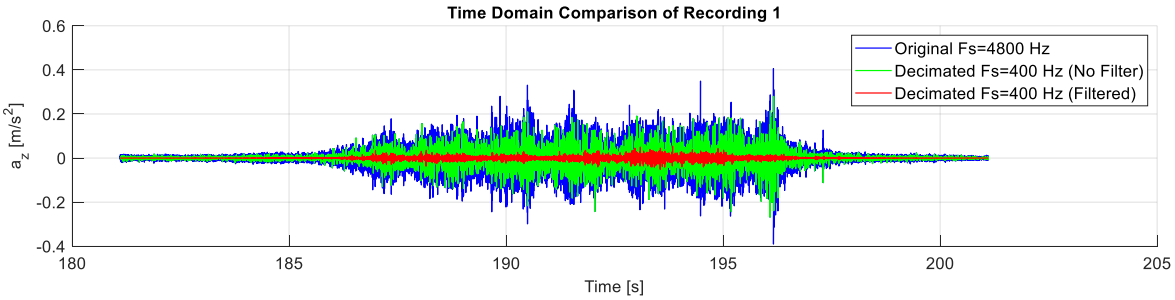

Figure 3.30 *Comparison among the original, decimated and decimated with filter signals for the first recording in the time domain for section 3*

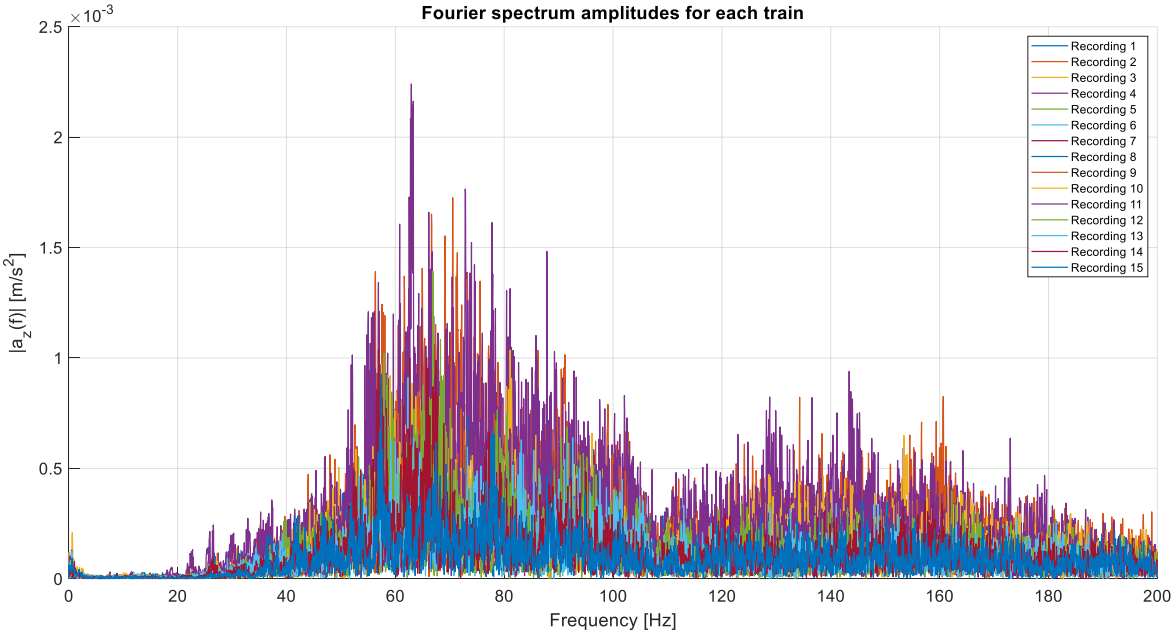

Figure 3.31 *Fourier transform of decimated and filtered signals for all the recordings in section 3*

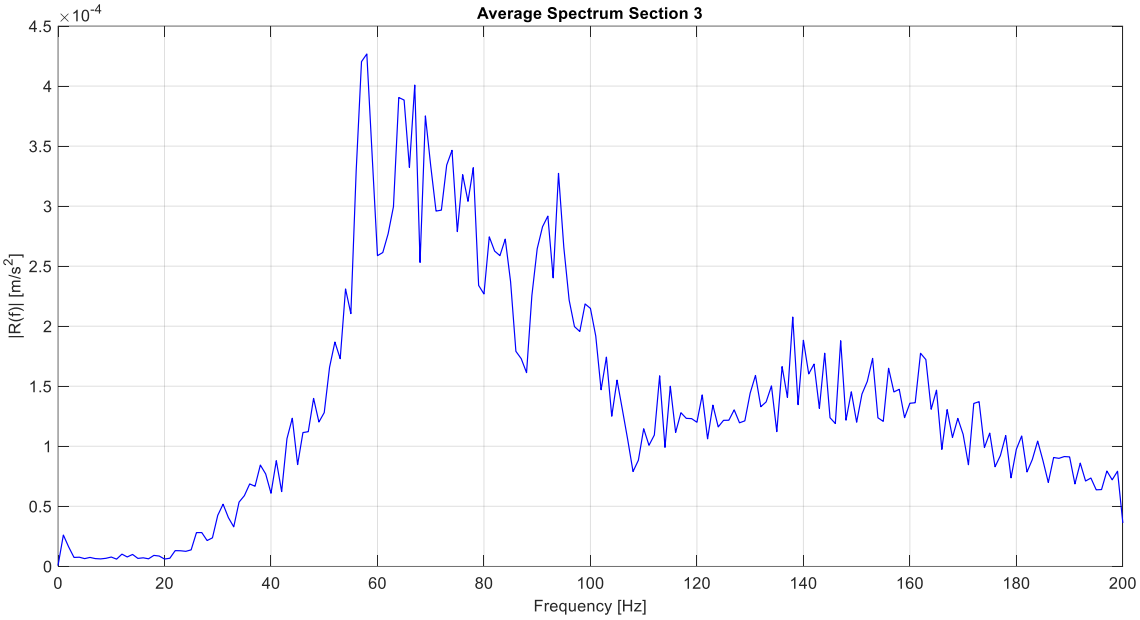

Figure 3.32 *Average spectrum R(f) of all recordings for section 3*

3.3.3.4 Section 4

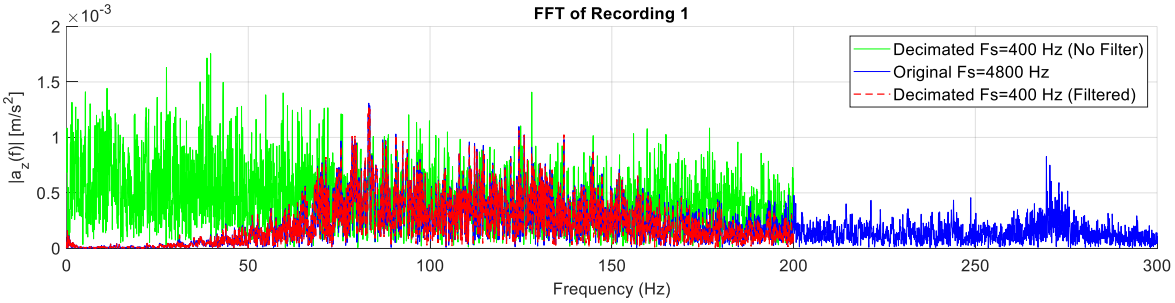

Figure 3.33 *Comparison among the original, decimated and decimated with filter signals for the first recording in the frequency domain for section 4*

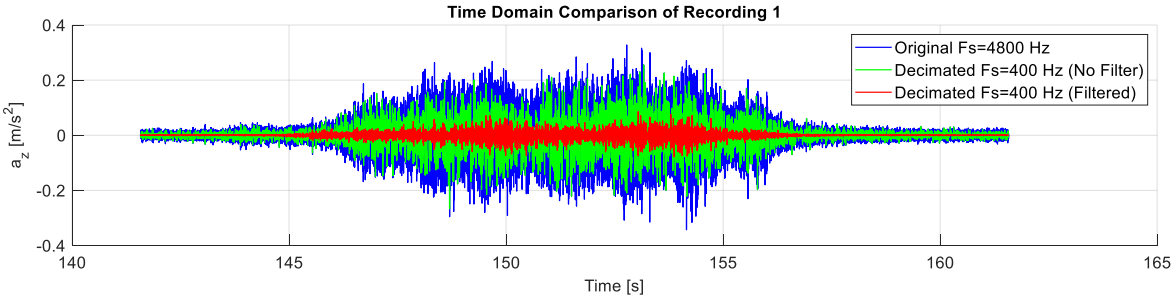

Figure 3.34 *Comparison among the original, decimated and decimated with filter signals for the first recording in the time domain for section 4*

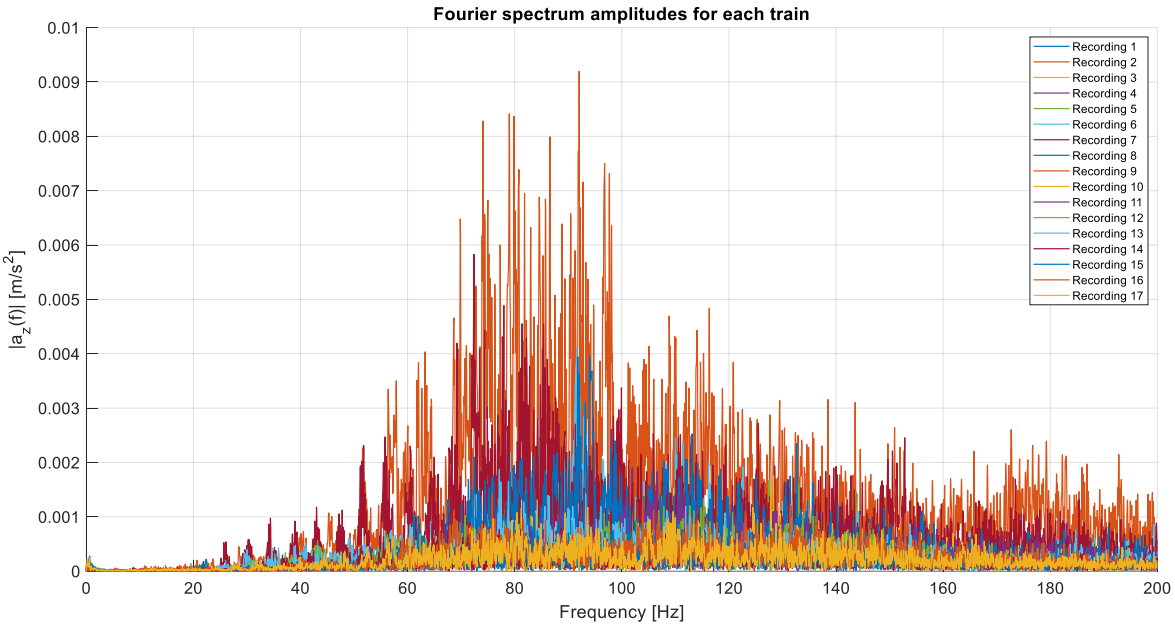

Figure 3.35 *Fourier transform of decimated and filtered signals for all the recordings in section 4*

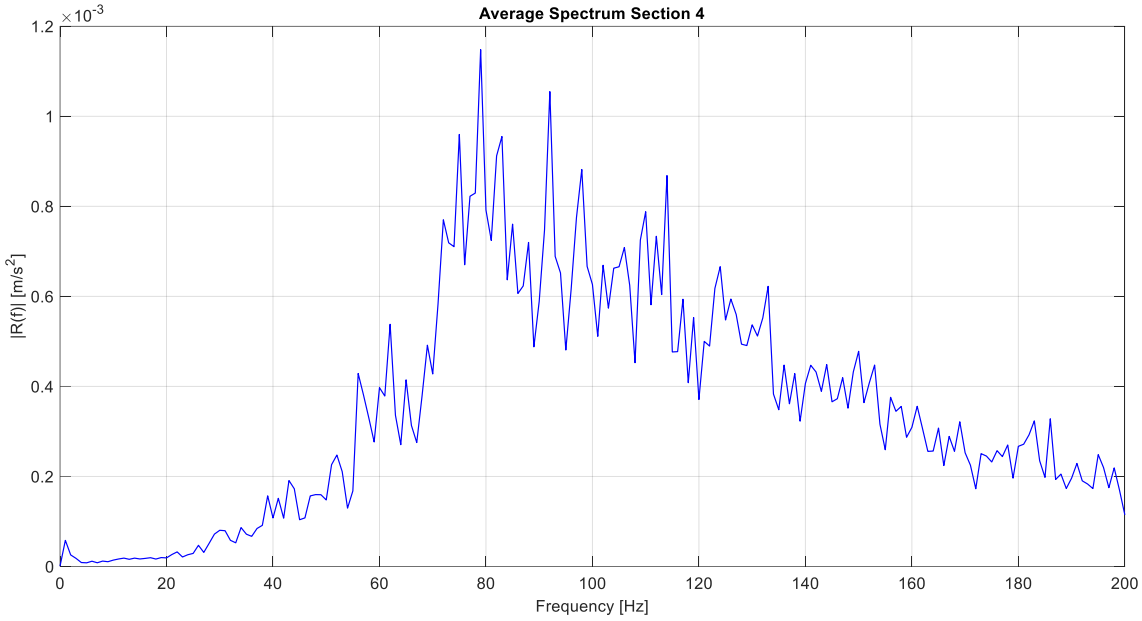

Figure 3.36 *Average spectrum R(f) of all recordings for section 4*

3.3.3.5 Section 5

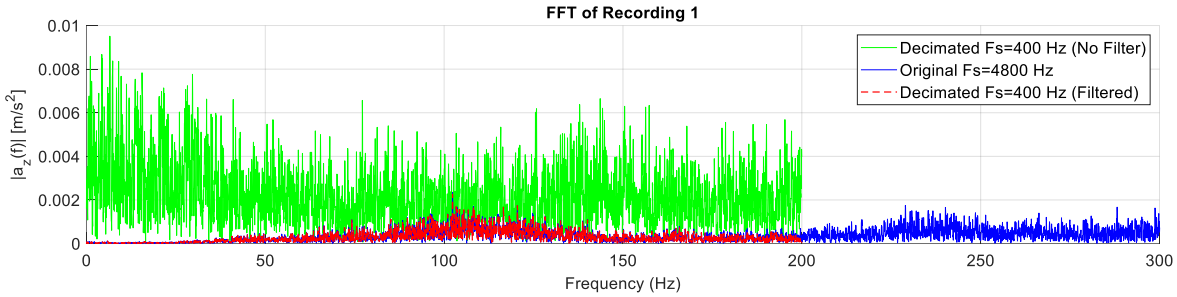

Figure 3.37 *Comparison among the original, decimated and decimated with filter signals for the first recording in the frequency domain for section 5*

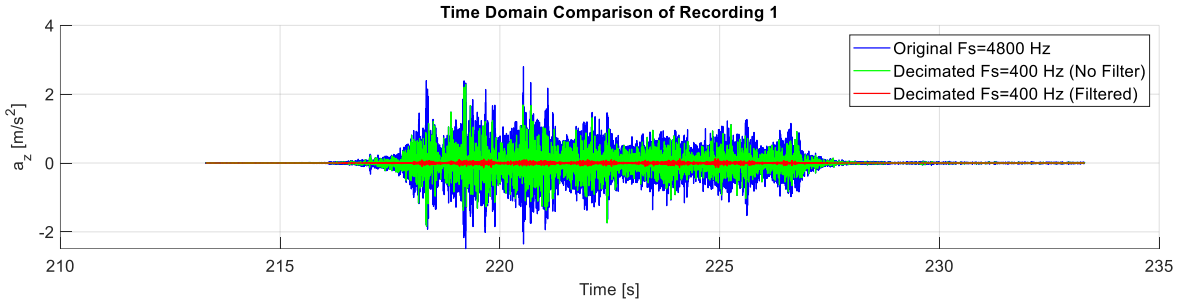

Figure 3.38 *Comparison among the original, decimated and decimated with filter signals for the first recording in the time domain for section 5*

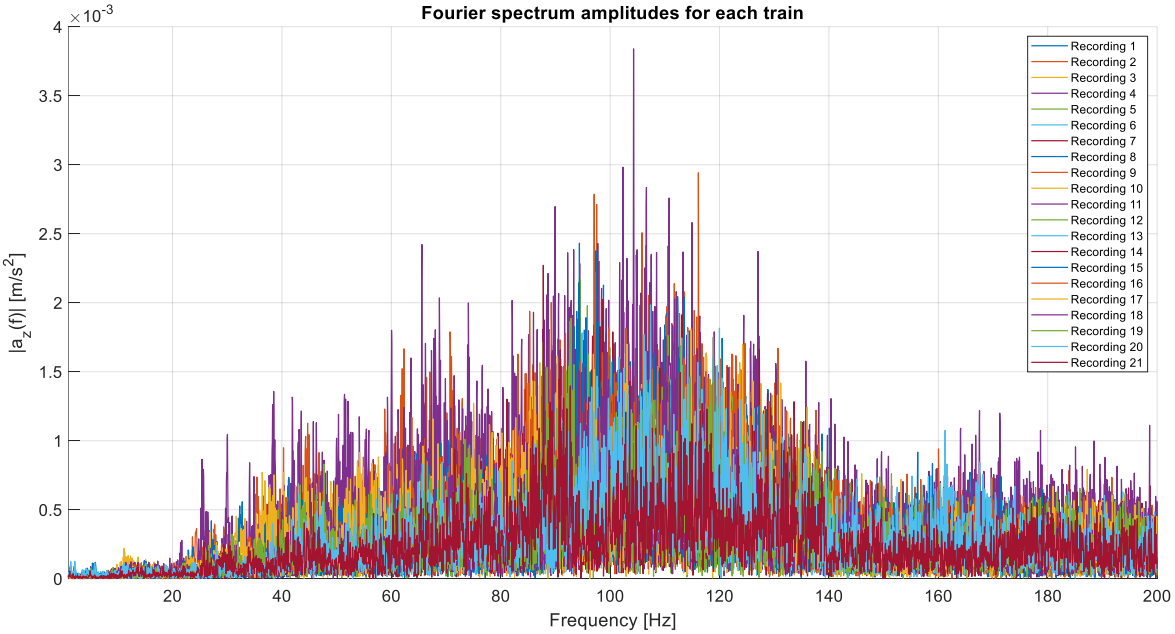

Figure 3.39 *Fourier transform of decimated and filtered signals for all the recordings in section 5*

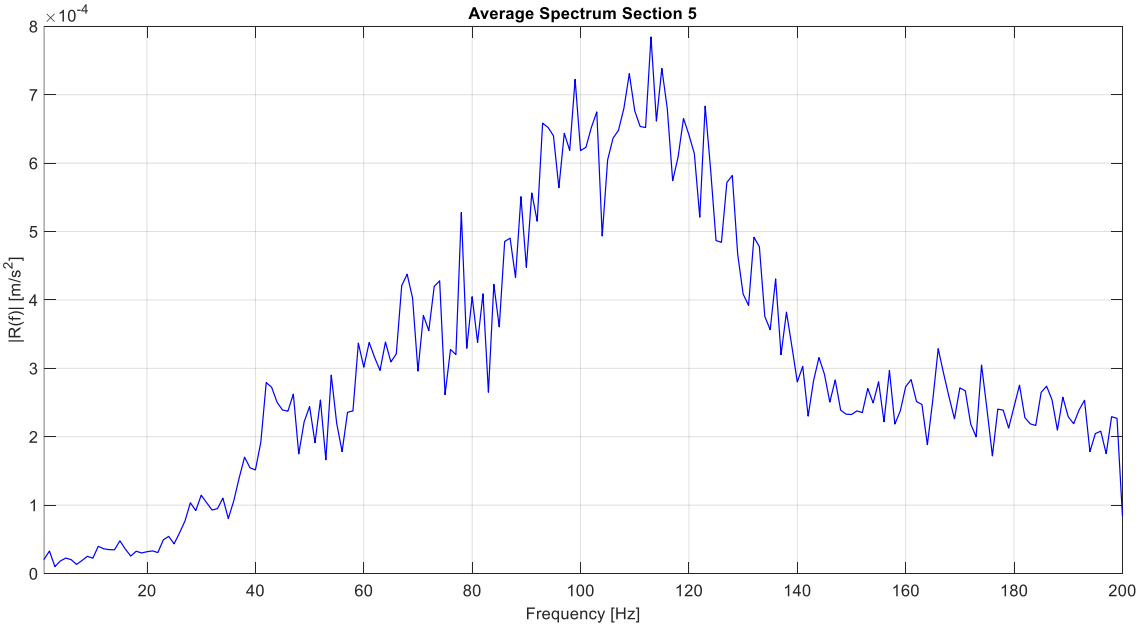

Figure 3.40 *Average spectrum R(f) of all recordings for section 5*

3.3.3.6 Section 6

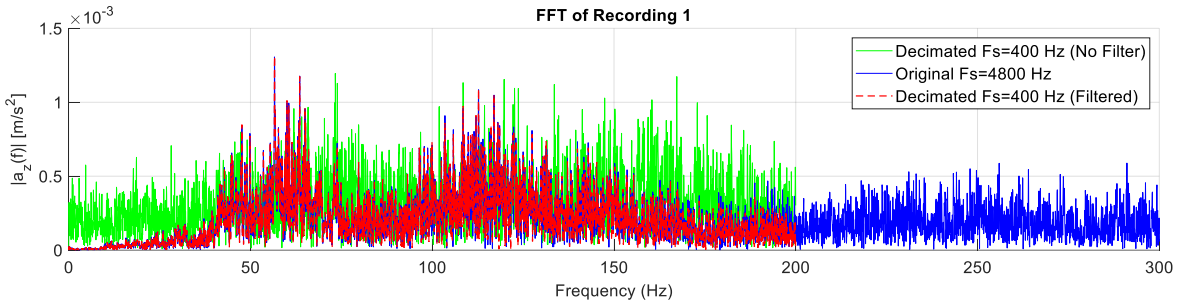

Figure 3.41 *Comparison among the original, decimated and decimated with filter signals for the first recording in the frequency domain for section 6*

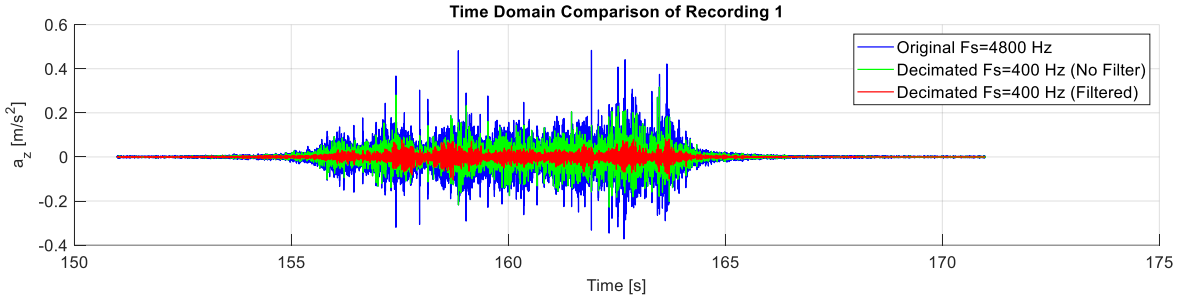

Figure 3.42 *Comparison among the original, decimated and decimated with filter signals for the first recording in the time domain for section 6*

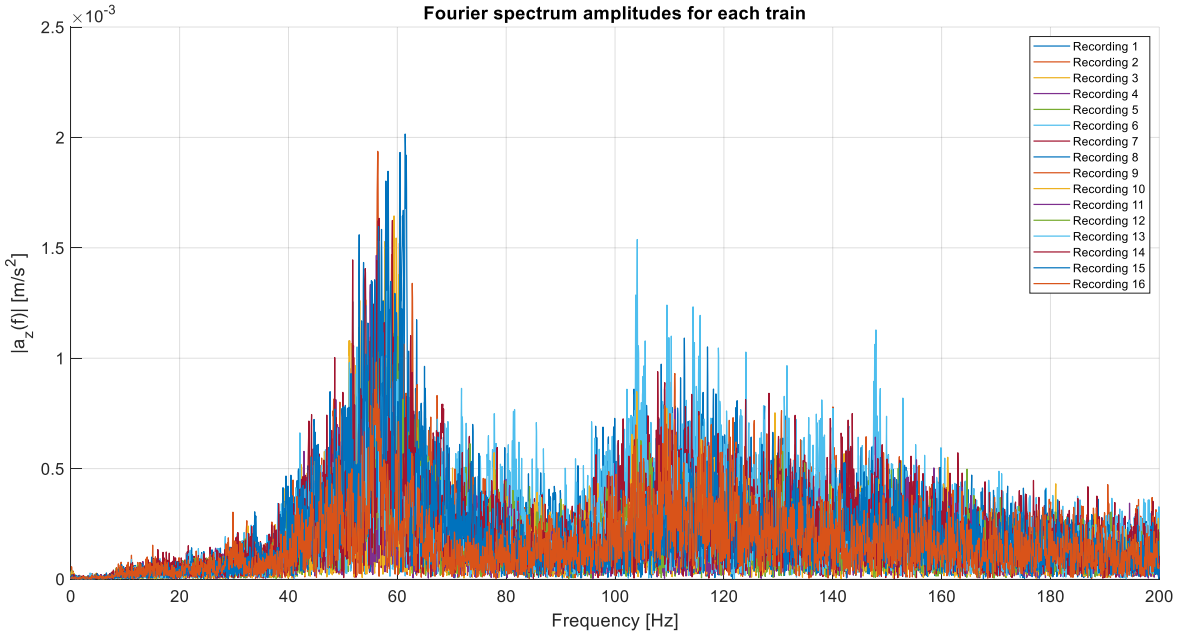

Figure 3.43 *Fourier transform of decimated and filtered signals for all the recordings in section 6*

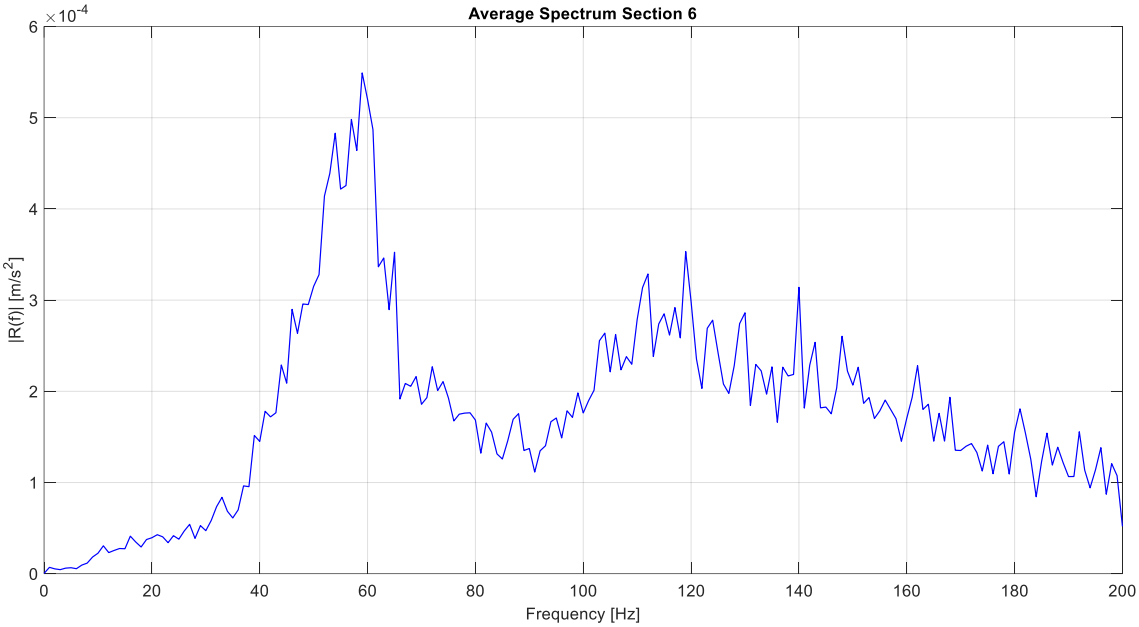

Figure 3.44 *Average spectrum R(f) of all recordings for section 6*

3.3.3.7 Section 7

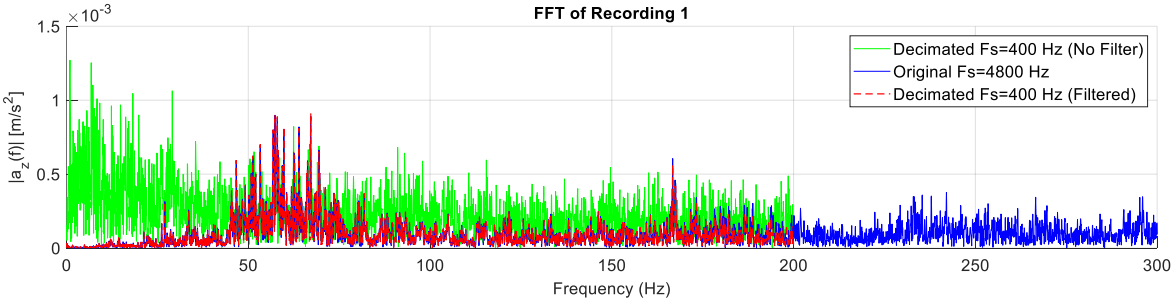

Figure 3.45 *Comparison among the original, decimated and decimated with filter signals for the first recording in the frequency domain for section 7*

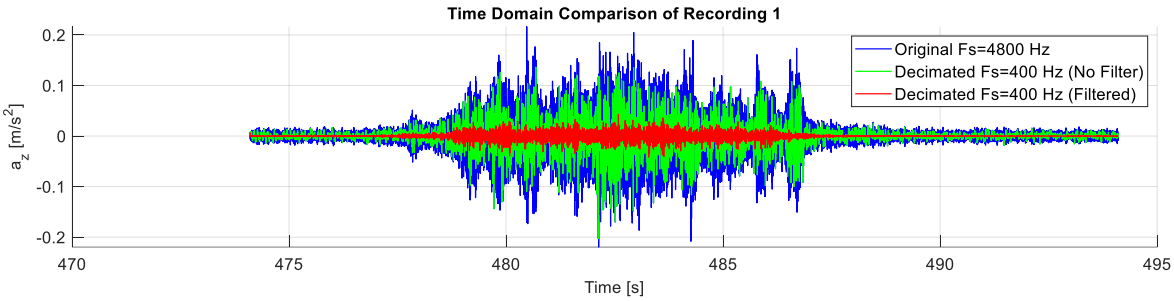

Figure 3.46 *Comparison among the original, decimated and decimated with filter signals for the first recording in the time domain for section 7*

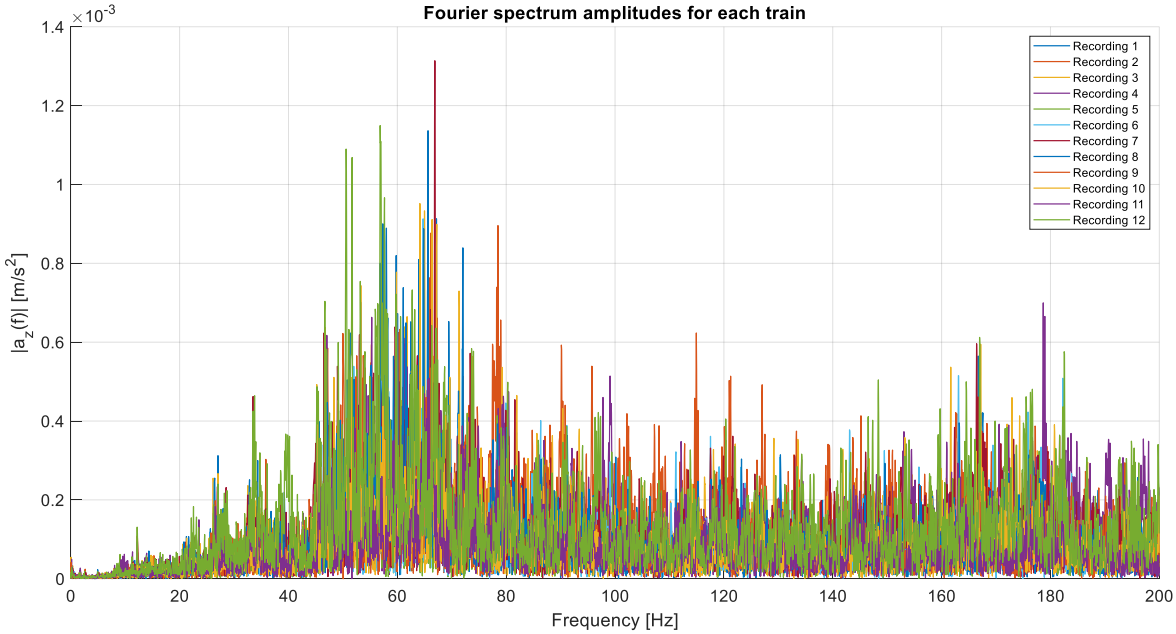

Figure 3.47 *Fourier transform of decimated and filtered signals for all the recordings in section 7*

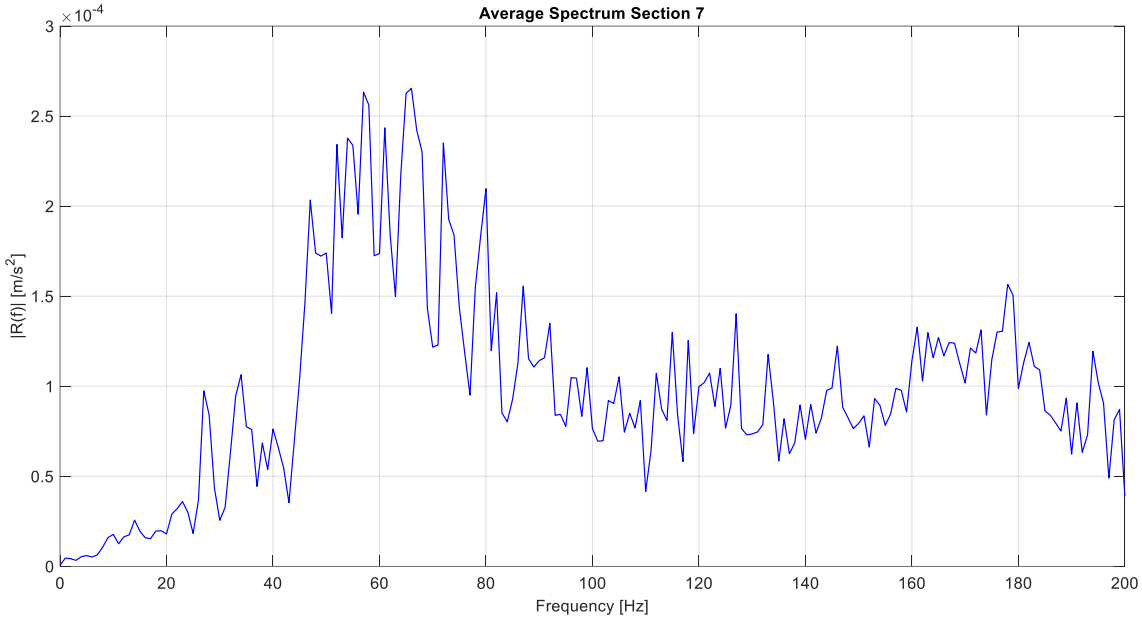

Figure 3.48 *Average spectrum R(f) of all recordings for section 7*

3.3.4 Average spectrum comparison

The frequency responses for the seven sections are presented in **Figure 3.49** .This comparison allows for the identification of common characteristics in both amplitude and frequency. Notably, the amplitude of the response for all sections remains within the same order of magnitude. A consistent peak is observed across all seven sections within the 45–65 Hz range. Additionally, for sections 4 and 5, a significant frequency response is evident between 80 and 120 Hz. A distinct peak in the very low-frequency range, around 2–5 Hz, is also observed across all sections. To investigate the physical causes behind these recurring frequency peaks, a review of similar studies found in the literature is presented.

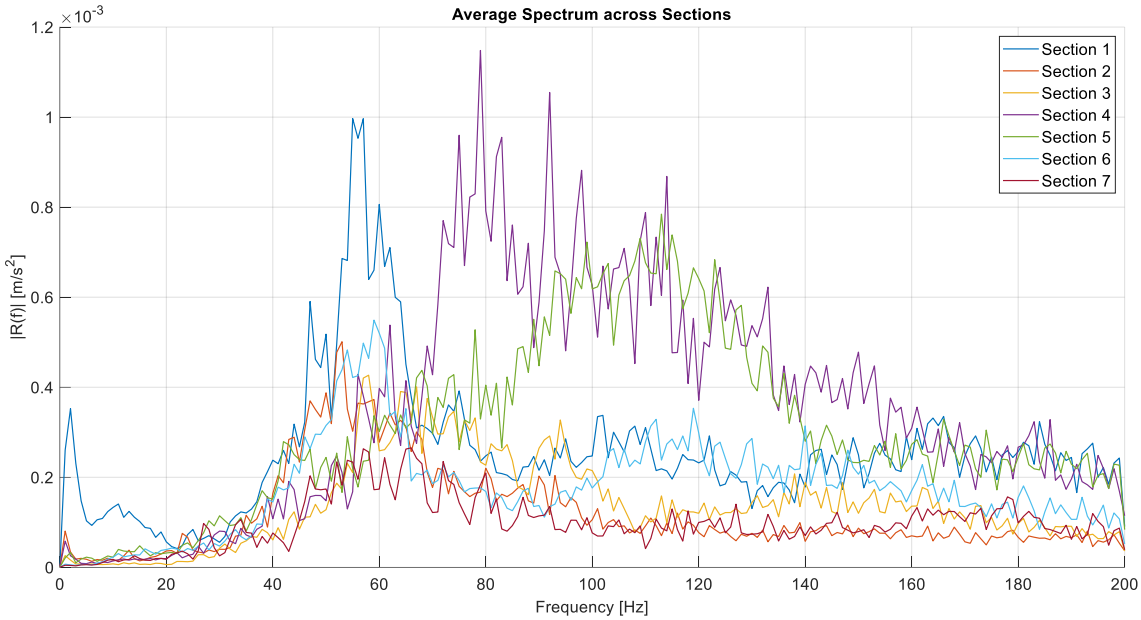

Figure 3.49 *Average spectrum R(f) across sections*

In [47], a study conducted in a metro tunnel employed acceleration and displacement sensors strategically positioned along steel rails, track beds, and tunnel walls to capture real-time dynamic responses during train operations. The data were analysed in both the time and frequency domains, with particular attention to vibration levels and one-third octave band representations. The study focused on average acceleration responses for trains traveling at speeds ranging from 50 to 60 km/h on UIC60 rails with a cast-in-place concrete track bed. The results showed that the frequency distribution of the tunnel lining's response closely resembled that of the track bed, characterized predominantly by low- to mid-frequency vibrations. Notably, the Fourier transform analysis revealed a consistent peak around 60 Hz for both cracked and uncracked tunnel lining sections coinciding with the peak observed across all sections analysed in this study.

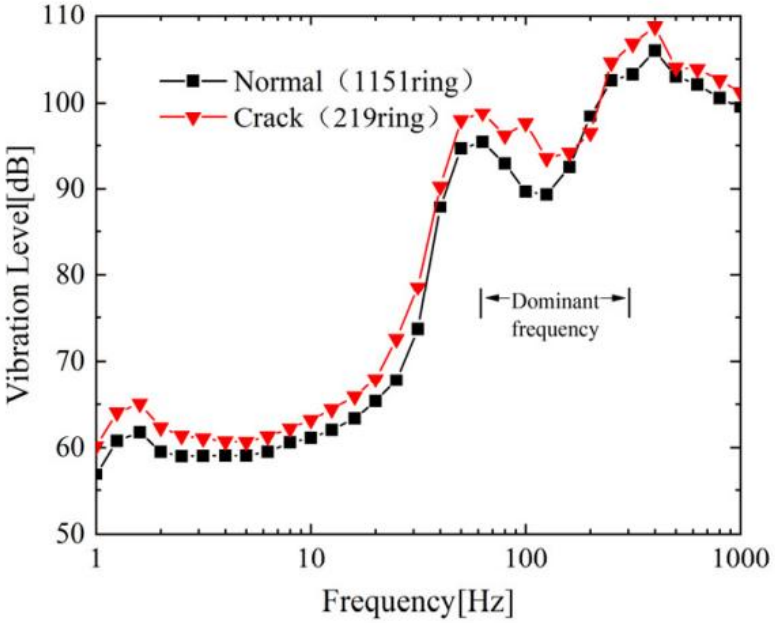

Figure 3.50 *One-third octave frequency of tunnel wall response from [47]*

In [18], a comprehensive field measurement campaign was carried out in a slightly curved section between Zui Baichi Station and South Songjiang Station of the Shanghai Metro Line 9. Accelerometers were installed on the tunnel wall, within the soil layers, and on the ground surface to capture the dynamic response characteristics of the track–tunnel–ground system. Additionally, an elastoplastic numerical simulation that incorporated soil–water coupling was conducted using finite element methods to evaluate acceleration, dynamic displacement, and excess pore water pressure. In the field measurements, the accelerometer placed on the tunnel wall was located at a height of 0.55 meters above the track bed level. The track bed was constructed of concrete, and the rails were connected to it via discrete rail pads.

The measurement results indicated that high-frequency components (>500 Hz) attenuate rapidly during propagation. The dominant frequency content of the rail is concentrated in the middle- and high-frequency ranges, approximately 25–400 Hz and 1000–1500 Hz, while the dominant frequencies of the track bed, soil layers, and ground surface decrease progressively to below 400 Hz, 200 Hz, and 100 Hz, respectively. Although the track bed and tunnel wall exhibit broad frequency bands, the high-frequency content is significantly attenuated compared to that of the rail. As shown in **Figure 3.51**, the dominant frequency range for the tunnel wall is between 25 Hz and 400 Hz, with two notable peaks at 31.5 Hz and 125 Hz. According to [18], the first peak is associated with the natural frequency of the tunnel–ground system, while the second corresponds to the natural frequency of the rail–track system.

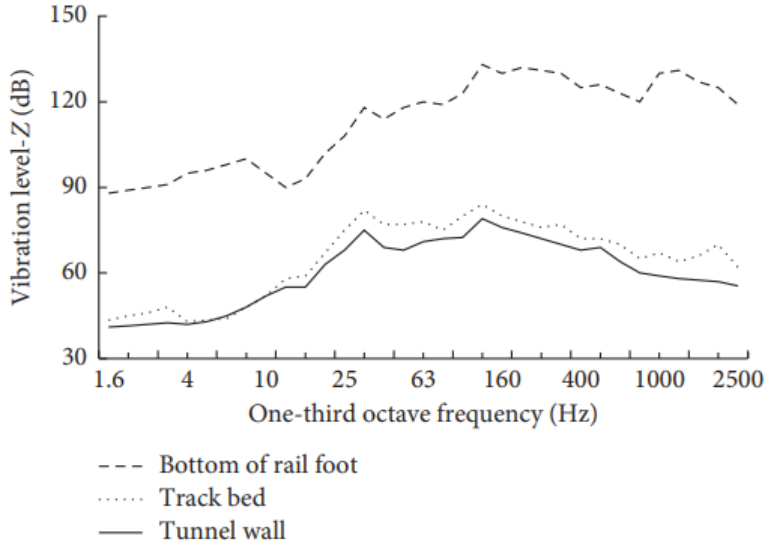

Figure 3.51 *One-third octave frequency of tunnel wall response from [18]*

In [48] , a semi-analytical periodic tunnel–soil model incorporating a track slab was proposed to predict ground vibrations generated by underground train loads. The model accounts for the longitudinal periodicity of supporting forces and decomposes train-induced loads into generalized modal functions. Its formulation is validated through both literature comparisons and in-situ experimental data collected from Hefei Metro Line 1.

The field measurements were conducted between Wanghucheng and Gedadian stations, where vertical accelerations were recorded on the tunnel wall and at four ground surface points (20–50 m from the tunnel). A six-carriage type-B train passed the test section at approximately 60 km/h. High-

resolution accelerometers recorded data at a sampling frequency of 2049 Hz over a 10-second window. The recorded signals were low-pass filtered with a 100 Hz cut-off using the Fourier transform.

Figure 3.53 shows the frequency spectra of the predicted and measured vertical vibrations due to the passage of the train in the tunnel. The vertical vibrations mainly spread within the range 40-100 Hz, due to the effects of wheel-track resonance (resonance of the unsprung mass of the carriage on the track) and due to the short-wavelength track irregularities. The frequency spectrum has another, less evident, peak within 20-40 Hz caused by the passage of the train on the track supported by the periodic fasteners (f = v/L = 27.8 Hz). The dominant frequency of vibrations caused by metro trains is approximately 65 Hz in the narrow frequency band.

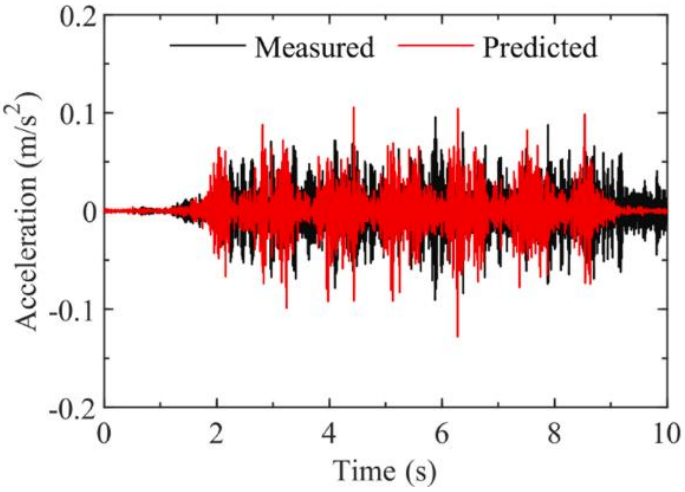

Figure 3.52 *Comparison of measured (black line) and predicted (red line) vertical acceleration in time domain on the tunnel wall from [48]*

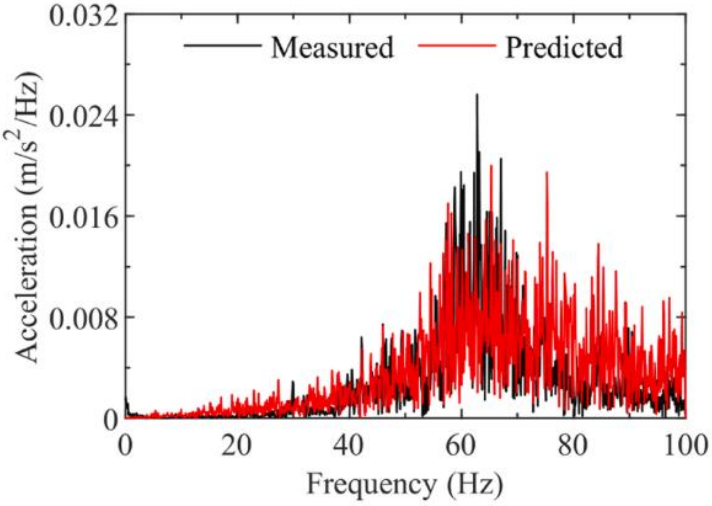

Figure 3.53 *Comparison of measured (black line) and predicted (red line) vertical acceleration spectrum in frequency domain on the tunnel wall from [48]*

In [49], a five-parameter model was proposed to simulate ballast vibration, assuming a cone-shaped load transmission from the sleeper to the ballast. The model incorporates shear stiffness and damping effects to capture the interaction between adjacent ballast masses, thereby reflecting the

continuity and coupling of the interlocking ballast particles. The model was validated through a full-scale field experiment where the ballast frequency was excited by a moving train at 60 km/h speed, showing good agreement between simulated and measured results. Importantly, the study found that ballast vibrations predominantly occur in the mid-frequency range, with resonance frequencies calculated between 70–100 Hz and measured between 80–110 Hz.

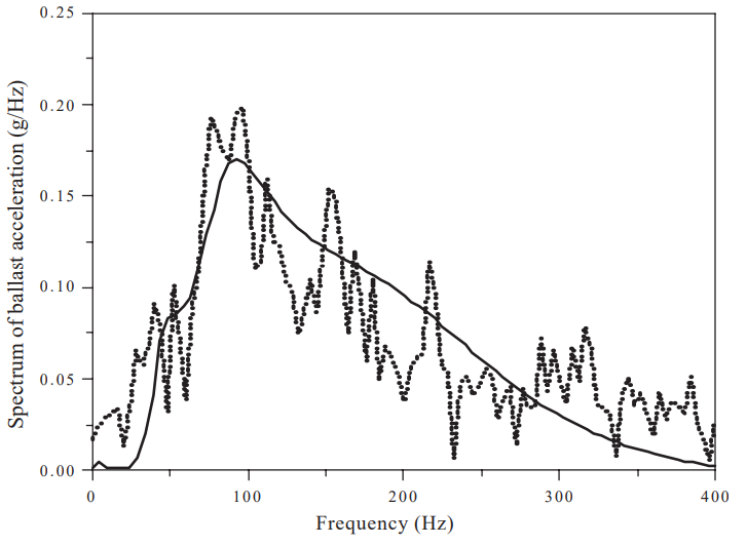

Figure 3.54 *Comparison of frequency spectra of the ballast accelerations between experimental (dashed) and theoretical (continuous) from [49]*

Furthermore, considering the simplified case of one-dimensional shear wave propagation in a horizontally layered medium, the fundamental resonance frequency can be estimated using the relation $f = \frac{c_s}{4h}$, where c_s is the shear wave velocity and h is the ballast thickness. For a typical shear wave velocity of 150 m/s and a ballast thickness range from 0.4 to 0.6 m, the resulting resonance frequency is in the range of 63-94 Hz, which is consistent with the observed spectral range of 70-100 Hz for ballasted sections 4 to 7 (**Figure 3.49**). This supports the hypothesis that the ballast layer contributes to a distinct dynamic response in the frequency domain.

From **Figure 3.49**, it can be concluded that from the analysis of the frequency domain response across the various tunnel sections, some recurring spectral features have been observed. Notably, a consistent peak at 60 Hz appears in nearly all sections, regardless of supporting track type. This is consistent with [47] and [48] and is probably related to the wheel-track response i.e. the unsprung mass oscillation resonance. Additionally, a secondary peak around 100 Hz is present, but this is predominantly observed in sections featuring ballasted tracks. This trend suggests a possible resonance phenomenon linked to the ballast layer according to [49]. Further analysis considering the three-dimensionality of the problem and comparison with literature studies on tunnel measurements will help to consolidate these findings.

3.4 Load-acceleration transfer function – 2D FE model

As stated in expression (3.1), in a linear dynamic analysis the harmonic force $Q(f)$ and the system response $R(f)$ are related through the frequency response function, denoted as $H(f)$, also referred as the transfer function. In this study, $H(f)$ is determined using a 2D finite element (FE) model developed in Abaqus. A steady-state linear analysis is performed to estimate the system's response

to a unit harmonic load. The response is evaluated at a point on the inner tunnel wall face, located 2 meters above the rail level, which corresponds to the same position where the acceleration measurements were recorded. To illustrate the procedure, the case of sections S1 (a. Moscova-Garibaldi-Lotto) and S4 (d. Sesto Marelli – Villa San Giovani) are shown in detail.

3.4.1 Geometry

3.4.1.1 Tunnel section

The geometry of the reinforced concrete tunnel section was defined based on the drawings presented earlier in this document. It is worth noting that, in some cases, minor simplifications were made to avoid meshing singularities or to omit details that would not significantly affect the final results.

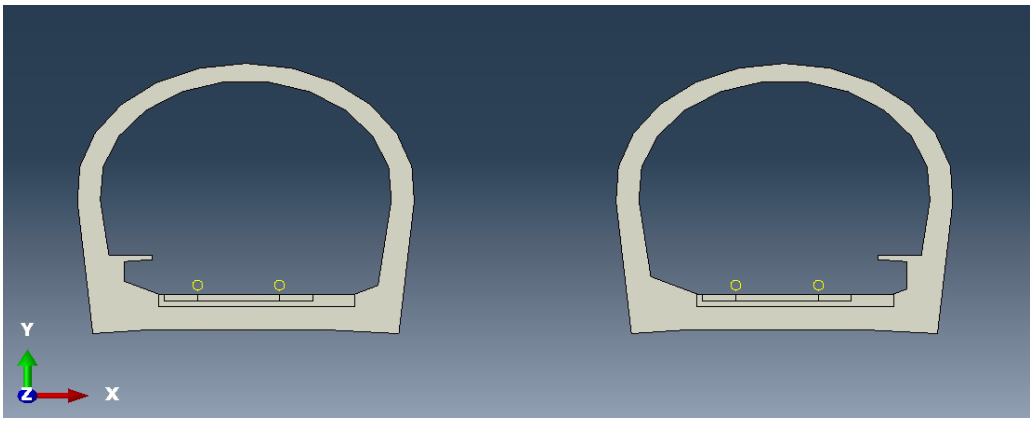

Figure 3.55 *Tunnel section geometry for section 1 in Abaqus*

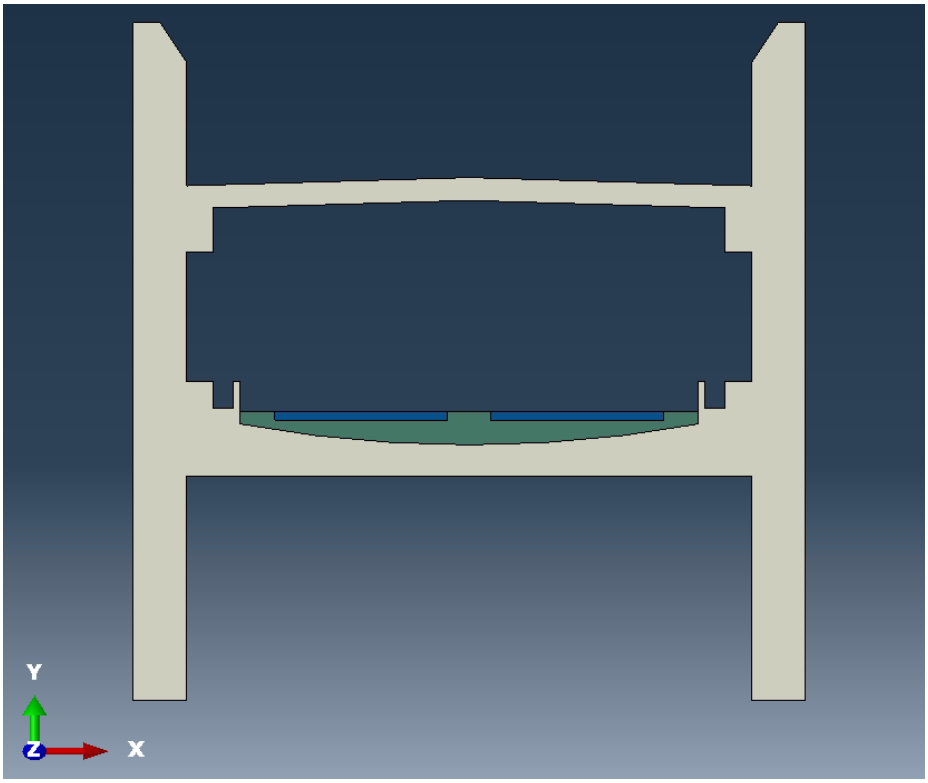

Figure 3.56 *Tunnel section geometry for section 4 in Abaqus*

3.4.1.2 Soil

The soil was modelled with a semicircular shape having a radius of 260 meters, slightly larger than the maximum wavelength expected in the system. This semicircular configuration is commonly used in half-space soil-structure models, as it facilitates the simulation of the radiation condition by means of representing an unbounded domain through the implementation of infinite elements. A similar approach was implemented in [8], where a convergence check was performed using soil domain diameters of 204 meters and 304 meters. The results showed no significant differences in horizontal and vertical displacements at both the surface and rail levels. Therefore, the radius chosen in this study, given the similarity on the meshing resolution and the frequency range considered, is deemed sufficient to ensure accurate results.

The maximum wavelength expected in the system which can be estimated as 220 m considering the expression (3.7).

$$\lambda_{max} = \frac{v_{s\,max}}{f_{min}} \tag{3.7}$$

Where the $v_{s\,max}$ is the maximum shear wave propagation velocity expected in the system, and f_{min} is the minimum frequency considered in the model. In this case, f_{min} is considered 1 Hz, under which the response can be considered static. The value of $v_{s\,max}$ is assumed to correspond to the shear wave propagation velocity in the unsaturated soil, which is higher than that in saturated soil. Using the unsaturated soil properties provided in Table 3.5 and applying Equation (2.46), a value of $v_{s\,max} = 220\,\frac{m}{s}$ was adopted.

Moreover, the saturated and unsaturated phases of the soil were modelled. To estimate the depth of the water table, values from piezometric measurements reported in [9] were considered. This source indicates that a subsurface layer with a high proportion of sand and gravel is typically present beneath the city of Milan. This layer hosts the city's shallowest aquifer, which extends to a depth of approximately 40 meters. The water table within this layer is influenced by water inflows from the countryside north of Milan, as well as by seasonal hydrological variations and anthropogenic demands [50].

Data collected from four piezometers located within the city in March 2012 showed a water table depth of 13.6 meters. Additional data from the municipality, spanning the period from 2014 to 2018, indicated that the water table depth typically ranges between 12 and 14 meters. Based on this information, it is reasonable to assume a water table level of 14 meters below street level for the purposes of this thesis.

The *Abaqus* model of the soil is illustrated in **Figure 3.58** and **Figure 3.59**.

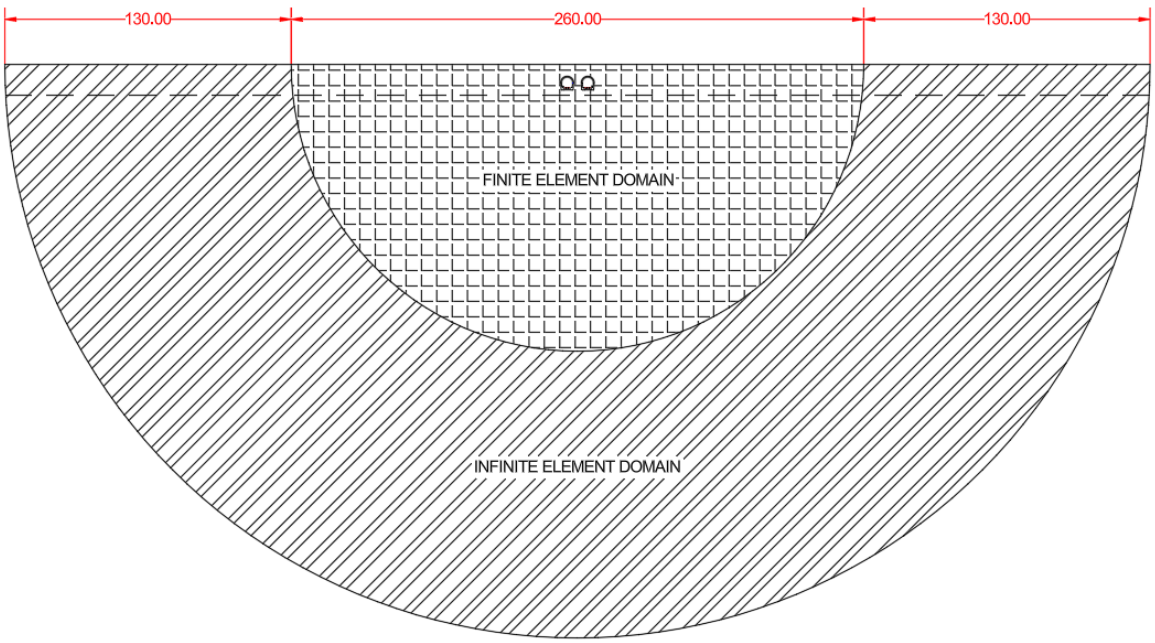

Figure 3.57 *Geometry of the global 2D model in meters*

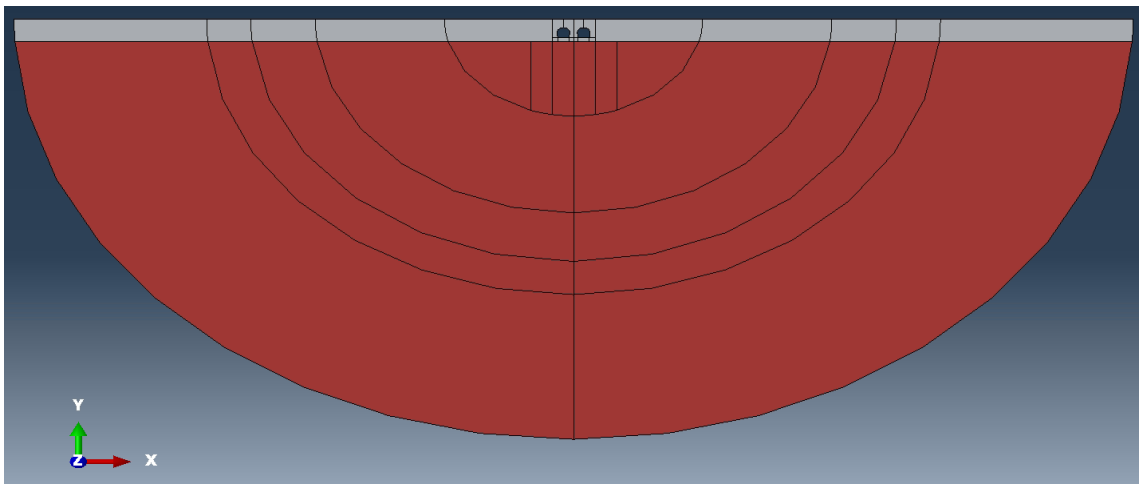

Figure 3.58 *Soil geometry for section 1 in ABAQUS: Unsaturated (grey), Saturated (brown)*

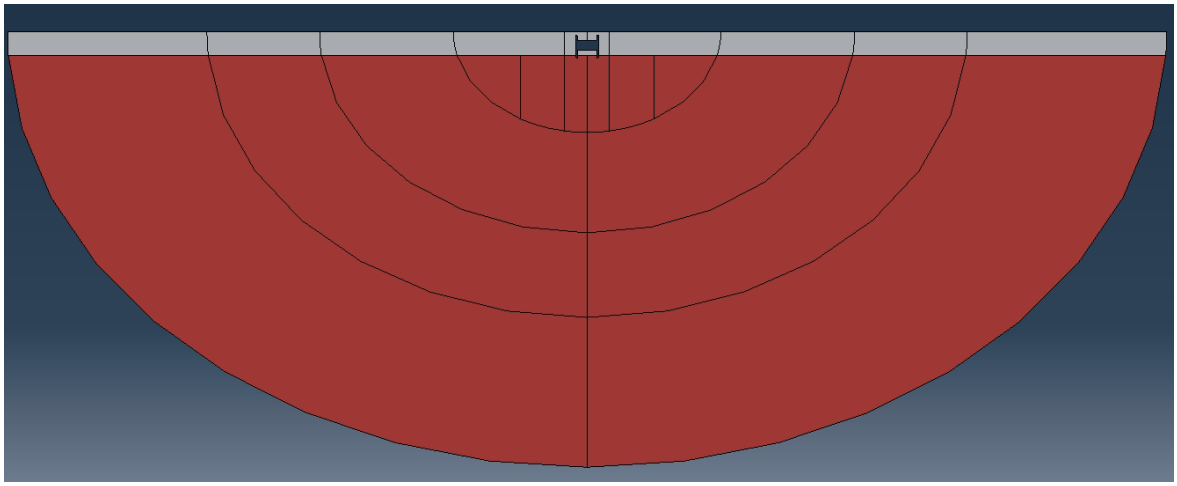

Figure 3.59 *Soil geometry for section 4 in ABAQUS: Unsaturated (grey), Saturated (brown)*

3.4.2 Materials

The material properties were considered as in previous studies [8] [9] [11] [36] and theorized as linear elastic isotropic materials with hysteretic damping. As mentioned, the soil was divided in two layers, the unsaturated and saturated layer. However, each of these layers was considered as linear elastic monophase were the relative motion of particles of solid and water was neglected. This assumption is reasonable as the analysis is conducted in the low-frequency range.

For sections 1 and 2, the models did not include ballast or sleepers. Instead, the rails were assumed to be directly fixed to the concrete slab through a steel plate and an elastomeric pad. The modelling approach for these track supports is explained in a subsequent section. As a result, the only material considered for these sections was reinforced concrete.

In contrast, section 3 featured wooden sleepers embedded in a slab track. Therefore, both concrete (for the tunnel structure) and wood (for the sleepers) were included in the model for this section.

For sections 4 through 7, the rail track was modelled as being supported by traditional wooden sleepers resting on ballast. Consequently, the materials incorporated into these models were reinforced concrete for the tunnel structure, wood for the sleepers, and ballast.

The mechanical properties of the materials were considered as in previous studies and are summarized in Table 3.5 and illustrated for sections 1 and 4 in **Figure 3.60** and **Figure 3.61** respectively.

Table 3.5 Material parameters considered in the ABAQUS model

Material	E [MPa]	ν [-]	ρ [Mg/m^3]	μ [-]
Reinforced concrete	30000	0.2	2.5	0.06
Ballast	310	0.2	1.6	0.2
Sleepers	940	0.1	1	-
Unsaturated soil	200	0.3	1.6	0.01
Saturated soil	225	0.462	2	0.01

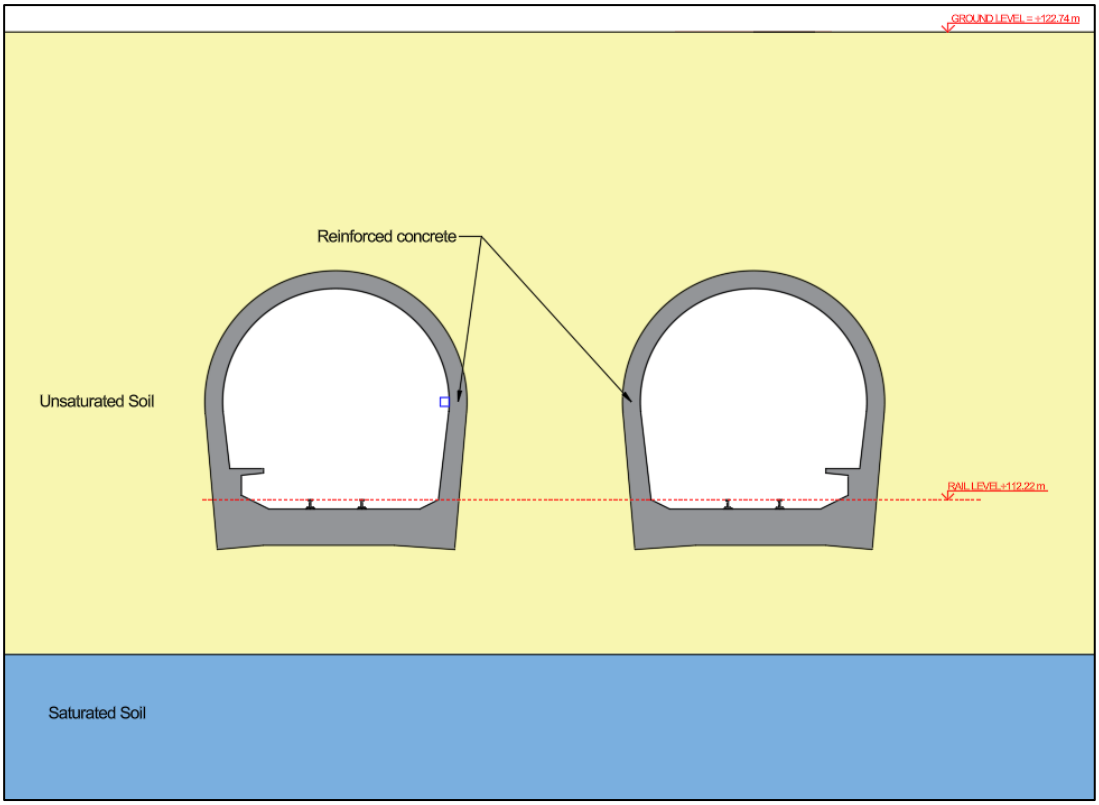

Figure 3.60 *Materials used in Abaqus in section 1*

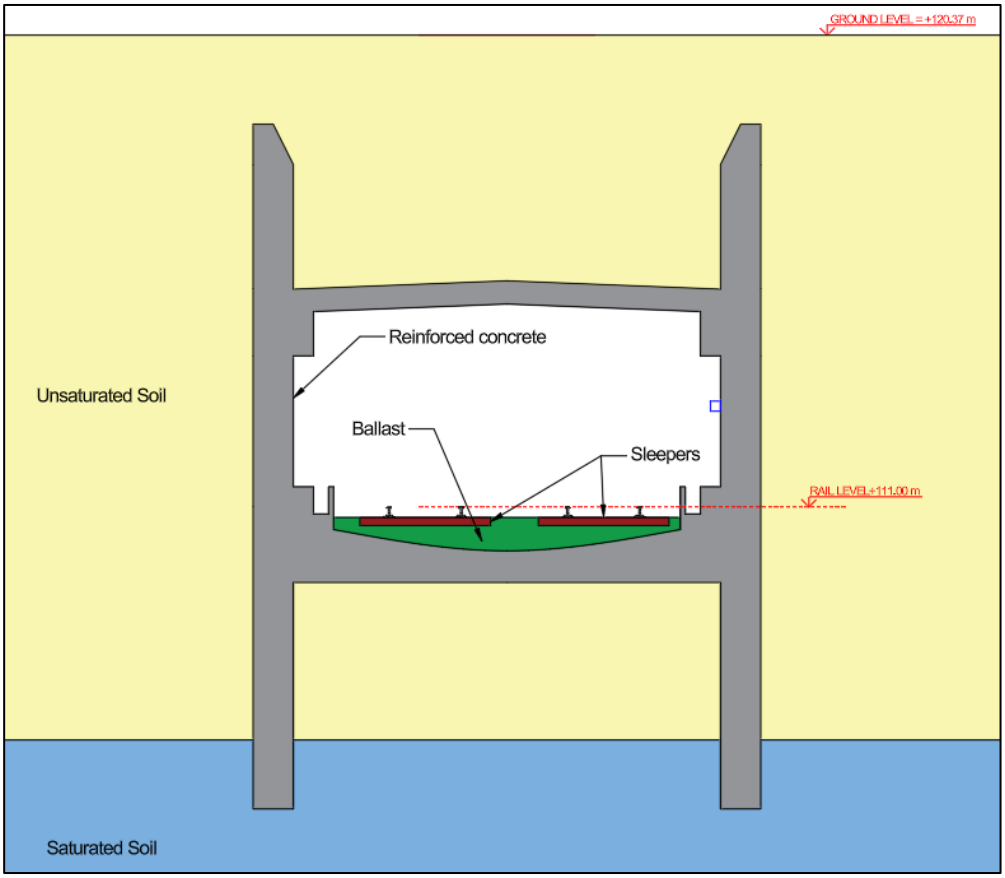

Figure 3.61 *Materials used in Abaqus for section 4*

3.4.3 Interaction

The interaction between the two parts, the tunnel and the soil, was modelled as surface-to-surface interaction with a finite sliding formulation [51]as illustrated in **Figure 3.62** and **Figure 3.63**. Considering *hard contact* for the normal contact and tangential behaviour *Penalty* type with a friction coefficient of 0.55 according to previous studies [8].

It is worth noting that, since a steady-state frequency-domain analysis is performed, Abaqus automatically linearizes the contact interaction. This means that the direction of loading is not resolved step-by-step, as it would be in a time-domain analysis, but only in terms of magnitude and phase. In static analyses, the "hard contact" condition prevents the slave surface from penetrating the master surface at constraint locations and does not allow the transfer of tensile stress across the tunnel–soil interface [51]. Similarly, tangential contact governed by Coulomb friction is inherently nonlinear, as the shear stress depends on the normal stresses. However, in the frequency domain, Abaqus does not distinguish whether the interface is in compression or tension at a given time instant. As a result, when a unilateral "hard contact" condition is defined, it is effectively treated as a linearized, always-active bilateral constraint, enforcing kinematic compatibility across the interface.

Although this simplification may introduce some inaccuracy near the interface, it is reasonable to neglect this effect given the small-strain conditions of the simulation. In fact, similar assumptions have been made in previous analytical solutions [52].

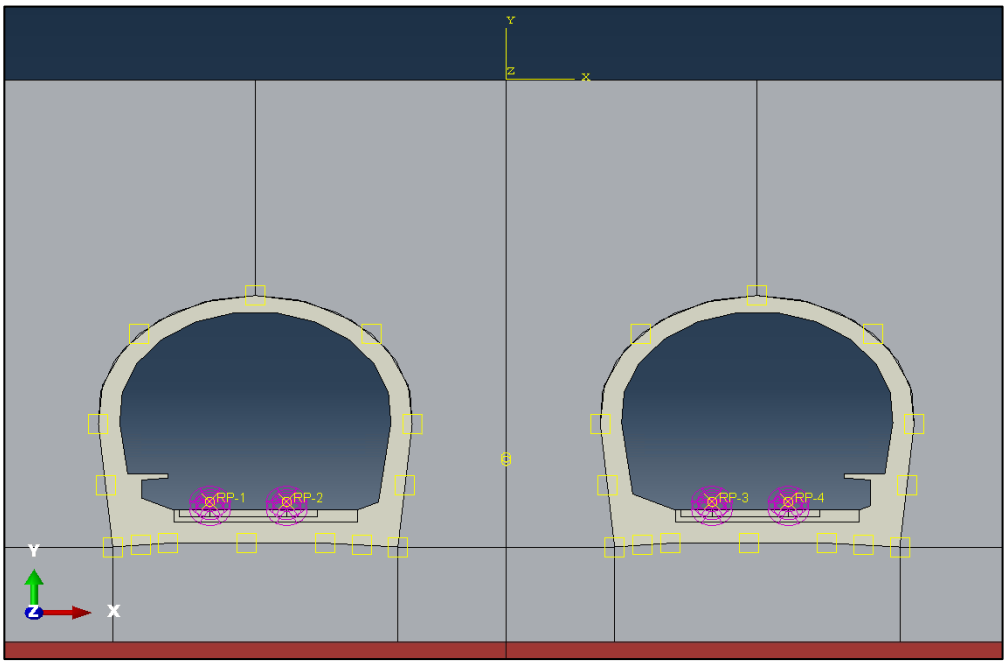

Figure 3.62 *Surface-to-surface interaction for section 1 in Abaqus*

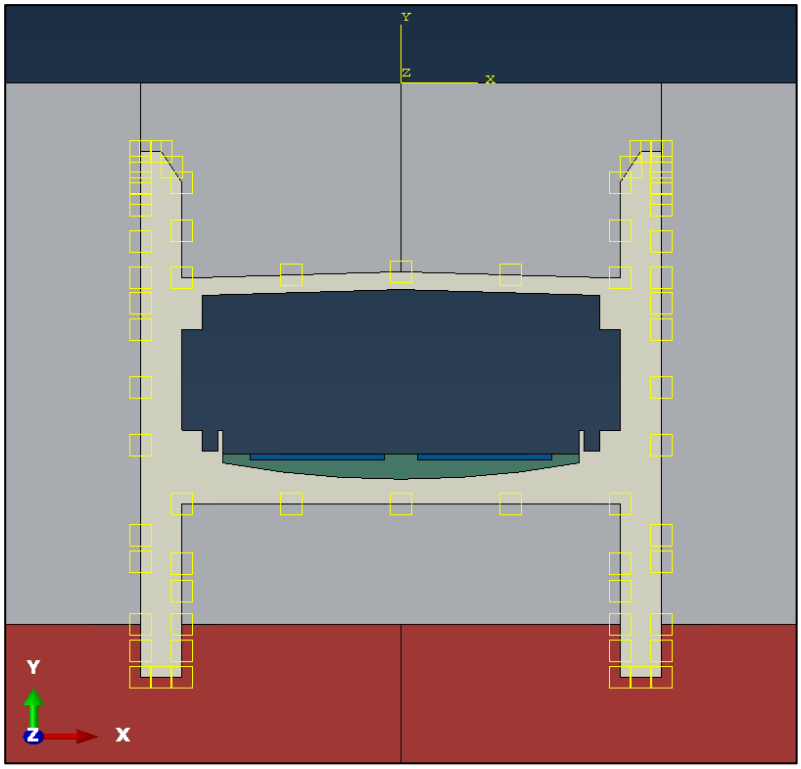

Figure 3.63 *Surface-to-surface interaction for section 4 in Abaqus*

3.4.4 Modelling of discrete elastomeric pads

For Sections 1 and 2, where the rails are directly supported on the slab track through discrete elastomeric pads (see **Figure 3.6**) it is necessary to model the interaction between the slab track and the forces transmitted by the wheel axles. This interaction was represented using discrete springs (see **Figure 3.64**). The dynamic stiffness of the rail track supports was provided by MM as $k_{sup} = 62500\ kN/m$. Considering a spacing between discrete supports of s=0.75 m, the equivalent spring stiffness per unit length for the 2D model is calculated using the expression (3.8) resulting in a value of $k_{eq} = 83333\ kN/m/m$.

$$k_{eq} = \frac{k_{sup}}{s} \tag{3.8}$$

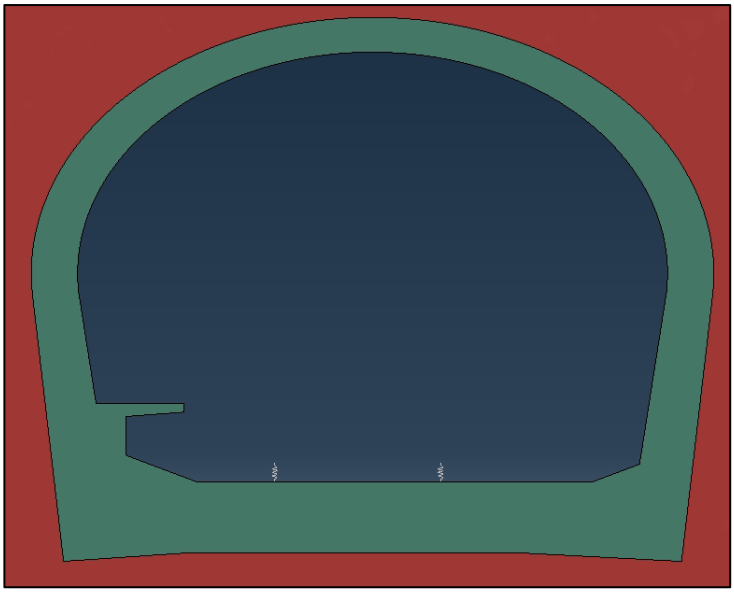

Figure 3.64 *Spring modelling of the connection support for section 1 in Abaqus*

These springs were implemented as simple discrete elements with Hookean stiffness using the tool SPRING2 from Abaqus which connect two nodes acting in a fixed direction.

In order to investigate the influence of the normalization of the longitudinal stiffness of elastomeric pads on the transfer function magnitude, a comparison was carried out between a discrete stiffness implementation ($k_{sup} = 62500\ kN/m$) and a continuous, longitudinally distributed stiffness ($k_{eq} = 83333\ kN/m/m$). The discrete stiffness was implemented in the same manner as the continuous case, but with a different stiffness value assigned to the discrete springs positioned along the load application axis. The results of this comparison are shown in the figures below.

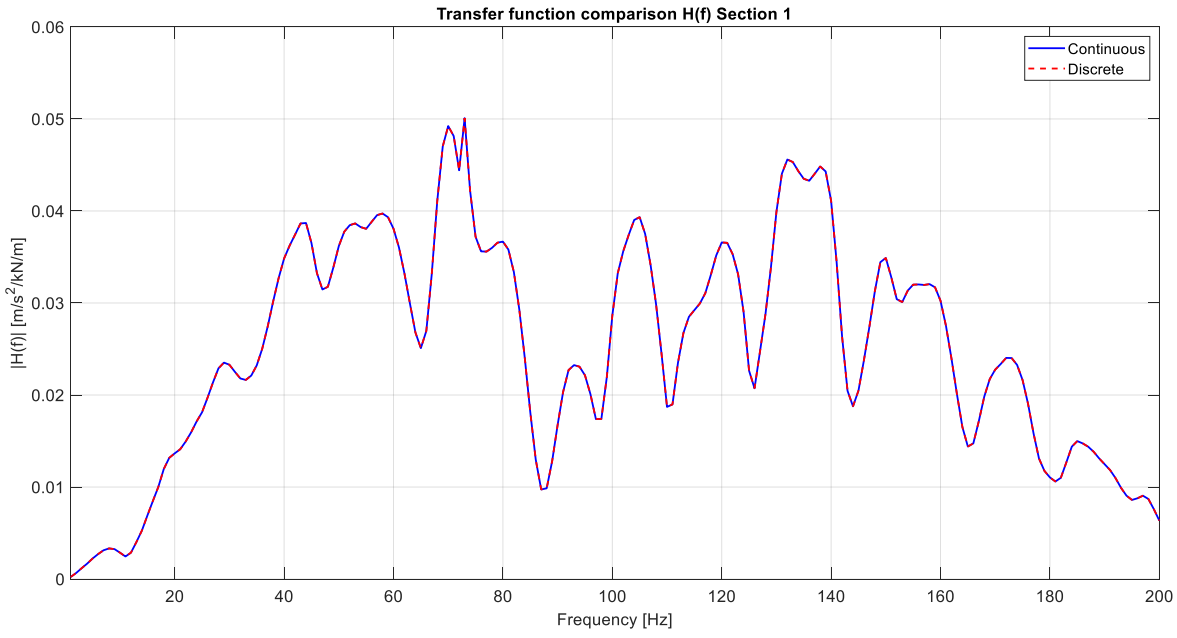

Figure 3.65 *Transfer function magnitude comparison between continuous and discrete elastomeric pads stiffness for Section 1*

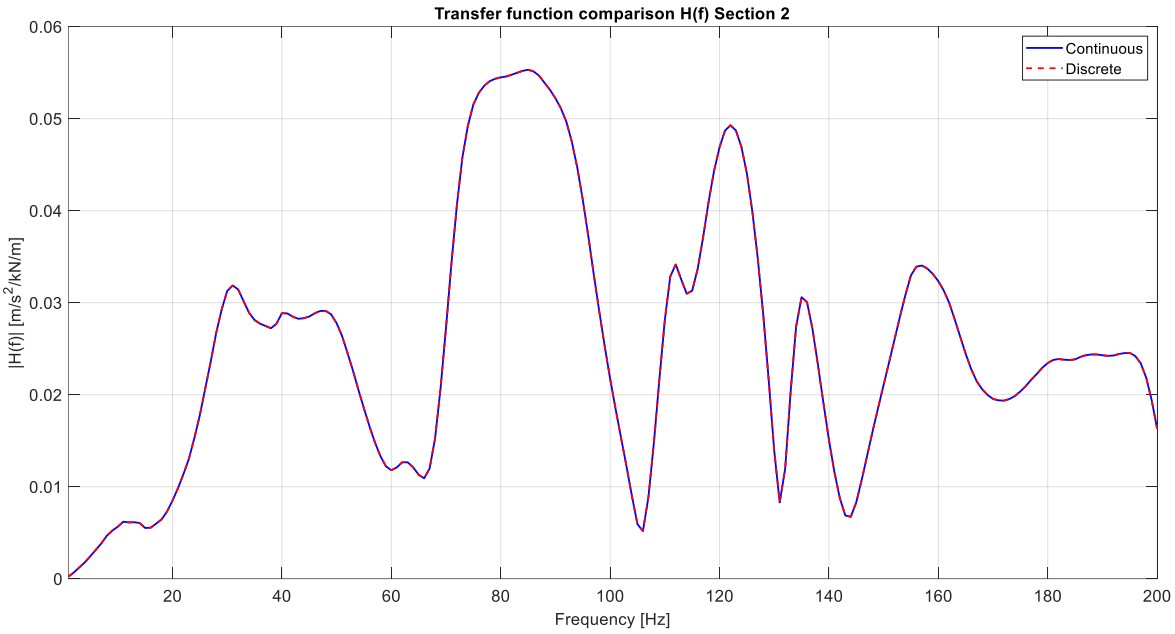

Figure 3.66 *Transfer function magnitude comparison between continuous and discrete elastomeric pads stiffness for Section 2*

It can be observed that the difference in magnitude is negligible, indicating that the influence of the chosen stiffness model is minimal. Therefore, the continuous longitudinally distributed equivalent elastomeric pad stiffness was adopted for both sections.

3.4.5 Boundary conditions

In general, every finite element model must be confined within a finite boundary. In fact, it is not feasible to model an unbounded domain with an infinite number of finite elements as trying to simulate the behaviour of the soil in the real world. Typically, these boundaries are defined and applied using reasonable assumptions regarding the boundary conditions. However, when a dynamic analysis is performed, the resulting wave propagation causes that when using standard finite boundary elastic waves are reflected back into the domain and interfere with the ongoing waves, altering the wave field. To address this issue, artificial boundary conditions are introduced to simulate an infinite domain while keeping the computational model finite. These artificial boundaries are specifically designed to absorb outgoing waves and prevent unwanted reflections, ensuring that the results accurately represent an unbounded medium. Many techniques have been developed in the literature to assess this issue.

3.4.5.1 Perfectly Matched Layer Method

The Perfectly Matched Layer (PML) method is a widely used approach for simulating wave propagation in unbounded or large domains, particularly in problems involving radiation or scattering. Unlike classical absorbing boundary conditions (ABCs), PML offers greater flexibility and efficiency and can be easily integrated with numerical methods such as finite difference, finite volume, finite element, spectral element, or discontinuous Galerkin methods [53]. Introduced in the mid-1990s for electromagnetic wave simulations in 2D and 3D domains, the PML technique involves surrounding the computational domain with artificial absorbing layers. These layers are designed to prevent reflections by allowing outgoing waves to enter and be exponentially damped without spurious reflections, regardless of angle or frequency.

While the method performs exceptionally well in continuous formulations, in discrete numerical implementations, some reflections can still occur due to numerical dispersion and the finite thickness of the absorbing layers. However, these reflected components are typically negligible in practice, especially if the PML is properly designed. Due to its simplicity, efficiency, and strong absorption characteristics, the PML method is considered highly effective and is adopted across various applications involving heterogeneous media. Studies like [54] apply this method for boundary conditions to estimate the ground vibration responses induced by the dynamic loads in a tunnel.

3.4.5.2 Gradually damped artificial boundary

Another approach is the one called *Gradually damped artificial boundary*. The method proposed in [55] states that instead of applying the boundary at the plane of the boundary, is better to gradual increase the damping towards the end of the model. In this way the idea is to damp down the propagating wave progressively such that very minimum or no waves will be reflected back by the boundary. To create an artificial boundary in order to damp down the oscillations, section of elements near the finite boundary is first being divided into n element sets similar to strips as shown in **Figure 3.67**.

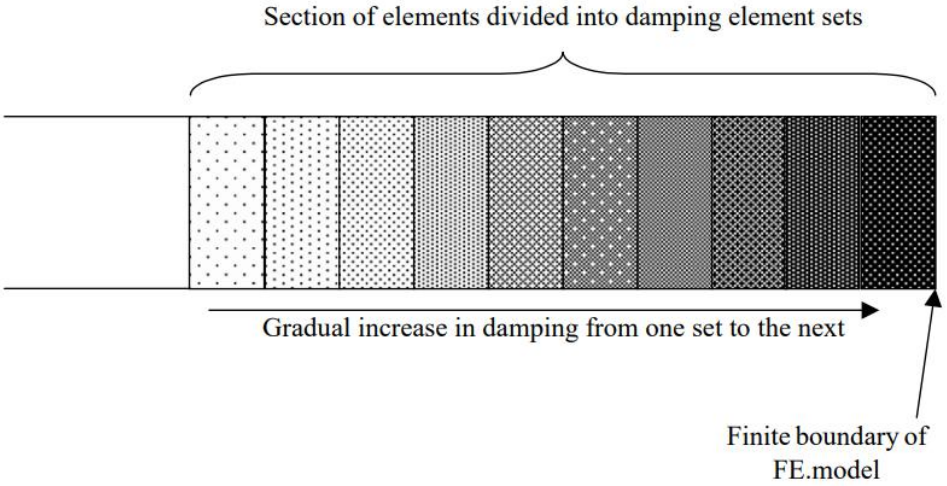

Figure 3.67 *Artificial damping boundary section from [55]*

The damping of the strips should be carried out gradual enough to avoid any spurious reflection from any sudden damping; and that the damping must also be sufficient to fully damp down the oscillations. The first condition requires the length of the damping section to be sufficiently long while the second condition requires the value of the constant factor, to be sufficiently large. The results obtained showed very good comparison with the strip element method (SEM) [56], which had been proved to have good results and is claimed that after a comparison with the infinite elements available in Abaqus following the Lysmer and Kuhlemeyer conditions resulted in not satisfactory results. Even though this method showed good analytical result and being able to use on most finite element packages with different geometries for its application, the method may be relatively tedious and may be computationally expensive depending on the model being analysed.

Furthermore, in [5], a high-efficiency 2.5D finite element approach incorporating a gradually damped artificial boundary is proposed to calculate ground vibrations generated by subway trains. By comparing the computed responses of the ground surface due to a rectangular load moving inside

soil stratum using the proposed method with the semi-analytical solution, it was found that the 2.5D finite element method can calculate the ground response with very high accuracy.

3.4.5.3 Infinite elements

Another type of solution is the use of so-called infinite elements. These elements are typically placed in models where the domain is divided into a *near field* and a *far field* with conventional finite elements used for the former and infinite elements for the latter.

As explained in [57] , in steady-state dynamic frequency domain analyses, infinite elements are employed to create "quiet" boundaries that minimize wave reflections and maintain the initial static forces. Consequently, the far-field nodes within the infinite elements do not displace during the dynamic response. However, these elements do not contribute to analysis procedures based on the eigenmodes of the system.

During dynamic steps, infinite elements introduce additional normal and shear tractions on the finite element boundary, proportional to the corresponding velocity components at the boundary. These boundary damping constants are selected to minimize the reflection of dilatational and shear wave energy back into the finite element mesh. While optimal energy transmission occurs only for plane waves impacting the boundary orthogonally in an isotropic medium, this approach generally yields satisfactory results for a variety of wave types.

In dynamic analyses that follow a static preload, as often seen in geotechnical problems, infinite elements apply the static stress from the initial analysis along with additional damping tractions at the boundary. Since these elements lack stiffness during the dynamic phase, they may permit some rigid body motion, though this effect is typically negligible. To optimize energy transmission without trapping or reflecting waves, the boundary between finite and infinite elements should be as perpendicular as possible to the incoming wavefronts.

An advantage of this solution is that computational costs remain unaffected compared to other methods, as the infinite part of the domain is assembled exactly corresponding to the finite elements at the edge of the *near field* domain, thereby maintaining banded and symmetric matrices.

The analytical derivation to obtain the correct damping attenuation parameters is well explained in the *Abaqus Theory Manual* [58] based on the solution proposed by *Lysmer and Kuhlemeyer* [59] and is explained in the following lines.

Considering the solution of equations from (2.17) to (2.19) , and adopting a reference frame where x is the horizontal coordinate and y the vertical one. Following a nomenclature adopted in *Abaqus* replacing the displacement fields for plane waves as $u_x = u$, $v = u_y$ and $w = u_z = 0$. The displacement field of plane P waves can be described as:

$$u_x = f(x \pm v_p t) \quad ; \quad u_y = 0 \tag{3.9}$$

Where v_p is the P wave's velocity defined in (2.30). The displacement field for plane S waves is:

$$u_y = f(x \pm v_s t) \quad ; \quad u_x = 0 \tag{3.10}$$

Where v_s is the S wave's velocity defined as (2.45).

Considering a boundary at $x = L$ of a medium modelled by finite elements in the region $x < L$. Introducing a distributed damping on this boundary such that:

$$\sigma_{xx} = -d_p \dot{u}_x \tag{3.11}$$

$$\sigma_{xy} = -d_s \dot{u}_y \tag{3.12}$$

Where d_p and d_s are damping constants chosen to avoid reflection of longitudinal and shear wave energy back into the domain $x < L$.

As plane longitudinal waves approaching the boundary have the form of $u_x = f_1(x - v_p t)$ with $u_y = 0$, if they are totally reflected, the longitudinal plane reflection waves will have the form of $u_x = f_2(x + v_p t)$ with $u_y = 0$. Given the linearity of the problem, total displacement is described as $f_1 + f_2$. The corresponding stresses for this linear superposition, according to expression (2.11) are:

$$\sigma_{xx} = (\lambda + 2G)(f_1' + f_2') \tag{3.13}$$

Moreover, the velocity can be written as:

$$\dot{u}_x = -v_p(f_1' - f_2') \tag{3.14}$$

Hence, to satisfy the required damping behaviour at the boundary $x = L$, equation (3.11) must be equal to (3.13). Substituting (3.14) into (3.11) yields:

$$(\lambda + 2G - d_p v_p) f_1' + (\lambda + 2G - d_p v_p) f_2' = 0 \tag{3.15}$$

Ensuring that $f_2 = 0$ (so $f_2' = 0$) for any f_1 ,such no reflections are present, the following condition must be met:

$$d_p = \frac{\lambda + 2G}{v_p} = \rho v_p \tag{3.16}$$

Following a similar procedure for shear plane waves results in:

$$d_s = \rho v_s \tag{3.17}$$

These values of boundary damping are incorporated into the infinite elements in *Abaqus.*

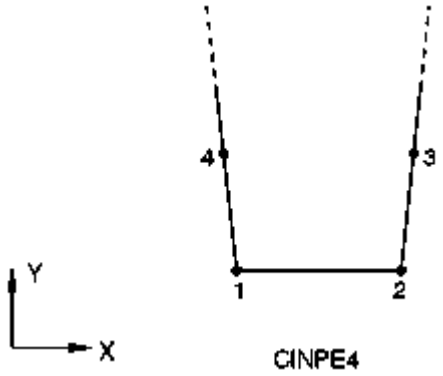

Figure 3.68 *Infinite element of the 4-node linear plane strain type (CINPE4) from [57]*

A comparison was made in [8] between the *gradually damping artificial boundary* method and the *infinite elements* boundary method for a two-dimensional tunnel–soil finite element linear elastic model. Infinite elements were positioned along the outer circular edge of the semicircular domain to prevent artificial wave reflections at the boundary. By measuring the response at a point located on

the free surface at a horizontal distance of 16 m from the tunnel axis, it was observed that using the gradually damping boundary method resulted in disturbances in the vertical displacement and vertical acceleration within the 0–40 Hz frequency range. These disturbances were not present when using infinite elements, implying that the former method may introduce reflections at lower frequencies.

Considering these results, the lower computational cost associated with infinite elements, and the fact that standard absorbing boundaries are already implemented in most commercial FE packages such as Abaqus, the infinite element method was selected for boundary modelling in the present study.

3.4.6 Mesh discretization

The model domain is divided into two main regions: the *near field*, modelled with finite elements, and the *far field*, which corresponds to the model boundary and is represented using infinite elements, (see **Figure 3.57**). The *near field* was primarily meshed using 4-node linear plane strain elements with reduced integration, known in *Abaqus* as *CPE4R*. A small proportion of 3-node linear plane strain elements (*CPE3*) was also used to improve mesh quality given the *Quad-dominant* meshing option in *Abaqus*.

As previously described, the *far field*, representing the outer boundary, is meshed using infinite elements of type *CINPE4*, which are 4-node plane strain continuum infinite elements (see **Figure 3.68**). These elements are not directly available in Abaqus/CAE and must therefore be implemented by modifying the input text file generated by the Job Manager.

These elements are positioned along the outer edge of the semicircular domain, at a distance sufficient to prevent artificial wave reflections in the area of interest. This approach effectively simulates an unbounded soil medium.

Infinite elements perform optimally when incident waves strike the boundary perpendicularly, an assumption supported by the semicircular geometry of the model. To ensure correct implementation in *Abaqus*, the *Sweep* mesh control must be applied with the sweeping direction-oriented outward from the domain [57].

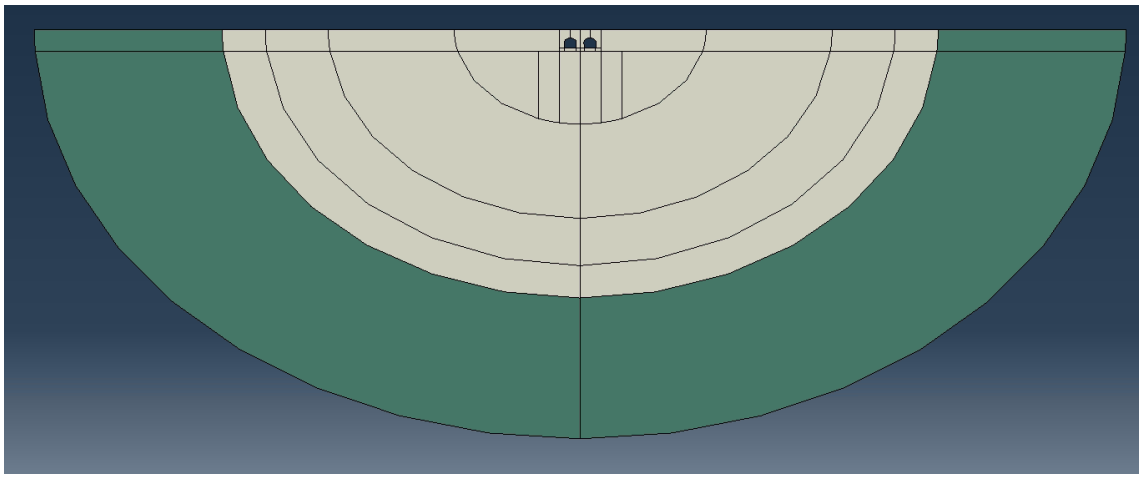

Figure 3.69 *Element types in Abaqus (White=CPE4R, Green=CINPE4)*

When defining the mesh size, a trade-off between model accuracy and computational cost must be considered. If the mesh elements are too large, the wave behaviour will not be captured accurately; on the other hand, a very fine mesh significantly increases computational demand, which may

become prohibitive. A common reasonable criterion is to include at least 10 elements per wavelength to ensure sufficient resolution of wave propagation.

Considering that the maximum frequency of the analysis is 200 Hz, and the minimum shear wave velocity is the one corresponding to the saturated soil, the minimum wavelength was estimated by the following expression.

$$\lambda_{min} = \frac{v_{s\,min}}{f_{max}} \tag{3.18}$$

Using the properties listed in Table 3.5 and expression (2.46) the minimum shear velocity is $v_{s\,min} = 196\,m/s$. Substituting into equation (3.18) the minimum wavelength is approximately $\lambda_{min} = 0.98m$. To satisfy the 10-element-per-wavelength criterion ($n_{el} = 10$), using expression (3.19) the smallest mesh size is $\Delta x = 0.1m$.

$$\Delta x = \frac{\lambda_{min}}{n_{el}} \tag{3.19}$$

This mesh resolution was applied within a 60-meter radius around the tunnel. In regions of special interest, such as where the load is applied, and in the ballast and sleeper zones, the mesh size was refined further to 0.05 m. Between 60- and 120-meter radius, the mesh size was gradually incremented from 0.1m to 0.25m. Beyond 120 meters, the element size, both for finite and infinite elements, was set 0.25m to optimize computational efficiency.

Previous studies support this meshing strategy. In [8], 20 elements per wavelength were used for frequencies between 1 and 100 Hz, yielding an element size of 0.1 m. Then, when reaching the external edge of the mesh, the element size was increased up to 0.25m, these values are consistent with the present study. Moreover, [60] reports that for 2D problems similar to this one, mesh sizes smaller than 0.5 m yield peak ground acceleration errors under 10%, which is acceptable for engineering purposes. In [9], a 0.1 m mesh was used near the sleepers (where loads are applied), while a 0.2 m mesh was used in a 20×15 m area surrounding the tunnel, increasing to 0.5 m beyond this zone. That study considered a frequency range of 1-250Hz. In light of these references, the mesh sizing strategy adopted in this study is both reasonable and consistent with validated practices.

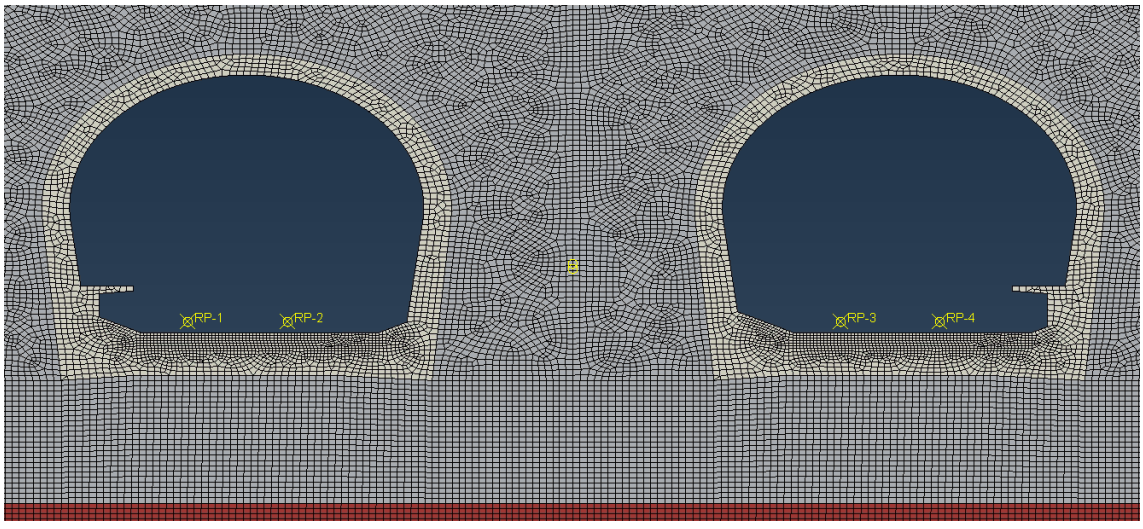

Figure 3.70 *Meshing implementation in tunnel section region for section 1 in ABAQUS*

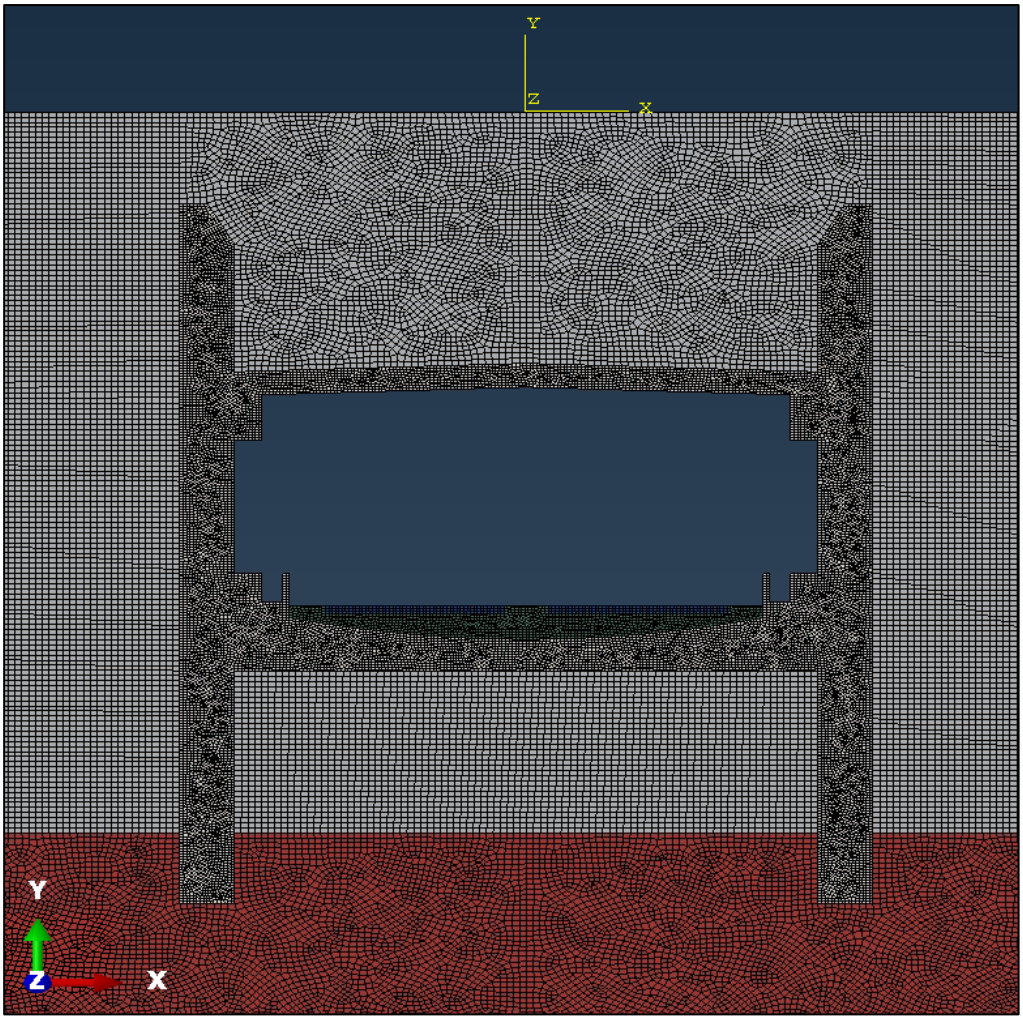

Figure 3.71 *Meshing implementation in tunnel section region for section 4 in ABAQUS*

3.4.7 Loads and analysis type

The goal of this numerical model is to determine the transfer function $H(f)$ for the seven sections. To this end, a unit longitudinally distributed harmonic load of the train is applied by introducing two in-phase loads of amplitude $0.5\ kN/m$ at the wheel–rail contact points. The resulting response of the numerical model can be used to compute the transfer function through equation (3.1). In this study, a linear "direct" steady-state dynamic analysis is performed in the frequency domain.

For structures subjected to continuous harmonic excitation, *Abaqus* provides a "direct" steady-state dynamic analysis procedure. This method is derived using a perturbation approach, where the perturbed solution is obtained by linearizing the response about the current base state. The dynamic virtual work equation (3.20) is discretized; then, strain and stress are expressed in terms of the discretized displacement equations (3.27) and (3.28). The resulting system (3.34) is solved, with the force increment (3.32) as the known term and the displacement increment (3.33) as the unknown. Viscous damping can be included using the Rayleigh damping coefficients defined in the material properties. The same procedure can also be applied to coupled acoustic-structural problems, including radiation boundaries and infinite elements. The complete derivation of the final matrix equations from the dynamic virtual work principle is detailed below following [61].

The dynamic virtual work equation can be written as:

$$\int_{\mathrm{V}} \rho\, \delta\mathbf{u} \cdot \ddot{\mathbf{u}}\, dV + \int_{\mathrm{V}} \rho\, \alpha_c\, \delta\mathbf{u} \cdot \dot{\mathbf{u}}\, dV + \int_{\mathrm{V}} \delta\boldsymbol{\varepsilon} : \boldsymbol{\sigma}\, dV - \int_{\mathrm{S_t}} \delta\mathbf{u} \cdot \mathbf{t}\, dS = 0 \tag{3.20}$$

where $\dot{\mathbf{u}}$ and $\ddot{\mathbf{u}}$ are the velocity and the acceleration, ρ is the density of the material, α_c is the mass proportional damping factor (part of the Rayleigh damping assumption), $\boldsymbol{\sigma}$ is the stress, $\mathbf{t}$ is the surface traction, and $\delta\boldsymbol{\varepsilon}$ is the strain variation that is compatible with the displacement variation $\delta\mathbf{u}$. The discretized form of equation (3.20)[3] is:

$$\delta u^{\mathrm{N}}\{M^{NM}\ddot{u}^M + C_{(m)}^{NM}\dot{u}^M + I^N - P^N\} = 0 \tag{3.21}$$

Where M^{NM} is the mass matrix, $C_{(m)}^{NM}$ is the mass damping matrix, I^N is the internal load vector and P^N is the external load vector and are given by the following definitions.

$$M^{NM} = \int_{\mathrm{V}} \rho\, \mathbf{N}^N \cdot \mathbf{N}^M\, dV \tag{3.22}$$

$$C_{(m)}^{NM} = \int_{\mathrm{V}} \rho\, \alpha_c \mathbf{N}^N \cdot \mathbf{N}^M\, dV \tag{3.23}$$

$$I^N = \int_{\mathrm{V}} \boldsymbol{\beta}^N : \boldsymbol{\sigma}^M\, dV \tag{3.24}$$

$$P^N = \int_{S_t} \mathbf{N}^N \cdot \mathbf{t}\, dS \tag{3.25}$$

In here, the matrixial notation indicated in the Abaqus Theory Manual is considered, where *N* and *M* stands for the rows and columns of the matrix.

For steady-state harmonic response, it is assumed that the system undergoes small harmonic vibrations about a stressed configuration (denoted by subscript 0). Since steady-state dynamics is a perturbation procedure, the computed response defines the deviation from this base state. The change in internal force vector due to harmonic perturbation is:

$$\Delta I^N = \int_{\mathrm{V}} [\Delta\boldsymbol{\beta}^N : \boldsymbol{\sigma} + \boldsymbol{\beta}^N : \Delta\boldsymbol{\sigma}]\, dV \tag{3.26}$$

Where the change in stress is:

$$\Delta\boldsymbol{\sigma} = \mathbf{D}^{el} : (\boldsymbol{\Delta\varepsilon} + \boldsymbol{\beta_c \Delta\dot{\varepsilon}}) \tag{3.27}$$

[3] Following tensor notation, the operators · and : denote the dot product and the double contraction (also called the double dot product) between two tensors, respectively. In both cases, the resulting quantity is a scalar.

where $\mathbf{D}^{el}$ is the elastic stiffness matrix of the material and $\boldsymbol{\beta_c}$ is the stiffness proportional damping factor. The strain and strain rate increment follow from the displacement and velocity increment according to:

$$\boldsymbol{\Delta\varepsilon} = \boldsymbol{\beta}^M \Delta u^M \quad , \quad \boldsymbol{\Delta\dot{\varepsilon}} = \boldsymbol{\beta}^M \Delta \dot{u}^M \tag{3.28}$$

This allows us to write equation (3.21) as:

$$\delta u^{\mathrm{N}}\{M^{NM}\ddot{u}^M + (C^{NM}_{(m)} + C^{NM}_{(k)})\dot{u}^M + K^{NM}u^M - P^N\} = 0 \tag{3.29}$$

Where the stiffness matrix is given by

$$K^{NM} = \int_V [\frac{\partial \boldsymbol{\beta}^N}{\partial x} : \boldsymbol{\sigma_0} + \boldsymbol{\beta}^N : \mathbf{D}^{el} : \boldsymbol{\beta}^M]\, dV \tag{3.30}$$

And the stiffness damping matrix is given by

$$C^{NM}_{(k)} = \int_V \beta_c \boldsymbol{\beta}^N : \mathbf{D}^{el} : \boldsymbol{\beta}^M\, dV \tag{3.31}$$

For harmonic excitation and response, we can write the linearized increments of displacement amplitude and force amplitude in terms of the real and imaginary parts with the following expressions.

$$\Delta u^M = (Re(u^M) + iIm(u^M))e^{i\Omega t} \tag{3.32}$$

$$\Delta P^N = (Re(P^N) + iIm(P^N))e^{i\Omega t} \tag{3.33}$$

Where Ω is the circular frequency, i is the imaginary number and e is Euler's number. Substituting the expressions for harmonic excitation and response in Equation (3.21) and writing the result in matrix form yields

$$\begin{bmatrix} \mathrm{Re}(\mathrm{A}^{NM}) & Im(A^{NM}) \\ Im(A^{NM}) & -\mathrm{Re}(\mathrm{A}^{NM}) \end{bmatrix} \begin{Bmatrix} Re(u^M) \\ Im(u^M) \end{Bmatrix} = \begin{Bmatrix} Re(P^N) \\ Im(P^N) \end{Bmatrix} \tag{3.34}$$

Where A^{NM} is a complex matrix which real and imaginary parts are defined by

$$\mathrm{Re}(\mathrm{A}^{NM}) = K^{NM} - \Omega^2 M^{NM} \tag{3.35}$$

$$\mathrm{Im}(\mathrm{A}^{NM}) = -\Omega(C^{NM}_{(m)} + C^{NM}_{(k)}) \tag{3.36}$$

Note that both the real and imaginary parts of A^{NM} are symmetric. The procedure is executed in *Abaqus* using a direct steady-state dynamic analysis step. Real and imaginary components of loading can be defined. The solver provides results in terms of amplitudes and phase angles for all element and nodal variables at each frequency step. For this procedure all amplitude references must be given in the frequency domain.

For this study, a direct steady-state analysis was performed over a frequency range from 1 to 200 Hz with a frequency step of 1 Hz. The choice of a 1 Hz step was primarily driven by considerations of computational cost. While a smaller frequency step would increase resolution, it would also significantly raise computational demands.

The effect of using a finer frequency step in both the transfer function and the power spectral density (PSD) of the load is evaluated in [11] where a comparison between 0.05 Hz and 1 Hz steps is presented. The primary objective of this analysis is to compare the results with the standard spectrum, which is expressed in one-twelve-octave bands. The results indicate that reducing the frequency step does not meaningfully affect the outcome when comparing with the standard as these octave bands already aggregate frequencies into relatively broad intervals.

Therefore, using a frequency step smaller than 1 Hz would not offer notable advantages for this analysis. Since the standard spectrum is averaged over wide bands, a 1 Hz resolution is sufficient to ensure a meaningful and accurate comparison. In summary, decreasing the frequency step further would only increase computational load without yielding practical improvements in accuracy for this specific application.

Since the model is based on a 2D plane strain assumption, the unit loads in Abaqus are expressed in terms of force per unit length (kN/m), meaning the applied forces are distributed over the rail length. Hence, two in phase, longitudinally distributed harmonic nodal loads with amplitude of 0.5 kN/m were applied on each rail sleeper location.

To reflect the actual measurement conditions, the load configuration simulates the passage of a single train, as shown in **Figure 3.72** and **Figure 3.73**. Because the model represents an asymmetric load case, the response is also expected to be asymmetric.

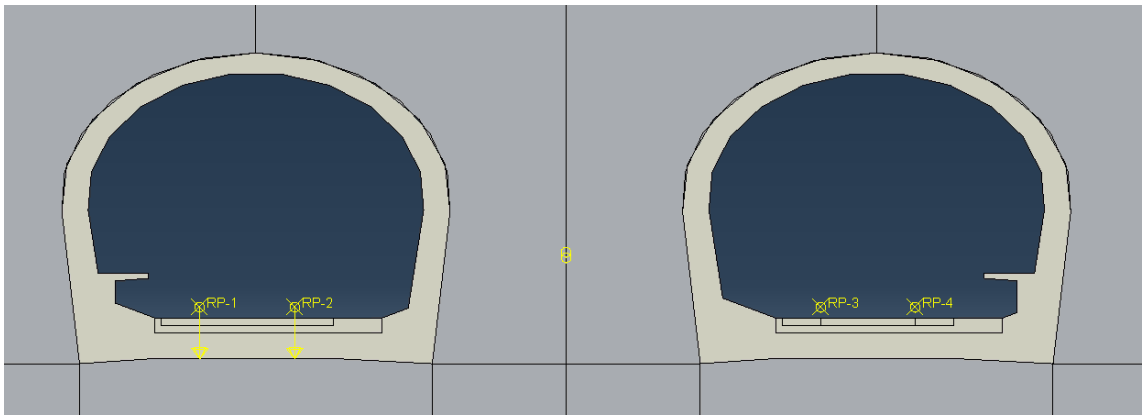

Figure 3.72 *Load point of application for section 1 in Abaqus*

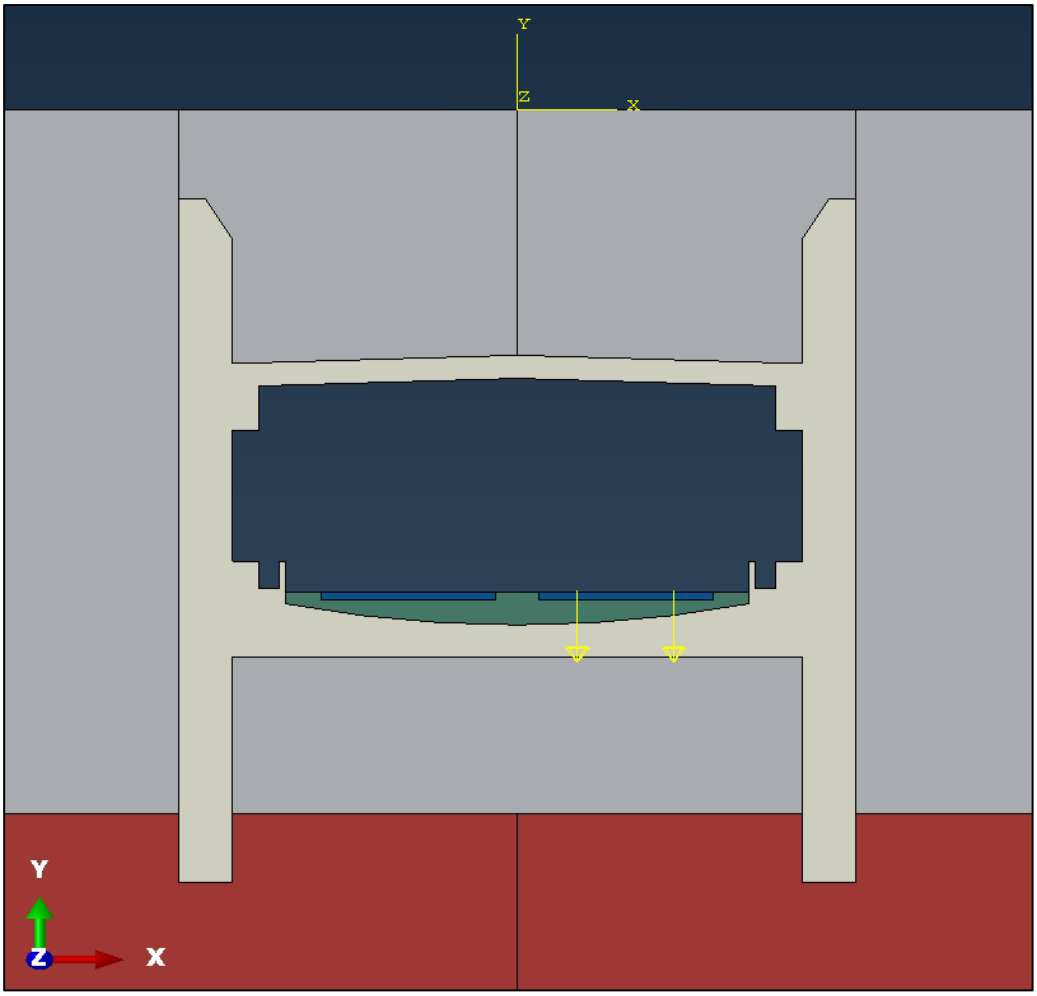

Figure 3.73 *Load point of application for section 4 in Abaqus*

3.4.8 Results

Finally, the transfer function magnitude $|H(f)|$ is obtained at the same point where the accelerometer was placed 2 meters above the railway level, (see **Figure 3.74** and **Figure 3.75**) by extracting the vertical acceleration in terms of magnitude (m/s^2) and phase angle (rad), see from **Figure 3.76** to **Figure 3.79** . The transfer functions magnitudes and phase angles for sections 1 and 4 are shown.

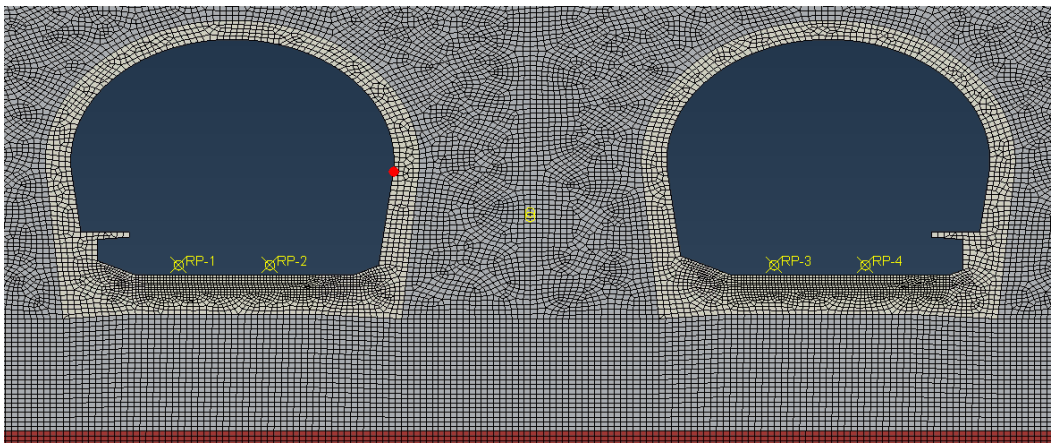

Figure 3.74 *Point of analysis for the transfer function for section 1 (in red)*

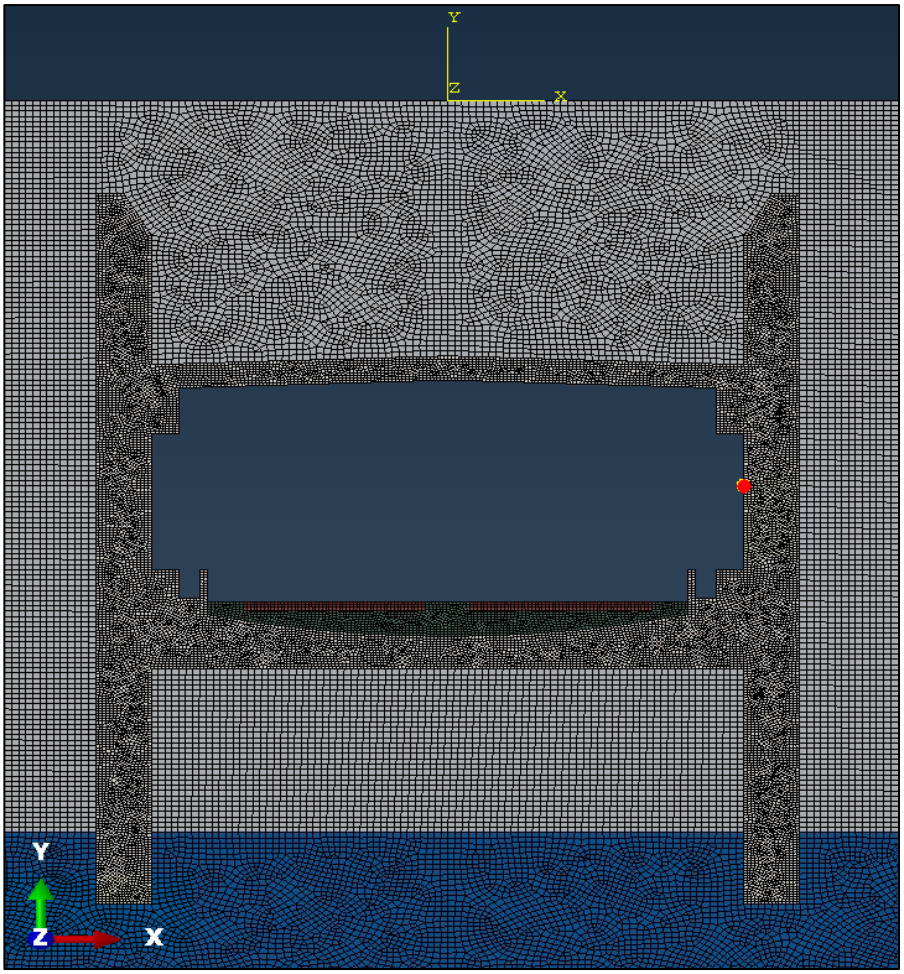

Figure 3.75 *Point of analysis for the transfer function for section 4 (in red)*

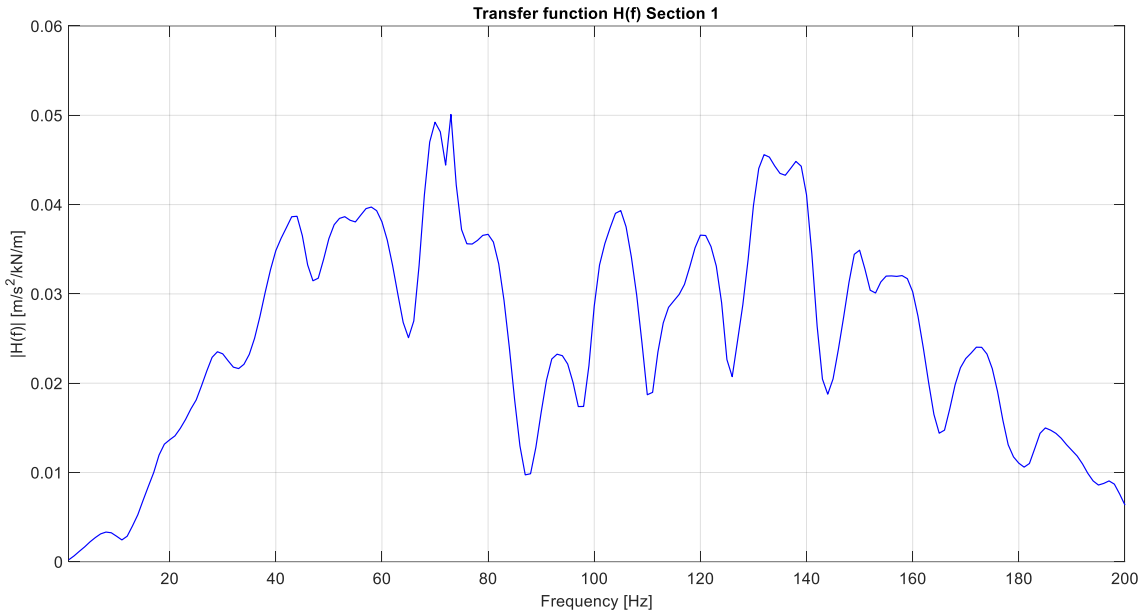

Figure 3.76 *Magnitude of the frequency transfer function for section 1 in* $m/s^2/kN/m$

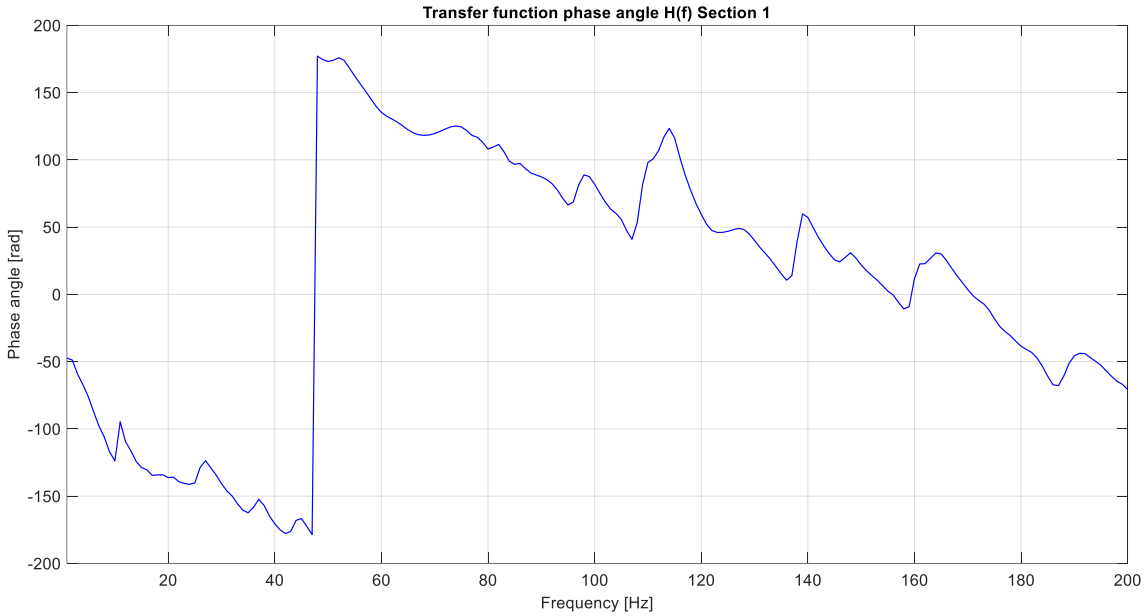

Figure 3.77 *Phase angle of the frequency transfer function for section 1 in rad*

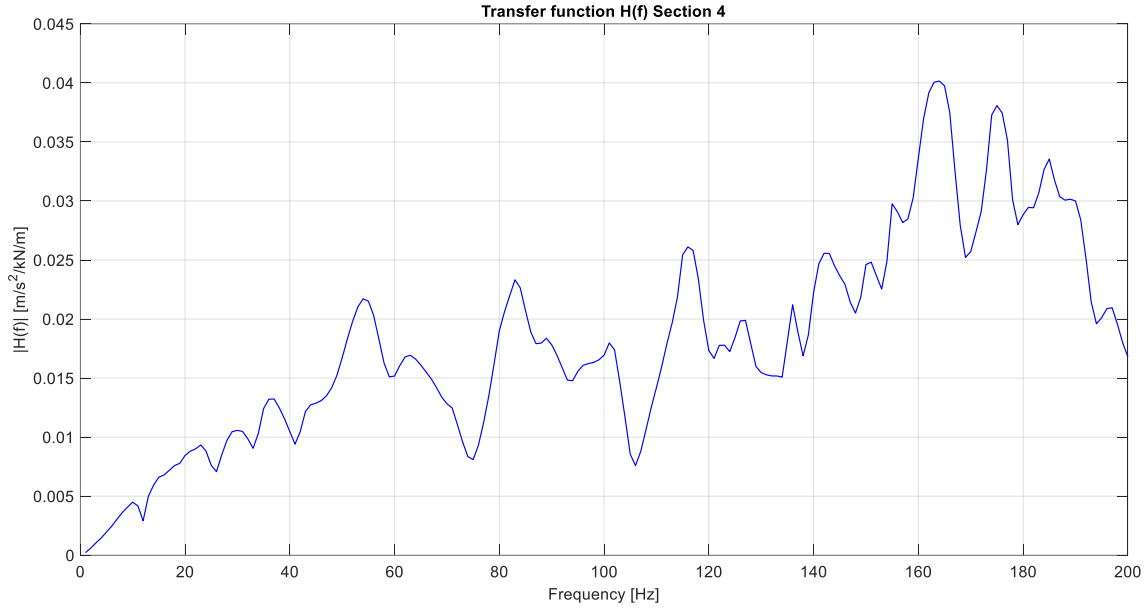

Figure 3.78 *Magnitude of the frequency transfer function for section 4 in* $m/s^2/kN/m$

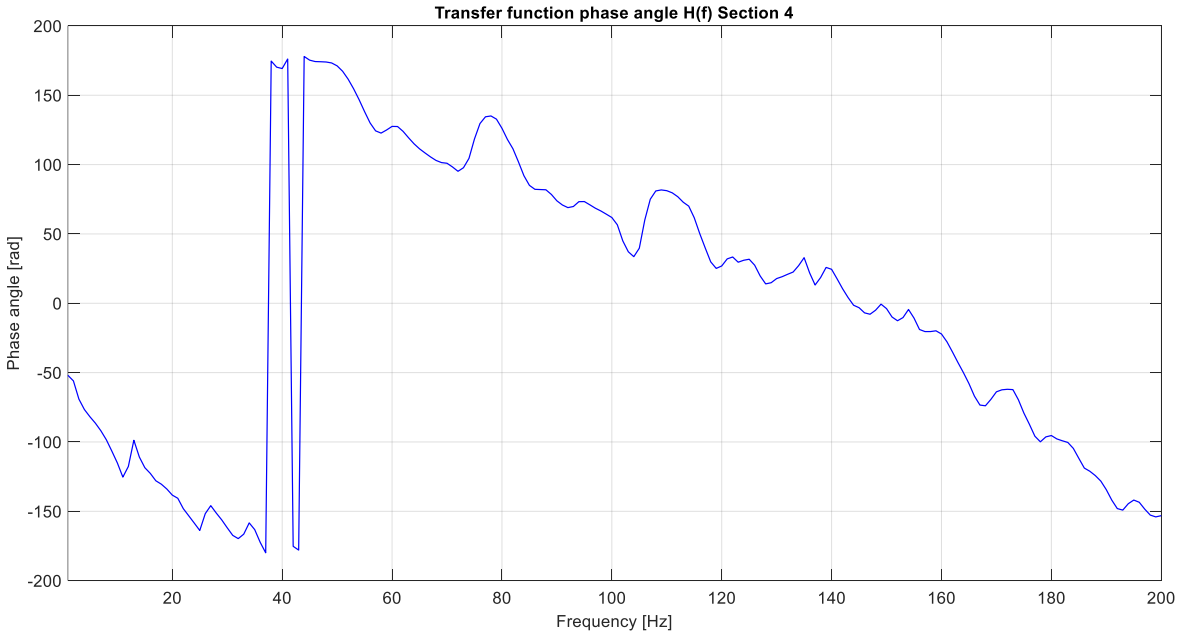

Figure 3.79 *Phase angle of the frequency transfer function for section 4 in rad*

The same procedure described for sections 1 and 4 was applied to all remaining sections. The corresponding transfer functions are presented collectively in the **Figure 3.80**.

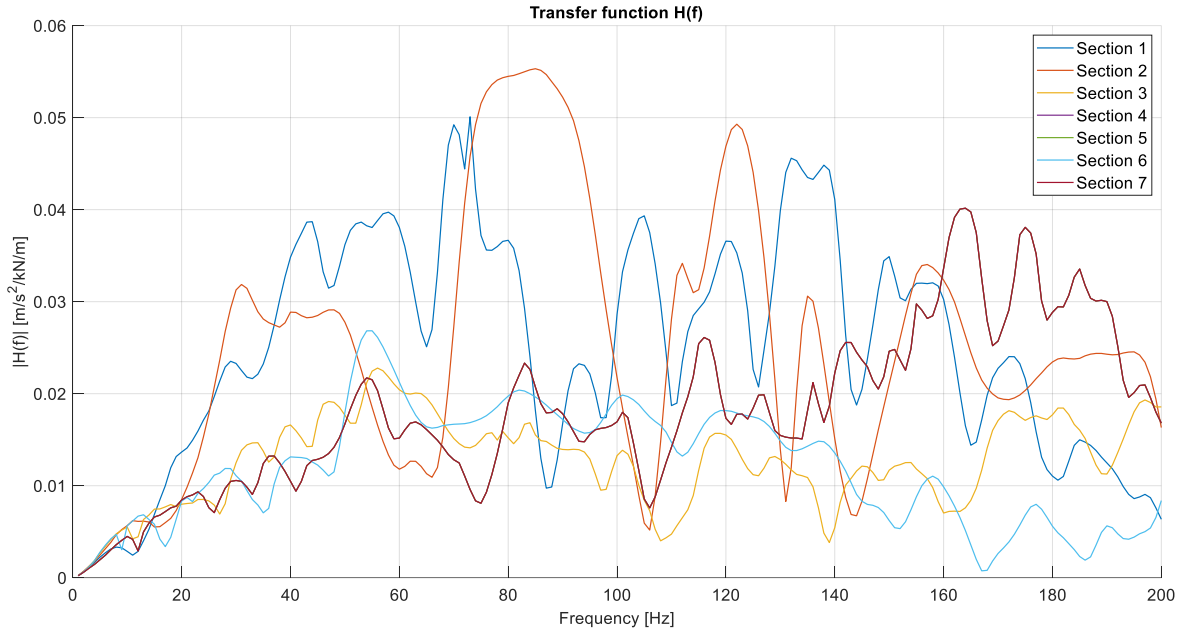

Figure 3.80 *Magnitude of the frequency transfer function across all sections in* $m/s^2/kN/m$

In general, all the transfer function magnitudes are within the same order of magnitude. As explained in the subchapter 3.4.1, sections 4, 5, and 7 share the same assumed geometry; therefore, their transfer function plots are identical. A noticeable distinction can be observed between the sections where the rails are supported by elastomeric pads (sections 1 and 2) and those where the

rails are supported by sleepers and ballast layers (sections 4 to 7). Specifically, the transfer function magnitudes for sections 1 and 2 are slightly higher than those of the ballasted sections, particularly in the frequency range of 20–140 Hz. This difference could be attributed to the absence of ballast in sections 1 and 2. Additionally, it may also be influenced by geometric differences: the first two sections have a double circular tunnel shape and are located at shallower depths, whereas the latter sections feature a box-shaped geometry and are situated deeper underground. As for the box sections, the trends of the transfer functions are quite similar to each other up to a frequency of 130 Hz, showing greater differences at higher frequencies. It can also be observed that at higher frequencies, the Section 6 show a quite lower amplitude than the rest, this might be attributed to fact that its double-boxed shape tends to minimize the vibrations in this frequency range.

3.5 Inversion and dynamic load spectrum

3.5.1 Dynamic load spectrum

Once the response of the tunnel to the passing train $R(f)$ and the transfer functions $H(f)$ are available, the magnitude of the one-sided Fourier spectrum of the dynamic load force $Q_d(f)$ is calculated by means of the inversion using equation (3.1). The plots of $Q_d(f)$ for all the seven sections of analysis are illustrated below.

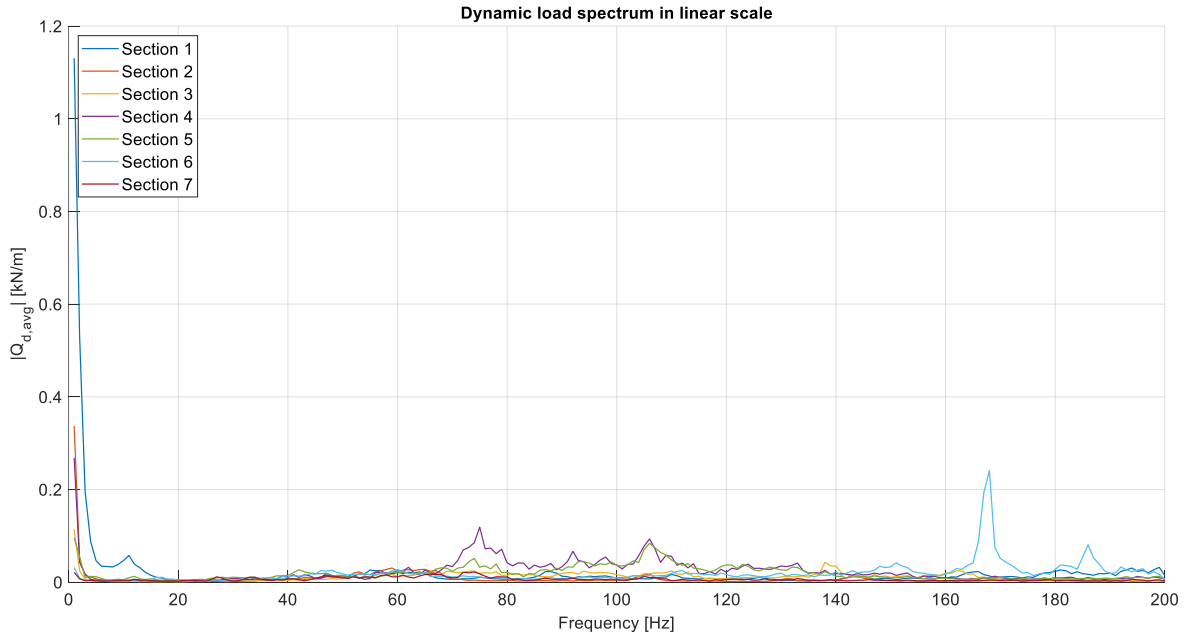

Figure 3.81 *Dynamic load spectrum in kN/m (linear scale)*

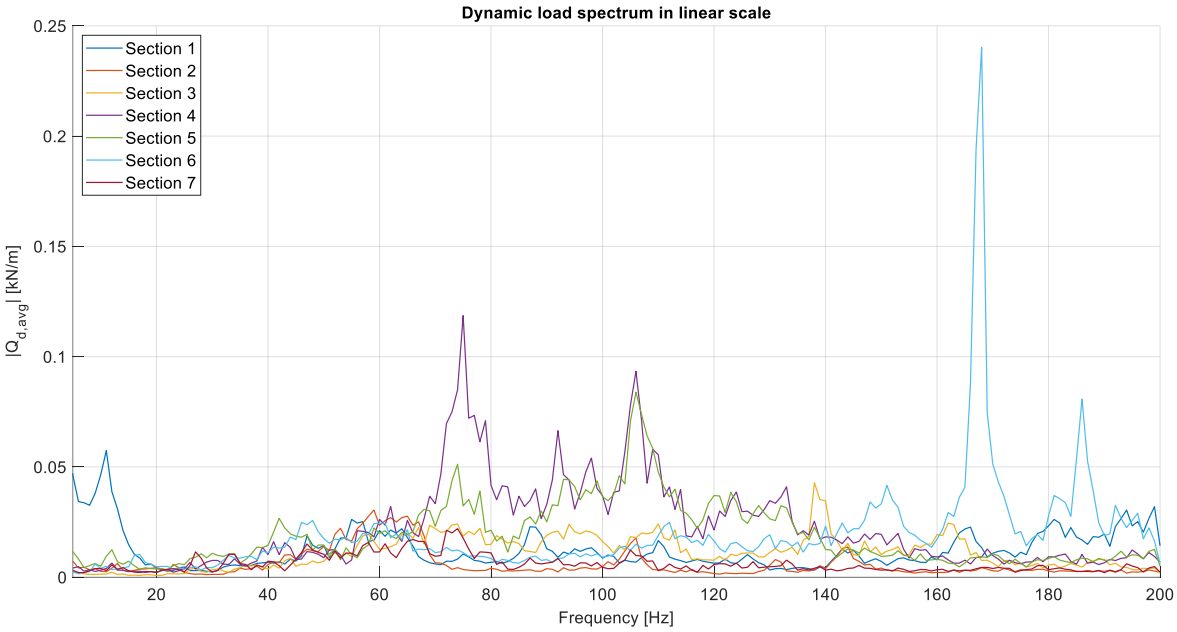

Figure 3.82 *Dynamic load spectrum in kN/m (linear scale, zoomed view)*

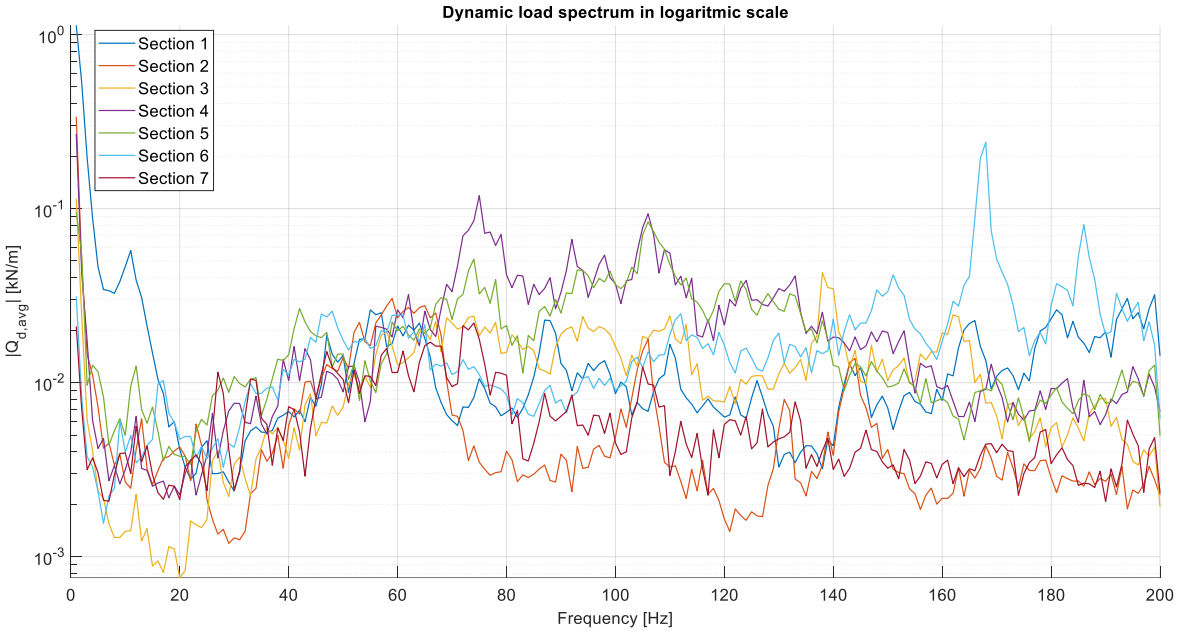

Figure 3.83 *Dynamic load spectrum in kN/m (logarithmic scale)*

A common peak at very low frequencies, in the range of 0–5 Hz, is evident across all sections. Additionally, a distinct peak appears at around 12 Hz. In general, a more energetic frequency band is observed between 60–140 Hz for Sections 4 and 5, corresponding to higher magnitudes in the average response $R(f)$. Another notable peak occurs at 192 Hz in the case of Section 6. Although $R(f)$ or this section does not exhibit a significant peak at this frequency, the transfer function $H(f)$ shows a very low value. Since $Q_d(f)$ is inversely proportional to $H(f)$, this low value in the transfer function causes a peak to emerge in the graph of $Q_d(f)$. The low value in the transfer function for section 6 is likely associated with the increased stiffness due to the presence a double horizontal slab. This stiffer configuration appears to cause strong amplification of $Q_d(f)$ in at 192 Hz.

3.5.2 Power spectral density

To analyse the power distribution of the load spectrum, the Power Spectral Density (PSD) can be computed. This allows for a comparison of the signal's energy distribution across frequency bands, rather than focusing on individual frequency values. The PSD is typically obtained by squaring the magnitude of the FFT and dividing by the bandwidth.

In this study, the magnitude of the dynamic load spectrum was derived through an inversion procedure based on recorded acceleration response measurements. In this context, analysing the load spectrum using the PSD is advantageous, as it helps identify frequency bands with concentrated power, rather than just isolated amplitude peaks.

Given that the dynamic load spectrum is derived from data considered to be a stationary time-dependent random process, where the mean and variance are invariant under time translation, and correlation and covariance depend only on the time lag, it follows that the dynamic load itself exhibits the characteristics of a stationary random process.

Accordingly, the mathematical procedure for determining the PSD of a stationary random process will be presented in the following lines. As described in Chapter 5 of [62], the spectral density functions can be defined via correlation functions. This consists of a method where a single Fourier transform is taken of a previously calculated correlation function.

The autocorrelation function $R_{xx}(\tau)$ is defined in equation (3.37)

$$R_{xx}(\tau) = E[X(t)X(t+\tau)] \tag{3.37}$$

Where t is the time, τ the time lag and $E[.]$ is the expectation operator defined as

$$E[X(t)] = \int_{-\infty}^{+\infty} X(t)p(x)\,dx \tag{3.38}$$

Where $X(t)$ is the time-dependent random process and $p(x)$ is the probability density function associated to the random process.

Assuming that the autocorrelation function $R_{xx}(\tau)$ as defined in equation (3.37) exist and that the integrals of their absolute values are finite, then the Fourier transform of the autocorrelation function is

$$S_{xx}(f) = \int_{-\infty}^{+\infty} R_{xx}(\tau)e^{-i2\pi f\tau}\,d\tau \tag{3.39}$$

The inverse Fourier transform of (3.39) yields to

$$R_{xx}(\tau) = \int_{-\infty}^{+\infty} S_{xx}(f)e^{i2\pi f\tau}\,df \tag{3.40}$$

By using the properties of odd and even properties of sin and cosine it can be obtained

$$R_{xx}(\tau) = 2\int_{0}^{+\infty} S_{xx}(f)\cos(2\pi f\tau)\,df \tag{3.41}$$

The one-sided autospectral density function where the frequency f varies over $(0, \infty)$ is defined by

$$G_{xx}(f) = 2S_{xx}(f) \quad , 0 < f < \infty \; (\, otherwise\; zero) \tag{3.42}$$

By replacing (3.42) in (3.41)

$$R_{xx}(\tau) = \int_0^{+\infty} G_{xx}(f)\cos\,(2\pi f\tau)\, df \tag{3.43}$$

If the stationary random process is characterized by a null mean and variance σ_{xx}^2, then:

$$R_{xx}(0) = \int_0^{+\infty} G_{xx}(f)\, df = \sigma_{xx}^2 \tag{3.44}$$

Assuming a discretised bandwidth Δf where the random process shows a constant spectral amplitude in each bandwidth. The expression (3.44) can be written as

$$\int_{f_{I,j}}^{f_{S,j}} G_{xx,j}(f)\, df = G_{xx,j}\Delta f_j = \sigma_{xx,\Delta f_j}^2 \tag{3.45}$$

Where in the $j-th$ frequency band of size Δf_j and $G_{xx,j}$ is the assumed constant value if the autospectrum. Considering that the variance is a descriptor of the dispersion of the data with respect to the mean value, is reasonable to consider this equivalent to the amplitude of the dynamic load spectrum in the $j-th$ frequency band. Therefore, for each band on the one-sided autospectral density function may be estimated as:

$$G_{xx,j}(f) = \frac{Q_d^2(f_j)}{\Delta f_j} \tag{3.46}$$

A similar approach was considered in [9] for the estimation of the dynamic load spectrum amplitude from the one-sided autospectral density function. In the case of this study, the expression (3.46) can be used for the estimation of the power spectral density written as follows.

$$PSD_{Q_d} = \frac{\left|Q_{d,avg}\right|^2}{\Delta f} \tag{3.47}$$

The bandwidth considered for the comparison among all the different sections has an uniform frequency resolution Δf that can be obtained by the inverse of the original time step $\Delta f = 1/20\; s = 0.05\; Hz$. The results are shown below.

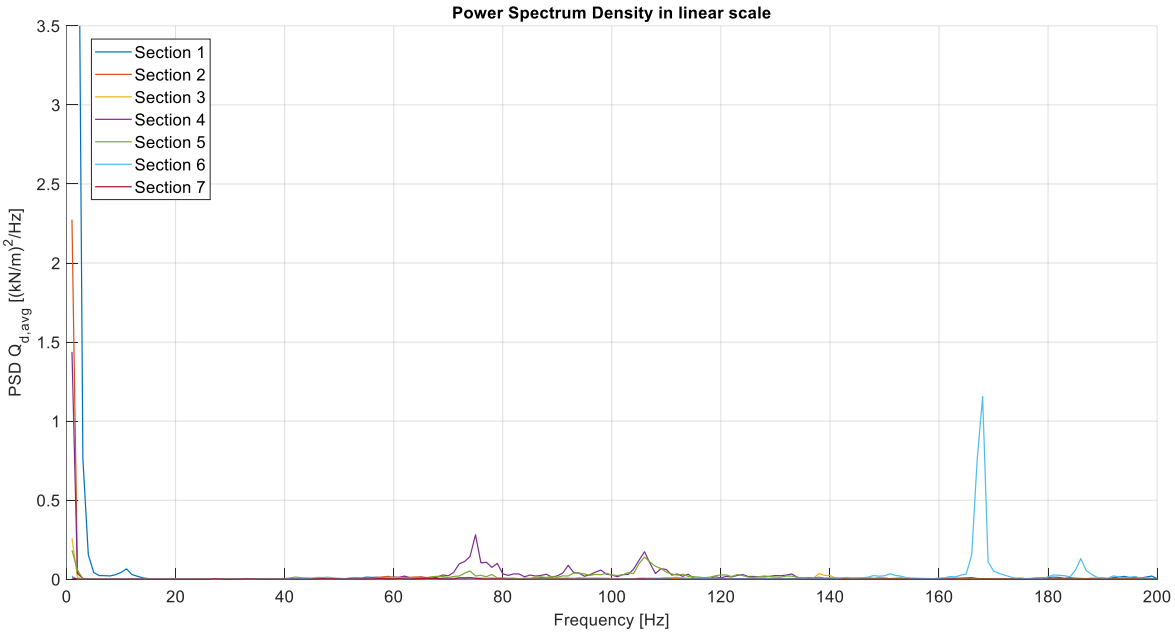

Figure 3.84 *Power spectral density in* $(kN/m)^2/Hz$ *(linear scale)*

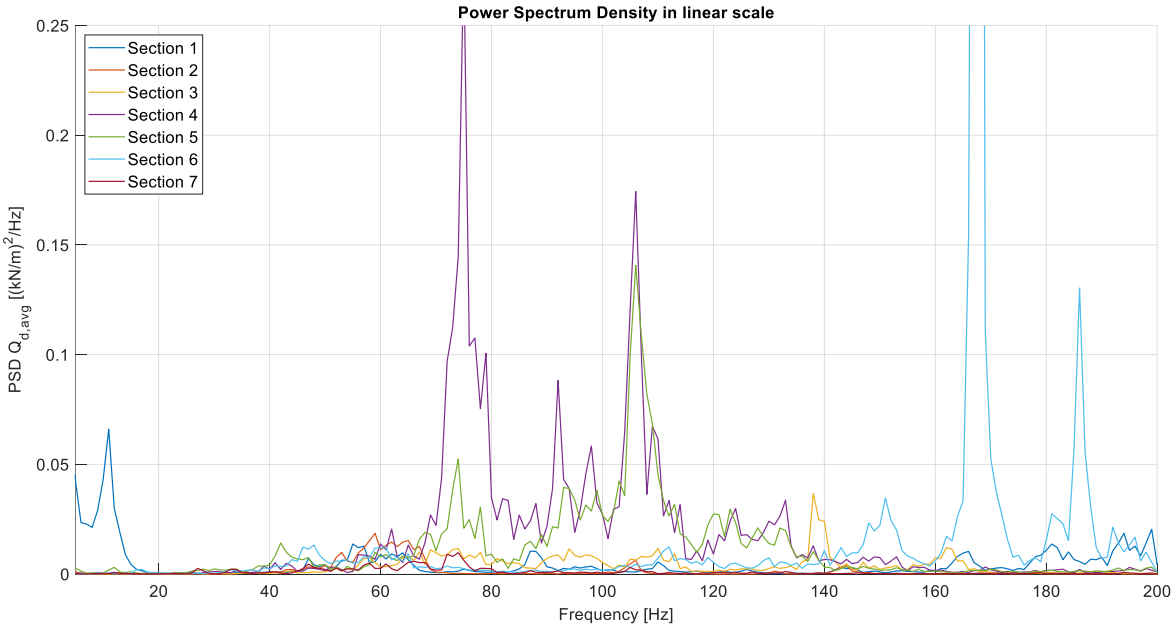

Figure 3.85 *Power spectral density in* $(kN/m)^2/Hz$ *(linear scale, zoomed view)*

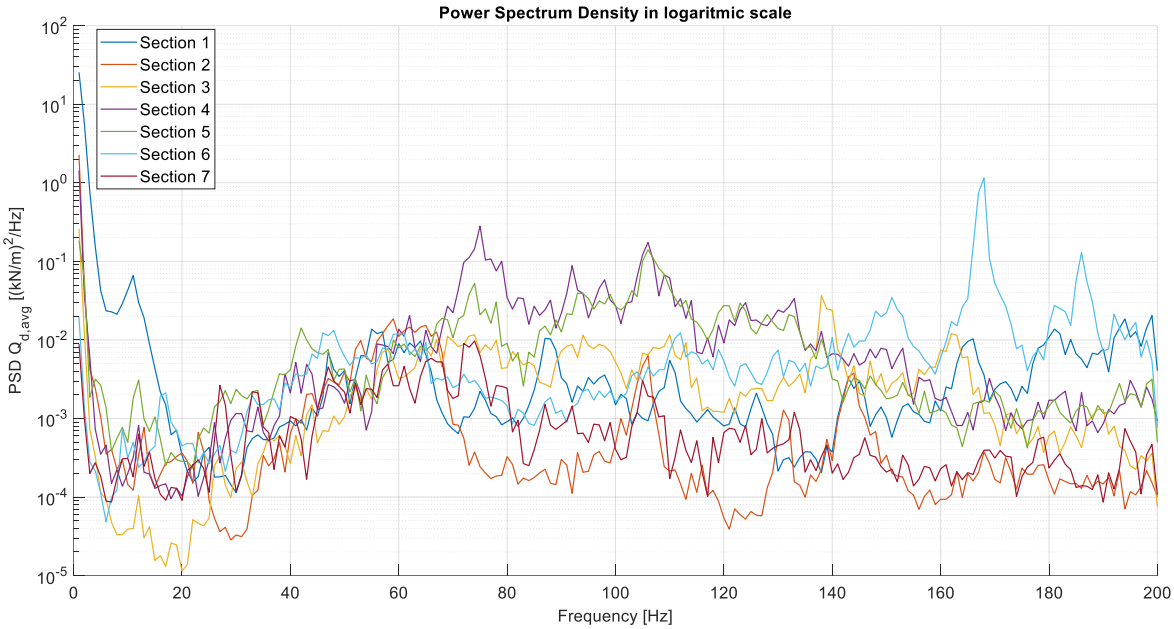

Figure 3.86 *Power spectral density in* $(kN/m)^2/Hz$ *(logarithmic scale)*

Chapter 4
Results and Discussion

4.1 Comparison with the UNI – 11389 standards

4.1.1 Load spectrum of the UNI 11398-1 standard

In this chapter, a comparison is made between the obtained power spectral densities and the one provided by the Italian Standard UNI 11389. Part 1 of the standard outlines that an experimental methodology was used to determine the axle load spectrum $Q_{d\ UNI}\ (f)$, i.e., the spectrum of the load transmitted through the wheel–rail interface. The standard details the procedures required to evaluate this spectrum on an operational railway line [12] which involves two main phases: recording vibrations generated during train passages and conducting dynamic tests with applied loads on the rails. It is also indicated that vibrations measurements must comply with the specifications in Part 4: *On-line monitoring* of the same standard, while the dynamic load tests are to be performed following the instructions provided in Part 3: *Laboratory tests*.

To evaluate the transfer function linking the railway load to the tunnel wall acceleration, two main excitation techniques are employed: sinusoidal and impulsive loading. Sinusoidal excitation is carried out using a vibrodyne system integrated into the track (as shown in Figure 66), while impulsive excitation involves the use of a dynamic hammer. When both the excitation and the measurement are conducted within the same tunnel cross-section, the approach can be treated as two-dimensional. Then, the load-acceleration transfer function is obtained by relating the applied forces to the measured responses within the same localized area of the tunnel.

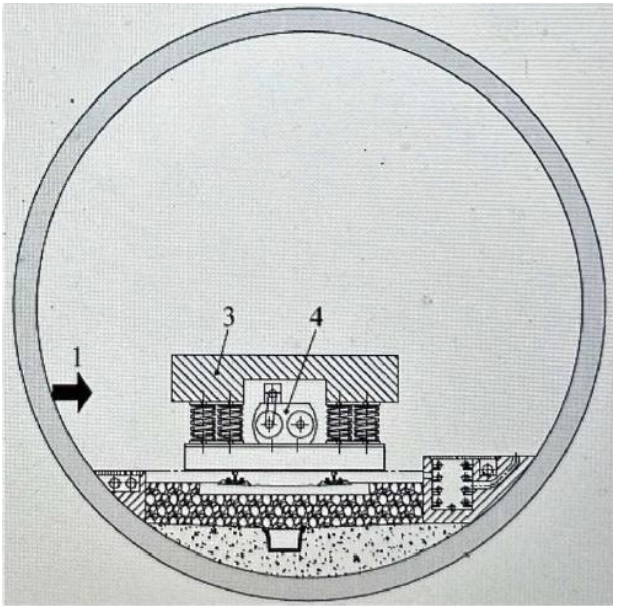

Figure 4.1 *Scheme for the evaluation mode of the rail transport load spectrum from [12]*

The load spectrum, in twelve-octave bands, provided by the standard is determined with the following expression.

$$Q_{d\,UNI} = \varepsilon(f) * Q_v \tag{4.1}$$

Where $\varepsilon(f)$ is a dimensionless load spectrum in twelve octave bands tabulated which plot is as the following.

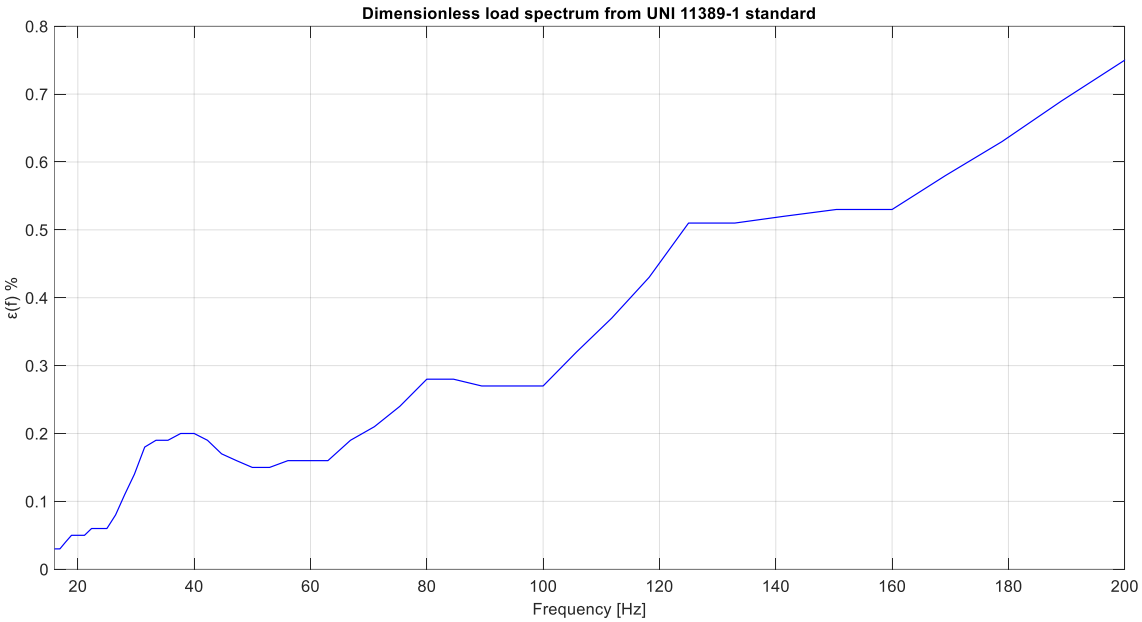

Figure 4.2 *Dimensionless load spectrum from UNI 11389-1*

Q_v is the static vertical load that can be estimated by the following expression.

$$Q_v = \frac{g * m_{tot}}{n_{assi}} \tag{4.2}$$

In the above expression g is the gravity acceleration, m_{tot} is the total mass of the train and n_{assi} is the number of axles of the train. According to [45], the fully loaded train with all seats occupies plus 6 passengers per quare meter has a total mass of 287112 kg, moreover, the train of the Milano metro has 24 axles, then the static vertical load is equal to $Q_v = 117{,}36\ kN$. Consequently, the load spectrum from UNI standard for the considered case is shown below.

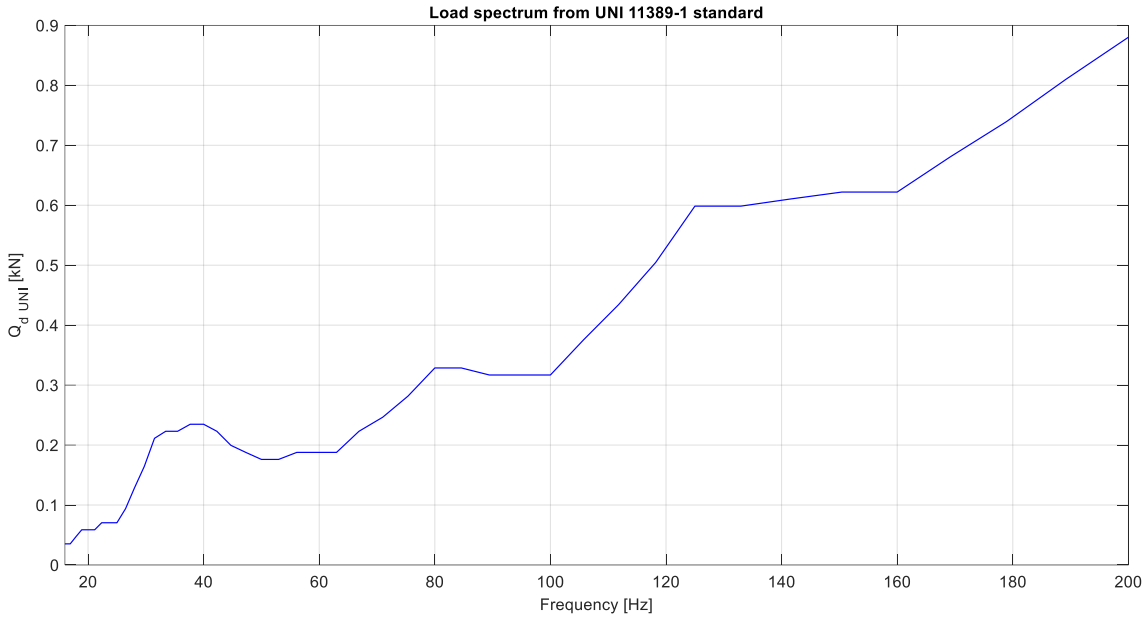

Figure 4.3 *Load spectrum according to UNI 11389-1*

Some important considerations should be noted regarding the UNI standard. According to the specification, the dimensionless spectrum was derived based on a natural single-track tunnel equipped with pre-stressed reinforced concrete sleepers placed on ballast, using UNI 60 rails. Furthermore, the experimental phase assumed a train speed of 50 km/h and a static vertical load of 160 kN. Therefore, these conditions differ from those generally considered in the comparisons conducted in this study

4.1.2 Power spectral density comparison

Once the standard load spectrum is computed, it is useful to calculate its power spectral density (PSD) in order to enable a comparison with the PSD obtained through the inversion procedure. AS explained before, the PSD allows to carry out the comparison over equivalent relevant bandwidths rather than at individual frequency components. By using expression (3.47) the power spectral density for the case of the UNI standard load spectrum can be written as:

$$PSD_{Q_{d,UNI}}(f_j) = \frac{\left|Q_{d,UNI}(f_j)\right|^2}{\Delta f} \tag{4.3}$$

Where f_j is the central frequency of the twelfth-octave band and Δf_j is the relative bandwidth.

On the other hand, to enable the comparison between the spectrum obtained through the inversion procedure and the one defined in the standard, it is necessary to present the PSD in one-twelfth-octave bands. This can be efficiently accomplished using MATLAB's Signal Processing Toolbox. Specifically, the PSD plots shown in **Figure 3.84** can be converted into one-twelfth-octave bands using the built-in *poctave* function, which returns the power spectrum values corresponding to the central frequencies for a specified number of bands per octave (in this case, 12). The bandwidth of each band is then determined using the *signal.internal.octave.computeOctaveBands* function. By dividing each power spectrum value by its corresponding frequency bandwidth, the PSD in one-twelfth-octave bands is obtained. The resulting comparison between the original PSD and the octave-band representation for section 1 is illustrated in **Figure 4.4**.

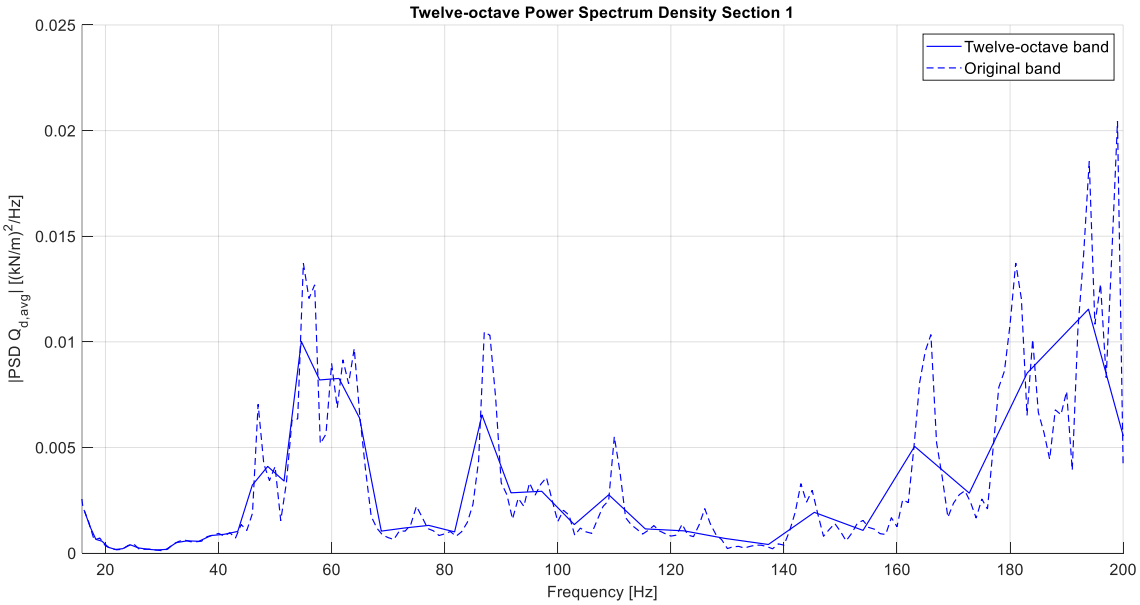

Figure 4.4 *PSD comparison in original bandwidth and twelve octave bands for section 1*

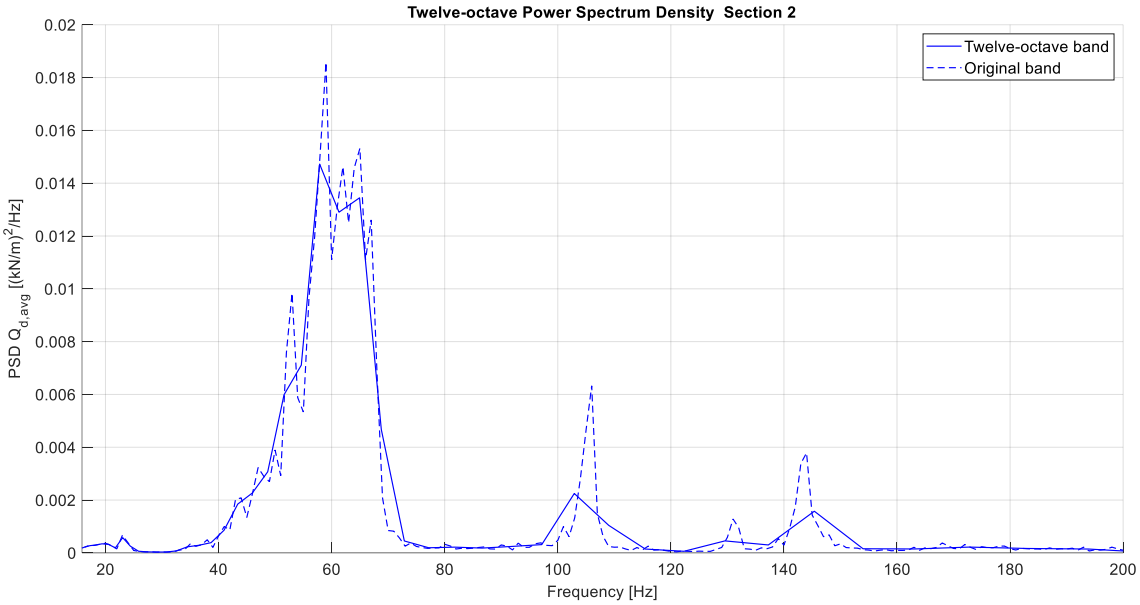

Figure 4.5 *PSD comparison in original bandwidth and twelve octave bands for section 2*

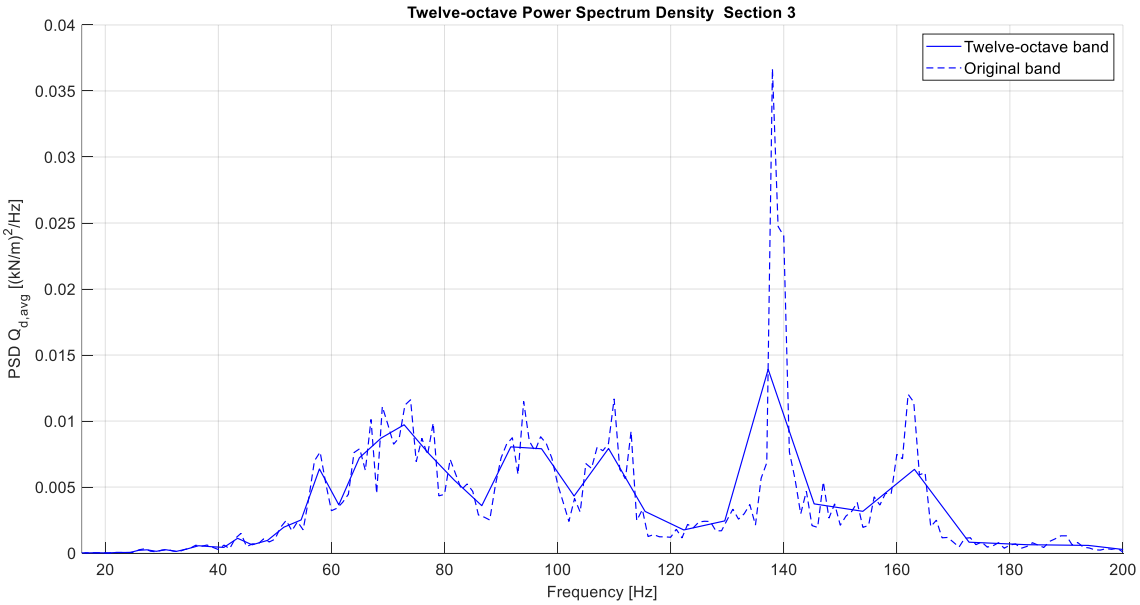

Figure 4.6 *PSD comparison in original bandwidth and twelve octave bands for section 3*

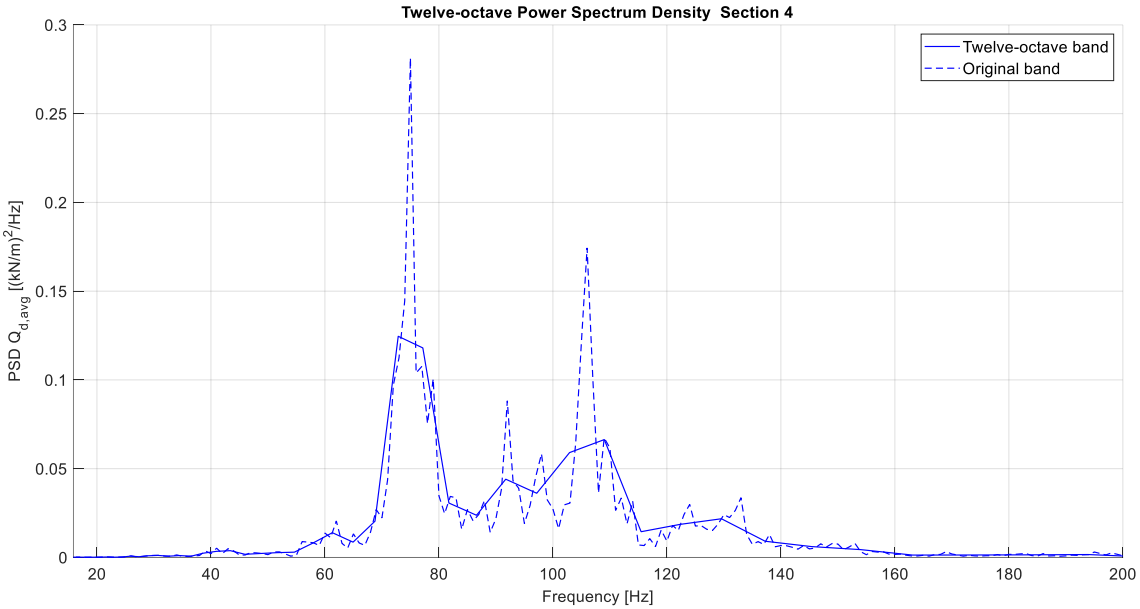

Figure 4.7 *PSD comparison in original bandwidth and twelve octave bands for section 4*

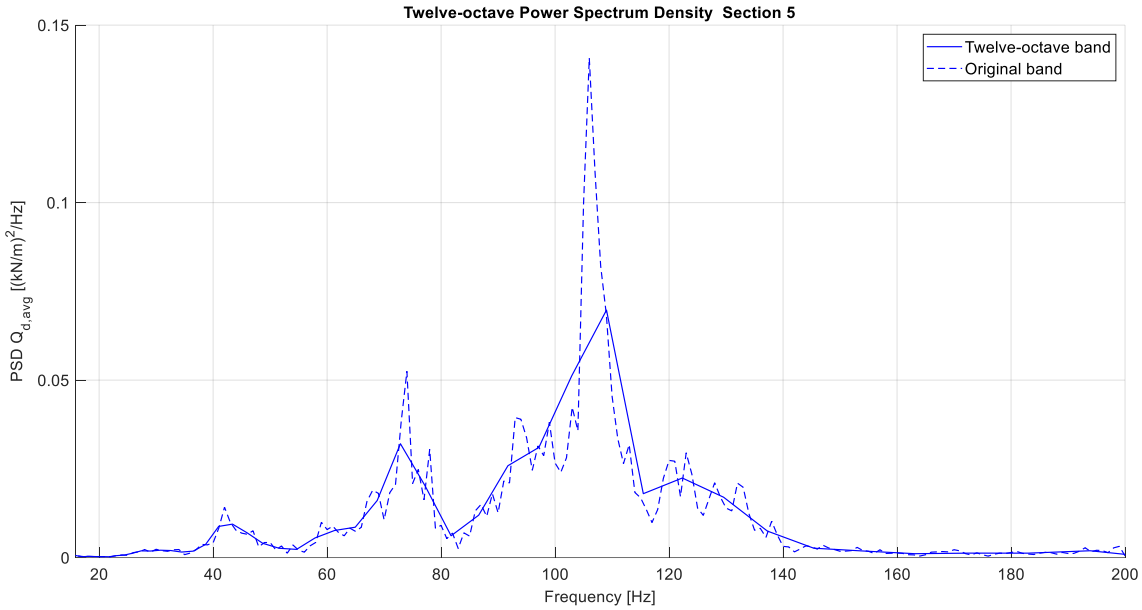

Figure 4.8 *PSD comparison in original bandwidth and twelve octave bands for section 5*

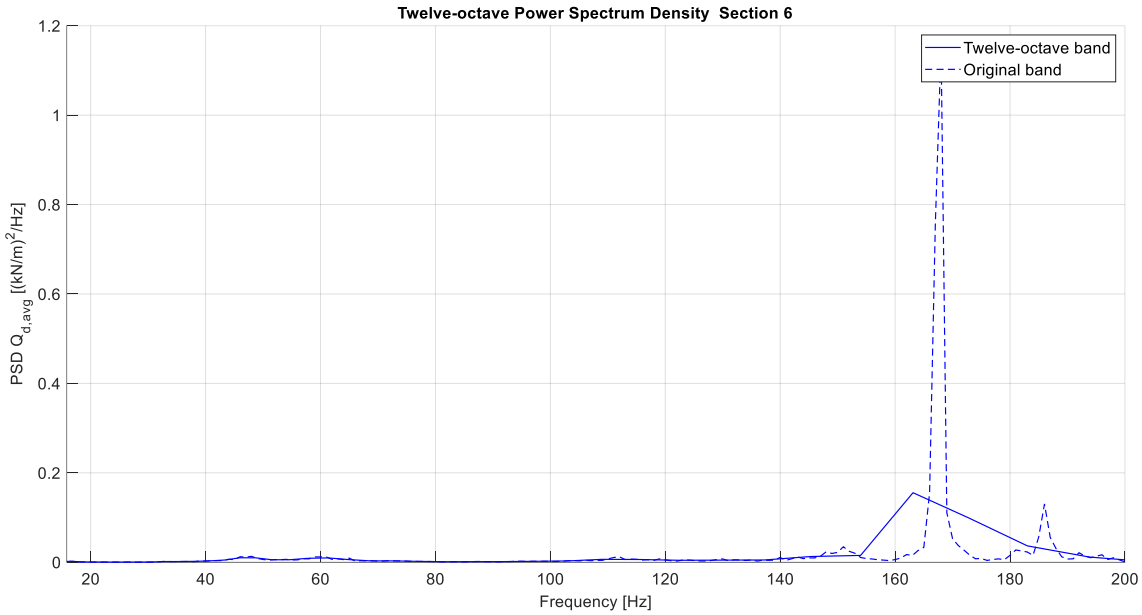

Figure 4.9 *PSD comparison in original bandwidth and twelve octave bands for section 6*

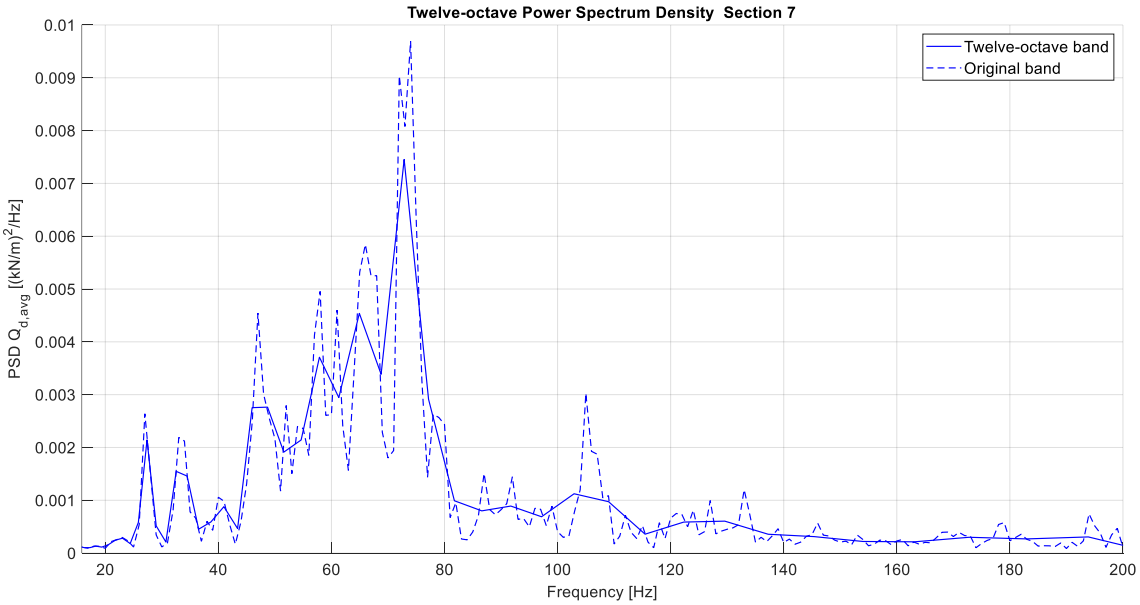

Figure 4.10 *PSD comparison in original bandwidth and twelve octave bands for section 7*

It is important to note that the PSD from the UNI standard is expressed in units of kN^2/Hz, whereas the PSDs obtained through the inversion procedure are expressed in $(kN/m)^2/Hz$. This difference arises because the load spectrum in the UNI standard was derived experimentally by applying either a concentrated or sinusoidal load (in kN), whereas the inversion procedure is based on a two-dimensional plane strain assumption, where the resulting loads are distributed along the tunnel's longitudinal direction and expressed in kN/m. The comparison between the PSD defined by the UNI 11389-1 standard and those obtained through the inversion procedure is shown for all sections in **Figure 4.11**.

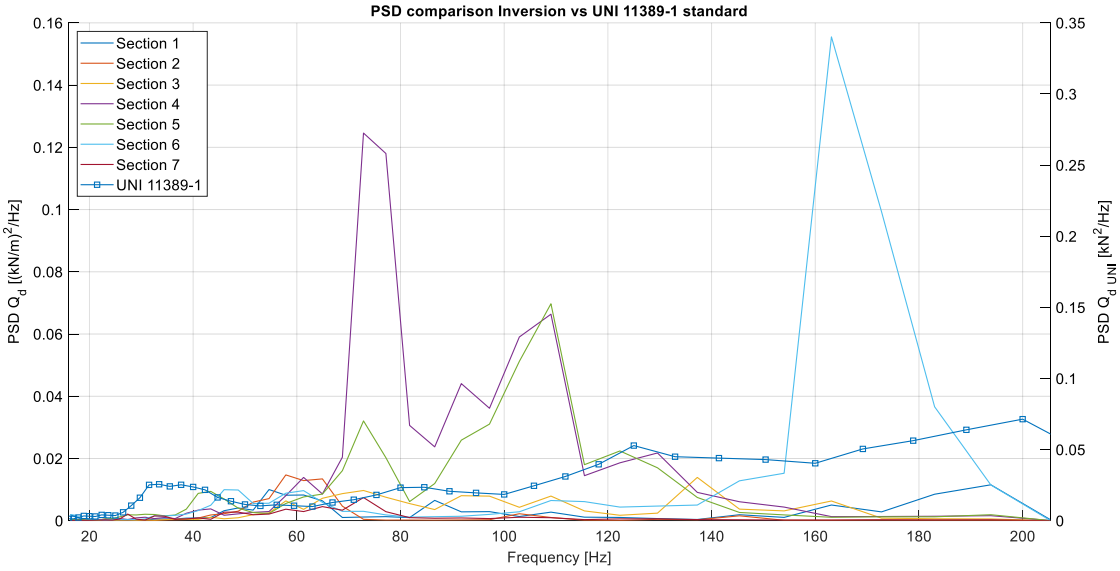

Figure 4.11 *PSD comparison between the UNI 11389-1 standard and the obtained by the inversion procedure in twelve-octave bands*

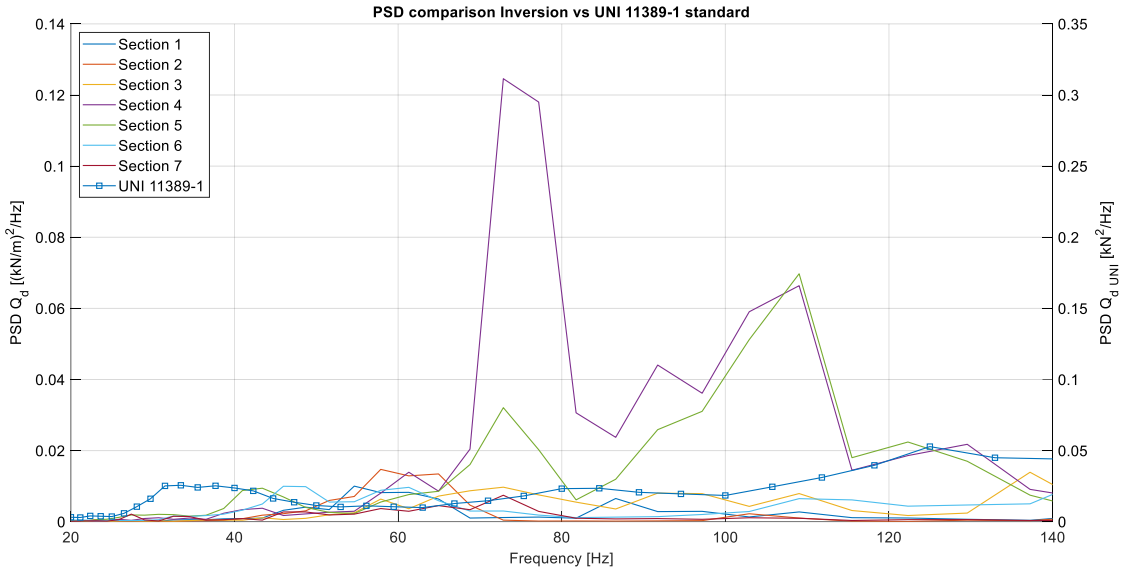

Figure 4.12 *PSD comparison between the UNI 11389-1 standard and the obtained by the inversion procedure in twelve-octave bands (zoomed view)*

As shown in **Figure 4.11**, the load spectra generally exhibit values of the same order of magnitude, except for Sections 4, 5, and 6. For Section 6, a distinct peak at 165 Hz is attributed, as previously discussed, to the very stiff behaviour of the double slab structure at that frequency. A smaller peak is also observed around 60 Hz, consistent with the frequency range found in the other sections.

The UNI spectrum displays a bump around 30 Hz, which is not observed in any of the sections analysed in this study. Moreover, the trend exhibit by the standard does not correspond to any of the analysed sections. It is important to note, as discussed in a previous chapter, that the conditions under which the UNI standard spectrum was developed differ significantly from those considered in this study.

Sections 4 and 5 show spectral magnitudes that differ significantly from the rest. However, some trends in their frequency content still correspond with those of other sections. For instance, a first bump appears around 70 Hz, common to Sections 4, 5, and 7. A counter peak around 85 Hz is also observed in Sections 1, 3, 4, and 5. Another peak near 110 Hz is shared by Sections 1, 3, 4, 5, and 6, while a smaller peak near 130 Hz appears only in Sections 4 and 5. Differences in train velocity and wagon weight may be contributing factors to the discrepancies.

In the zoomed-in view of the plot (see **Figure 4.12**), Sections 1 and 2, both characterized by similar geometry and rail-track materials, show a first bump in the 55–65 Hz range. However, they differ in their second peaks: Section 1 shows a peak around 85 Hz, while Section 2 peaks at approximately 100 Hz. Section 1 also presents a smaller bump at around 110 Hz.

Section 3, which is the only non-ballasted section with wooden sleepers, displays a shifted first bump at approximately 70 Hz. This is followed by a second, slightly smaller bump near 95 Hz, and a third, comparable in magnitude to the second, at around 110 Hz. This third peak aligns in frequency with those of Sections 1 and 6. Although Sections 4 and 5 also exhibit peaks in this region, their magnitudes are significantly different.

4.2 Correlation with expected critical frequencies

According to the literature [63] [64], since railway tracks are supported by discrete supports, the train wheels tend to oscillate vertically as they travel along the track at a certain speed. This oscillation occurs at a frequency known as the sleeper passing frequency f_s , which is velocity-dependent and can be calculated using the following expression:

$$f_s = \frac{v}{d} \tag{4.4}$$

Where v is the train velocity and d is the support's distance.

Furthermore, the wheelbase distance (i.e., the distance between two axles within the same bogie) and the inter-bogie distance (i.e., the distance between axles of two different bogies) introduce additional sources of load oscillation as the train passes. This occurs because the moving trolley loads are applied to the section under analysis with a periodicity whose wavelength corresponds to these characteristic distances. When the frequency of these oscillations is close to a natural frequency of the system, amplification of the dynamic response may occur. The excitation frequency generated by the moving load can be estimated using the following expressions.

$$f_{axle} = \frac{v}{d_{axle}} \tag{4.5}$$

$$f_{bogie} = \frac{v}{d_{bogie}} \tag{4.6}$$

Where v is the train velocity, d_{axle} is the distance between axles, d_{bogie} is the distance between two consecutive bogies (see **Figure 4.13**). In this chapter, both types of excitation frequencies will be considered as expected sources of dynamic loading. These frequencies will be calculated and plotted alongside the tunnel's frequency response obtained from field measurements, in order to assess the level of correlation between the theoretically expected excitations and the observed response.

4.2.1 Critical distances

According to the train geometry and supports spacing the critical distances are the following. The inter-boogie and wheelbase distances according with the figure below are $d_{bogie} = 8.95\ m$ and $d_{axle} = 2.15\ m$ respectively while for the sleepers' spacing distances of $d_{s1} = 0.60\ m$ and $d_{s2} = 0.30\ m$ were considered.

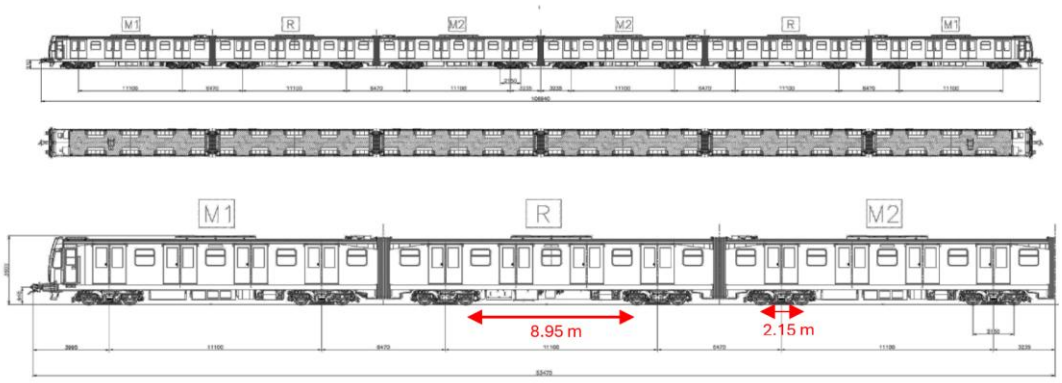

Figure 4.13 *Inter boogie and wheelbase axle distances in the Leonardo train*

Figure 4.14 *Sleepers' spacing d_{s1}=0.60m (left) and d_{s2}=0.30m (right)*

4.2.2 Average velocity and expected frequencies computation

The measurements carried out by P&P LMC S.R.L. also include rail displacements measured using strain gauges. The data, as with the accelerations, are collected in separate .ASCI files for each train passage and are organized in the following columns:

- Est. 1 base ext: Refers to the base of the external rail, measurements in $\mu m/m$
- Est. 2 base ext: Refers to the head of the external rail, measurements in $\mu m/m$
- Est. 3 base ext: Refers to the base of the internal rail, measurements in $\mu m/m$
- Est. 4 base ext: Refers to the head of the internal rail, measurements in $\mu m/m$
-

In this case as well, the data were acquired at a sampling frequency of 4800 Hz, corresponding to a sampling period of $2{,}08\ x\ 10^{-4}\ s$. Each signal, corresponding to the passage of a single train was recorded over a time window of approximately 20 seconds, which includes both the approach and departure phases of the vehicle. As an example, in **Figure 4.15** is plotted the acceleration and the 4 extensometers measurements in the time domain for the first recording of section 1.

It is evident the presence of peaks and that the number of these, which is equal to 24, coincides with the number of axles of the train. Therefore, the distance between the first and last axle of the train L, divided by the time interval between the first (t_1) and last peak (t_f) in strain gauge time history, allows the calculation of the average train speed (v_{train}) according to expression (4.7). The train velocity for each recording and the average are shown in Table 4.1.

$$v_{train} = \frac{L}{t_f - t_1} = \frac{L}{\Delta t_{axle}} \tag{4.7}$$

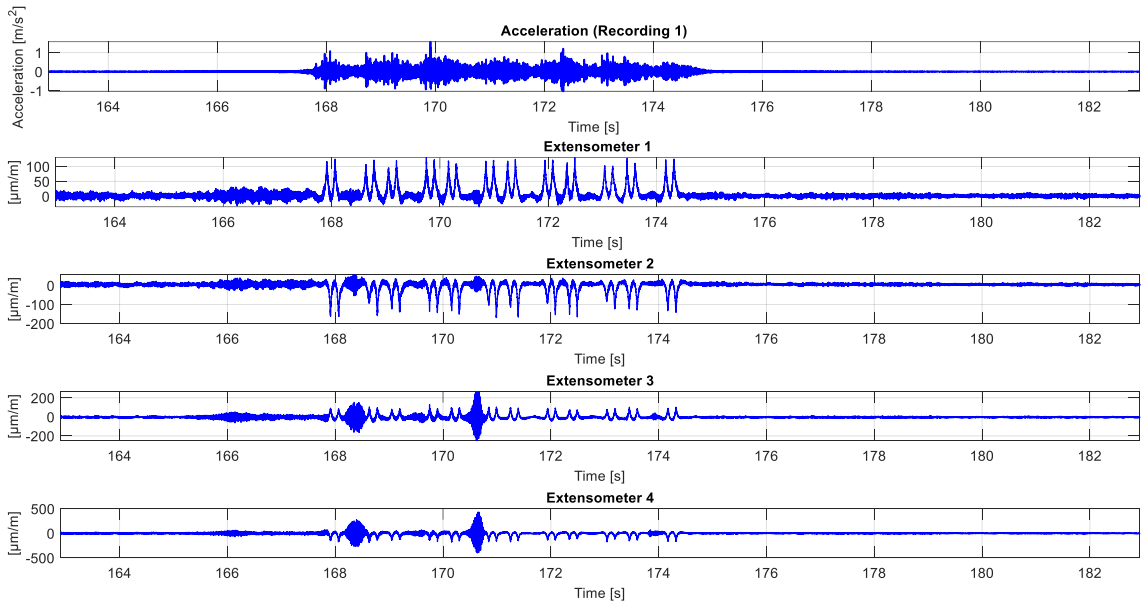

Figure 4.15 *Recording of vertical accelerations and extensometers displacements (1=suola est., 2=fungo est.,3=suola int. and 4=fungo int.) for the first recording of section 1*

Table 4.1 Average train velocity computation for section 1

Recording	t1 (s)	tf (s)	Δt (s)	L (m)	v (m/s)	v (km/h)
1	167.91	174.32	6.41	101.1	15.77	56.78
2	160.01	166.20	6.19	101.1	16.33	58.80
3	189.85	196.09	6.24	101.1	16.19	58.30
4	97.03	103.64	6.60	101.1	15.31	55.13
5	119.24	125.61	6.37	101.1	15.87	57.14
6	138.51	144.71	6.19	101.1	16.33	58.78
7	82.85	89.03	6.18	101.1	16.36	58.89
8	201.60	208.04	6.44	101.1	15.70	56.52
9	93.30	99.54	6.24	101.1	16.20	58.33
10	151.16	157.30	6.14	101.1	16.47	59.28
11	114.90	121.24	6.33	101.1	15.96	57.45
12	112.82	119.05	6.23	101.1	16.23	58.42
13	179.91	186.20	6.29	101.1	16.08	57.89
14	108.49	114.76	6.27	101.1	16.13	58.07
15	87.55	93.72	6.17	101.1	16.39	58.99
16	167.68	174.21	6.53	101.1	15.48	55.74
17	100.36	106.67	6.31	101.1	16.02	57.68
18	89.55	96.14	6.60	101.1	15.33	55.18
19	144.67	150.87	6.20	101.1	16.30	58.69
20	130.55	136.76	6.21	101.1	16.28	58.61
21	107.19	113.41	6.23	101.1	16.24	58.46
22	121.36	127.60	6.24	101.1	16.20	58.33
23	107.73	114.11	6.38	101.1	15.85	57.06

24	171.39	177.72	6.33	101.1	15.98	57.52
25	117.67	123.98	6.31	101.1	16.02	57.68
				Average	16.04	**57.75**
				Std. Dev.	0.32	**1.15**

The averages and standard deviations of the velocities for each section are summarized in the following table.

Table 4.2 Averages and standard deviations of the train velocities for each section

Section	**Average (km/h)**	**σ (km/h)**
1	57.75	1.15
2	54.00	3.89
3	37.82	3.56
4	44.82	8.80
5	40.11	2.87
6	47.83	0.83
7	52.13	1.63

Then the expected frequencies were computed by dividing the velocities by the assumed distances. The expected frequencies are summarized in the table below.

Table 4.3 Expected frequencies

	Distance =	**d_{bogie}=8.95m**	**d_{axle}=2.15m**	**d_{s1}=0.6m**	**d_{s2}=0.3m**
Section	v (km/h)	f1 (Hz)	f2 (Hz)	f3 (Hz)	f4 (Hz)
1	57.75	1.79	7.46	26.73	53.47
2	54.00	1.70	7.06	25.29	50.58
3	37.82	1.19	4.96	17.79	35.58
4	44.82	1.42	5.90	21.13	42.27
5	40.11	1.23	5.10	18.29	36.57
6	47.83	1.48	6.16	22.09	44.18
7	52.13	1.60	6.65	23.81	47.62

4.2.3 Validation of the expected frequencies

To validate whether the expected frequencies were effectively excited in the recorded average responses $R(f)$ these were plotted together for comparison. In the following graphs, the obtained average spectra with 1 Hz resolution are presented alongside the expected frequencies for the seven sections.

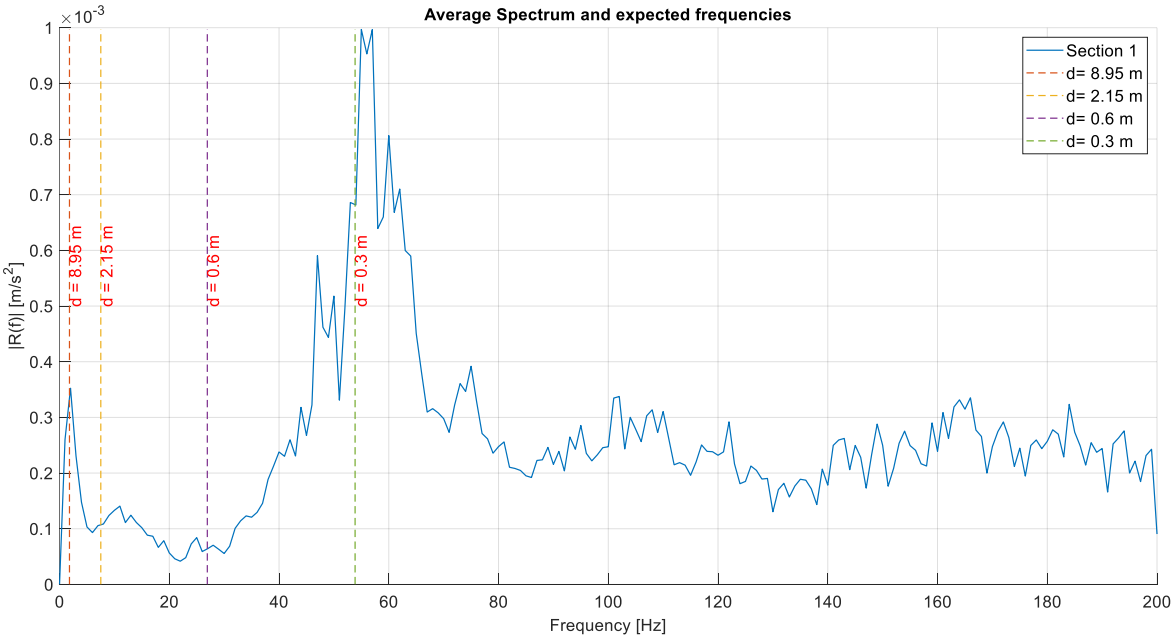

Figure 4.16 *Average spectrum with expected frequencies for Section 1*

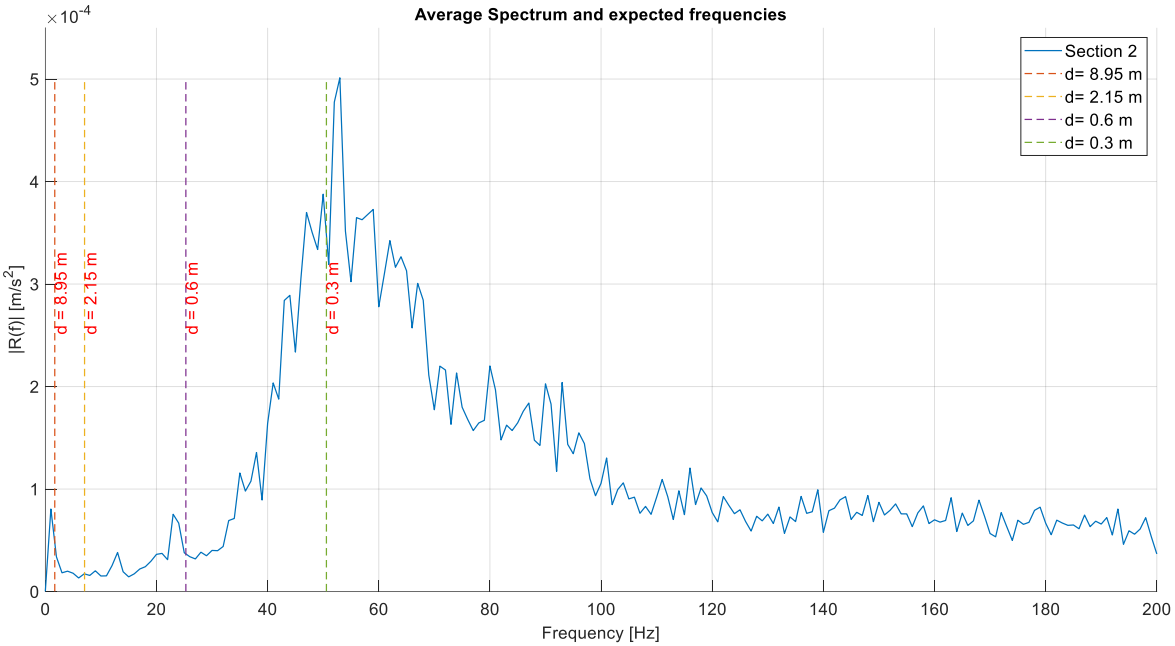

Figure 4.17 *Average spectrum with expected frequencies for Section 2*

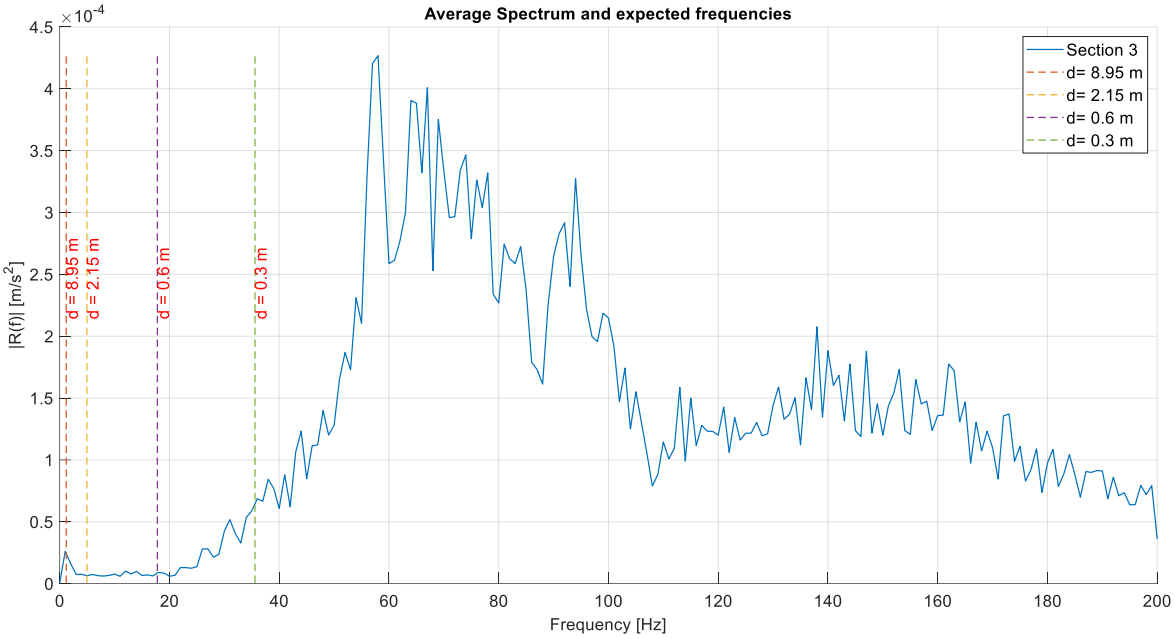

Figure 4.18 *Average spectrum with expected frequencies for Section 3*

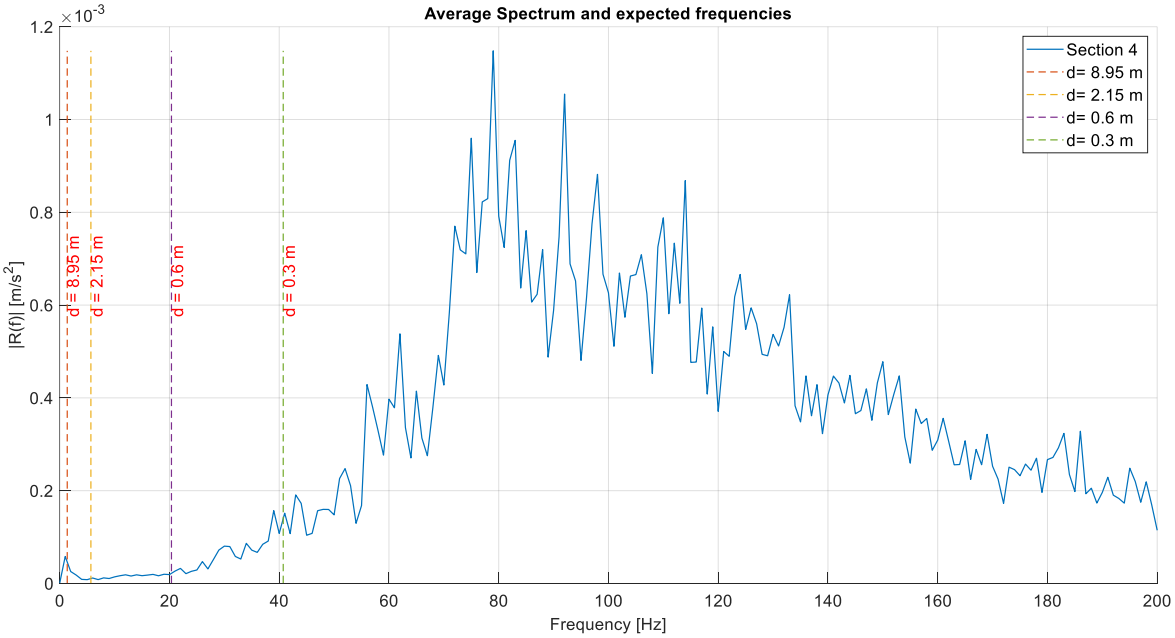

Figure 4.19 *Average spectrum with expected frequencies for Section 4*

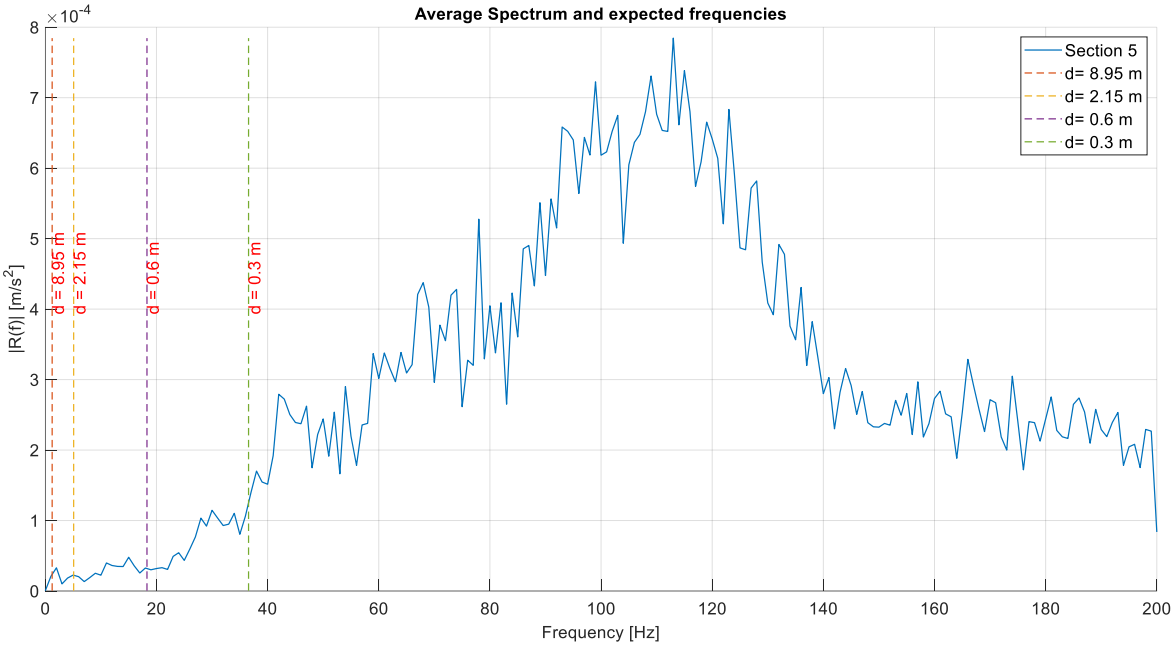

Figure 4.20 *Average spectrum with expected frequencies for Section 5*

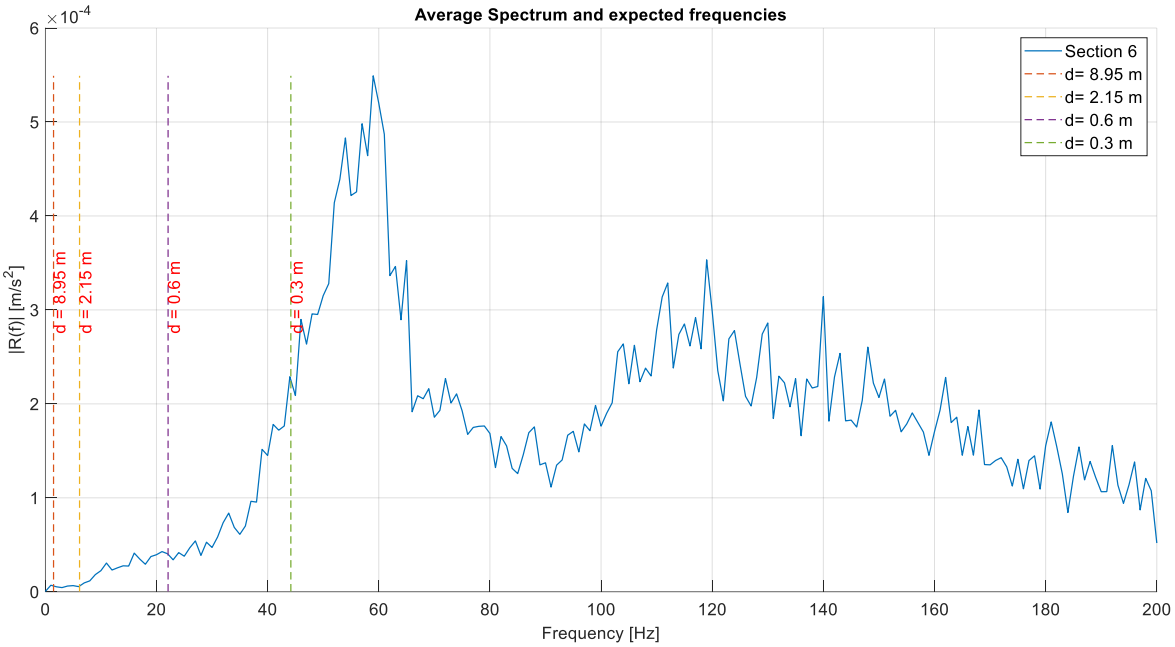

Figure 4.21 *Average spectrum with expected frequencies for Section 6*

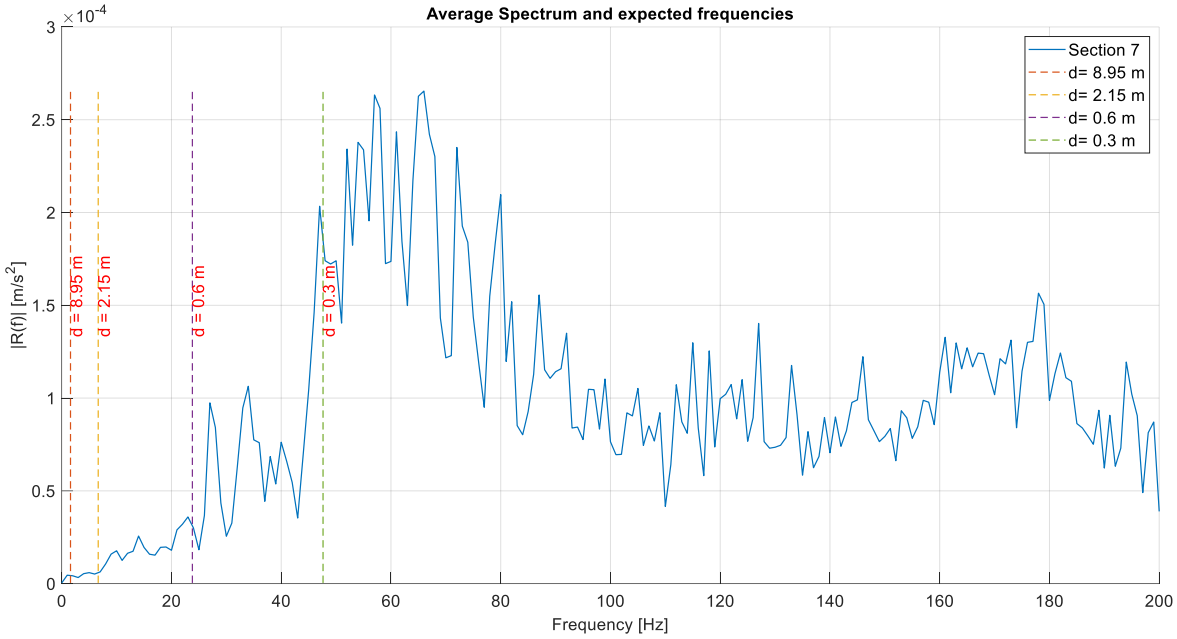

Figure 4.22 *Average spectrum with expected frequencies for Section 7*

A correlation of the peak at a frequency around 1.5 Hz can be observed for all seven sections corresponding with the first expected frequency. This frequency is the one corresponding to the inter-boogie distance d=8.95m. This might suggest that expression (4.5) provides a correct estimation of the possibles load oscillation frequency, the one associated with the periodicity of the inter-bogie distance.

For the rest of expected excited frequencies, the wheelbase frequency and the sleepers' passing frequency, no clear correlation is observed. This might indicate that the load periodicity induced by these sources of oscillations is not causing a noticeable amplifying effect in the system in this range of frequencies. According to [64], the sleeper's passing frequency are important when these coincide with the wheel-track natural frequency causing resonance, these observations were done of high-speed trains in which the sleepers' passing frequencies are higher.

As explain in subchapter 3.3, studies like [18] indicate that the peaks at around 30Hz and 125 Hz are associated with the natural frequency of the tunnel-ground system and the rail track system respectively. This suggests that expressions (4.4) and (4.5) might be oversimplified when it comes to detect higher frequency load components.

Chapter 5
Conclusions

In this chapter, a summary of the study is provided, including key research findings in relation to the stated aims and questions, along with the contributions and value of this work. The chapter also outlines the study's limitations and proposes opportunities for future research.

This study presents a detailed analysis of the dynamic behaviour of the Milan Metro lines M1 and M2 by investigating seven different tunnel sections during train passage. The research focused on applying an inversion procedure of accelerations to obtain the dynamic load spectrum for each section, using in-situ acceleration measurements and two-dimensional (2D) finite element models to estimate the load-acceleration transfer functions. The measured responses were processed and compared across sections in the frequency domain to identify patterns influenced by known variables discussed in existing literature. The load-acceleration transfer function was computed using 2D FEM models due to their computational efficiency and flexibility for parametric studies, compared to more refined three-dimensional (3D) approaches. The resulting dynamic load spectra were then compared with the UNI 11389 standard to validate the findings.

The first step of the inversion procedure involved processing the measured acceleration at the tunnel wall. Disturbed signals were discarded, and the remaining ones were adjusted to have a uniform time duration. A filtering and decimation process was applied to prepare the signals for averaging, after which a representative acceleration magnitude response spectrum was obtained for each section. Comparison across sections revealed recurring spectral features: a consistent peak around 60 Hz appeared in nearly all sections, regardless of track type. According to the literature, this peak is associated with the wheel–track system response, particularly the resonance of the unsprung mass. A secondary peak around 100 Hz was observed, predominantly in ballasted track sections, suggesting a resonance related to the ballast layer.

A comparison was also made between the measured frequency response and frequencies associated with the sleeper passing frequency and the periodicity of moving loads. A shared peak around 1.5 Hz was identified in all sections, corresponding to the excitation induced by the inter-bogie distance. This supports the applicability of expressions proposed in the literature for estimating such excitation. However, no clear correlation was found for frequencies associated with the wheelbase distance or sleeper passing frequency. These may be influenced by more complex interactions in the track–tunnel–soil system, which exhibit inherently three-dimensional behaviour and would require more detailed studies.

Another key aspect of this work was the use of a 2D model to calculate the transfer function. This choice was primarily motivated by its computational efficiency compared to 3D modelling. The 2D approach enabled the development of seven models, allowing investigation of geometrical differences, tunnel depth, and elastomeric pad stiffness normalization. Such a broad parametric study would have been impractical using 3D models due to time and resource constraints. Results showed a noticeable distinction between circular and box-shaped tunnel sections. In particular, the circular

sections (Sections 1 and 2) exhibited slightly higher magnitudes between 20–140 Hz. This was attributed to their geometry and shallower depth compared to deeper, box-shaped tunnels. The absence of ballast in Sections 1 and 2 may also contribute to this difference.

The resulting dynamic load spectra were compared with the UNI 11389 standard. While most sections showed similar order of magnitude, notable discrepancies were found in Sections 4, 5, and 6. In Section 6, a distinct peak at 165 Hz was attributed to the stiff behaviour of the double-slab structure. The UNI standard includes a bump around 30 Hz, which was not present in any of the measured data. Overall, the spectral trend from the standard did not correspond to any of the analysed sections. It is important to note that the standard was developed under different experimental conditions, as previously discussed. The deviations seen in Sections 4 and 5 can be attributed to variations in experimental and structural condition such as tunnel geometry, soil parameters, number and type of tracks, and the rail support system including elastomeric pads and sleeper types.

This thesis suggests that the 2D inversion procedure, although it cannot fully capture the three-dimensional nature of the problem, it can reasonably represent the dynamic response of the analysed sections and provide valuable parametric insights. The dynamic load spectra obtained here may still be useful for qualitative analysis; however, they should not be considered fully accurate due to the inability of the 2D model to represent out-of-plane effects. Amplification mechanisms involving the track–tunnel–soil system and the wheel–rail contact are inherently three-dimensional, and modes affecting the response and resulting load spectra cannot be accurately captured with 2D models. A more comprehensive 3D model would be necessary to compute accurate load–acceleration transfer functions at measurement points along the longitudinal direction. To overcome the high computational cost of a full 3D model, an effective alternative could be the use of 2.5D numerical models, which exploit problem invariance and have been successfully implemented in the literature by combining finite element (FE) and boundary element (BE) formulations.

Chapter 6
Bibliography

[1] "Examples of benefits of underground urban public transportation systems," *Tunnelling and Underground Space Technology*, vol. 2, no. 1, pp. 5–54, Jan. 1987, doi: 10.1016/0886-7798(87)90141-6.

[2] "Transit Project Openings in 2025: A Global Review – The Transport Politic." Accessed: May 23, 2025. [Online]. Available: https://www.thetransportpolitic.com/2025/01/12/transit-project-openings-in-2025-a-global-review/

[3] "Storia della Metropolitana Milanese." Accessed: May 04, 2025. [Online]. Available: http://www.sottomilano.it/storia.htm

[4] S. Zhou, C. He, H. Di, P. Guo, and X. Zhang, "An efficient method for predicting train-induced vibrations from a tunnel in a poroelastic half-space," *Eng Anal Bound Elem*, vol. 85, pp. 43–56, Dec. 2017, doi: 10.1016/J.ENGANABOUND.2017.09.013.

[5] X. C. Bian, W. F. Jin, and H. G. Jiang, "Ground-borne vibrations due to dynamic loadings from moving trains in subway tunnels," *Journal of Zhejiang University: Science A*, vol. 13, no. 11, pp. 870–876, Nov. 2012, doi: 10.1631/JZUS.A12ISGT5/METRICS.

[6] "Vibrazioni o rumore della metropolitana | Missione Rumore - Associazione italiana per la difesa dal rumore." Accessed: Apr. 10, 2025. [Online]. Available: https://www.missionerumore.it/in-casa-tua-hai-le-vibrazioni-o-il-rumore-della-metropolitana/

[7] H. Mungamuri, "Experimental Analysis on the effectiveness of reducing ground-borne vibrations using different track systems: A case study of Milan subway system.," Politenico di Milano, 2023. Accessed: May 23, 2025. [Online]. Available: https://www.politesi.polimi.it/handle/10589/198842

[8] F. Rigoni, "Effect of water table's depth in subway-induced vibrations: case of Line M1 in Milan," Politecnico di Milano, 2021.

[9] N. Pontani, "A numerical approach to investigate the role of partial saturation in the vibration induced by underground railway traffic," 2023. Accessed: Apr. 21, 2025. [Online]. Available: https://www.politesi.polimi.it/handle/10589/213452

[10] E. ROSSETTI, "Una procedura per il calcolo delle vibrazioni dovute al passaggio di treni nei tunnel ferroviari," Politecnico di Milano, 2023. Accessed: Mar. 01, 2025. [Online]. Available: https://www.politesi.polimi.it/handle/10589/208632

[11] V. Maugeri and L. Martinelli, "Relazione preliminare Punto B: definizione dello spettro di carico del treno a partire da misure di vibrazione - Contratto MM 16.11.2023," Milano, Feb. 2025.

[12] Ente Nazionale di Normazione, "Vibrations - Assessment of the Static and Dynamic Behavior of Railway Track Systems, UNI 11389-1," Milan, 2011.

[13] C. Esveld, *Modern Railway Track Second Edition*, 2e ed. Dior Zwarthoed-van Nieuwenhuizen, 2001.

[14] G. Lombaert and G. Degrande, "Ground-borne vibration due to static and dynamic axle loads of InterCity and high-speed trains," *J Sound Vib*, vol. 319, no. 3–5, pp. 1036–1066, Jan. 2009, doi: 10.1016/J.JSV.2008.07.003.

[15] K. Knothe and S. L. Grassie, "Modelling of Railway Track and Vehicle/Track Interaction at High Frequencies," *Vehicle System Dynamics*, vol. 22, no. 3–4, pp. 209–262, Jan. 1993, doi: 10.1080/00423119308969027.

[16] D. P. Connolly, G. Kouroussis, O. Laghrouche, C. L. Ho, and M. C. Forde, "Benchmarking railway vibrations – Track, vehicle, ground and building effects," *Constr Build Mater*, vol. 92, pp. 64–81, Sep. 2015, doi: 10.1016/J.CONBUILDMAT.2014.07.042.

[17] Q. Y. Xu, X. Ou, F. T. K. Au, P. Lou, and Z. C. Xiao, "Effects of track irregularities on environmental vibration caused by underground railway," *European Journal of Mechanics - A/Solids*, vol. 59, pp. 280–293, Sep. 2016, doi: 10.1016/J.EUROMECHSOL.2016.04.005.

[18] Q. Huang, P. Li, D. Zhang, H. Huang, and F. Zhang, "Field Measurement and Numerical Simulation of Train-Induced Vibration from a Metro Tunnel in Soft Deposits," *Advances in Civil Engineering*, vol. 2021, no. 1, p. 6688746, Jan. 2021, doi: 10.1155/2021/6688746.

[19] Roberto. Villaverde, "Fundamental concepts of earthquake engineering," p. 949, 2009.

[20] R. Lancellotta, "Geotechnical Engineering," Jul. 2008, doi: 10.1201/9781482265934.

[21] G. Lombaert, G. Degrande, and D. Clouteau, "The influence of the soil stratification on free field traffic-induced vibrations," *Archive of Applied Mechanics*, vol. 71, 2001.

[22] M. Schevenels, G. Degrande, and G. Lombaert, "The influence of the depth of the ground water table on free field road traffic-induced vibrations," *INTERNATIONAL JOURNAL FOR NUMERICAL AND ANALYTICAL METHODS IN GEOMECHANICS Int. J. Numer. Anal. Meth. Geomech*, vol. 28, pp. 395–419, 2004, doi: 10.1002/nag.342.

[23] R. G. Lyons, *Understanding Digital Signal Processing Third Edition*.

[24] A. V. . Oppenheim and R. W. . Schafer, *Discrete-time signal processing*, 2nd ed. 1999.

[25] X. Sheng, "A review on modelling ground vibrations generated by underground trains," *International Journal of Rail Transportation*, vol. 7, no. 4, pp. 241–261, Oct. 2019, doi: 10.1080/23248378.2019.1591312.

[26] A. V. Metrikine and A. C. W. M. Vrouwenvelder, "SURFACE GROUND VIBRATION DUE TO A MOVING TRAIN IN A TUNNEL: TWO-DIMENSIONAL MODEL," *J Sound Vib*, vol. 234, no. 1, pp. 43–66, Jun. 2000, doi: 10.1006/JSVI.1999.2853.

[27] P. Koziol, C. Mares, and I. Esat, "Wavelet approach to vibratory analysis of surface due to a load moving in the layer," *Int J Solids Struct*, vol. 45, no. 7–8, pp. 2140–2159, Apr. 2008, doi: 10.1016/J.IJSOLSTR.2007.11.008.

[28] X. Sheng, C. J. C. Jones, and D. J. Thompson, "Modelling ground vibration from rail traffic using the discrete wavenumber finite and boundary element methods," 2002. Accessed: May 17, 2025. [Online]. Available: https://eprints.soton.ac.uk/379500/1/TM899.pdf

[29] J. A. Forrest and H. E. M. Hunt, "A three-dimensional tunnel model for calculation of train-induced ground vibration," *J Sound Vib*, vol. 294, no. 4–5, pp. 678–705, Jul. 2006, doi: 10.1016/J.JSV.2005.12.032.

[30] J. A. Forrest and H. E. M. Hunt, "Ground vibration generated by trains in underground tunnels," *J Sound Vib*, vol. 294, no. 4–5, pp. 706–736, Jul. 2006, doi: 10.1016/J.JSV.2005.12.031.

[31] M. F. M. Hussein and H. E. M. Hunt, "A numerical model for calculating vibration from a railway tunnel embedded in a full-space," *J Sound Vib*, vol. 305, no. 3, pp. 401–431, Aug. 2007, doi: 10.1016/J.JSV.2007.03.068.

[32] S. Gupta, Y. Stanus, G. Lombaert, and G. Degrande, "Influence of tunnel and soil parameters on vibrations from underground railways," *J Sound Vib*, vol. 327, no. 1–2, pp. 70–91, Oct. 2009, doi: 10.1016/J.JSV.2009.05.029.

[33] T. Balendra, K. H. Chua, K. W. Lo, and S. L. Lee, "Steady-State Vibration of Subway-Soil-Building System," *J Eng Mech*, vol. 115, no. 1, pp. 145–162, Jan. 1989, doi: 10.1061/(ASCE)0733-9399(1989)115:1(145).

[34] K. H. Chua, K. W. Lo, and T. Balendra, "Building Response due to Subway Train Traffic," *Journal of Geotechnical Engineering*, vol. 121, no. 11, pp. 747–754, Nov. 1995, doi: 10.1061/(ASCE)0733-9410(1995)121:11(747).

[35] S. Zhou, X. Zhang, H. Di, and C. He, "Metro train-track-tunnel-soil vertical dynamic interactions – semi-analytical approach," *Vehicle System Dynamics*, vol. 56, no. 12, pp. 1945–1968, Dec. 2018, doi: 10.1080/00423114.2018.1444182.

[36] F. Perotti, M. Tomasin, S. Alfi, and A. Collina, "A decoupled numerical procedure for modelling soil interaction in the computation of the dynamic response of a rail track," *Procedia Eng*, vol. 199, pp. 2573–2578, Jan. 2017, doi: 10.1016/J.PROENG.2017.09.335.

[37] W. Gardien and H. G. Stuit, "Modelling of soil vibrations from railway tunnels," *J Sound Vib*, vol. 267, no. 3, pp. 605–619, Oct. 2003, doi: 10.1016/S0022-460X(03)00727-2.

[38] Q. Xu, Z. Xiao, T. Liu, P. Lou, and X. Song, "Comparison of 2D and 3D prediction models for environmental vibration induced by underground railway with two types of tracks," *Comput Geotech*, vol. 68, pp. 169–183, Jul. 2015, doi: 10.1016/J.COMPGEO.2015.04.011.

[39] J. Katsikadelis, *Boundary elements: theory and applications*. 2002.

[40] L. Andersen and C. J. C. Jones, "Coupled boundary and finite element analysis of vibration from railway tunnels—a comparison of two- and three-dimensional models," *J Sound Vib*, vol. 293, no. 3–5, pp. 611–625, Jun. 2006, doi: 10.1016/J.JSV.2005.08.044.

[41] X. Sheng, C. J. C. Jones, and D. J. Thompson, "Modelling ground vibration from railways using wavenumber finite- and boundary-element methods," *Proceedings of the Royal Society A: Mathematical, Physical and Engineering Sciences*, vol. 461, no. 2059, pp. 2043–2070, 2005, Accessed: May 18, 2025. [Online]. Available: /doi/pdf/10.1098/rspa.2005.1450

[42] R. Paolucci, A. Maffeis, L. Scandella, M. Stupazzini, and M. Vanini, "Numerical prediction of low-frequency ground vibrations induced by high-speed trains at Ledsgaard, Sweden," *Soil Dynamics and Earthquake Engineering*, vol. 23, no. 6, pp. 425–433, Aug. 2003, doi: 10.1016/S0267-7261(03)00061-7.

[43] E. Kausel, "Thin-layer method: Formulation in the time domain," *Int J Numer Methods Eng*, vol. 37, no. 6, pp. 927–941, Mar. 1994, doi: 10.1002/NME.1620370604;WGROUP:STRING:PUBLICATION.

[44] L. Meirovitch, *Fundamentals of Vibrations*. Waveland Press, 2010.

[45] Hitachi Rail Italy, "Metro Leonardo - Dichiarazione Ambientale di Prodotto," no. Pistoia, 2017.

[46] "butter - Butterworth filter design - MATLAB." Accessed: May 25, 2025. [Online]. Available: https://www.mathworks.com/help/signal/ref/butter.html#bucsfsr-1

[47] Q. Zhou *et al.*, "Measuring Vibrations of Subway Tunnel Structures with Cracks," *Buildings 2024, Vol. 14, Page 2660*, vol. 14, no. 9, p. 2660, Aug. 2024, doi: 10.3390/BUILDINGS14092660.

[48] M. Ma, L. Xu, W. Liu, and X. Tan, "Semi-analytical solution of a coupled tunnel-soil periodic model with a track slab under a moving train load," *Appl Math Model*, vol. 128, pp. 588–608, Apr. 2024, doi: 10.1016/J.APM.2024.01.038.

[49] W. M. Zhai, K. Y. Wang, and J. H. Lin, "Modelling and experiment of railway ballast vibrations," *J Sound Vib*, vol. 270, no. 4–5, pp. 673–683, Mar. 2004, doi: 10.1016/S0022-460X(03)00186-X.

[50] T. Bonomi, "Groundwater level evolution in the Milan area: natural and human issues," in *IAHS PUBLICATION*, Birmingham: In Impacts of Urban Growth on Surface Water and Groundwater Quality (Proceedings of IUGG 99 Symposium HS5), Jul. 1999, pp. 195–202.

[51] Dassault Systèmes, "30.1.2 Contact pressure-overclosure relationships," in *ABAQUS Analysis User's Manual*, Dassault Systèmes.

[52] Z. Yuan, A. Boström, and Y. Cai, "Benchmark solution for vibrations from a moving point source in a tunnel embedded in a half-space," *J Sound Vib*, vol. 387, pp. 177–193, Jan. 2017, doi: 10.1016/J.JSV.2016.10.016.

[53] F. Pled and C. Desceliers, "Review and Recent Developments on the Perfectly Matched Layer (PML) Method for the Numerical Modeling and Simulation of Elastic Wave Propagation in Unbounded Domains," *Archives of Computational Methods in Engineering 2021 29:1*, vol. 29, no. 1, pp. 471–518, Apr. 2021, doi: 10.1007/S11831-021-09581-Y.

[54] Y. Wang, M. Zhou, Y. Cao, X. Wang, Z. Li, and M. Ma, "Simplified Tunnel–Soil Model Based on Thin-Layer Method–Volume Method–Perfectly Matched Layer Method," *Applied Sciences 2024, Vol. 14, Page 5692*, vol. 14, no. 13, p. 5692, Jun. 2024, doi: 10.3390/APP14135692.

[55] G. R. Liu and S. S. Quek Jerry, "A non-reflecting boundary for analyzing wave propagation using the finite element method," *Finite Elements in Analysis and Design*, vol. 39, no. 5–6, pp. 403–417, Mar. 2003, doi: 10.1016/S0168-874X(02)00081-1.

[56] G. R. Liu and J. D. Achenbach, "A Strip Element Method for Stress Analysis of Anisotropic Linearly Elastic Solids," *J Appl Mech*, vol. 61, no. 2, pp. 270–277, Jun. 1994, doi: 10.1115/1.2901440.

[57] Dassault Systèmes, "22.2 Infinite elements," in *ABAQUS Analysis User's Manual*, Dassault Systèmes.

[58] Dassault Systèmes, "3.3.1 Solid infinite elements," in *ABAQUS Theory Manual*, Dassault Systèmes.

[59] J. Lysmer and R. L. Kuhlemeyer, "Finite Dynamic Model for Infinite Media," *Journal of the Engineering Mechanics Division*, vol. 95, no. 4, pp. 859–877, Aug. 1969, doi: 10.1061/JMCEA3.0001144.

[60] Q. Xu, Z. Xiao, T. Liu, P. Lou, and X. Song, "Comparison of 2D and 3D prediction models for environmental vibration induced by underground railway with two types of tracks," *Comput Geotech*, vol. 68, pp. 169–183, Jul. 2015, doi: 10.1016/J.COMPGEO.2015.04.011.

[61] Dassault Systèmes, "2.6.1 Direct steady-state dynamic analysis," in *ABAQUS Theory Manual*, 2.6.1 Direct steady-state dynamic analysis.

[62] J. Bendat and A. Piersol, *Random data: analysis and measurement procedures*. 2011.

[63] T. Arvidsson, A. Zangeneh, D. Cantero, and A. Andersson, "Influence of Sleeper Passing Frequency on Short Span Bridges: Validation against Measured Results," Apr. 2017.

[64] X. Wu, W. Cai, M. Chi, L. Wei, H. Shi, and M. Zhu, "Investigation of the effects of sleeper-passing impacts on the high-speed train," *Vehicle System Dynamics*, vol. 53, no. 12, pp. 1902–1917, Dec. 2015, doi: 10.1080/00423114.2015.1091085.